Impact of Vane Trailing Edge Damage on Turbine Stage Performance

A thesis submitted for the degree of
Doctor of Philosophy
Hilary term, 2025



Zelimhan Raduev
Supervised by Prof. Thomas Povey

Oriel College
Osney Thermofluids Institute
University of Oxford

This page is intentionally blank

Abstract

High-pressure nozzle guide vanes operate under extreme mechanical and thermal stresses, with gas temperatures almost a third as hot as the Sun's surface. As a result, trailing edge burn-back is inevitable, and yet, its impact on performance remains largely unknown.

This research investigates the impact of four levels of burn-back damage (based on a statistical analysis of in-service deterioration data), from new to severely damaged, on vane-row and stage performance using a combination of high-fidelity experimental, numerical, and modelling methods.

High-fidelity experiments were conducted at the University of Oxford's Engine Component AeroThermal facility, an annular test rig operating at engine-representative Mach and Reynolds numbers, and coolant flow conditions. These experiments were complemented with simulations to provide further insights into the underlying aerodynamic mechanisms. The vane-row results showed that increasing burn-back led to increased loss and significant wake distortion due to the formation of a strong pair of counterrotating pair of vortices at the burn-back edges (vorticity continuity forcing paired and opposing structures), increased overall vane capacity, and led to significant changes in the vane exit whirl angle distributions.

Following validation of the simulation method, the study was extended to full-stage unsteady simulations incorporating a downstream rotor row. Surprisingly, increasing burn-back reduced loss in the rotor-relative frame due to weakened secondary flows. This reduction offset the increased loss in the vane leading to only marginal changes in the overall stage efficiency. Burn-back also decreased stage-specific work driven by tangential velocity changes, and increased stage reaction from intra-stage pressure variations.

This research provides a comprehensive analysis of the impact of vane trailing edge damage on turbine performance, evaluates the predictive accuracy of numerical methods for performance penalties, and contributes significantly to whole-life engine performance modelling.

This page is intentionally blank

Dedication

I dedicate this thesis to my homeland, Chechnya, whose history, struggles, and resilience continue to motivate my every endeavour, and to the United Kingdom, which gave my family safety, opportunity, and hope when we had nothing.

This page is intentionally blank

Acknowledgments

First and foremost, I would like to thank Allah (SWT) for His countless blessings, without which this work would not have been possible.

Next, I would like to express my sincere gratitude to my supervisor, Prof. Thomas Povey, for his mentorship over the last five years. I feel extremely fortunate to have learned from such a rigorous academic and an exceptional person—I cannot thank him enough. I am also grateful to my industrial supervisor, Dougal Jackson at Rolls-Royce, for his constant support, insight, and patience throughout this project. I extend my gratitude as well to Prof. Budimir Rosic, who, despite not being my supervisor, generously offered guidance during my time at the lab.

Many people contributed to this thesis, and while I cannot name everyone, some deserve special mention. In the blowdown group, I thank Nafiz Chowdhury for his tireless support with my experiments, Andrew Messenger for his engineering advice, Daniel Burdett and Mathias Michaud for their patience in answering my questions and helping shape my research, and Paul Beason for his help with the test facility operations. At Rolls-Royce, I thank Lionel Goh and Ali Cem Boge for their help with the Hydra code, and Roshen Jaswantlal and Marcus Meyer for their assistance with other aspects of my work. To those in my group who made the lab enjoyable, I thank Aravin Dass Naidu, Jonas Amend, James Cartledge, Matthew Stokes, and Lucas Rey. Of those outside my group, for the same reason, I thank Alexandar Murray, Andrew Pilkington, Jamie Saw, Ben Coulton, Simla Saglam, Nikolas Karefyllidis, and Michael van de Noort. In the wider lab, I thank Dominic Harris and Duncan Blake for their help machining engine parts, and Craig Parsons for his invaluable IT support.

I would also like to thank Timur Mozurho and my sister-in-law, Medina Tiganj, for their enthusiasm and encouragement. Lastly, I wish to thank my older brother, Johar Raduev, whose selfless dedication to our family gave me the peace of mind to pursue this doctorate, and my mother, Lidia Radueva, for her unwavering support and sacrifices, even when wishing I were home more often. This thesis is as much theirs as it is mine.

This page is intentionally blank

Contents

Abstract ..... **iii**
Dedication ..... **v**
Acknowledgments ..... **vii**
Contents ..... **ix**
Nomenclature ..... **xi**
Chapter 1 – Introduction **1**
1.1 – Background 1
1.2 – Research outcomes 4
1.3 – Thesis structure 5
Chapter 2 – Review of related literature **9**
2.1 – Vane and rotor loss mechanisms 9
2.2 – Loss sensitivity to trailing edge design 15
2.3 – Stage interaction loss mechanisms 23
2.4 – Vane flow capacity and influencing factors 29
2.5 – Trailing edge damage mechanisms 35
2.6 – Loss sensitivity to trailing edge damage 39
Chapter 3 – Trailing edge damage shapes **45**
3.1 – Introduction 45
3.2 – Data available and summary of statistics used 45
3.3 – Design space and chosen geometries 46
3.4 – Machining process 47
Chapter 4 – Vane aerodynamic performance **51**
4.1 – Introduction and literature review 52
4.2 – Trailing edge damage shapes 55
4.3 – Experimental method 57
4.4 – Numerical method 59
4.5 – Results and discussion 61
4.5.1 – Distributions of local KE loss coefficient 62
4.5.2 – Axial vorticity distributions 64
4.5.3 – Radial distributions of circumferentially-averaged KE loss coefficient 68
4.5.4 – Radial distributions of circumferentially-averaged exit flow angle 72
4.5.5 – Vane loading distributions 75
4.5.6 – Boundary layer profiles and loss 77
4.5.7 – Coolant mass flow rates and loss with introduction of coolant 82
4.5.8 – Overall aerodynamic performance 84
4.5.9 – Impact on capacity and stage performance 86
4.6 – Conclusions 86
Nomenclature 89
References 90
Chapter 5 – Vane flow capacity **93**
5.1 – Introduction and literature review 94
5.1.1 – Current study 99

5.2 – Trailing edge damage shapes 99
5.3 – Experimental method 100
5.4 – Numerical method 104
5.5 – Results and discussion 106
5.5.1 – Vane exit circumferential static pressure distributions 106
5.5.2 – Overall vane flow capacity 109
5.5.3 – Correlation to geometrical parameters 112
5.5.4 – Coolant capacity 112
5.5.5 – Impact of coolant capacity on vane capacity 114
5.5.6 – Vane boundary layer characteristics 116
5.5.7 – Aerodynamic flow field 118
5.6 – Conclusions 128
Nomenclature 130
References 132
Chapter 6 – Turbine stage performance 135
6.1 – Introduction and literature review 136
6.1.1 – Impact of burn-back on engine life and fuel consumption 137
6.1.2 – Impact of burn-back on vane and stage aerodynamic performance 138
6.1.3 – Current study 140
6.2 – Trailing edge damage shapes 140
6.3 – Numerical method 142
6.4 – Performance parameters 146
6.4.1 – Loss coefficients 146
6.4.2 – Whirl angle 148
6.4.3 – Capacity, reaction, specific work, and efficiency 148
6.5 – Numerical validation 150
6.6 – Results and discussion 154
6.6.1 – Distributions of local KE loss coefficient 155
6.6.2 – Distributions of axial vorticity 158
6.6.3 – Radial distributions of circumferentially averaged loss coefficient 161
6.6.4 – Plane-averaged and mixed-out KE loss 164
6.6.5 – Radial distributions of circumferentially averaged pressures and angles 166
6.6.6 – Radial mass flow distributions 171
6.6.7 – Capacity and mass flow analysis 172
6.6.8 – Vane and blade loading isentropic Mach number distributions 175
6.6.9 – Velocity triangle analysis 178
6.6.10 – Overall stage performance 180
6.7 – Conclusions 183
Nomenclature 187
References 188
Chapter 7 – Conclusions 193
7.1 – Recommendations for future work 195
References 199
Appendix 1 – Numerical method detail 205
Appendix 2 – Measurement uncertainty 211
Statements of authorship 219

Nomenclature

The results chapters take the form of peer-reviewed journal papers. To maintain consistency with the published (or in-review) papers, those chapters have their own separate nomenclature identical to the journal submission. Instead, in this nomenclature the acronyms, symbols, and subscripts used in the rest of this thesis (i.e., introduction, literature reviews, and appendices) are listed.

Acronyms

BPP	blade passing period
BR	blowing ratio
CAD	computer aided design
CAP15	capacity 15 ECAT configuration
CEESI	Colorado Engineering Experiment Station, Inc.
CFD	computational fluid dynamics
DLR	German aerospace center
ECAT	engine component aerothermal facility
ECAT+	engine component aerothermal facility plus
HP	high-pressure
HPT	high-pressure turbine
HPV	hub passage vortex
KE	kinetic energy
NGV	nozzle guide vane
PS	pressure surface
PV	passage vortex
RGG	rotating cascade tunnel Göttingen
SS	suction surface
TE	trailing edge
TET	turbine entry temperature
TLV	tip leakage vortex

Romans

A	area [mm^2]
A_{BB}	burn-back area [mm^2]
A_{eff}	effective flow area [mm^2]
A_{ref}	reference area [mm^2]
C_d	discharge coefficient [–]
C_{t}	tangential chord length [mm]
C_x	axial chord length [mm]
C^*	critical flow function [–]
c_{p}	specific heat capacity [J kg^{-1} K^{-1}]
c_{pb}	base pressure coefficient [–]
d	tangential depth of burn-back [mm]

F	result [-]
h_1	radial location of the damage feature at the trailing edge [mm]
h_2	radial location of the damage feature at the damage front [mm]
I	momentum flux ratio [–]
M	Mach number [–]
$\dot{m}$	mass flow rate [kg s^{-1}]; uncorrected mass flow to the vane [kg s^{-1}]
$\dot{m}'$	actual mass flow delivered to the vane [kg s^{-1}]
$\dot{m}''$	mass flow correction term [kg s^{-1}]
p	pressure (total or static) [Pa]
R	universal gas constant [J kg^{-1} K]
r	radius [mm]
S	span height [mm]
T	temperature (static or total) [K]
t	trailing edge thickness [mm] / time [s]
t_r	rotor passing period
u	local velocity [ms^{-1}]
V	volume [m^3]
w	geometric throat width [mm]
w_1	width of burn-back at TE [mm]
w_2	width of burn-back at damage front [mm]
x	axial position [mm]
Y^+	non-dimensional wall distance [-]

Greeks

β	impingement angle [rads]
Γ	flow capacity [kg s^{-1} $K^{1/2}$ Pa^{-1}]
δ^{99}	boundary layer thickness [mm]
δ^*	boundary layer displacement thickness [mm]
θ	boundary layer momentum thickness [mm]
γ	ratio of specific heat capacities [–]
ζ	KE loss coefficient [–]
ζ_p	profile loss coefficient [–]
η	efficiency [–]
ρ	local density [kg m^{-3}]
σ	bias uncertainty [–]
$\sigma^{\%}$	bias uncertainty as a percentage [%]
X	$(\gamma - 1)/\gamma$

Subscripts

0	stagnation condition
1	upstream of NGV; mainstream; Geometry 1
2	downstream of NGV / upstream of rotor; film coolant stream; Geometry 2
3	downstream of rotor; TE slot coolant stream; Geometry 3
4	Geometry 4
BB	burn-back region
CCN	case coolant nozzle
HCN	hub coolant nozzle

c	coolant condition
cc	case coolant condition
engine	engine condition
hc	hub coolant condition
m	Mainstream condition
ref	reference value
rig	rig condition
s	isentropic condition
throat	throat condition

This page is intentionally blank

Chapter 1 – Introduction

This chapter begins by providing background information on the research showing where the work fits in. The outcomes of the research are then discussed, before concluding with a summary of the thesis structure, including a brief description of each chapter.

1.1 – Background

The application of gas turbines to aircraft propulsion has revolutionised global transportation, shaping the modern world. Without it, society would not be as advanced as it is today. At the heart of this invention is a machine capable of converting the chemical energy in the fuel into thrust that can propel a large civil aircraft carrying a full passenger payload at speeds more than twice as fast as the fastest Formula 1 car. It is an engineering marvel. Since its first application by Sir Frank Whittle in the early 1930s, the gas turbine has undergone many incremental improvements, with each generation pushing closer to the boundaries of what is physically possible.

Modern civil gas turbine engines consists of five main components which include: the fan, which accelerates the bypass flow that produces the majority of the aircraft's forward thrust; the compressor, which compresses the incoming air, subsequently raising the pressure and temperature; the combustor, where fuel is sprayed into the already pressurised air and ignited to further raise the gas temperature; the turbine, which extracts the energy from the hot gases to drive the fan and compressor through shaft work; and lastly, the propelling nozzles, which expand the bypass and exhaust streams to produce the engine's net thrust. The compressor and turbine components are also staged to incrementally optimize compression and expansion, thereby improving engine performance. These components are illustrated in the assembled engine of Figure 1.1, with the red box highlighting the high-pressure turbine stage (HPT), immediately downstream of the combustor, where the temperatures and pressures are highest. This region is the focus of this research.

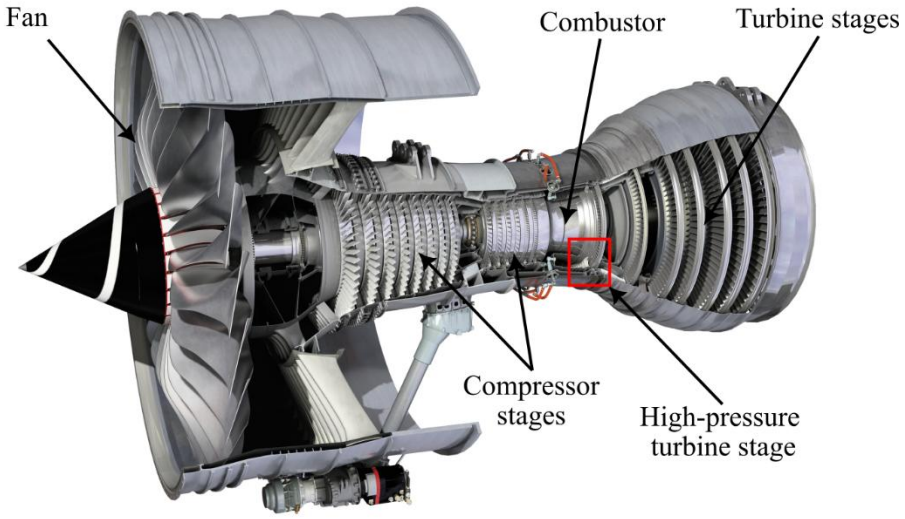


Figure 1.1: Rolls-Royce Trent 900 engine, adapted from Rolls-Royce [1].

The thermodynamic processes that govern gas turbine performance are detailed in many engineering textbooks (e.g., Dixon and Hall [2]) and so are omitted here for brevity. A key takeaway is that the engine power and efficiency are strongly influenced by the compressor inlet to exit pressure ratio, as well as the turbine entry temperature (TET). On the latter, more simply, higher TET typically yield more powerful and efficient engines. And so, over the decades since the first engine, this has been the trend, as shown in Figure 1.2 for temperature. Initially, the increasing TET was facilitated by material advancements, however, from the 1960s onwards, the advancements were supplemented with innovative cooling technologies using cooler compressor air to cool turbine components. More recently, from the 2000s, ceramic thermal barrier coatings, which have lower conductivity than the metal alloys, were applied to component surfaces to allow for even higher temperatures. Today, the gas temperatures far exceed the melting point of any turbine component material.

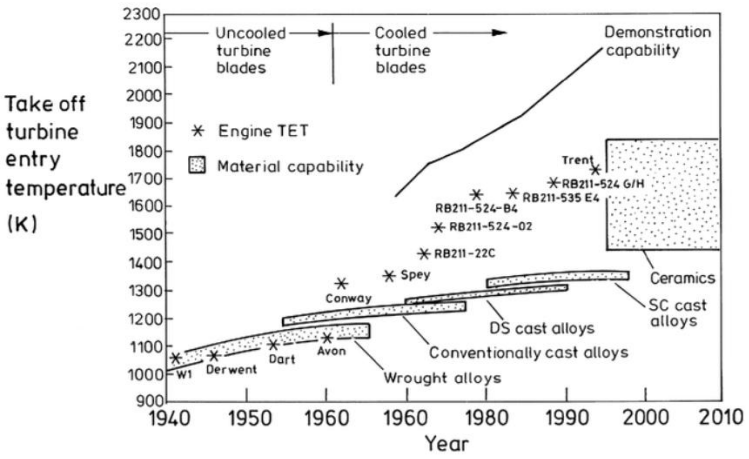


Figure 1.2: Trend in turbine entry temperature for Rolls-Royce jet engines since 1940 (from Cumpsty and Heyes [3]).

However, excessive TET can have negative impact on the engine. Cumpsty and Heyes [3] describe the setting of the TET as a balancing act between engine performance and turbine component life. Despite advancements made in aeroengine technology, the extreme conditions in which turbine components operate often lead to inevitable deterioration over time, which consequently has negative effects on the engine performance. The deterioration can manifest itself in many ways, but of particular concern to this research is *burn-back* damage, where the trailing edge of turbine components experience material loss due to erosion and oxidation, the latter of which is strongly affected by temperature (Cumpsty and Heyes [3]). Preventing this damage while maintaining adequate thrust is impossible. The key question, therefore, is how detrimental is this damage feature to engine performance? Surprisingly, the answer to this remains largely unknown: a notable gap exists in the open literature, with only a handful of studies investigating this phenomenon—most of which rely on simplistic, non-engine-representative experimental setups. In theory, this damage feature should be of significant concern as it will influence the aerodynamics of the turbine stage, leading to performance and efficiency penalties, also leading to increased fuel consumption and reduced component life.

This research aims to address this critical knowledge gap by investigating the impact of burn-back using a combination of high-fidelity experimental, numerical, and modelling methods. The findings from this work have the potential to inform future component designs,

improve maintenance strategies, and ultimately, lead to a more efficient engine operation over a longer period. Given the global push for a more environmentally sustainable aviation industry, this is crucial.

1.2 – Research outcomes

This research uses the Engine Component AeroThermal (ECAT) facility at the University of Oxford for high-accuracy aerodynamic performance evaluation, under engine representative operating conditions. Real engine parts with simulated burn-back designs (based on real deterioration data) are used to experimentally quantify the impact of nozzle guide vane (NGV) trailing edge damage on aerodynamic performance loss and flow capacity changes. This experimental campaign is complemented with a computational fluid dynamics (CFD) campaign that accurately matches the measured data, producing a fully validated numerical process that predicts the impact of this type of damage on performance. These two data sets are analysed to develop an understanding of the underlying mechanisms responsible for changes observed in performance. The experimental data is also used to generate empirical correlations for key performance parameters so deterioration assessments can be improved within industry, in fact, the data produced from this work has already been implemented within Rolls-Royce.

The above work shows significant impact on the downstream turbine rotor inlet conditions, and thus, the validated CFD method mentioned is extended so that full stage unsteady simulations can be performed. These simulations allow the impact of NGV trailing edge damage on turbine stage performance to be quantified, and as before, the underlying mechanisms to be identified and reported for better understanding.

To date, this research has culminated in *three* journal paper submissions in the premier journal for this field, two of which have been published, and one other which is presently in review.

1.3 – Thesis structure

The high-level overview of the thesis structure is shown in Figure 1.3, where the arrows show the flow of information. An integrated-style thesis is presented consisting of three journal papers, complemented with an introduction, literature review, trailing edge damage shapes, conclusions, and appendices chapters. The contents of each chapter are now briefly summarised.

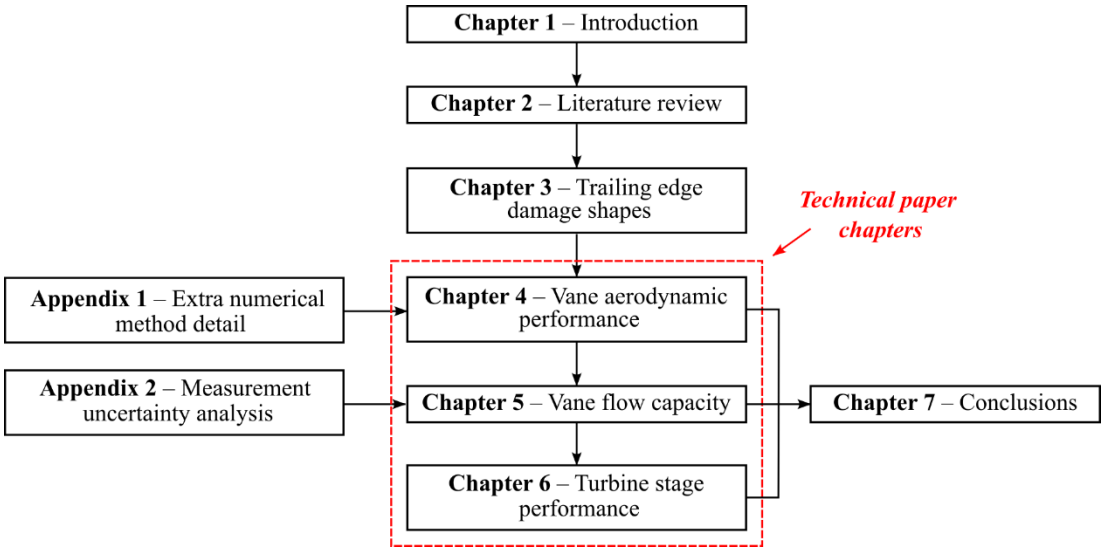


Figure 1.3: High-level overview of thesis structure.

In *Chapter 1*, the background and scope of this research is discussed, followed by an overview of the research outcomes and the structure of this thesis and work.

In *Chapter 2*, the relevant literature on turbine row and stage loss mechanisms, vane flow capacity, and the impact of trailing edge damage on performance are reviewed. The focus is on aspects of turbine aerodynamics that are directly affected by the type of trailing edge damage central to this research. The self-contained journal chapters also have their own literature review.

In Chapter 3, the trailing edge burn-back geometries investigated in this research are defined. Statistical analysis of industry supplied deterioration data generated service representative burn-back damage geometries, from which three damaged geometries (in

addition to the undamaged baseline) were selected. The chapter also details the machining process used to produce these shapes in the experiments.

In *Chapter 4*, the impact of trailing edge burn-back on the aerodynamic performance of cooled transonic high-pressure NGVs is investigated. This chapter takes the form of a *journal paper*, presently published [4]. It considers four levels of burn-back damage and use a high technology-readiness-level (TRL) engine parts annular cascade facility to perform area traverse measurements. The engine-representative experimental data is complemented with validated CFD simulations to understand the underlying mechanisms responsible for any change. This chapter concludes that increasing burn-back leads to the formation of a pair of counterrotating vortices at the edges of the burn-back; significant increase in total pressure loss and secondary kinetic energy; and significant variation in exit whirl angle affecting rotor inlet conditions. These effects, among others, are quantified and the implications for whole-life engine performance considered. To the authors' knowledge, this is the most comprehensive study of its type and complements the very few other related studies in the open literature well.

In *Chapter 5*, the impact of trailing edge burn-back on the flow capacity of cooled transonic high-pressure NGVs is investigated. This chapter takes the form of a *journal paper*, presently published [5]. It considers the same four levels of burn-back damage but operate the high TRL facility in blow-down mode where the facility pressures and mass flow rates are allowed to decay during the run (rather than kept steady) so a full capacity characteristic can be measured. The ultra-low uncertainty experimental capacity characteristic is also complemented with a numerical characteristic, generated by running validated CFD simulations at five different operating points for each build. As before, this is to understand the underlying mechanisms responsible for any change. This chapter concludes that increasing burn-back leads to a monotonic increase in overall flow capacity and coolant capacity, and very importantly, contrary to industry practices, shows that an exchange rate of unity should not be expected between flow capacity and geometric throat area. The main factor influencing flow capacity is shown to be the static pressure field changes in the passage. This factor, among

others, are quantified and the implications for engine performance are considered. To the authors' knowledge, this is the first study of its type.

The previous two studies showed that trailing edge damage has a significant effect on the row performance, but to consider the wider implication on the engine performance, in *Chapter 6*, the impact of NGV trailing edge burn-back on the performance of a cooled transonic HPT stage is investigated. This chapter, like the previous two, takes the form of a *journal paper*, presently in review [6]. It considers the same four levels of burn-back damage as the previous two chapters; however, the results in this chapter are mostly from unsteady stage simulations (based on extending a validated numerical method). This chapter concludes that increasing burn-back surprisingly leads to a decrease in rotor relative loss, which offsets the increase in vane loss leading to only a marginal change in stage efficiency. The latter effect is despite significant changes in stage reaction, specific work, intra-stage pressures, and velocity triangles. The underlying physics of these effects are studied, and the changes in different performance parameters are quantified. To the authors' knowledge, this is also the first study of its type.

In *Chapter 7*, the key findings from this thesis are summarised, and areas of future research are outlined.

In *Appendix 1*, some extra detail omitted regarding the numerical method form the journal papers is documented for completeness of the thesis.

In *Appendix 2*, the uncertainty in the experimental measurements of vane capacity is estimated and the method is documented.

This page is intentionally blank

Chapter 2 – Review of related literature

This chapter reviews literature on the following topics: loss mechanisms present in a modern high-pressure turbine (HPT) stage; the impact of the trailing edge design on performance; vane flow capacity, and its influencing factors; and trailing edge damage mechanisms along with their impact on performance.

2.1 – Vane and rotor loss mechanisms

Today, the mechanisms influencing vane and rotor efficiencies are broadly categorised into three main groups: profile losses, secondary flow losses (sometimes referred to as endwall losses), and tip leakage losses. These loss mechanisms are seldom independent and rather, interact with each other significantly. Denton [7] provides a comprehensive review of these mechanisms, but they are briefly covered here before progressing to trailing edge design and flow associated losses.

Profile loss is characterised by any loss that will arise in the absence of endwall interaction, in other words, loss that will be present in a cascade with an infinite span (Day [8]). This loss was further categorised by Mee et al. [9] into boundary layer, shock, and trailing edge losses. Boundary layer loss is caused by the entropy generation due to viscous friction actions in the boundary layer. This loss is significantly higher on the suction surface due to the cubed relationship between entropy production rate and the near wall freestream velocity (Denton [7]). Shock wave loss occurs due to entropy generation caused by the rapid heat conduction and high viscous stresses that arise when air molecules are suddenly compressed and decelerated across a shock wave. Shock waves are extremely thin, so they create steep velocity, pressure, and temperature gradients when generated. Shock wave-boundary layer interaction also leads to entropy generation, primarily because a separation bubble will be formed at the foot of the shock, either rapidly thickening the boundary layer or causing earlier laminar-to-turbulent transition. The trailing edge loss component is mostly due to the mixing of the pressure and suction side streams, which is highly dependent on the trailing edge

geometry (particularly its thickness and shape, discussed more later). Here the loss is caused by entropy generation due to the shearing action between the freestream layers as they mix in the wake region. In their work, Mee et al. [9] experimentally measured the contribution of the boundary layer and shock wave terms and attributed the remaining to the trailing edge term (i.e., subtracted the first two terms from the measured overall loss). They showed the loss contribution from each term as a function of exit Mach number, as shown in Figure 2.1. In the subsonic regime, for their blade design, the boundary layer loss term dominated (accounting for as much as 66% of the total loss when $M = 0.6$), however, this term monotonically decreased with increasing Mach number (accounts for 54% of the total loss when $M = 0.9$). The mixing term (a catch-all term for everything else, including trailing edge flow) is of similar magnitude to the boundary layer loss but is always less in this regime. In the supersonic regime, with the rapid rise in shock wave related and mixing losses, the boundary layer became a smaller contributor (accounting for only 25% of the total loss), and the mixing loss became the dominant term, accounting for as much as 60% of the total loss. These results are obviously specific to their blade design and operating conditions. In general, all three terms contribute significantly to the total loss and so cannot be neglected.

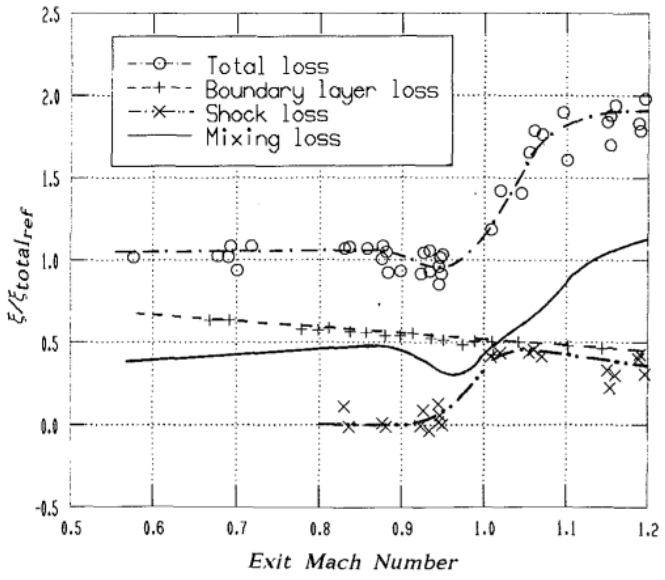


Figure 2.1: Decomposition of the overall profile loss term, from Mee et al. [9].

Secondary flow is more technically an umbrella term for flows (usually vortical in nature) that deviate from the main flow through the passage. They are typically not intentional but a natural consequence of the flow physics around the blade design, and this flow leads to losses in efficiency. In the traditional sense, it mostly refers to the flow structures that develop near the endwalls, and while tip leakage flow could also technically be considered a type of secondary flow, it is often treated separately due to its distinct characteristics and formation mechanisms. To be consistent with the traditional framework, they are separately discussed here too.

The results from this thesis show the formation of another significant secondary flow that is referred to as the burn-back vortices. These are highly disruptive, enhance other secondary flow, and ultimately lead to significantly higher aerodynamic losses (will be discussed in later results chapters).

Endwall secondary flow is due to the interaction between the upstream endwall boundary layer and the leading edge of the vane or blade. There are many illustrative models drawn to explain the interaction (with slight variations), and these are reviewed comprehensively by Langston [10] and Lampart [11]. The latter review is the more recent. The most common model is that of Sharma and Butler [12], as shown in Figure 2.2. In this model, the endwall boundary layer separates as it meets the leading edge stagnation point, forming a horseshoe vortex that wraps around the leading edge. This horseshoe vortex has two distinct legs, counter-rotating to each other, with one moving along the pressure side and the other moving along the suction side. The pressure side leg of the horseshoe vortex, otherwise referred to as the passage vortex, is drawn into the passage and migrates towards the suction side as it travels through the passage due to the cross-passage pressure gradient. The suction side leg, commonly referred to as the counter vortex, remains somewhat attached until the passage vortex reaches the suction side, after which they interact. There is some discrepancy between models with what happens next. Sharma and Butler [12] and Wang et al. [13] propose that the counter vortex wraps around the passage vortex, while other authors like Goldstein and Spores [14], and Doerffer and Amecke

[15] say that the counter vortex moves with the passage vortex, remaining right above it. Regardless of the model used, this passage vortex system radially migrates away from the endwalls as it progresses through the passage, and downstream of the trailing edge. In its movement, it entrains the nearby surface boundary layer and wake fluid, eventually mixing out with the mainstream flow. Wang et al. [13] and Doerffer and Amecke [15] also report formation of corner vortices due to flow separation at the junction between the endwall and the vane or blade surface.

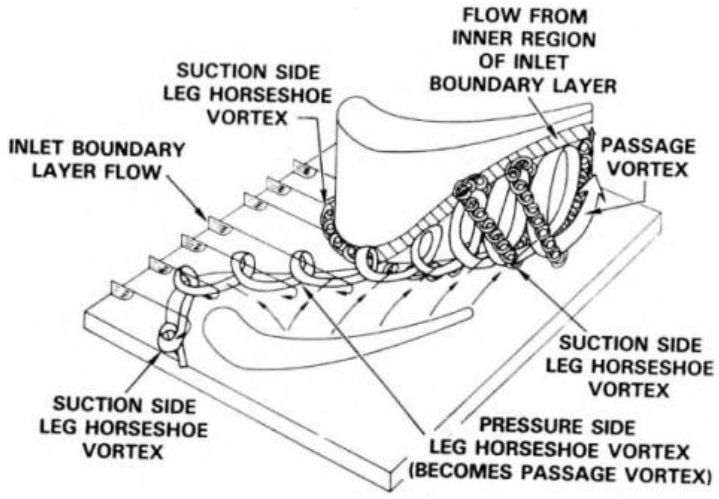


Figure 2.2: Endwall secondary flow model by Sharma and Butler [12], the vortices are intentionally exaggerated for the sake of clarity.

Denton [7] explains that a new endwall boundary layer must develop after the upstream endwall boundary layer separates at the leading edge. This new layer is also subject to the cross-passage pressure gradient and to an entraining effect from the main passage vortex system; this means that the endwall boundary layer fluid is continuously being entrained into the passage (strengthening the passage vortex), keeping the endwall boundary layer thin. In the case of a single stage cascade (with a vane row followed by a blade row), this endwall boundary layer will eventually be allowed to develop undisturbed when downstream of the vane row, and at some point, will meet the next blade row, and upon meeting the leading edge, again develop into a passage vortex.

In the case of blade rows with tip clearance (for rotating parts), the secondary flow behaviour is slightly different near the tip. The development of the above-discussed passage vortex system and a tip clearance vortex is illustrated by Sieverding in [16] in Figure 2.3. The tip clearance dynamics are also different depending on if the blade is shrouded or not. For the latter, Lampart [11] explains that the presence of a tip gap (unless it is a very small gap) means there is no stagnation point on the endwall where the horseshoe vortex may form, and therefore it is typically absent (note that for completeness, in specific cases, for example, due to jet impingements or transverse pressure gradients, a horseshoe vortex may still form). Rather, the flow approaching the leading edge is divided into two streams that are attracted to two different low static pressure zones. One stream is migrated by the cross-passage pressure gradient towards the adjacent blade's suction surface; Lampart refers to this as the tip wall passage vortex. The other stream leaks across the tip gap due to the pressure difference between the pressure and suction sides of the blade and leads to entropy generation when mixing with the primary flow (Denton [7]). This vortex is called the tip-leakage vortex (TLV) and is the dominant structure that is commonly the largest source of aerodynamic loss for rotating blade rows.

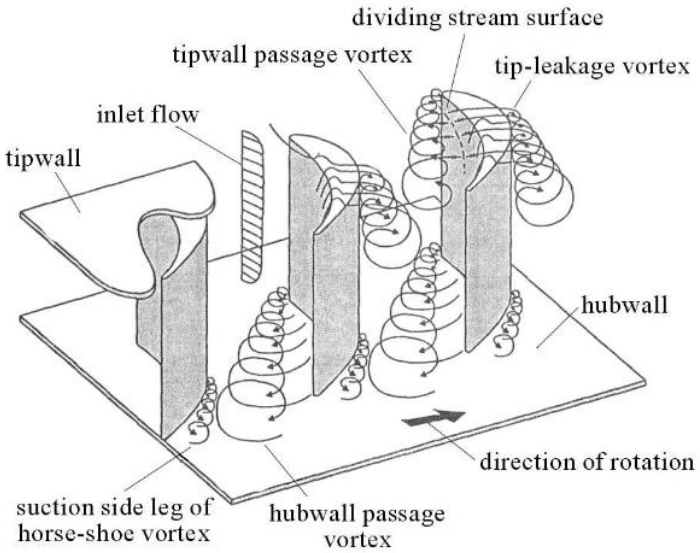


Figure 2.3: Tip clearance secondary flow model by Sieverding [16].

When blades are shrouded, the gap between the tip and casing is geometrically smaller. This reduces leakage flow, which in turn lowers the strength of the tip-clearance vortex and the aerodynamic losses associated with it. Salvadori et al. [17] reinforce the Sieverding model by numerically visualising the mentioned blade passage secondary flow together, as shown in Figure 2.4. They further show that the TLV is the greatest source of secondary flow entropy generation in the blade row, as seen on the downstream plane contour.

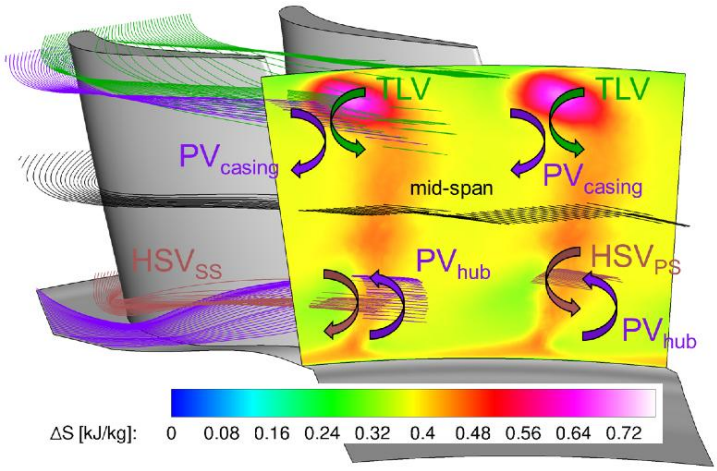


Figure 2.4: Numerical secondary flow visualisation from Salvadori et al. [17].

Film cooling systems can increase aerodynamic loss as a result of the coolant-mainstream flow mixing, and due to changes in profile loss mechanisms (due to the coolant stream and the physical presence of the coolant holes).Wilfert and Fottner [18] illustrated how the film coolant jet may interact with the upstream boundary layer and the mainstream flow, this is shown in Figure 2.5. They showed the formation of a kidney-shaped vortex, as well as the formation of a horseshoe vortex that follows the coolant jet. This effect scaled with coolant Mach number, i.e., at a higher blowing ratio, these two vortices are carried further. The presence of these vortices, and any strengthening, means increased entropy generation from the mixing process; in addition, it could mean thickening of the upstream boundary layer or earlier laminar-to-turbulent transition (both of which are also mechanisms of entropy generation).

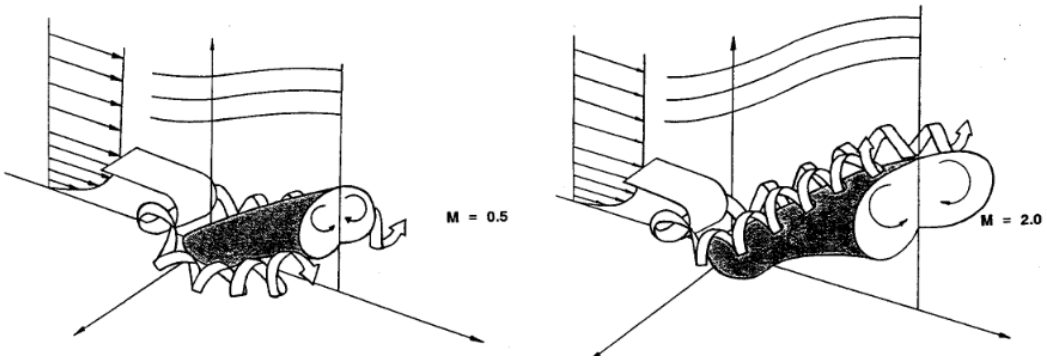


Figure 2.5: Film coolant flow interaction model by Wilfert and Fottner [18].

This section has briefly covered the main loss mechanisms present in the vane row or rotor row passages. Each of these, to some degree, is affected by NGV trailing edge damage and, in this thesis, is considered.

2.2 – Loss sensitivity to trailing edge design

Trailing edge loss was briefly mentioned under the profile loss section above. Due to its significance to loss, and relevance to the thesis topic (burn-back location), it will be further discussed here in the context of loss sensitivity to trailing edge design. The formation mechanism for trailing edge vortex shedding and shockwave generation will be discussed first, and then followed by the influence of the following factors on performance: trailing edge geometry (burn-back will change this); trailing edge thickness (burn-back pushes the trailing edge upstream where it is thicker); and slot coolant blowing ratio (burn-back opens up the slot area and affects coolant-mainstream pressure difference, altering the slot coolant mass flow).

Previously, Mee et al. [9] showed that the overall loss rapidly increased at transonic speeds due to the generation of trailing edge shocks. Denton and Xu [19] explain how these shocks are generated and show an illustration of the shock patterns, as shown in Figure 2.6. They explain that immediately downstream of the trailing edge is a region of low velocity fluid at nearly uniform pressure; commonly, these are termed base region and base pressure, respectively. This base region, which is triangular at high Mach numbers, is bounded by shear layers between the lower velocity fluid inside it and the higher velocity fluid outside it. The shear layers start at the separation points of the trailing edge where the surface flow separates

and end at the confluence point where the separated surface flow meets again. The initial surface flow separation generates expansion waves due to the change in direction, which propagates into the main flow (Schlieren images of this in Figure 2.7; Nash et al. [20] also show the formation of this in their work). The later meeting of these pressure side and suction side flows at the confluence point forces the two flows to turn again to a common direction, in doing so, compressing and then generating compression shockwaves that also propagate into the main flow. The propagated shockwave originating from the pressure side, impinges on the adjacent blade's suction side and affects the boundary layer (e.g., earlier transition, layer thickening, or sometimes separation). The shockwave originating from the suction side, continues to propagate downstream and interacts with the next blade row. The impact of this is significant in the case of turbine stages and is discussed in the stage interaction section later in detail. Downstream of the confluence point is a turbulent, unsteady wake that itself leads to entropy generation due to mixing and vorticity but also interacts with the later blade row, generating more losses.

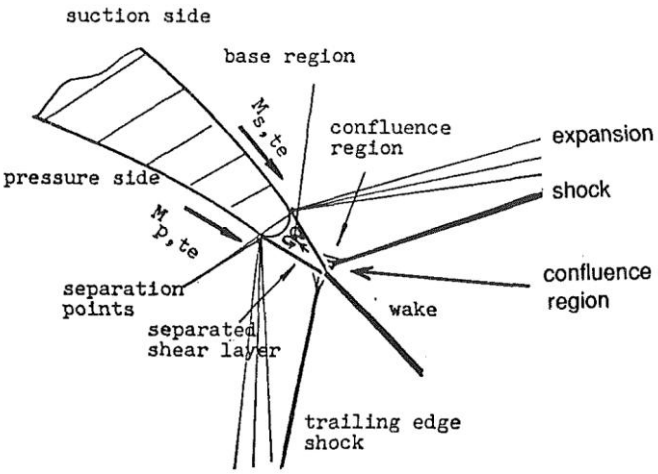


Figure 2.6: Transonic trailing edge shock generation model from Denton and Xu [19].

The unsteady nature of the wake is characterised by a large-scale periodic vortex pattern, commonly referred to as the von Karman vortex sheet [21]. Melzer and Pullan [22] explain that the shear layers that separate at the separation points (mentioned previously) alternately expand into the base region and roll up to form vortices. These vortices continue to grow,

entraining freestream flow until reaching a critical size and shedding off away from the trailing edge (see Figure 2.7 for the formation and evolution for different trailing edge geometries).

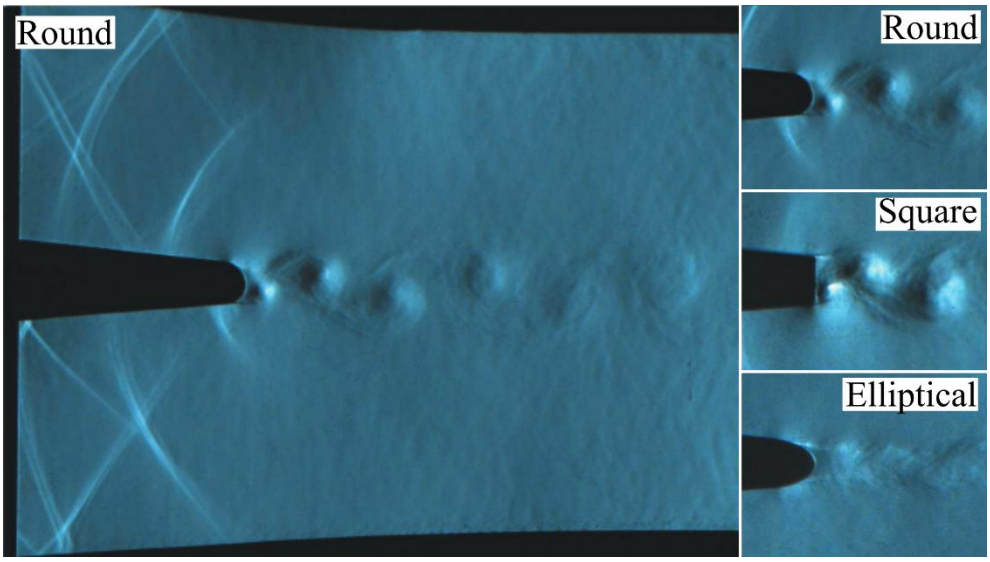


Figure 2.7: Schlieren images of trailing edge geometries with the same thickness (7.8% of blade throat width), at the same phase, and at Mach 0.7. Adapted from Melzer and Pullan [22].

An early study investigating the effect of trailing edge geometry and thickness on vane performance was by Prust and Helon [23]. They experimented on four trailing edge geometries (round, square, pressure side tapered, and suction side tapered), at five different thicknesses characterised as a percentage of the blade throat width (from 5% to 50%), and at a range of Mach numbers (from 0.5 to 0.9). Their results showed a general increase in kinetic energy loss coefficient with increasing trailing edge thickness, with the square trailing edge geometry showing the largest increase. They also showed that when comparing the different trailing edge geometries, the square design had the greatest loss; for instance, at 11% thickness, the square design loss was 0.5 percentage point greater than the round design. The round and tapered designs were all shown to be similar at the range of Mach numbers tested for most thicknesses. An interesting aspect of this study was that the authors only compared results up to a Mach number of 0.8, stating that above this, flow separation took place. Their results showed a rapid and significant increase in loss (except for square design) after this point, even though the overall flow was still subsonic, this was not explained, however, a more recent study by Melzer and Pullan [22] studied and explained this very mechanism.

In their work, Melzer and Pullan also studied the effect of different trailing edge geometries (sharp, round, square, elliptical) and thicknesses (from 1.9% to 7.8%) on loss. They complemented the loss measurements with Schlieren imagery. Plots of loss against Mach number for different configurations for their flat plate test are shown in Figure 2.8. The spikes in loss under subsonic bulk flow conditions were attributed to a specific shockwave generated. It is explained that in the vortex shedding process (see above), that if the expansion of the trailing edge flow into the base region is supersonic (normally due to the small radius of curvature of the flow around the trailing edge), an expansion shockwave will be generated that will propagate upstream, leading to total pressure loss and interference with surface boundary layers (i.e., increased profile loss). They reported that this transonic vortex shedding action could generate three times the loss of subsonic vortex shedding. The expansion shockwaves were evident when looking at the Schlieren images in Figure 2.7. They first noticed this in their results for their square and round geometries; for instance, at Mach number 0.75 for the rounded design, there was a large spike in loss despite subsonic main flow. The effect was less on the square design and negligibly so on the elliptical design. Using the Schlieren images, they explained that although transonic shedding was present at lower Mach numbers, the square geometry limited the shedding cycle so the vortices could not strengthen further after some point. In comparison, the round shape continued to strengthen the vortex motion with increasing Mach number. The elliptical design suppressed transonic vortex shedding as the shear layers leaving the trailing edge remained stable and did not roll up into vortices until much later, meaning that the vortices could not directly interact with the trailing edge and generate the expansion waves. This is also why, in all conditions and thicknesses, the elliptical design had lower loss than the round and square designs. Beside this, in accord with Prust and Helon [23], the square design had the greatest loss at most conditions (except at the thickest design above Mach 0.6), and generally, the loss increased with increasing thickness for all designs at all Mach number conditions.

For completeness, both Prust and Helon, and Melzer and Pullan use a sharp trailing edge design as the reference case. This is considered the perfect shape that will produce a clear separation at the trailing edge and a thin wake consequently. However, due to manufacturing and structural integrity requirements, a thickness is required.

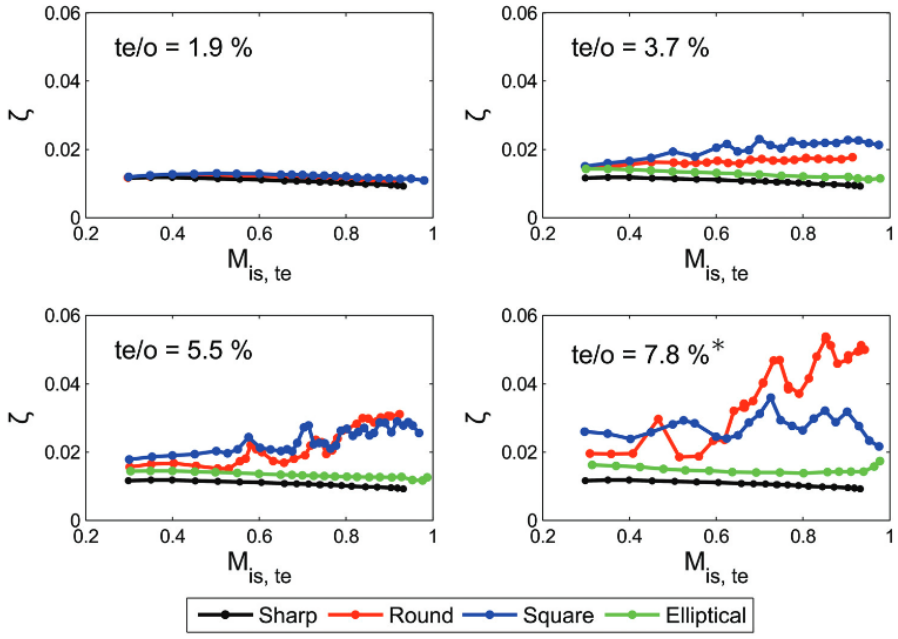


Figure 2.8: Loss plotted against Mach number for different trailing edge geometries and thicknesses, from Melzer and Pullan [22] (where te is the trailing edge thickness, and o is the throat width).

The larger loss for the square geometry was also explained by Nash et al. [20] who looked at the base pressures behind square and round trailing edge geometries with 10% (percentage of chord) thickness at a range of Mach numbers. They found that the base pressure of the square design was at some conditions half that of the round design, but after approximately 0.55 Mach number, the base pressure of the round design rapidly dropped. This is in accord with Figure 2.8 where the round design loss rapidly rises above the square design around 0.6 Mach number. Granovskiy et al. [24] also showed, in accord with the studies mentioned before, increased profile loss for square designs when compared with round designs. The base region is important because mixing between the low momentum fluid in the base region and the higher momentum fluid outside it, is a significant source of entropy generation, for instance, Denton [7] gives a simplified profile loss coefficient expression as below

$$\zeta_p = -\frac{c_{\mathrm{pb}} t}{w} + \frac{2\theta}{w} + \left(\frac{\delta^* + t}{w}\right)^2 \tag{2.1}$$

where c_{pb} is the base pressure coefficient, t is trailing edge thickness, w is the throat width, θ is the boundary layer momentum thickness, and δ^* is the boundary layer displacement thickness. The first term represents the loss due to the base pressure acting on the trailing edge, the second term is the mixed-out loss of the boundary layer at the trailing edge, and the third term is the loss arising from the combined blockage of the trailing edge and boundary layer.

Nash et al. [20] also investigated the effect of a trailing edge cavity (with no coolant, and normally referred to as a trailing edge slot) on the base pressures and found that under subsonic conditions, the base pressure in the cavity design was always less than the normal square design without the cavity. At supersonic conditions, they were the same. This suggested that it had a noticeable effect on the subsonic vortex shedding but little on transonic vortex shedding. The latter point is critical for trailing edge loss. It is now generally known that some coolant air ejection into the base region can increase the base pressure, affecting the vortex shedding process and at times reducing loss. There is, however, a negative effect if too much coolant is injected into the main flow. Motallebi and Norbury [25] study this with Schlieren imagery and base pressure measurements. They explain that small amounts of coolant injection interrupt the vortex shedding, pushing it further downstream, increasing the base pressure, and reducing losses. They then explain with further coolant injection, that if the coolant velocity matches that of the freestream, the coolant splits the wake into two distinct wakes, for which separate vortex shedding occurs, each with a much higher shedding frequency than the original single wake, leading to higher losses. Later Melzer and Pullan [26] do add that while the increase in loss is mostly true when coolant velocity matches mainstream, there are some specific cases where transonic vortex shedding may not re-establish, depending on the boundary layer thickness. The subject of blowing ratio in the context of modern trailing edge designs will be discussed in the following paragraph.

The trailing edge slot concept was adopted to reduce aerodynamic loss (at the very least by way of base pressure alteration), and over time, two main designs prevailed in modern civil aircraft engines. One was a centred-ejection design with equal length pressure and suction side lips, and the other was a cutback pressure side lip design (also referred to as the suction side overhang design), where the suction side lip was longer than the pressure side. An illustration of these two designs is shown in Figure 2.9.

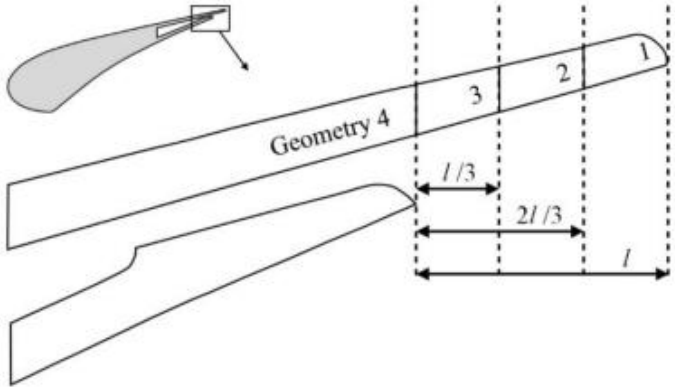


Figure 2.9: Illustration of cutback trailing edge geometries, where Geometry 1 is a suction side overhang design, and Geometry 4 is a centred ejection design, from Burdett and Povey [27].

Melzer and Pullan [26] compared the two designs experimentally and also used Schlieren imaging to visualise the wake dynamics. In their work, they changed the cutback length between 0% (centred ejection) to 100% cutback (14% axial chord length suction side lip overhang design). They tested between Mach 0.30 to 0.90 at five different blowing ratios between 0% (i.e., no coolant) to 90%. Figure 2.10 shows the normalised kinetic energy loss coefficient for each design as a function of blowing ratio at an exit Mach number of 0.75. The general trend for all geometries is a loss decrease with coolant ejection as it suppresses vortex shedding, but as the coolant velocity reaches mainstream velocity, as mentioned previously, there is a reappearance of vortex shedding as the wake is split in two (each with its own vortex shedding mechanism), so the loss increases. They also show that the design rankings depend on the blowing ratio. At low blowing ratios ($0 < \mathrm{BR} < 0.2$) the medium length (50–75% cutback) designs appeared superior. The authors explain that the medium length designs are sufficiently long to disrupt full-width vortex shedding, whereas the longest design (100%

cutback), is long enough that the flow from the pressure side lip reattaches on the suction side lip before it reaches the trailing edge, in effect meaning the suction side lip behaves as an independent trailing edge with its own vortex shedding. The shorter cutback (25% cutback) weakens full width vortex shedding but does not suppress it. At medium blowing ratios ($0.3 < BR < 0.6$) the low-to-medium length (25–50% cutback) designs were best, but the other designs were not far off. This is because at this blowing ratio, the coolant flow had mostly enough momentum to disrupt vortex shedding by itself, without the need of the geometry to assist, hence the losses were relatively low compared to the centred design with no coolant. At high blowing ratios ($BR > 0.8$) as the coolant velocities approached that of the freestream (as explained previously), there was a rapid rise of the low-to-medium length designs, and generally all designs had similar loss values.

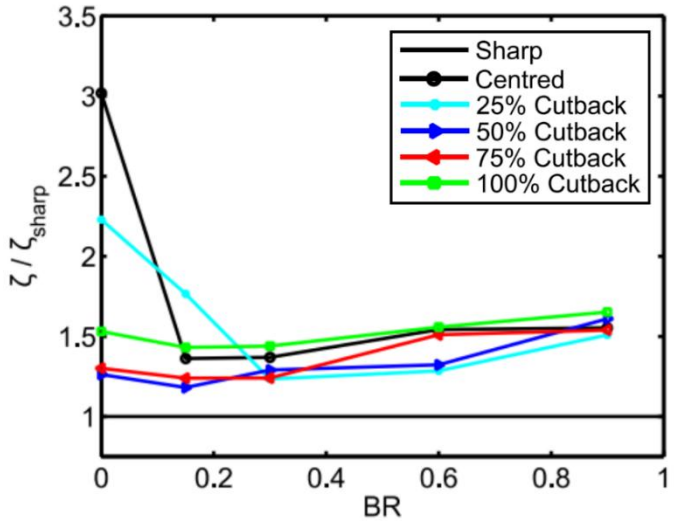


Figure 2.10: Comparison of loss for different trailing edge designs plotted against blowing ratio at exit Mach number of 0.75, adapted from Melzer and Pullan [26].

More recently, Burdett and Povey [27] investigated the effects of varying the suction side overhang length experimentally and numerically. The geometry, like Melzer and Pullan, varied from a design with approximately 14% axial chord overhang length to a 0% (i.e., centred design). They used the ECAT facility at the University of Oxford (Kirollos et al. [28]) to take area traverse measurements at an exit Mach number of 0.97. Their results showed that, in accord with Melzer and Pullan [22], moving from an overhang design to a centred design

meant a change in vortex shedding mode, i.e., the vortex shedding dynamics changed from one where smaller vortices were shed at the suction side lip at a higher frequency to one where larger vortices were shed across the entire base region at a lower frequency. In their case, this led to increased mixed-out loss for the centred design, which rose by 22% when compared to the longest overhang design. The increase in loss was primarily attributed to changes in the base pressure as the effect of their overhang length designs on vane surface boundary layer and secondary and endwall flow were shown to be small.

2.3 – Stage interaction loss mechanisms

In addition to the loss mechanisms present in individual rows, there are interaction mechanisms between the stationary vane row and rotating blade row that are also important for loss considerations. For a transonic turbine stage, the three main interaction processes are the vane wake-blade row, the vane secondary flow vortex-blade row, and the vane shock-blade row interactions. It will be shown in the later results chapters that burn-back affects all three of these interaction mechanisms. In this section, they will be discussed separately, however, in practice they occur simultaneously and interact with each other in complex ways.

First, the vane wake-blade interaction is discussed. This is the interaction between the vane wake and the downstream blade row. Gaetani [29] regards the wake impact on the blade passage as either a velocity defect of the blade inlet flow, or the transport of the vane loss filament (wake) through the blade row. In the former case, the wake undergoes flow underturning and impinges the blade row leading edge with negative incidence. The negative incidence effect agrees with Lefcort [30] who continued to say that this will change the lift characteristics of the blade. The shifting to an off-design operation point is nonoptimal. Salvadori et al. [17] reinforce this and add that the wake is a source of further unsteadiness for the downstream blade row.

Returning to Gaetani, in the latter case, as the vane wake approaches the blade row, it is bowed, stretched, and chopped by the blade leading edge and then transported inside the blade

passage (in accord with Payne et al. [31]). Here, the wake is influenced by the cross-passage gradient and inclined towards the suction side, but degenerates into a pair of legs, one moving near the suction side and the other near the pressure side. The splitting into two legs is caused by the higher convection rate in the mid-passage flow compared to blade surface flows (Chaluvadi et al. [32]). As this pair progresses through the passage, the leading part continues to migrate towards the suction side. The suction side leg of the transporting wake especially continues to be pushed towards the blade suction surface at a faster rate (higher convection on the suction side compared to the pressure side), eventually interacting with the surface boundary layer, thickening it or causing earlier laminar-to-turbulent transition. The pressure side leg is significantly stretched, which, according to Chaluvadi et al. [32] accelerates vortex dissipation and thus, flow mixing. This vane wake transport is illustrated by the solid black line in Figure 2.11 as a function of time with respect to the rotor-blade passing period. This entire process is case specific and depends on many factors such as the vane wake strength, the fluid Reynolds number, the axial distance between the component rows, and so on.

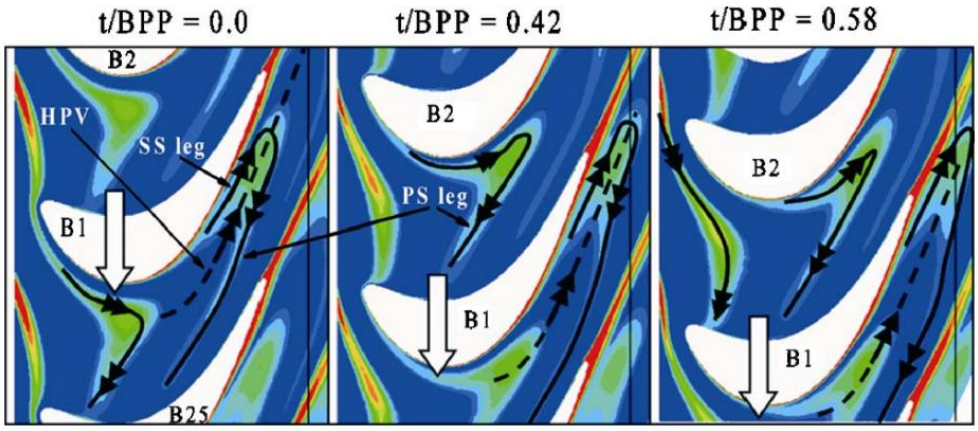


Figure 2.11: Vane wake/vortex transport model by Gaetani et al. [33], where *t* is time, BPP is the blade passing period, and HPV is the hub passage vortex.

Next, the vane vortex-blade interaction is discussed. This is based on how the secondary flow from the vane and the row of blades downstream interact with each other, i.e. how vortical structures (like passage vortex, counter vortex, etc.) are transported through the turbine stage. Gaetani [29] reports that the basic mechanism (bowing, stretching, and chopping effects on secondary flow) is identical to that of the vane wake-blade interaction but with two distinct

differences. Firstly, unlike the wake which has no streamwise vorticity (since a von Kármán vortex street's axis is parallel to blade span), these vortical structures have their own streamwise vorticity characteristics, like intensity and direction of rotation, which means they, as expected, interact differently with the blade. And secondly, the vane secondary flow is a localised flow field feature, unlike the wake (mostly uniform across the span), which means that the effect on the blade row will also be localised.

To explain the significance of the streamwise vorticity component, the vane wake/vortex transport model in Figure 2.11 is used again. Gaetani et al. [33] explain that as the vane secondary flow with streamwise vorticity nears the blade leading edge, like before, it is bowed, stretched, and then chopped. However, as the vortex is transported inside the passage, the suction side leg retains the same sense of rotation as the vane hub passage vortex, whereas the pressure side leg changes in the opposite sense. While the suction side leg continues to be pushed into the suction side of the blade, the pressure side leg is significantly smeared and stretched as it is being transported through the passage. As these vortices meet the blade's own developing passage vortex, depending on the rotational direction, they either enhance or reduce its intensity. Gaetani et al. argue that if the interacting vortices are co-rotating, then they might merge and strengthen, while if they are counter-rotating (like the pressure leg of the vane hub passage vortex), the meeting might lead to rapid kinetic energy dissipation and thus weakening of the rotor native vortex. The co-rotating vortex merging is discussed in Cerretelli et al. [34], and the energy dissipation when two counter-rotating vortices interact is discussed in Bin et al. [35]. The vane wake/vortex transport model of Chaluvadi et al. [32] is also shown in Figure 2.12. This was based on a combination of experimental smoke flow visualisation and unsteady simulations, and their findings were largely in agreement with Gaetani et al. [33].

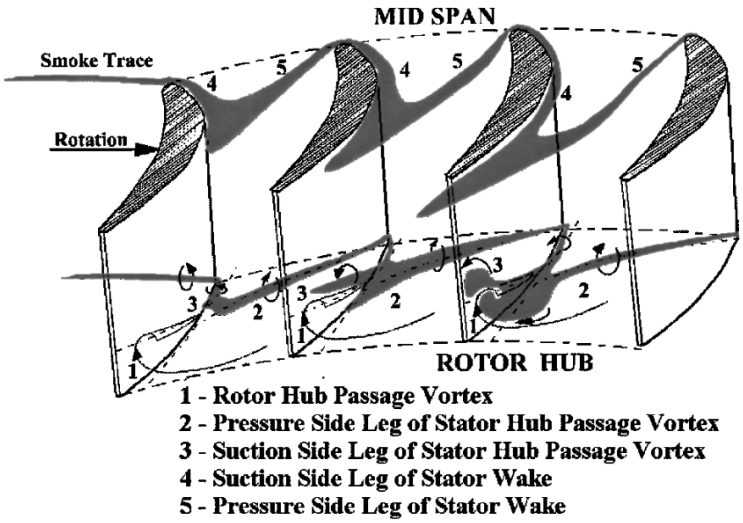


Figure 2.12: Vane wake/vortex transport model by Chaluvadi et al. [32].

Binder [36] investigated the impact of vane exit flow ingestion into the blade passage on the blade turbulence production and found that in general, the cutting of the vane wake and (more significantly) secondary flow considerably increased random unsteadiness in the blade passage. This was attributed to a vortex breakdown process (as explained earlier). The energy of the vortex motion was reported to be converted to the random unsteadiness during the breakdown. This process was also reported to influence other aspects of the flow (e.g., boundary layer and blade secondary flow).

Finally, the vane shock-blade interaction is discussed. This is related to the interaction between the shocks generated by transonic vanes (expected for high-pressure stage nozzles at cruise conditions, certainly at the hub region) and the downstream blade row. Denos et al. [37] say this interaction is more dominant than the vane wake-blade interaction, Miller et al. [38] add that it is an order of magnitude greater than the vane wake-blade interaction. As discussed previously (see trailing edge design section), there are two primary shock phenomena occurring in a transonic turbine stage. The first is the oblique shock that originates from the pressure side of the vane and impinges on the adjacent vane's suction side. The effect of this on profile loss has already been discussed above (relating to boundary layer behaviour), but the increased profile loss will mean a larger wake and thus, an enhanced vane wake-blade interaction. The other is the shockwave that originates from the suction surface and propagates

downstream to the blade row. These are both shown as a function of time with respect to the rotor passing period on the normalised density gradient contour snapshots of Figure 2.13. The snapshots reveal a complex shock system in the stage, with some shocks moving downstream, some upstream, and all at different intensities. Starting at the first frame of the figure, Paniagua et al. [39] explain that when the vane and blade leading edges are aligned, the suction side originating shock (marked A in figure) impinges directly on the blade crown; this impact generates a reflected shock (marked C) that travels upstream towards the adjacent blades pressure side and then back toward the vane (this sequence is observed in the snapshots). As the blades rotate, the vane suction side originating shock completes the sweeping of the rotor crown, i.e., it moves towards the leading edge [37] and past it, after which it diffuses and loses strength. The blade's pressure side originating shock (marked D) is weak initially and remains too weak in later snapshots to impinge fully on the adjacent blade's suction side. The vane's pressure side originating shock (marked B) initially impinges the adjacent vane's suction side; this impact also generates a weakly reflected shock. This weakly reflected shock later strengthens, and when crossing the wake, it bends to accommodate the low-speed wake, causing a new shock wave to be generated that is reflected back toward the vane.

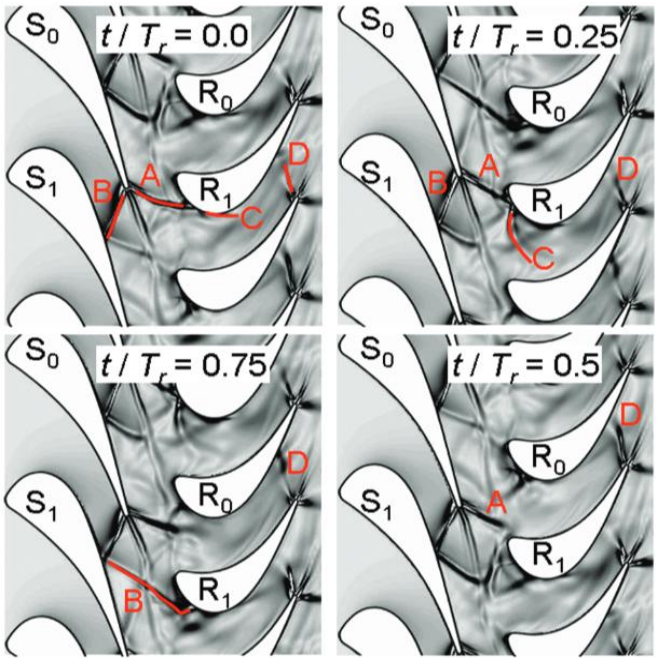


Figure 2.13: Vane shock evolution through turbine stage, adapted from Paniagua et al. [39] where t is the time, and T_f is the rotor passing period.

The shock structure behaviour described above agrees with Denos et al. [37] who took surface pressure measurements at different points around the blade, as shown in Figure 2.14 as a function of time. They observed significant pressure unsteadiness in the leading edge region of the blade, with a small effect on the pressure side and late suction side. The rapid increase in static pressure (e.g., for location 4) was attributed to the initial vane left-running shock impingement on the blade crown, and the subsequent pressure decrease was observed after the left-running shock completed its sweeping of the blade leading edge region.

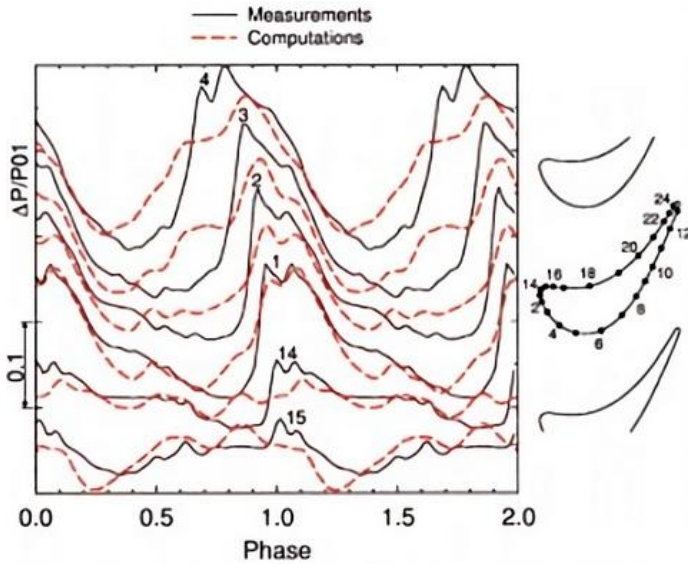


Figure 2.14: Pressure fluctuations measured in the leading edge region gauge points (1–4 and 14–15) from Denos et al. [37].

Rubechini et al. [40] investigated the evolution of the above-discussed shock structures at varying operating conditions (between vane choking and blade choking). In accord with previously discussed studies, they also reported the presence of the pressure side and suction side originating shocks. In their study, for their stage design, at a Mach number of unity, they reported a relatively weak normal shock for the vane pressure side originating shock. With increasing Mach number, this shock became more oblique and reflected more like in Figure 2.13. There is disagreement as to whether the vane suction side originating shock that impinges the blade leading edge interacts with the boundary layer enough to be a significant issue, some authors, for e.g., Gaetani [29] say that at the leading edge the boundary layer has not developed enough for the shock to destabilise it, others e.g., Payne et al. [31] say that the shock could

cause earlier laminar-to-turbulent boundary layer transition at the blade leading edge, or that the effect of the shock at the blade leading edge has significant effect on the freestream velocities in the blade passage. Generally, this will be dependent on the blade design, and the subsequent blade loading distribution.

For completeness, Gaetani [29] adds that the axial gap between the vane and blade rows is critical to control the strength of all the shock actions, i.e., the wider the gap is, the less strong the shock will be as the shock decay rate is generally quite high. The selection of this gap size is a balancing act: at high gaps, the flow is allowed to mix out more, leading to lower overall total pressure but uniform flow; and at low gaps, it is the opposite, and rather, a largely nonuniform flow enters the next blade row, generating more loss within the blade passage.

To summarise, all three types of stage interaction mechanisms have a significant effect on the aerodynamics of the stage, and because of the location of the burn-back on the trailing edge, it is expected that this damage feature will be equally consequential.

2.4 – Vane flow capacity and influencing factors

Flow capacity is a critical performance parameter that essentially measures the quasi-non-dimensional mass flow passing through the engine. It is typically set by the first stage NGV, primarily because it is in the narrowest part of the engine and is mostly near choke or choked. It is most simply defined as

$$\Gamma = \frac{\dot{m}\sqrt{T_{01}}}{p_{01}} \tag{2.2}$$

where $\dot{m}$ is the mass flow passing through the vane, T_{01} is the upstream total temperature, and p_{01} is the upstream total pressure. The parameter is not entirely non-dimensional, but this formulation does remove the dependency on the total pressure and temperature.

The vane trailing edge sits in the *controlling region* (the wider transonic region around the point of minimum area) of the mainstream passage flow, which means that flow capacity is sensitive to any trailing edge changes. As shown in a later section, the trailing edge is subject

(inevitably) to damage that will over time cause changes in flow capacity, and thus changes in performance as the engines moves away from the design condition; for instance, Burdett et al. [41] reported an exchange rate as high as 0.2 for efficiency and up to unity for engine power output. Despite the inevitability and the importance of flow capacity, there are (as far as the author is aware) no studies that specifically study the impact of vane trailing edge damage on flow capacity. There are, however, a few studies that investigate the factors that influence flow capacity, these are now reviewed to provide context to the wider field.

Fielding [42] considered the impact of frictional losses on vane flow capacity. Fielding developed a boundary layer method for estimating the change in vane capacity with loss; this was done by defining a restriction factor parameter, which described the reduction in effective flow area due to boundary layer blockage. This factor was expressed as a function of the profile loss coefficient (previous methods assumed the loss to be distributed evenly throughout the passage, leading to an underestimate of flow capacity). Although Fielding's method was useful with respect to considering the non-uniform distribution of loss in the passage in a one-dimensional point of view, there was no concept of a two- (or three-) dimensional potential flow field, which more recent research has shown is more significant.

For instance, Afanasiev et al. [43] [44] considered the effect of blade loading on flow capacity. In their study, they numerically investigated two annular vane rows with identical geometric throats but different loading distributions. Their designs are shown in Figure 2.15, the first vane was forward-loaded with an uncovered turning of 10 degrees, and the second vane was aft-loaded with an uncovered turning of 32 degrees. Their results showed capacity differences between the two vanes of up to 12% under subsonic conditions, and up to 5% under mildly supersonic conditions. The reason for this was the shifting of the controlling region depending on the loading, as illustrated in Figure 2.15. The forward-loaded vane had a sonic region (thick black line) mostly upstream of the geometric throat, whereas the aft-loaded vane's sonic region had moved downstream. In the latter case, the sonic region was fully downstream of the covered region and geometric throat of the vane. This study showed the

importance of vane aerodynamics in setting flow capacity and highlighted for the first time the flaws of reconciling capacity changes through accurate geometric throat measurements.

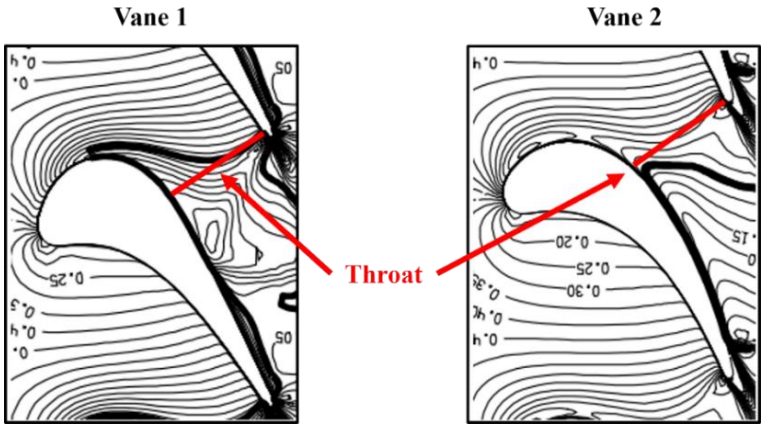


Figure 2.15: Midspan Mach number contours for forward-loaded vane (left) and aft-loaded vane (right). Thick black line is the sonic line, and thick red line is the geometric throat. Adapted from Afanasiev et al. [43].

Povey et al. [45] considered the impact of the exit static pressure definition when modelling a capacity characteristic. Isentropic capacity predictions based on a single mean pressure value (one-dimensional), a radial pressure profile (two-dimensional), and a radial and circumferential pressure profile (three-dimensional) were compared with an experimental trend. Their results are shown in Figure 2.16, and they showed that, as expected, higher fidelity methods had better agreement with experiment. Between the different methods, they reported differences of up to 1.5% in the capacity value for the same geometric throat (somewhat in accord with Afanasiev et al. [43]). The poor absolute accuracy of the models also highlights the difficulty in accurately estimating capacity. Note that pressure-field modelling is only one of many aspects of importance with respect to absolute capacity matching.

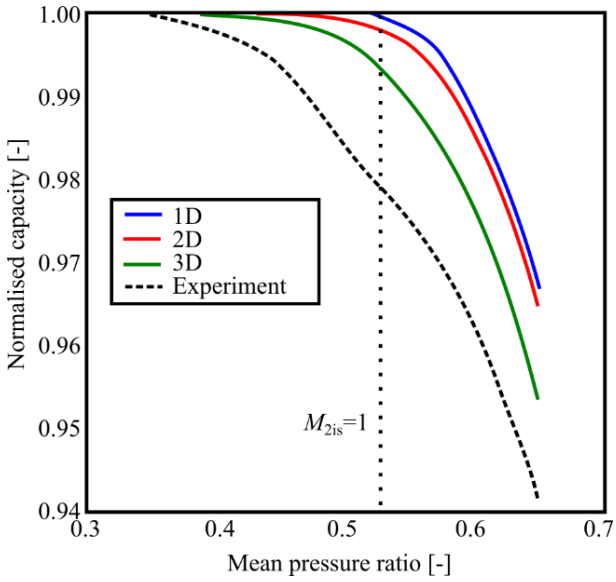


Figure 2.16: Comparison of modelled and experimental flow capacity trends (adapted from Povey et al. [45]).

In addition to vane loss and vane aerodynamics (or static pressure field), Povey et al. [45] adds that there are other factors of secondary influence that also affect capacity. They list them as: turbulence, affecting the boundary layer loss and by extension, vane loss; film cooling, affecting the boundary layer state, and passing through the throat as a partially mixed film; strong three-dimensional flow structures due to vane design, e.g., swept, leaned, or bowed vanes and endwall contouring; boundary layer separation or separation induced by tip leakage flow; and lastly, the trailing edge slot geometry and the blowing ratio, the latter affecting the flow dynamics of the base region.

In other work, Povey [46] analytically investigated the impact of film cooling on vane flow capacity using a control volume mixing model. The impact was expressed in terms of a mass flow correction parameter, which related the mass flow assuming partial mixing of mainstream and coolant streams, to the mass flow assuming mainstream conditions for the entire passage flow (that is to say, no coolant). Their results showed that at the cold-rig conditions, the introduction of coolant mixing reduced the mass flow by 0.21%. This was attributed to total pressure loss in the mixing layer. While at engine conditions, they showed that the introduction of coolant flow *increased* the mass flow by 1.67%. The increase, rather

than decrease, was attributed to the near wall density variation outweighing the effect of the near wall mixing loss.

Later, Hambidge and Povey [47] extended the previous work by performing a numerical investigation of the effect of film cooling on a modern vane with ten film cooling rows. The purpose was to consider the influence of the vane aerodynamic field, and to compare the numerical method against the analytical model from Povey [46]. Their results showed that for a system with a coolant-to-mainstream mass flow ratio of approximately 4% and at a Mach number of unity, the introduction of coolant predicted a decrease in vane capacity of 0.125%. The numerical method agreed well with the analytical model, which predicted a reduction of 0.144%. They reported that the late pressure side and suction side film rows had significantly more effect on the capacity change than the early film rows, and this was because these film rows injected coolant into the mainstream flow at a higher local Mach number (as seen in Figure 2.17). They then also demonstrated that simple additive superposition principles could be applied both numerically and analytically for this problem, with errors less than 0.012% of the vane capacity. They also presented the midspan Mach number distributions for the uncooled vane (left) and cooled vane (right), as shown in Figure 2.17. These contours showed that the sonic region (marked by the solid black line) was mostly downstream of the geometric throat (marked by the dashed line) in accord with Afanasiev et al. [43], and it showed that the sonic region was largely unaffected by the introduction of film cooling.

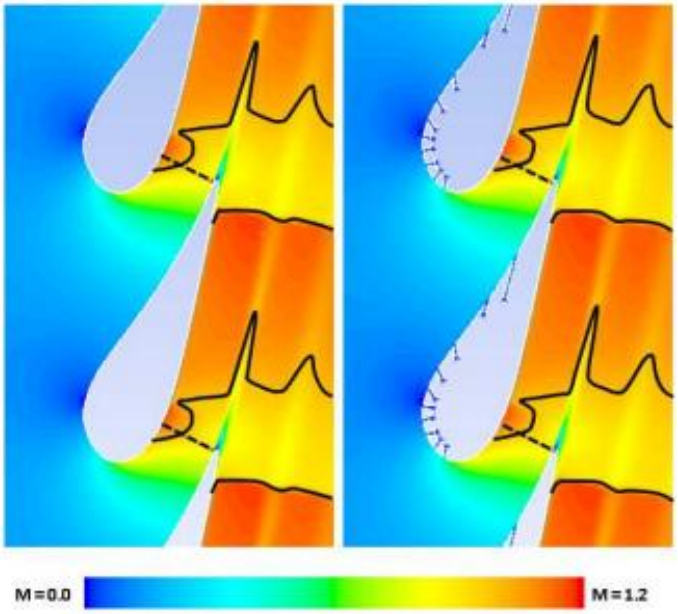


Figure 2.17: Midspan Mach number contours for uncooled vane (left) and cooled vanes (right) from Hambridge and Povey [47]. Solid black line is the sonic line, and dotted black line is the geometric throat.

Hogner et al. [48] and later Voigt et al. [49] (same group, similar methods) studied the secondary influence of the vane design within the manufacturing control limit, i.e., the impact of manufacturing scatter on vane capacity. Numerical simulations were performed on a significant number of as-manufactured real vanes, reconstructed from high-accuracy three-dimensional scans. Hogner et al. [48] investigated trailing edge related parameters, such as suction and pressure side lip radius and length, pressure side lip profile angle, and trailing edge slot width, height, and position. The effects were studied in isolation and in parallel to see the correlation between each other using a Monte Carlo simulation. Their results showed that the pressure side profile offset, and trailing edge slot position had the greatest influence, and they also demonstrated linear superposition of these two highlighting their relative independence. Voigt et al. [49] extended this study by considering more parameters, totalling twenty. Their results showed that stagger angle was best correlated with vane capacity, and endwall profile parameters were the least.

Most recently, for a vane of cut-back pressure side trailing edge design (typical of modern vanes), Burdett et al. [50] investigated the effects of varying the suction side overhang length

on flow capacity experimentally and numerically. The vane varied from a design with a 13.4% of axial chord lengths suction side lip overhang, to a design with 0% which is a centred-ejection design. They used an ultra-low capacity measurement method (described later and used in our work) and complemented it with high-fidelity numerical simulations. Their results showed that the vane with the centred design had a measured capacity 2.54% greater than the equivalent with the suction side lip overhang design. They reported that changes in film and trailing edge slot cooling were not significant with respect to the overall capacity change. Analysing the aerodynamic flow field around the controlling region, they found that the passage loss was also not a significant factor, rather it was the static pressure field that was highly sensitive to the trailing edge design changes, and the primary reason for changes in the overall vane capacity. This work showed that it is important to consider the aerodynamic changes more broadly to reconcile any capacity change. As stated before, capacity change can rarely be explained by considering changes in geometric throat alone.

This mostly exhausts the list of literature that studies factors influencing vane flow capacity, which is evidently scarce. Therefore, the vane capacity component of this thesis will provide a valuable and beneficial contribution to the field.

2.5 – Trailing edge damage mechanisms

There are two core mechanisms responsible for trailing edge burn-back, namely erosion and corrosion. Erosion is defined as the progressive loss of solid material caused by repeated impacts of solid particles entrained in the stream (Balan and Tabakoff [51]). Corrosion, by contrast, refers to degradation of the metallic substrate through chemical or electrochemical reaction with the environment, and in gas turbine hot sections, it primarily manifests as oxidation or hot corrosion. These mechanisms are discussed in turn, beginning with erosion.

The ingested particles that cause aircraft engine erosion are typically volcanic ash, desert sand, runway dust, combustion by-products (Swar et al. [52]) with diameters ranging between ~1 and 100 μm. Although these particles may be small, their specific gravities can be orders

of magnitude higher than the working gas (e.g., volcanic ash has a reported value of approximately 3000 kg/m^3), so they can possess enough inertia to deviate from the flow streamlines wherever the local Stokes number exceeds unity. Once diverted, these particles will impact compressor and turbine components.

Tabakoff et al. [53] reported as much when they investigated turbine blade erosion using particle trajectory simulations. They predicted erosion patterns on both coated and uncoated vanes and blades and reported that, owing to their higher inertia, solid particles ingested will deviate from the main gas flow streamlines and impact the components, causing severe erosion damage. Their results showed that the pressure surfaces were subject to significantly more particle impacts than the corresponding suction surfaces. They also saw that on the vane, the impacts were mostly distributed near the trailing edge with no visible radial variation in pattern, whereas on the rotor, the distribution was more evenly spread with a slight bias on the hub end. A schematic representation of the particle trajectories through a turbine-stage cross section is shown in Figure 2.18 (Hamed et al. [54]). They also emphasised the benefits of applying coatings to reduce erosion, for instance, by applying a rhodium platinum aluminide coating, they reduced the erosion rate by an order of magnitude.

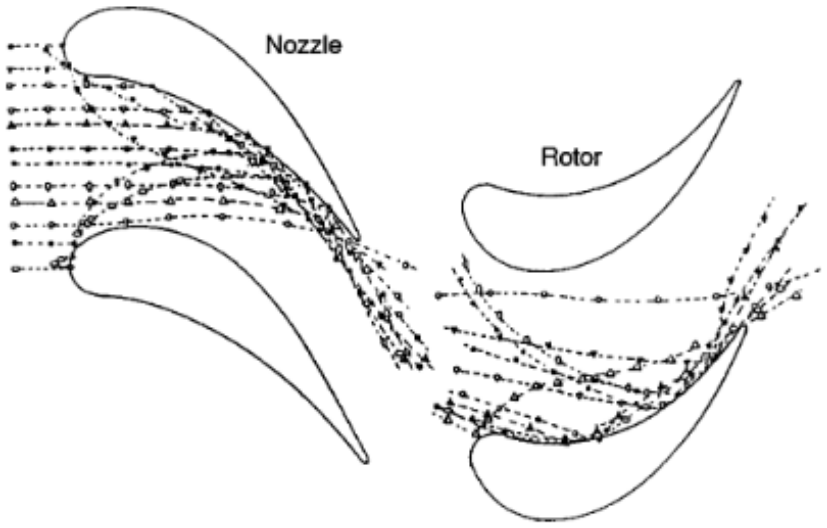


Figure 2.18: Particle trajectories through a turbine-stage cross section, from Hamed et al. [54].

According to Hamed et al. [54], the operating temperature as well as the solid particle's size, impact velocity, impingement angle, and surface material composition all affect the erosion rate of a given material. Swar et al. [52] experimentally investigated the erosion rates for a thermal barrier coated blade surface, and they also showed that it increased with impact velocity, environment temperature, and impingement angle for brittle materials. On the latter, in their study, erosion rate peaked between 20 and 30 degrees for an uncoated Inconel 718 alloy (a common nickel-based superalloy used in gas turbines) before tapering off, whereas when coated and thus brittle in nature, it peaked at normal incidence. Wakeman and Tabakoff [55] reinforced that the erosion rate increased steadily as the operating temperature and particle impact velocity rose. The temperature effect was to weaken the yield strength of the substrate, while the velocity effect was to increase the kinetic energy and thus the damage potential of each particle.

In modern engines, the nickel-based superalloy (commonly used superalloys include Inconel 718 and CMSX-4 [56]) is protected with a ceramic coating which acts as a thermal and chemical barrier. However, under repeated particle impact, micro-scale cracks can initiate in this brittle thermal barrier coating that merge to create delamination layers and eventually lead to spallation (the “stick-crack-deterioration” pathway). Once some spallation occurs, i.e., when the thermal barrier coating is compromised through cracking and spallation, the underlying bond coat and the superalloy substrate are directly exposed to hot gas stream leading to local surface temperature rises.

Corrosion now becomes the dominant damage mechanism, when the oxygen and other contaminants react with the metallic layer. When oxidised, initially, an oxide layer will form that provides temporary protection, however, this layer eventually cracks and spalls too, exposing more bare metal to the hot gas path. In the HPT stage (the focus of this research), the temperatures easily exceed a thousand degrees, leading to more oxidation. This damage not only weakens the mechanical strength of the components but also degrades precise parts such

as the NGV (the focus of this research) where changes in surface roughness, effective flow area change, and film cooling performance can have detrimental impact.

A still more aggressive concern for hot section components is hot corrosion, an accelerated form of oxidation that involves molten alkali-metal sulphates. The most common metal sulphate is sodium sulphate which forms when fuel-borne sulphur reacts with ingested salted contaminants, as discussed by Eliaz et al. [57] (especially prevalent when aircrafts cross oceans). Paterini et al. [58] reported that the presence of other contaminants such as lead, vanadium, and alkali halides can also enhance hot corrosion. They also emphasised that hot corrosion is directly correlated with operating temperature, as they showed that the operational life of nickel-based superalloys monotonically decreased with increasing temperature. Besides this, Eliaz et al. [57] reported that other factors such as the alloy composition, temperature cycles, gas composition, and velocity were other parameters that affect the rate of hot corrosion. Pang et al. [56] investigated the effects of sea salt on the corrosion of CMSX-4 at a fixed temperature and reported that sea salt, as expected, accelerated the corrosion processes, which scaled with the amount of salt deposited. Hot corrosion is typically categorised into two types, either Type I (or high temperature hot corrosion) or Type II (or low temperature hot corrosion). Type I hot corrosion is mainly observed between 800 and 950 degrees Celsius, and it leads to the fluxing of the protective oxide layer leading to rapid material degradation. This process can be divided into four stages from initial contact to failure: in the first stage there is slight roughening of the oxide layer due to localised breakdown; in the next, the roughness of the oxide layer continues to increase as more layer breakdowns occur, at this stage the mechanical integrity of the blade is still not affected; in the third stage, the oxide layer has been significantly penetrated and it is at this stage that the mechanical integrity of the blade is considered compromised; and in the final stage, hot corrosion will continue with or without the presence of sodium and can lead to “catastrophic” failure due to loss of structural material (Eliaz et al. [57]). On the other hand, Type II hot corrosion is mainly observed at slightly lower temperatures, between 650 and 800 degrees Celsius. This type of hot corrosion typically

manifests itself with a pitting effect on the oxide layer (Salehnasab et al. [59]) but will not typically dissolve (flux) or remove the oxide layer entirely. In general, both types of hot corrosion can occur at the same time due to temperature gradients across the engine part. Salehnasab et al. [59] reported that the effect of hot corrosion on the first stage nozzles of an industrial gas turbine were detrimental, as shown in Figure 2.19.

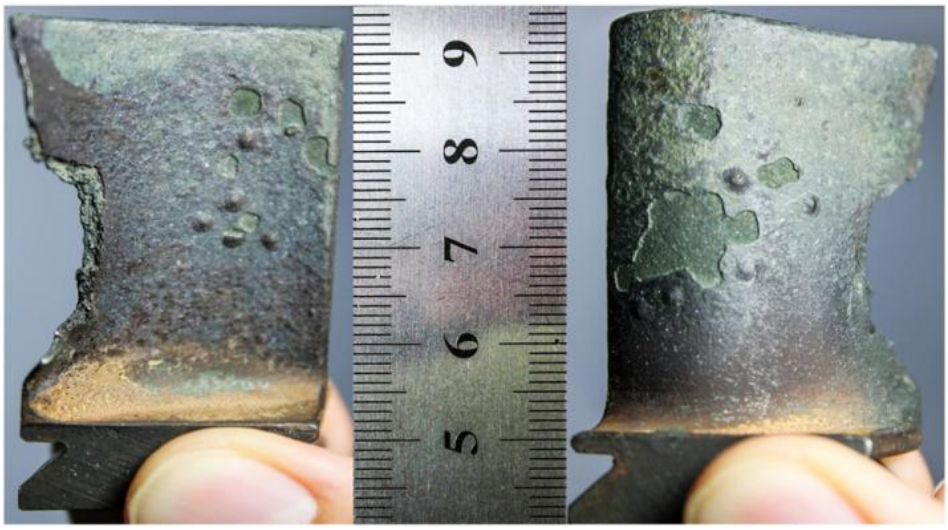


Figure 2.19: Pressure and suction surfaces of a first stage vane with hot corrosion damage, from Salehnasab et al. [59].

This section has described how erosion and oxidation mechanisms drive the progressive trailing edge material loss that produces the burn-back geometries investigated in this thesis.

2.6 – Loss sensitivity to trailing edge damage

One of the earliest works found in the open literature studying the impact of trailing edge damage on turbine component (vane or blade) performance was by Sjolander et al. [60]. These authors, in 1993, investigated the aerodynamic performance of uncooled turbine blades with simulated burn-back. Using a subsonic linear cascade, they took full area aerodynamic surveys two-fifths axial chords length downstream of the blade trailing edge. They assembled the blades so that an individual damaged blade (with semi-circular cutout trailing edge) had adjacent undamaged blades. Their results showed a significantly altered downstream wake. In the cutout region the flow was underturned, and outside this region the flow was overturned. The underturning effect was primarily attributed to metal angle alteration, and the overturning

effect was attributed to flow interaction with newly formed streamwise vortices at the edges of the cutout. The formation of this new secondary flow was also primarily responsible for the overall increase in total pressure loss downstream. The authors reported an increase in plane-averaged total pressure loss coefficient for the turbine with the deepest cutout of +45%. Interestingly, despite increased total pressure loss outside the cutout, their study showed slightly decreased total pressure loss in the cutout region. The latter was attributed to local thinning of the blade surface boundary layer due to fluid migration into the newly formed secondary flow at the edges of the cutout immediately after the trailing edge. To present day, this is one of the most relevant studies to our work despite being incompressible rather than compressible, uncooled rather than cooled, linear cascade rather than annular, and the article being a blade rather than a vane.

Within the same group, few years later, Islam and Sjolander [61] extended the previous study to investigate the effect of blade trailing edge damage (with semi-circular cutouts) on aerodynamic performance under transonic flow conditions. They took midspan total pressure measurements (rather than full area survey) and found again, that the total pressure loss in the cutout region was only marginally affected by the damage feature. They also reported, similarly, a monotonic increase in the flow underturning effect with increasing cutout size.

At least a decade passed before more studies were published in the open literature in this field. One of the earliest found was from Wang et al. [62]. These authors numerically investigated the effect of steam turbine NGV trailing edge damage on total pressure loss at subsonic conditions. They studied three trailing edge geometries (not exhaustive) with a single semi-circular cutout at different span locations (near the hub, at midspan, and near the case). They reported a monotonic increase in total pressure loss with increasing cutout size, regardless of location and shape. And when comparing the effect of location on total pressure loss, they found that the increase in the plane averaged total pressure loss was smallest when the cutout was at the midspan, and larger otherwise.

Later, Bouchard et al. [63] investigated the effect of NGV trailing edge distortion (rather than simulated burn-back) and minor cracks on aerodynamic performance. Trailing edge distortion was characterised by a trailing edge bend towards the pressure side or suction side. Using a transonic annular cascade, they took full circumferential total pressure traverse measurements at four span locations (near case, midspan, and two near hub). These measurements were half an axial chord length downstream of the trailing edge. They reported an increase in total pressure loss of 38% at both hub and case, an increase of 72% in the midspan region, and an overall total pressure loss increase of 51%.

On a slight tangent but still relevant to the work in this thesis were the studies relating to turbine blade forcing. The work by Meyer et al. [64] for example, studied the effect of NGV trailing edge *burn-back* damage on the downstream rotor blade forcing. They statistically analysed real in-service burn-back deterioration data and reported that the typical burn-back shape can be approximated with a trapezoid, as shown in Figure 2.20. They parameterised the burn-back shape using the depth of the damage feature (d), the widths of the damage feature at the trailing edge and damage front (w_1 and w_2), and the radial location of the damage feature at the trailing edge and damage front (h_1 and h_2). The statistical analysis carried out for the work in this thesis also came similar conclusions and therefore adopted their parameterisation method (shown later). Due to the high computing resource requirements, Meyer et al. [64] reduced the dimensionality of their burn-back shape to a triangular shape originating at midspan (so $h_1 = h_2$) and then ran full-stage whole-annulus unsteady simulations. They placed a single damaged vane into an otherwise undamaged stator row. They found significant alteration of the flow field downstream of the damaged vane with, surprisingly, little effect on the flow of the neighbouring vanes. They also reported that, as expected, the flow field of the damaged vane will lead to a reloading of the rotor blade when rotating past.

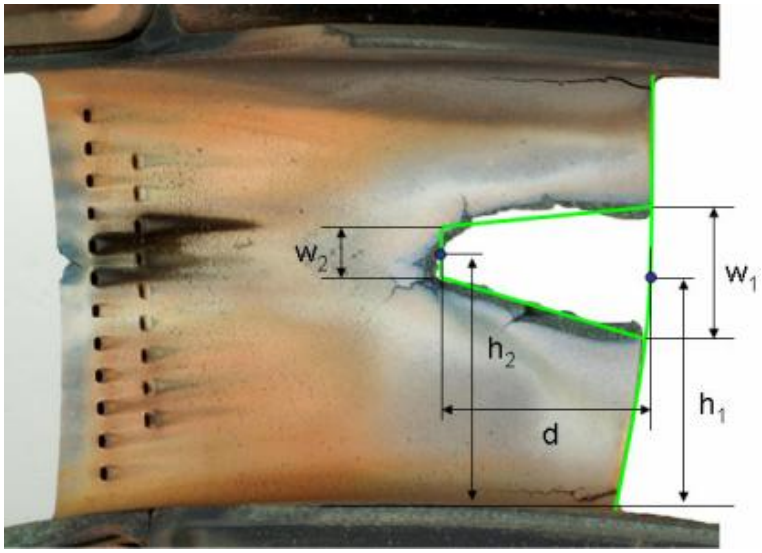


Figure 2.20: Ideal parameterisation of trailing edge burn-back shape, from Meyer et al. [64].

Two other studies on blade forcing include the work from di Mare et al. [65] and Rajput et al. [66]. Di Mare et al. [65] also performed full stage unsteady simulations of the forced response of the rotor blades to NGVs with triangular cutouts at the trailing edge. Their results supported those of Meyer et al. [64] relating to both the aerodynamic flow field and rotor forcing changes. Rajput [66] experimentally studied the effect of different vane cutout shapes (triangular, trapezoidal, and rectangular) on the rotor forcing using the Rotating Cascade Tunnel Gottingen (RGG) at the German Aerospace Centre (DLR) [67]. The RGG is a rotating annular cascade that can be operated at engine matched conditions of Mach number, Reynolds number, and non-dimensional speed. Rajput's results supported Meyer et al. [64] relating to rotor forcing changes. Note the specifics of the rotor blade forcing changes are not discussed as they are outside the scope of the current work.

Most recently, Michaud et al. [68], formerly of the same research group, used the Oxford ECAT facility to experimentally investigate the impact of general in-service deterioration on the aerodynamic performance of transonic cooled NGVs. They used engine parts with a combination of deterioration defects including increased surface roughness, thermal barrier coating spallation, damaged film cooling holes (e.g., collapsed), and mild trailing edge burn-back. They took full total pressure area traverse measurements downstream of the trailing edge

of a *rainbow-set* of vanes. A rainbow-set of vanes constitutes a combination of new vanes, mid-life vanes, and end-of-life vanes. Their results showed that on parts with mild trailing edge burn-back, vortices were formed at the edges of the burn-back (like previous studies) causing an increase in overall mixed-out loss of up to 33%. The trailing edge burn-back was also found to locally reduce exit flow angle, of up to 6 degrees for their most damaged part.

In a companion study, Michaud et al. [69] investigated the impact of in-service deterioration (the same parts) on the thermal performance of transonic heavily cooled NGVs. They performed in-situ overall cooling effectiveness measurements using the ECAT facility and reported greatest changes on the pressure surface, with area averaged overall cooling effectiveness changes of −1.8%, and −10.4% on this surface for the mid-life and end-of-life vanes, respectively. The corresponding implied changes in metal temperatures at engine conditions (mainstream and coolant temperatures of 1800 K and 900 K) were reported to be +12 K and +66 K on this surface for the mid-life and end-of-life vanes.

As far as the author is aware, that exhausts the list of literature openly found studying the impact of trailing edge damage on vane or rotor aerodynamic performance. Additionally, no studies were found that adequately studies the impact of this damage feature on the vane flow capacity.

This page is intentionally blank

Chapter 3 – Trailing edge damage shapes

3.1 – Introduction

The aim of this research was to parametrically test four different vane trailing edge burn-back designs, ranging from an undamaged reference part to three progressively more damaged designs. The burn-back shapes were based on real engine deterioration data. This section describes the available data, the statistical methods used to determine the damage geometries, and the subsequent machining process.

3.2 – Data available and summary of statistics used

The damaged designs were determined with some consultation with Meyer et al. [64], and using burn-back data provided by Rolls-Royce plc. The data included measurements from borescope imaging and normal photographs of burnt-back engine parts. The approach was to analyse the data using four different basic statistical methods to create a design space in which the final burn-back designs could be chosen. The four methods are briefly described as below

1. *Average shape method*. The mean burn-back profile was found using all available data and then defined as the medium damage geometry. A low damage geometry was determined by halving the mean damage depth while keep aspect ratios fixed, and a high damage geometry was obtained by extending the mean depth by fifty percent.
2. *Maximum depth method*. The maximum recorded depth was used as the upper limit, and then two equally spaced depths were defined between this maximum and the baseline trailing edge. All data at each damage depth (within a few millimetres) was then averaged.
3. *Quartile method*. Boxplot analysis of all data was used to determine geometries representative to the median, lower quartile, and upper quartile.
4. *Clustering method*. K-means clustering was applied to partition the dataset into three groups, with the mean of each group used as a damage geometry.

Comparison with Meyer et al. [64] showed two consistent trends: damage was greatest at the midspan; and the burn-back shape was typically trapezoidal.

3.3 – Design space and chosen geometries

The design space generated by the four analysis methods for each damage level is shown by the stem charts in Figure 3.1. The parameters listed are the depth of the damage feature (d) normalised by vane tangential chord (C_t), the widths of the damage feature at the trailing edge and damage front (w_1 and w_2) normalised by vane span height (S), and the burn-back area (A_{BB}) normalised by the product of the vane span height and tangential chord (A_{ref}). Final values selected for each damage level are also indicated on the stem charts. The corresponding burn-back geometries are also shown in the CAD images of Figure 3.2. These four geometries, ranging from undamaged to highly damaged, are referred to as Geometry 1 to Geometry 4.

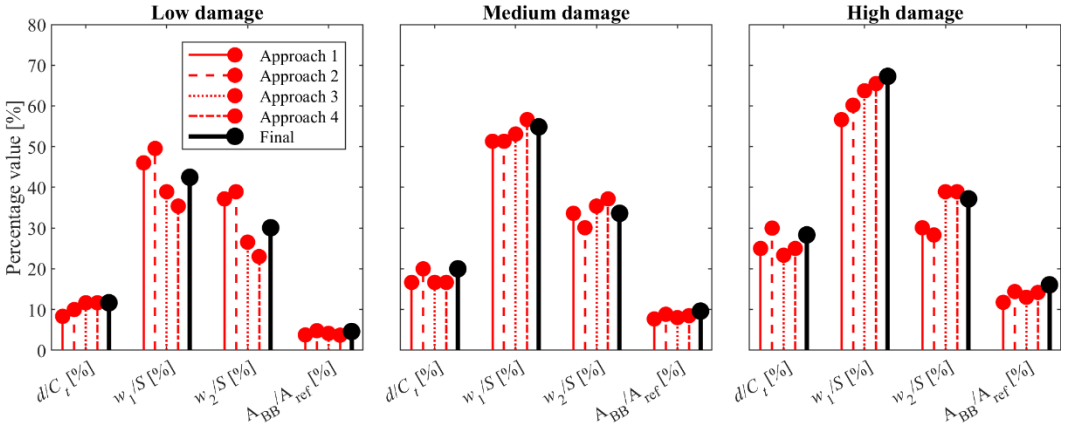


Figure 3.1: Stem charts showing burn-back design space generated by statistical analysis of deterioration data, the abscissa in order: damage depth normalised by tangential chord; damage widths at the trailing edge and damage front, normalised by span height; and burn-back area normalised by a reference value.

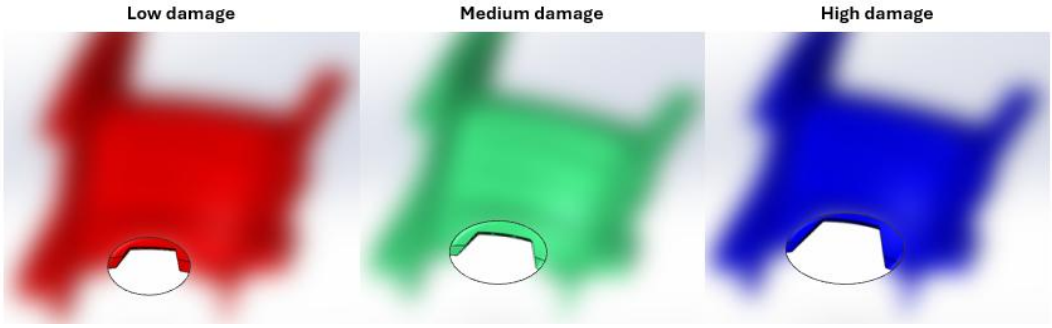


Figure 3.2: Final design choices illustrated on CAD (blurred for commercial reasons).

3.4 – Machining process

Aerodynamic loss and flow capacity measurements were performed in the Engine Component AeroThermal (ECAT) facility at the University of Oxford (photograph shown in Figure 3.3; a piping diagram is included in the appendix). This high-technology-readiness level facility uses an annular cascade of engine parts and can be operated at engine matched conditions of coolant-to-mainstream pressure and temperature ratio, Mach number, and Reynolds number (the facility and the measurement methods are discussed in detail in the results chapters). The experimental campaign began with the undamaged vane module, which was then transported to the laboratory workshop to be machined to the next damage level, and re-installed for further testing. This was repeated until all four geometries were experimentally tested.

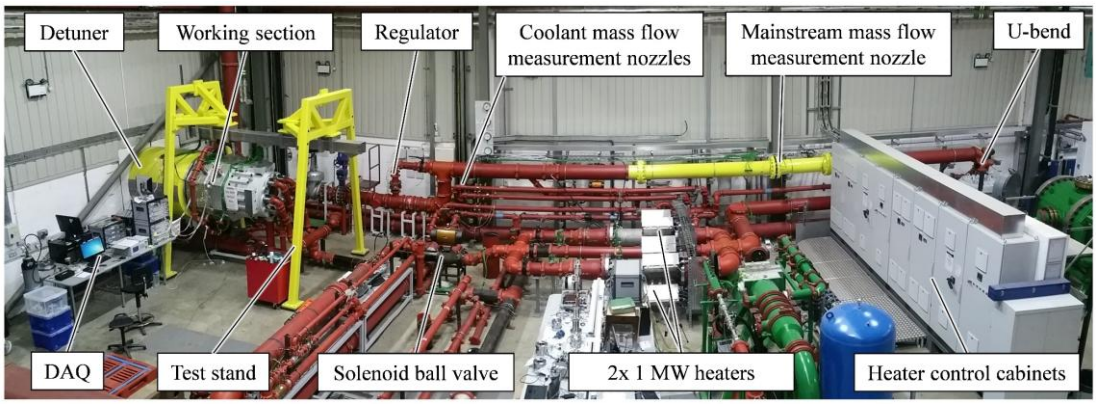


Figure 3.3: Photo of the ECAT facility at the University of Oxford [28].

To allow direct back-to-back comparisons between different builds, in-situ machining of *each* vane in the assembled vane module was adopted (removable from the main working section and shown in Figure 3.4). This was critical for flow capacity measurements, as Burdett et al. [50] reported that even a 0.1 mm deviation in geometric throat (e.g., due to a shift in seating when reassembling the vane module) could lead to a capacity change of 1% independently to the burn-back damage feature.

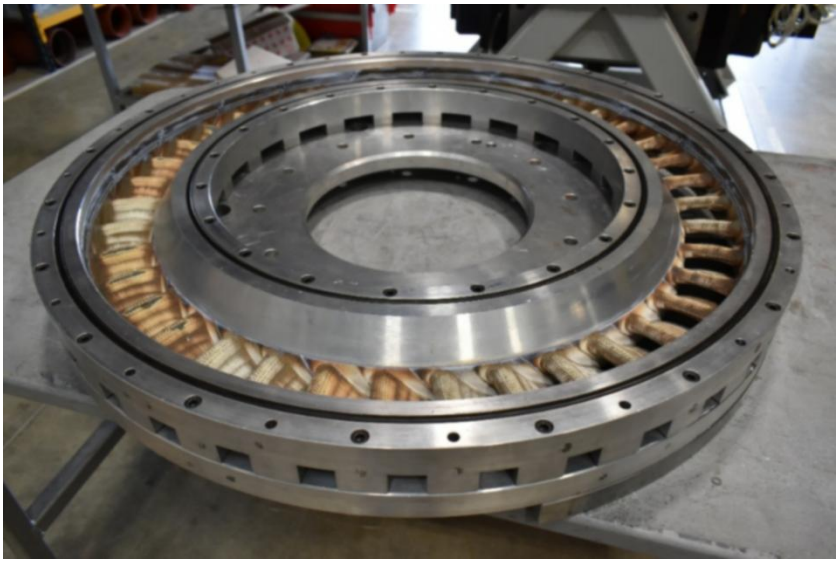


Figure 3.4: Assembled vane ring module (Geometry 1), image marginally blurred for commercial reasons.

Note that in both the experiments and simulations, *each* vane in the vane module assembly were damaged equally, this was despite analysis of the burn-back trends showing that approximately only 30% of vanes in a vane set will be damaged, with random and unequal severity. This compromise was necessary due to the time constraints of the project. In general, di Mare et al. [65] and Meyer et al. [64] both showed that the impact of a single damaged vane in an otherwise undamaged set was only significant in the two passages next to the damaged vane and quickly disappeared in the passages further away, this should be kept in mind when interpreting loss measurement results. With respect to flow capacity, the principle of linear superposition was an expected characteristic, making this compromise relatively insignificant.

During handling and machining, ground-steel fixture plates were bolted onto the assembled vane module to ensure rigid support of the module. This module, with the fixture plates attached, was mounted on the rotating staging bed of an SM3500 three-axis CNC milling machine, with one plate temporarily removed for access (see picture in Figure 3.5; CAD version of the vane module with fixture plates is shown in Figure 5.3).



Figure 3.5: Assembled vane module mounted on the CNC machine rotating staging bed.

Cutting paths were generated using computer aided manufacturing software relative to a zero-location defined by a custom resin 3D printed insert (see Figure 3.6). The insert fitted between vanes and had features to locate midspan and trailing edge. These features were located and zeroed against using an edge finding tool.

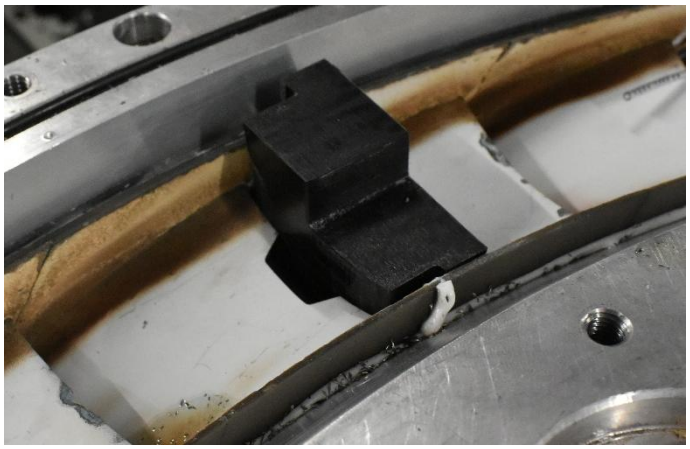


Figure 3.6: Custom resin 3D printed insert for determining cutter zero location.

Once zeroed, the edge finding tool was replaced with a 3 mm diameter solid carbide cutter, orientated parallel to the vane ring axis. Once cut, slip gauges were used to check cut widths and depth. Pictures of Geometry 1 and Geometry 4 are shown in Figure 3.7.

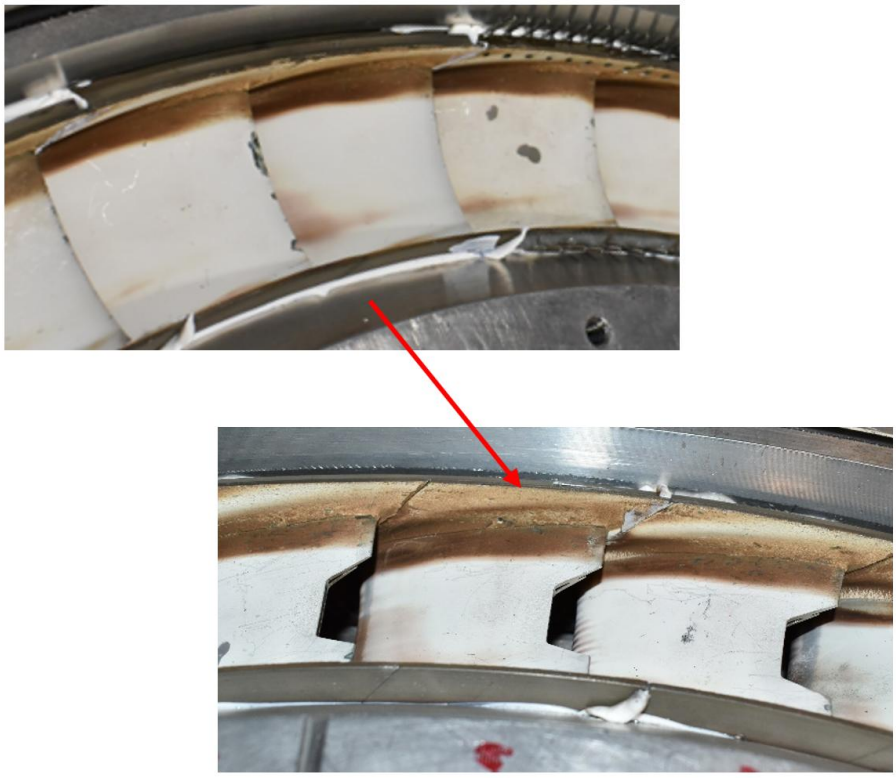


Figure 3.7: Detailed images of the Geometry 1 and Geometry 4 assembled vane modules.

The preceding sections have described the selection, design, and manufacture of the trailing edge burn-back geometries used in this research. These four geometries form the basis for all subsequent experimental and numerical investigations presented in the following chapters.

Chapter 4 – Vane aerodynamic performance

This chapter builds directly on the vane burn-back damage geometries defined in Chapter 3 and provides an in-depth analysis of their aerodynamic consequences. The work is presented in the form of a peer-reviewed journal article[1].

Abstract

In this paper we consider the impact of trailing edge burn-back on the aerodynamic performance of cooled transonic high-pressure nozzle guide vanes. We consider four levels of burn-back ranging from new parts to severely damaged parts. High-fidelity experimental aerodynamic performance data was taken in the Engine Component AeroThermal facility at the University of Oxford, at engine matched conditions of Mach number, Reynolds number, and coolant-to-mainstream pressure ratio. Experimental data are compared to results of computational fluid dynamics simulations to provide further insights into the mechanisms affecting performance. We find that for fixed row pressure ratio, increasing burn-back leads to: both increased loading, and increased forward loading; increased film cooling flow due to re-loading and increased trailing edge flow due to slot area increase; increased overall boundary layer loss; a significant increase in exit secondary kinetic energy associated with newly formed counterrotating vortices at the edges of the burn-back region; and increased variation in exit whirl angle. We quantify these effects and consider implications for whole-life engine performance.

Publication status and co-author contributions

This *journal* paper titled "*Impact of Trailing Edge Damage on Nozzle Guide Vane Aerodynamic Performance*" has been accepted for publication in the ASME Journal of Turbomachinery [4]. The co-author contributions are as follows. Zelimhan Raduev (student):

[1] The text in this chapter is a verbatim reproduction of the published, multi-author, journal paper with some clarifications. It has also been stylistically adapted to match the typeface, margins, and pagination of this thesis.

determined burn-back designs; collected all experimental data; performed all simulations; wrote processing scripts of experimental and numerical data; analysed all experimental and numerical data; generated all figures; and was responsible for the manuscript writing. Dougal Jackson (industry contact): provided engine parts for experiments; provided deterioration data so burn-back designs can be determined; and contributed with analysis ideas. Nafiz Chowdhury (research associate): supported experimental campaign helping collect all experimental data. Thomas Povey (supervisor): supervised all aspects of the work. A statement of authorship is included at the end of the thesis.

4.1 – Introduction and literature review

In operational engines, transonic high-pressure (HP) nozzle guide vanes (NGVs) are subject to trailing edge (TE) erosion and oxidation damage (or, so-called, *burn-back*). Loss of TE material changes the aerodynamic loading of the vane and can significantly change the aerodynamic performance of the row and stage. To build whole-life engine models, the aerodynamic consequences of TE damage need to be both understood and quantified.

Sjolander et al. [1] investigated the aerodynamics of uncooled turbine blades with simulated TE damage in a low-speed linear cascade (Re = 3×10^5, M = 0.5, and Tu = 0.3%) with flow incidence angles ranging from −10 to +15 degrees. Area traverse measurements were taken two-fifths of an axial chord length downstream of the TE. The blades were arranged so that an individual damaged blade (semi-circle cut-outs with depths equal to 15% or 25% of the blade tangential chord, C_t) had adjacent undamaged blades. As expected, the authors observed under-turning of the flow in the cut-out region, and—more interestingly—over-turning outside the cut-out region. Regions of over-turning were associated with streamwise vortices at the edges of the cut-out. The authors also found, perhaps surprisingly, that in the cut-out region the losses were lower for the damaged blade than the undamaged blades. This was attributed to local thinning of the boundary layer (BL) due to the migration of BL fluid towards the notch edges. Overall, however, the blade with 25% cut-out depth (based on tangential chord) suffered an increase in plane-averaged loss of 45%. The fact that this is the

most relevant study to the current one (despite being incompressible rather than compressible, linear rather than annular, the article being a turbine blade not a stator vane, and the component being uncooled as opposed to cooled) demonstrates the scarcity of literature in this area.

In a later—related—study in a transonic linear cascade (Re = 1×10^6, M = 1.2, and Tu = 4%) Islam [2] performed midspan loss measurements two-fifths of an axial chord length downstream of the TE of uncooled turbine blades with simulated TE damage (semi-circle cut-outs with depths equal to 10% and 20% of C_t). They found that midspan aerodynamic loss, as expected, would rise with increasing Mach number but, surprisingly, did not change significantly with the introduction of 10% or 20% cut-out depths. They also found that mid-span exit flow angles were significantly altered, with an increase in magnitude of under-turning with increasing exit Mach number and cut-out depth.

Wang et al. [3] numerically studied the impact TE damage shape, location, and size (four levels of cut-out with depths between 9% and 37% of C_t) on the total pressure loss of a subsonic steam turbine nozzle (M = 0.5). The following TE geometries were studied: three geometries with a single semi-circle cut-out located at different span locations (near the hub, midspan, and near the case); one geometry with two semi-circle cut-outs at 25% and 75% span; and one geometry with an undamaged midspan region but significant burn-back near the case and hub. They found that loss increased with cut-out depth for all cut-out shapes. For semi-circular cut-outs, the increase in loss was smallest when the cut-out was at the midspan, and larger when it was at other span locations.

Bouchard et al. [4] investigated the performance of uncooled NGVs with TE distortion (rather than simulated burn-back) in a transonic annular cascade. The measurement plane was half an axial chord downstream of the TE. Their geometries included those with TE distortions towards the pressure surface (PS) and suction surface (SS), and with minor cracks at the TE. Total pressure traverse measurements were performed at four span locations (near-case; midspan; and two near-hub locations) for damaged and undamaged NGVs. They reported an

increase in loss due to TE distortion of 38% at both hub and case; an increase of 72% in the midspan region; and an overall loss increase of 51%.

Meyer et al. [5] and di Mare et al. [6] performed unsteady numerical simulations of the forced response of the HP turbine interacting with NGVs with triangular cut-out shapes. Both studies were full-stage whole-annulus with a single damaged vane into an otherwise undamaged stator row. Rajput [7] performed experiments of HP turbine forced response with upstream NGVs with different cut-out shapes (triangular, trapezoidal, rectangular) in the Rotating Cascade Tunnel Göttingen (RGG) at the German Aerospace Center (DLR) (Kost and Giess [8]), a rotating annular cascade that can be operated at engine-matched conditions of Mach number, Reynolds number, and non-dimensional speed ($N/\sqrt{T}$). All of these studies had the following common findings: significant alteration of the flow field downstream of the damaged vane, with surprisingly little effect on the flow downstream of neighbouring vanes; counterrotating vortices downstream of the TE of vanes with simulated burn-back (as expected, since opposing vortical structures of equal strength must exist to preserve the divergence-free vorticity field); and the alteration of the rotor blade loading when rotating past the damaged NGV as a result of distortion of the NGV exit flow.

Michaud et al. [9] experimentally investigated the impact of in-service deterioration on the aerodynamic performance of heavily cooled transonic NGVs. The study used service-exposed vanes which exhibited: increased surface roughness; thermal barrier coating spallation; damaged film cooling holes; and mild TE burn-back. Experiments were performed in the Engine Component AeroThermal (ECAT) facility at the University of Oxford, an engine parts annular cascade operated at engine matched conditions of Mach number, Reynolds number and coolant-to-mainstream pressure ratio. A full area traverse was performed a quarter axial chord downstream of the TE using a combination of a single-hole probe (near endwalls), and a five-hole probe (roughly between 6%–93% span region). A rainbow-set of new, mid-life, and end-of-life vanes was used to allow direct back-to-back measurements of the impact of deterioration. The authors found that deterioration caused an increase in overall mixed-out

loss of up to 33% and flow under-turning of up to 6 deg. On parts with mild TE burn-back, vortices were formed at the edges of the burn-back region. In a complementary study Michaud et al. [10] experimentally investigated the impact of in-service deterioration (the same parts) on the thermal performance of heavily cooled transonic NGVs. They performed ex-situ (i.e., in the absence of the potential field developed by the vane) measurements of coolant capacity for each vane, and in-situ measurements of overall cooling effectiveness. The mean change in film coolant capacity and TE slot coolant capacity from new vanes were −2.20% and −4.87% respectively for the mid-life vanes, and −5.77% and −16.80% respectively for the end-of-life vanes. They also found changes in overall film cooling effectiveness were greatest on the PS, and late suction surface SS; they measured changes in area-averaged overall cooling effectiveness of −1.83% and −10.41% on the PS of mid-life and end-of-life vanes, respectively.

In this paper we perform a detailed parametric study of the impact of TE burn-back on performance, validating our methods using experimental data from the Engine Component AeroThermal (ECAT) facility at the University of Oxford. This is an annular engine-parts facility operated at engine-matched conditions of Mach number, Reynolds number, and coolant-to-mainstream pressure ratio. The parts used in this study were typical of a modern civil jet engine and were heavily film cooled. The data and resulting analysis are relevant to whole-life modelling of turbine states.

4.2 – Trailing edge damage shapes

In this paper we investigate four geometries with different levels of simulated TE damage, ranging from new parts to severely burnt-back parts. The geometries are illustrated in Figure 4.1. We refer to these as Geometry 1 to Geometry 4. Illustrations of the midspan-sections of these geometries are presented in Figure 4.2, with the lines of minimum geometric area highlighted. The lines through the TE material show the cutter tool path used to generate the burn-back in the experiments (and replicated in the simulations), aligned parallel to the nozzle ring axis. We parameterise the geometries using the depth of the damage feature, d, the width of the damage feature at the TE plane, w_1, and the width of the damage feature at the damage

front, w_2. We compare the burn-back area, A_{BB}, to a reference area, A_{ref}, equal to the product of the tangential chord (C_{t}) and the span height (S). A summary of the values of these characterisation parameters, for each of the four geometries, is given in Table 4.1.

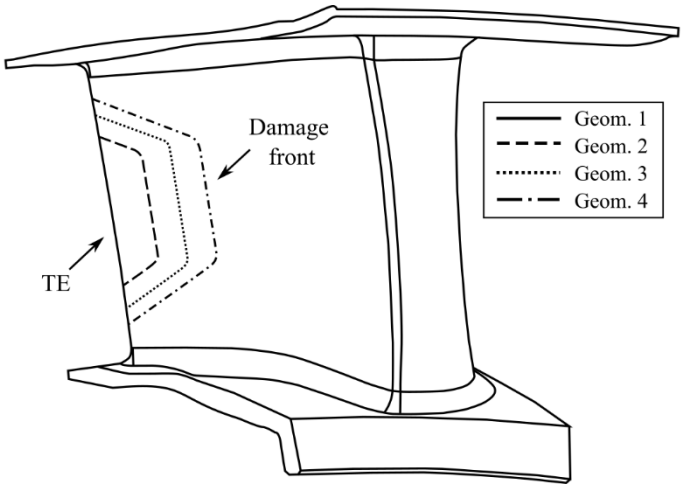


Figure 4.1: Illustrations of Geometry 1–4.

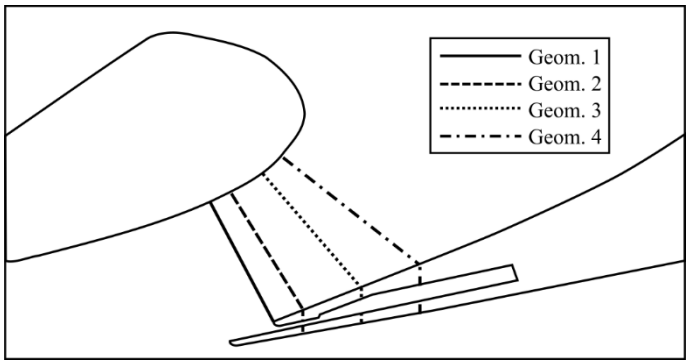


Figure 4.2: Midspan-section illustrations of Geometry 1–4 with geometric minimum area lines.

Table 4.1: Parametric descriptions of Geometry 1–4.

Non-dimensional damage shape parameters	Geom. 1	2	3	4
Burn-back depth, d/C_{t} [%]	0	10.8	19.2	27.5
Burn-back width at TE, w_1/S [%]	0	42.5	54.6	66.8
Burn-back width at damage front, w_2/S [%]	0	29.8	33.3	36.8
Burn-back area, $A_{\mathrm{BB}}/A_{\mathrm{ref}}$ [%]	0	3.9	8.4	14.2

The form and size of these damage shapes is based on a statistical analysis of hundreds of real engine parts subject to TE burn-back. The data showed that TE burn-back regions were

often approximately trapezoidal in form and that the mean centre of the damage front was approximately at mid-span. Similar analysis and conclusions can be found in Meyer et al. [5].

4.3 – Experimental method

Area traverse measurements for Geometry 1–4 was performed using the Engine Component AeroThermal (ECAT) facility at the University of Oxford. The ECAT facility is a high technology-readiness-level (TRL) blowdown facility normally configured with an annular cascade of real-engine NGV parts. It has the capability for very accurate metal effectiveness, capacity, and aerodynamic loss measurements at non-dimensionally matched engine conditions (M, Re, and p_{0c}/p_{01}). The facility can be operated with and without a combustor simulator. A schematic of the ECAT facility working section (configured without the combustor simulator) is shown in Figure 4.3.

Pressurized air is supplied to the facility from large tanks which feed the mainstream and coolant flows. For the current experiments the ECAT facility was operated in regulated mode, such that operating conditions are maintained constant for over 60 seconds during a run. This allows aerodynamic traverse measurements at a single operating point. The operating conditions used in this study are summarized in Table 4.2.

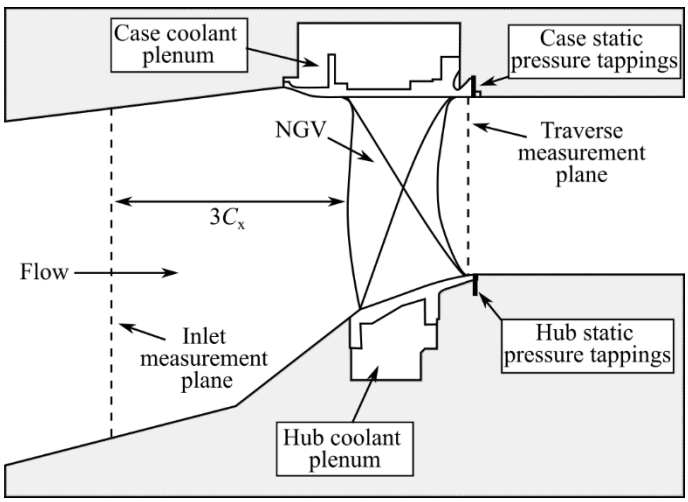


Figure 4.3: Schematic of ECAT facility working section (without combustor simulator), adapted from Michaud et al. [9].

Table 4.2: ECAT facility operating conditions used for this study.

Variable	Value
Mainstream inlet total pressure, p_{01} (bar)	2.0
Mainstream inlet total temperature, T_{01} (K)	287
Coolant inlet total temperature, T_{0c} (K)	287
Vane pressure ratio, p_{exit}/p_{01} (–)	0.534
Coolant-to-mainstream pressure ratio, p_{0c}/p_{01} (–)	1.026
Reynolds number based on tangential chord, Re (–)	1.6×10^6
Exit Mach number, M_{exit} (–)	0.98

The mainstream flow inlet total pressure and total temperature were measured using four pitot probe rakes and four K-type thermocouple rakes three axial chord lengths upstream of the vane leading edge (LE). Exit static pressure was evaluated using 84 surface static tappings distributed over six vanes (out of forty), with tappings located a third of an axial chord-length downstream of the TE midspan location. Area traverse measurements were performed at a single axial plane located a quarter axial chord length downstream of the vane TE. The inlet measurement plane, static pressure tapping locations, and the traverse measurement plane are marked in Figure 4.3.

For the area traverse measurements, a radial-circumferential traverse mechanism was used. In the 5.8%–93.2% span region a five-hole probe (with tip diameter of 2.8 mm) calibrated over a wide range of Mach numbers ($0.3 \leq \text{M} \leq 1.4$) and incidence angles ($\pm40^{\text{o}}$ in both pitch and yaw directions) was used to measure the total and static pressure, flow angles, and Mach number. In the near-wall regions (1.7%–5.8% span and 93.2%–97.5% span) a pitot probe (with tip diameter 0.8 mm) was used to measure the total pressure. Overall, 96% of the vane span (1.7%–97.5%) was surveyed. Probes were aligned with the mean metal angle to minimize the incidence angle. Traverse measurements covered 4.5 vane passages. Further details of the facility can be found in the following references: Kirollos et al. [11] present details of the facility architecture and operation; Messenger et al. [12] and Michaud et al. [13] provide details of high temperature operation and the independent adjustment of Re and M, respectively; the traverse system and traverse-data-reduction are described in detail in Burdett

et al. [14] including detailed uncertainty analysis; a comprehensive discussion of averaging methods in the context of this data is given by Burdett and Povey [15].

4.4 – Numerical method

CFD simulations were performed using the ANSYS-CFX solver with steady Reynolds-averaged Navier-Stokes (RANS) settings and second order discretization for the advection and turbulence terms. Simulations were performed with the baseline k-ω explicit algebraic Reynolds stress model (BSL-EARSM). Amend and Povey [16] demonstrated better agreement with similar experimental data for BSL-EARSM than other commonly used turbulence models (e.g. k-ω SST and Spalart-Allmaras turbulence models). The computational domain (Geometry 1) is shown in Figure 4.4: it includes a vane pair with two complete passages.

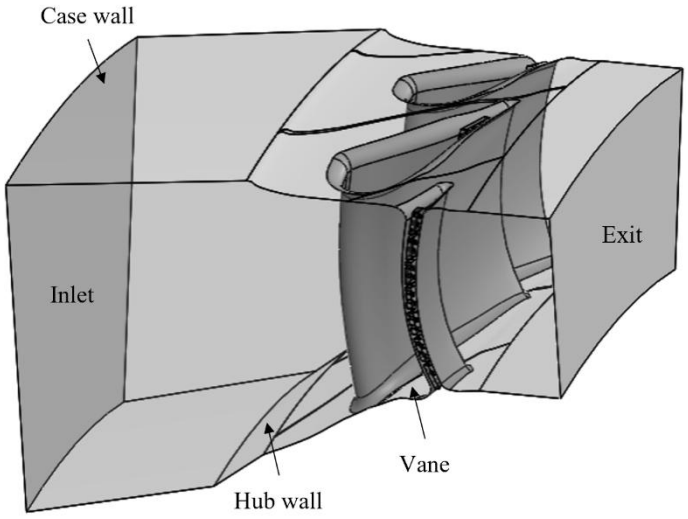


Figure 4.4: Computational domain (Geometry 1) for simulations.

An unstructured octree-based mesh was generated for each domain (Geometry 1–4) using BOXERmesh. A midspan view of the mesh for Geometry 1 is shown in Figure 4.5. The NGV surface and the internal walls of the TE slot was refined with 30 and 15 inflation layers respectively, with an initial step size of 3 μm to achieve y^+ values less than two on most of the wetted surfaces. The hub and case endwalls were refined with 25 inflation layers with an initial

step size of 6 μm to achieve y^+ values less than five. The mesh was refined in the wake, near the TE, in the throat area, and around the NGV surface. Wake refinement was optimised by exporting an iso-volume defined by a total pressure value from an initial uncooled RANS solution. Because octree-based meshes approximate curved surfaces in a stepped fashion, the near-wall prism layers are extruded from this faceted geometry, which can introduce an artificial surface roughness. With sufficient refinement, however, the step size becomes small relative to the boundary layer thickness, so the wall may appear effectively smooth to the solver. A mesh sensitivity study was performed to ensure that: all important solution parameters were independent of the mesh; and that the viscous sub-layer was captured within the near-wall inflation layers. The final meshes each had ~60 million cells. More mesh detail, as well as other numerical method details are discussed in Appendix 1.

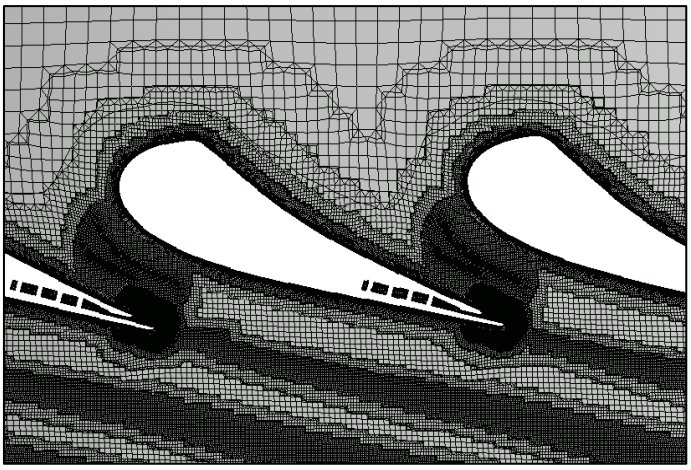


Figure 4.5: Midspan view of the mesh (Geometry 1)

Domain boundary conditions matched those of the experiment (Table 4.2). At inlet, radial profiles of total pressure, total temperature, turbulence length scale, and turbulence intensity were imposed; these were taken from experimental measurements at the inlet measurement plane (see Amend et al. [17] for further details of the upstream traverse mechanism and sample radial profiles). At exit, an area-averaged static pressure was imposed, with an unconstrained radial profile to satisfy radial equilibrium in the exit flow (Smith [18]). Particular care was taken to evaluate the vane exit static pressure in the CFD solutions at identical monitor points to experimental measurement locations: the exit static pressure boundary condition in the CFD

was then adjusted to exactly match the experimental value used for traverse measurements. Solid walls were set as adiabatic boundaries, a common simplification that prevents heat transfer at the wall. This assumption leaves the near-wall fluid hotter and less dense, which increases the displacement thickness, resulting in a thicker boundary layer than would be otherwise. Periodic boundaries were used in the circumferential direction. Film cooling was modelled using area patches (as individual source terms) with hole size and geometry, hole location, mass flow rate, and direction vectors specified on a per-hole basis. The TE slot was explicitly modelled including features such as ribs and pedestals. Within the TE slot for this particular design, chordwise ribs divide the plenum into fourteen ducts. The mass flow rate at each duct inlet was independently specified.

Coolant mass flow rates for individual film holes and the TE slot were determined using an in-house low-order (one-dimensional) internal flow solver, and then scaled to match the coolant-to-mainstream mass flow ratio measured in the experiments. This low-order code uses empirical correlations for friction factors and discharge coefficients (from Rowbury [19]) in a nodal representation of the internal cooling system. Coolant inlet total pressure and total temperature and the film cooling hole exit static pressures are imposed as boundary conditions. The external static pressure distribution was obtained from an initial uncooled CFD prediction.

4.5 – Results and discussion

In this section we consider the capability of the CFD method by detailed comparison of experimental and CFD results, and the impact of simulated TE burn-back on aerodynamic performance. The latter is progressed by considering the impact of increasing—simulated—burn-back on: local kinetic energy (KE) loss coefficient distributions; local axial vorticity distributions; radial distributions of circumferentially-averaged KE loss coefficient; radial distributions of circumferentially-averaged exit flow angle; BL profiles and loss; vane loading distributions and coolant loss; and overall aerodynamic performance.

4.5.1 – Distributions of local KE loss coefficient

As one metric for performance, we compare experimental measurements and CFD predictions of total pressure loss as measured by the local kinetic energy loss coefficient, ζ' (for discussion of loss metrics see Burdett and Povey [15]), defined by

$$\zeta'(r,\theta) = 1 - \frac{1 - \left(\frac{p_2(r,\theta)}{p_{02}(r,\theta)}\right)^{(\gamma-1)/\gamma}}{1 - \left(\frac{p_2(r,\theta)}{p_{01}}\right)^{(\gamma-1)/\gamma}} \tag{4.1}$$

where $p_2(r,\theta)$ and $p_{02}(r,\theta)$ are the local static and total pressures in the plane of interest, p_{01} is the inlet total pressure (assumed uniform), and γ is the ratio of specific heats (γ = 1.4 for air). Distributions of $\zeta'(r,\theta)$ in the downstream traverse measurement plane (see Figure 4.3) for Geometry 1–4 are shown in Figure 4.6. Both experiment and CFD-predicted distributions of $\zeta'(r,\theta)$ have been normalized by the experimentally measured mixed-out loss coefficient for Geometry 1, $\zeta'''''_{\mathrm{ref}}$ (defined later).

Consider now the CFD predictions of the local $\zeta'(r,\theta)$ distributions for Geometry 1. We see that the prediction captures the wake shape and secondary loss core locations well, but the peak value of ζ' in the wake is overpredicted due to undermixing in the absence of unsteady vortex shedding effects in RANS (with respect to the experiment) in the CFD solution. This is analysed in detail in Amend et al. [17] and Burdett and Povey [20]. We consider these predictions to be in excellent agreement with experiments.

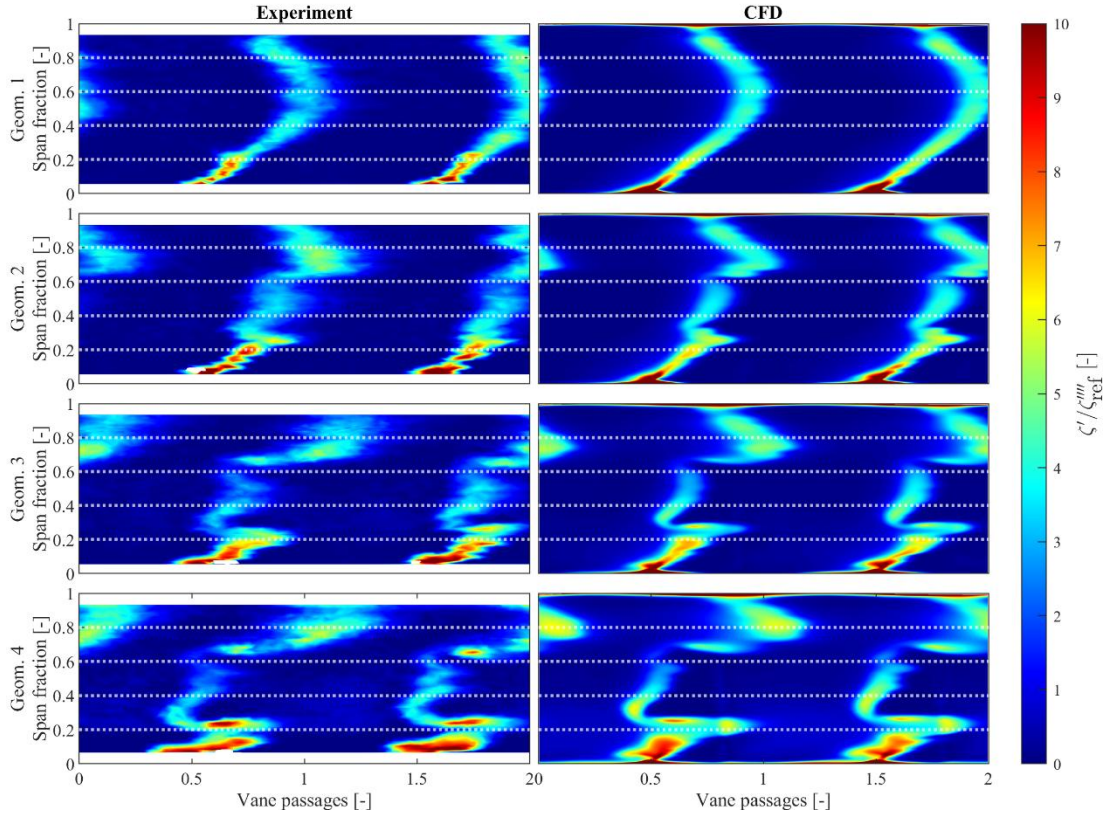


Figure 4.6: Distributions of normalised local KE loss coefficient, ζ' / ζ'''_{ref}, for Geometry 1–4 for: experiment (left column); and CFD predictions (right column). Data is viewed from downstream; the principal exit flow direction is clockwise.

Now consider the impact of TE burn-back. Considering the evolution of the loss coefficient distribution in both experiment (left column) and CFD (right column), with increasing TE burn-back we see the following effects:

1. Significant alteration of the shape of the wake, with an increasing counter-clockwise (CCW) *lag* of the wake in the burn-back region as the burn-back increases. This results from under-turning in the burn-back region due to TE material removal. Perhaps more interestingly, outside the burn-back region (near hub and case) there is increasing clockwise (CW) migration with increasing burn-back, indicating overturning of the flow. We will see later that this results from a formation of a vortex pair at the edges of the TE burn-back feature, which is expected from vorticity continuity (explained later).

2. Increased intensity of hub loss core, with CCW circumferential migration, and radial migration away from the wall.

3. Increased intensity of the casing loss core, with CW migration, and radial migration away from the wall.

4. Development of significant new loss cores at the edges of the burn-back region (at approximately 25% and 75% span) which strengthen with increasing burn-back. We later associate these loss cores with two distinct counterrotating vortices.

5. Radial migration of the wake fluid within the burn-back region from the burn-back corners (at approximately 25% and 75% span) towards the midspan (50% span) resulting in lower loss at the burn-back corners and higher midspan loss. The effect is to collect the loss at midspan.

6. Broadening of the wake outside the burn-back region, and thinning of the wake within the burn-back region. We quantify this in a later section.

For all four comparisons (Geometry 1–4) CFD predicted the wake shape and locations of secondary loss core locations well, but overpredicted the peak value of ζ' in the wake. Overall, we take the CFD method to perform adequately for the purpose of predicting general trends of downstream loss (both magnitude and distribution) whilst noting the tendency to be undermixed with respect to the experiment.

4.5.2 – Axial vorticity distributions

We will now investigate the impact of TE burn-back on the downstream secondary flow by interrogation of CFD simulations. We use the axial vorticity, ω_{x}, parameter in Cartesian coordinates

$$\omega_{\mathrm{x}} = \left(\frac{\partial v_{\mathrm{z}}}{\partial y} - \frac{\partial v_{\mathrm{y}}}{\partial z}\right) \tag{4.2}$$

where v_y and v_z are the components of the velocity vector normal to the axial direction in the measurement plane.

We first consider the secondary flow structures for Geometry 1. Local distributions of axial vorticity for uncooled RANS and cooled RANS simulations are shown in Figure 4.7. The SS is to the left of the wake, and the PS is to the right. The axial vorticity is normalised by the maximum freestream axial vorticity value of the cooled RANS solution. Here positive axial vorticity (red) indicates CCW rotation when viewed from downstream, and negative axial vorticity (blue) indicates CW rotation when viewed from downstream.

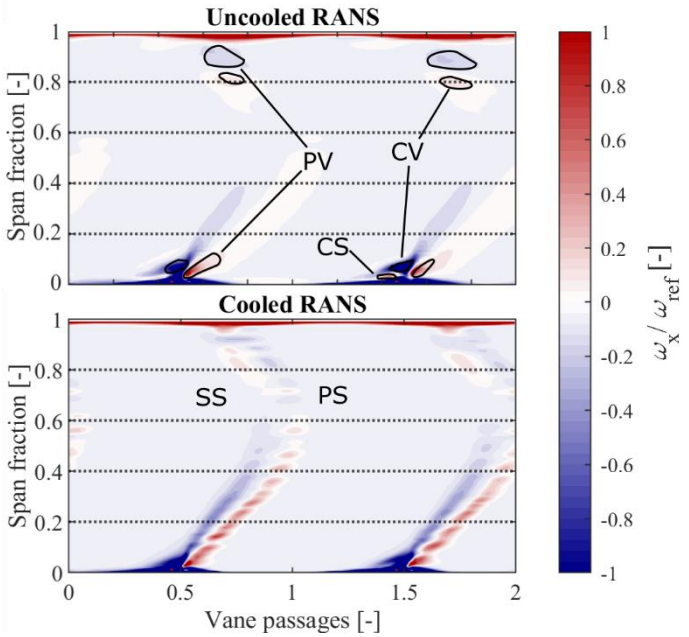


Figure 4.7: CFD-predicted axial vorticity distributions, ω_x, for: (top) uncooled RANS; and (bottom) cooled RANS. Data is viewed from downstream; the exit flow direction is clockwise. Marked in figure: passage vortex (PV); counter vortex (CV); and corner separation vortex (CS).

Consider first the uncooled solution. We mark in the figure: the PS legs of the horseshoe vortex or passage vortex, PV; the SS legs of the horseshoe vortex, or counter vortex, CV; and the corner separation vortex, CS. Here we use the terminology of Goldstein and Spores [21], which is in widespread use. These appear on the SS of the vane. The cooled solution is relatively similar to the uncooled solution, and shows many of the same weak vortex structures. We note additional small vorticity peaks along the line of the wake (apparently associated with individual coolant jets, based on the count), and an enhanced line of mildly

negative vorticity between 0% and 40% span on the SS of the wake, with an accompanying line of mildly positive (with respect to the background level) vorticity on the PS of the wake.

We now consider the CFD predictions for Geometry 1–4. Local distributions of axial vorticity for cooled-RANS simulations are shown in Figure 4.8. With burn-back we see:

1. Development of a pair of vortices at the edges of the burn-back region, marked B and C in plots for Geometry 2–4. These are illustrated in Figure 4.9. We discuss them later in this section. The two vortices are counterrotating relative to each other: the casing vortex has clockwise rotation; the hub vortex has counter-clockwise rotation. The intensity of these vortices increases with increasing burn-back: peak values of normalised axial vorticity for the burn-back vortex closest to the hub were 0.91, 1.37, and 1.56 for Geometry 2, 3 and 4 respectively.

2. Increasing displacement of the wake in the cut-back region with respect to the near-hub and near-case wake; this has already been commented on in the context of Figure 4.6.

3. Migration, distortion and growth of the case passage vortex (marked A in Figure 4.8), as a result of the interaction between the burn-back vortices and other secondary flow. This feature is tracked and marked A in plots for Geometry 2–4, and we can see it combining with other features.

4. Migration and distortion of the counter vortices (marked E in Figure 4.8; dotted regions show position in previous build).

In summary, with TE burn-back a pair of counterrotating vortices form at the burn-back edges. These strengthen with increasing burn-back, and result in two additional loss cores. The action of these additional secondary flows appears to enhance existing secondary flows.

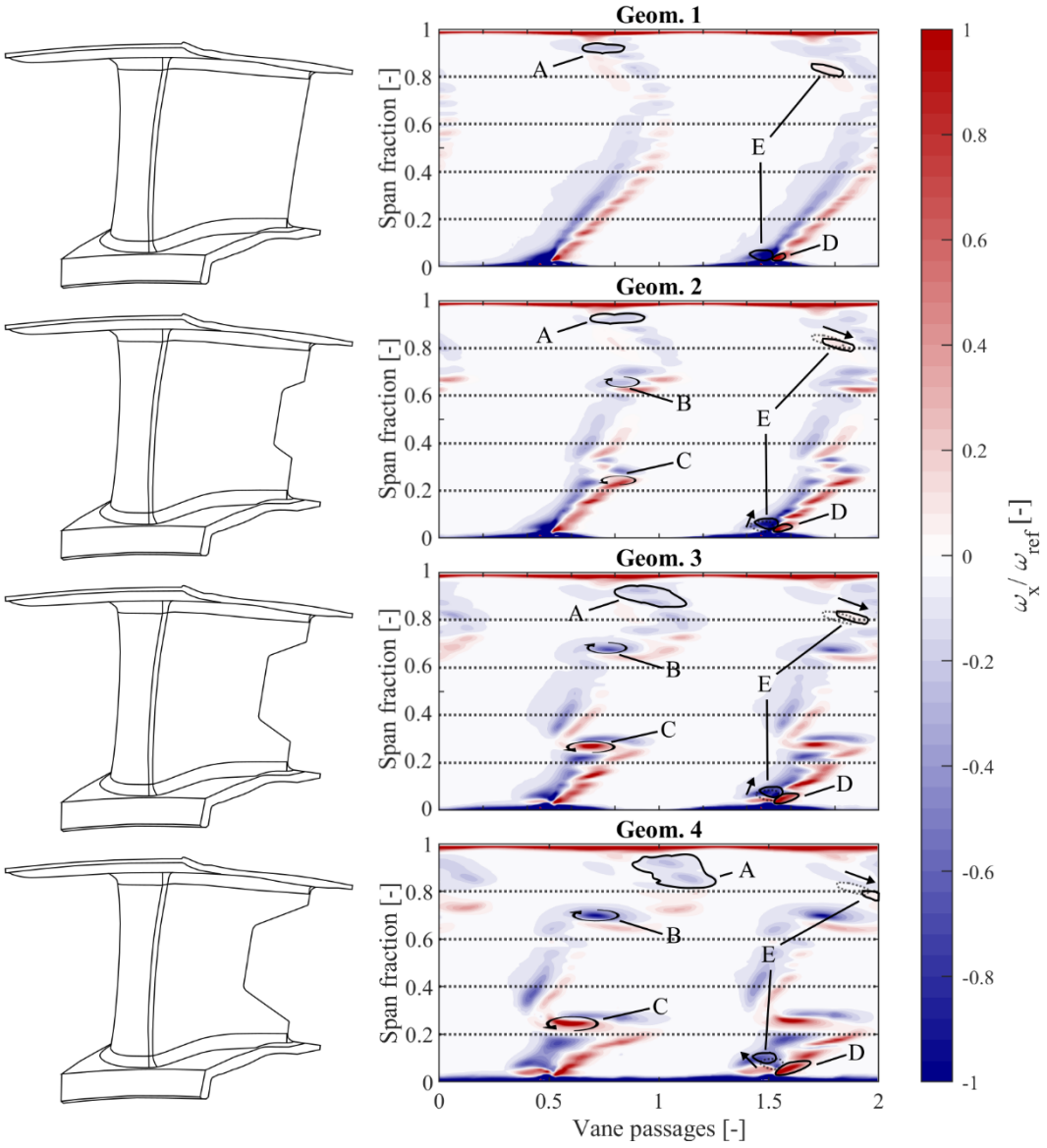


Figure 4.8: Axial vorticity distributions, ω_x, from CFD-prediction for Geometry 1–4. Data is viewed from downstream; and the exit flow direction is clockwise.

We now consider the burn-back vortices in more detail. A schematic of these vortices for Geometry 4 is shown in Figure 4.9. The schematic is based on the Q-criterion in the CFD solution. These counterrotating vortices form due to significantly mis-matched whirl and velocity at the edges of the burn-back region. In the burn-back region both the whirl and velocity are reduced compared to the neighbouring (higher and lower span) regions. This results in a shearing flow at the burn-back edges, that mixes out into a vortex. These vortices cannot occur singly or co-rotating because the vorticity field must remain divergence-free ($\nabla \cdot \omega = 0$), therefore, the shed vortex at one burn-back edge must be accompanied by an equal

and opposite vorticity at the other edge, ensuring a zero-sum process. In this way the pair satisfy both the continuity of vorticity and the conservation of circulation (Kelvin's theorem), making the formation of counter-rotating structures inevitable. The burn-back vortices are further visualised by PS and SS streamlines as shown in Figure 4.9.

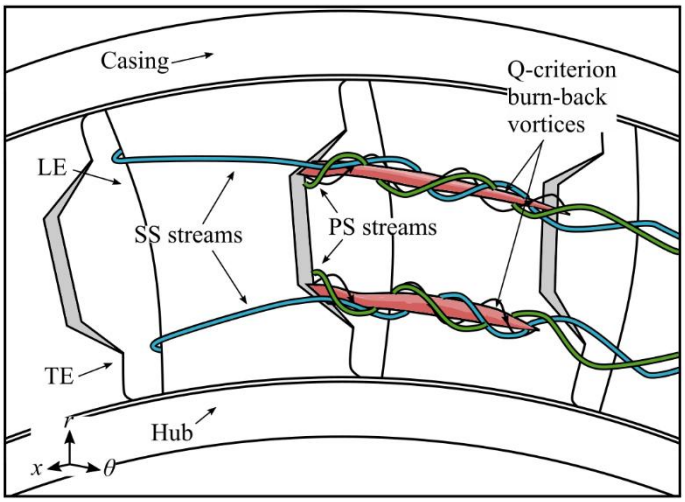


Figure 4.9: Schematic of burn-back vortices for Geometry 4, visualised by Q-criterion.

4.5.3 – Radial distributions of circumferentially-averaged KE loss coefficient

We now consider the experimentally-measured and CFD-predicted spanwise variation of the circumferentially-averaged loss coefficient, $\zeta''(r)$, defined by

$$\zeta''(r) = 1 - \frac{1 - \left(\frac{\bar{p}_2(r)}{\bar{p}_{02}(r)}\right)^{\frac{\gamma-1}{\gamma}}}{1 - \left(\frac{\bar{p}_2(r)}{p_{01}}\right)^{\frac{\gamma-1}{\gamma}}} \tag{4.3}$$

where $\bar{p}_2(r)$ is the circumferentially-area-averaged static pressure at a particular span height, r, and $\bar{p}_{02}(r)$ is the circumferentially-mass-flux-averaged total pressure.

Radial distributions of the loss parameter $\zeta''(r)$ are shown in Figure 4.10 for Geometry 1–4 for both experiment and CFD predictions. Experimental data are recorded in the 6% to 93% span range (limitations due to size of five-hole probe).

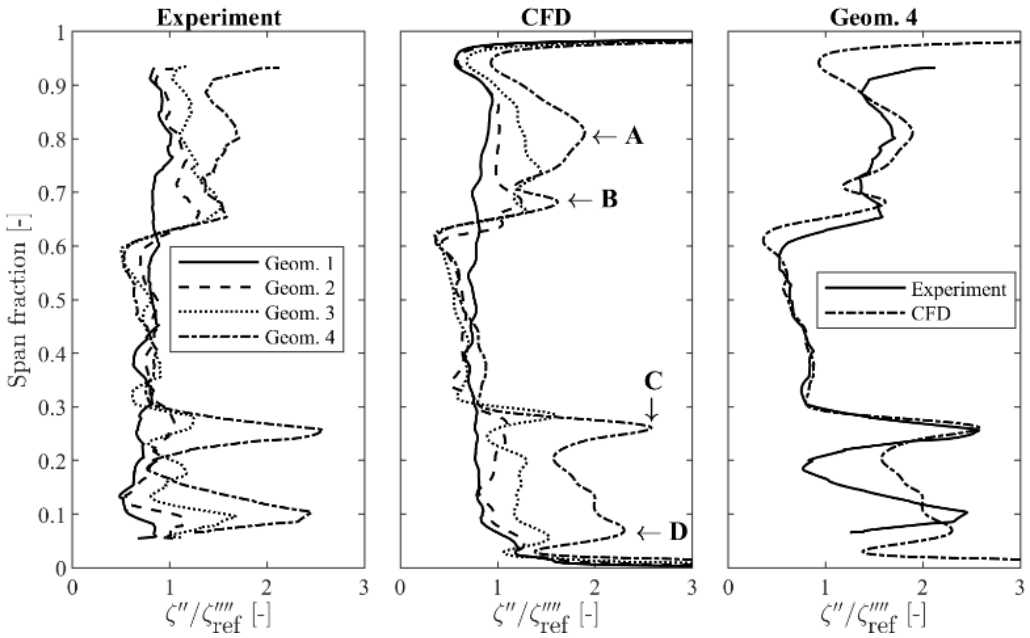


Figure 4.10: Radial distributions of circumferentially-mass-flux-averaged kinetic energy loss coefficient, $\zeta''(r)$, for Geometry 1–4: (left) experimental measurements; (middle) CFD predictions; and (right) comparison of experiment and CFD for Geometry 4.

Consider first the Geometry 1 data (solid line). In both the experimental data and CFD prediction, the loss coefficient is relatively uniform between 20% and 80% span. In this *profile-loss region* (loosely defined) loss is dominated by the BL development and TE flow, both of which depend on the surface Mach distribution and TE Mach number. The flow in this region is relatively unaffected by secondary flows. The mean values of $\zeta''/\zeta''''_{\mathrm{ref}}(r)$ in this span range was 0.800 for the experiment and 0.764 for the CFD, a good match. Small radial fluctuations are attributed to the intermittent chordwise slot within the TE (discussion in context of Figure 4.7); these can be seen in both the experiment and CFD. Outside of the profile-loss region, the loss increases rapidly in the approach to the endwalls (accumulation of low-momentum fluid in endwall region). Some of this endwall fluid is migrated away from the wall into secondary loss cores: see, for example, at 8% span in the experiment and 4% span in the CFD prediction.

Considering now the rest of the experimentally-measured data and CFD simulations, with increasing TE burn-back we see the following effects:

1. Development of two new loss cores (marked B and C in Figure 4.10) due to vortex formation at the edges of the burn-back region (see previous section). These move with the changing burn-back front (see Figure 4.1) and increase in magnitude with increasing burn-back (by 23% and 157% experimentally for vortex B and C, respectively, between Geometry 2 and Geometry 4).

2. Strengthening of the hub and casing loss cores with increasing burn-back (marked A and D in Figure 4.8 and Figure 4.10) and due to the interaction with the newly formed vortices at the edges of the burn-back region. The magnitude of the peak loss values increases between Geometry 1 and Geometry 4 by 86% at A and 189% at D.

3. The location of the hub and casing loss core peaks (at A and D) also move towards mid-passage with increasing burn-back (from 87% to 80% span for loss core A, and from 8% to 10% span for loss core D). This is due to inward migration of the SS flow towards the low-pressure burn-back region. The effect is shown by the surface streamlines patterns of Figure 4.11.

4. Disproportionate increase in hub region (5–25% span) loss arising from an increase in Mach number in this already high-M region (see section on vane loading distributions).

5. In the burn-back region (32–58% span for Geometry 4) the experimentally-measured mass-flux-averaged loss decreased slightly (by 8%) between Geometry 1 and Geometry 4. This is surprising because, despite shorter wetted surface length with burn-back, there is an increase in boundary layer loss (see later discussion). The result is explained by the fact that fluid in the wake is redistributed away from the midspan in the flow immediately downstream of the TE, as it is entrained into the burn-back vortices. Sjolander et al. [1] and Islam [2] report a similar result, also attributing it to wake fluid being swept into the burn-back vortices.

We also see that for all four simulations (Geometry 1–4), CFD predicts the radial profiles of loss well, with the radial locations and magnitudes of loss peaks determined accurately. A direct comparison between experiment and CFD is also made for Geometry 4 in the rightmost plot of Figure 4.10, the overlay shows excellent agreement lending confidence to the CFD method used in this study. We now calculate the change in mass-flux-averaged loss coefficient from the Geometry 1 case, for three regions of the flow: hub, 0–20% span; profile, 20–80% span; and case 80–100% span. These data are summarized in Table 4.3.

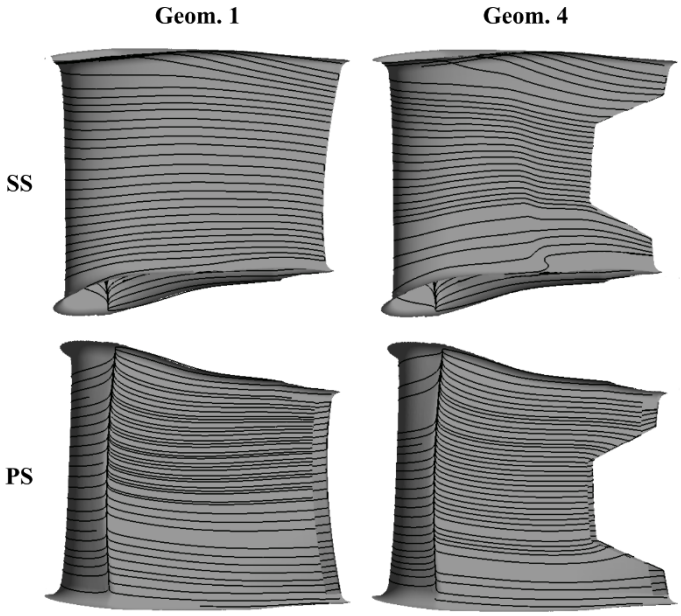


Figure 4.11: CFD-predicted vane surface streamlines for Geometry 1 and Geometry 4: (top) SS; and (bottom) PS.

Table 4.3: Percentage changes (from Geometry 1) in mass-flux-averaged loss coefficient for case, profile and hub regions.

Geom.	$\Delta\zeta''_{\mathrm{CASE}}$ [%]	$\Delta\zeta''_{\mathrm{PROFILE}}$ [%]	$\Delta\zeta''_{\mathrm{HUB}}$ [%]
Experiment			
$1 \rightarrow 2$	+7	+16	+27
$1 \rightarrow 3$	+26	+18	+80
$1 \rightarrow 4$	+72	+35	+141
CFD			
$1 \rightarrow 2$	+6	+5	+13
$1 \rightarrow 3$	+25	+12	+50
$1 \rightarrow 4$	+73	+41	+135

We see that the loss increased in all three regions for all three comparison points ($1 \rightarrow 2$, $1 \rightarrow 3$, and $1 \rightarrow 4$) for both the experimental results and CFD. The comparison of absolute changes measured experimentally and predicted by CFD was good; the average of ratios of individual terms (the nine ratios formed from data of Table 4.3) was 0.783 (c.f. unity for perfect prediction) with a standard deviation of 0.263. The loss increase was greatest at the hub (same result as Bouchard et al. [4]), middling at the casing, and smallest in the profile region.

4.5.4 – Radial distributions of circumferentially-averaged exit flow angle

We consider now the experimentally-measured and CFD-predicted spanwise variation of the circumferentially-mass-flux-averaged exit flow angle, $\beta'(r)$, for Geometry 1–4.

We consider now the experimentally-measured and CFD-predicted spanwise variation of circumferentially-averaged exit flow angle, $\beta'(r)$, for Geometry 1–4. In this work, averaged flow angles were obtained through mass-flux averaging, this is an approximation since momentum-flux averaging would be required to account for both axial and whirl momentum fluxes in the flow angle definition. Nevertheless, the same averaging method was applied consistently to all averaged angles reported in this thesis, so relative comparisons remain valid (although it should be kept in mind when interpreting results). Spanwise profiles for both experimental measurements and CFD predictions are shown in Figure 4.12.

Looking first at Geometry 1 (solid lines in Figure 4.12) data, we see that between 20% and 80% span the general trend in both experiment and CFD is an almost-linear increase in flow angle from hub to case. This broadly follows the TE PS metal angle (with expected deviation). In this region the mass-flow-averaged whirl angle was 75.6 degrees in the experiment, and 76.9 degrees in the CFD prediction, a 1.3 degree difference. The probe bias error was ±0.8 degrees quoted to 95% confidence (for uncertainty analysis see Burdett et al. [14] and Amend et al. [17]). We also note small geometric differences between the experiment and CFD CAD; the latter was the nominal design geometry and did not include surface roughness features, nor specific assessment of batch non-conformity.

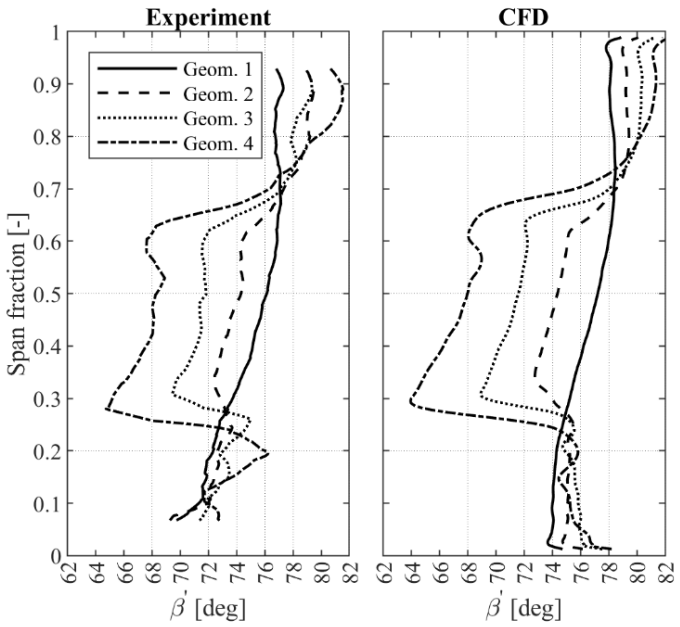


Figure 4.12: Radial distributions of circumferentially-mass-flux-averaged exit flow angle, $\boldsymbol{\beta'(r)}$, for Geometry 1–4 in: (left) experimental measurements; and (right) CFD predictions

Now consider the impact of TE burn-back. This leads to reduced turning in the burn-back region and—interestingly—increased turning outside the burn-back region. The measured peak values of *under*-turning (from the Geometry 1 reference) at 50% span were 1.9, 4.4, and 7.8 degrees for Geometry 2, 3, and 4 respectively. Corresponding values for *over*-turning at 85% span were 1.9, 2.4, and 4.5 respectively. The under-turning in the burn-back region can be partially attributed to metal angle reduction: the geometric changes between Geometry 1 and Geometry 2, 3, and 4 were 0.93, 1.81 and 2.69 degrees, respectively, accounting for—on average—42% of the measured under-turning at midspan. The remaining part of the under-turning effect is attributed to insufficient turning length with the truncated vane (effective increase in pitch-to-chord ratio on account of reduced chord length), leading to significant deviation angle at exit. The (milder) over-turning outside the burn-back region (an effect predominantly at the casing) is explained by an increase in peak SS Mach number at all span locations, causing a greater cross passage pressure gradient. In the spanwise locations outside the burn-back region, for which the vane surface length is unaffected, this enhances turning. For the Geometry 4 configuration, the experimental peak whirl angle (81.5 deg at 86% span) exceeds the local metal angle by 7.3 deg. The CFD was in very good agreement with the

experimental data for all four builds, but with a tendency to over-predict the degree of under-turning (by 1.2 degrees on average) and underpredict the degree of over-turning (by 0.8 degrees on average).

We use this data to establish simple (rule of thumb) linear relationships between the maximum TE burn-back damage depth, $d_{\mathrm{MAX}}/C_{\mathrm{t}}$ and; the maximum flow angle deviation (from nominal flow angle) in the burn-back region, $\Delta\beta'_{\mathrm{BB}}$; the maximum flow angle deviation outside the burn-back region, $\Delta\beta'_{\mathrm{non-BB}}$; and the mean flow angle deviation, $\Delta\beta'_{\mathrm{MEAN}}$. The experimental and CFD data points are shown in Figure 4.13. The forms $\Delta\beta'_{\mathrm{BB}} = -34d_{\mathrm{MAX}}/C_{\mathrm{t}}$, $\Delta\beta'_{\mathrm{non-BB}} = 15d_{\mathrm{MAX}}/C_{\mathrm{t}}$, and $\Delta\beta'_{\mathrm{MEAN}} = -9d_{\mathrm{MAX}}/C_{\mathrm{t}}$ were good fits to the data (R^2 values of 0.957, 0.911, and 0.840 respectively). We compare our data points with the study of Michaud et al. [9] (data plotted in Figure 4.13, not used for regression), who used a similar working section, followed similar procedures, and used vanes from the same engine family. An important difference is that this study uses idealised burn-back geometries whereas [9] used in-service deteriorated parts. Despite these differences, there is good agreement between the two datasets.

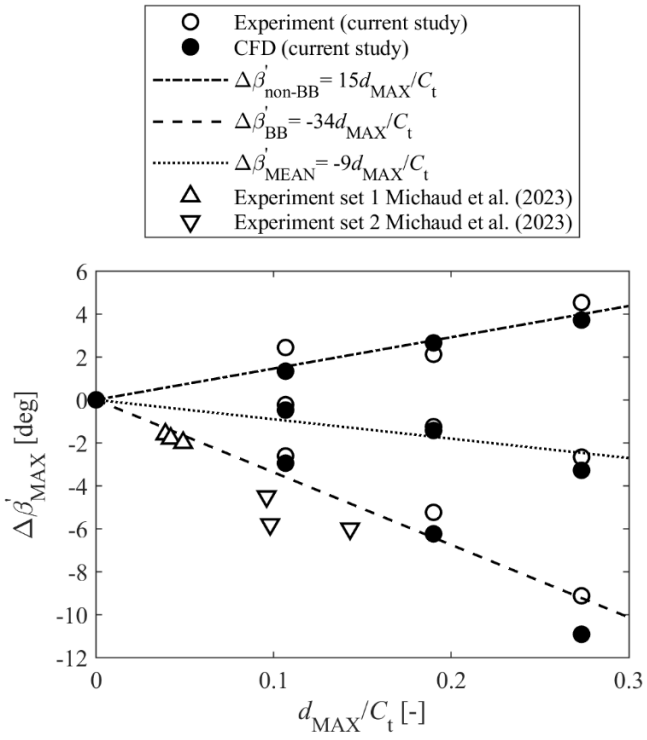


Figure 4.13: Maximum flow angle deviation (from nominal) with burn-back damage depth.

In summary, TE burn-back has a significant impact on the downstream vane exit flow angle distribution, partly as the direct result of TE material removal, but also due to the impact of new secondary flow vortices and vane re-loading in response to the material removal. This has implications for stage performance, and also rotor design, if acceptable stage performance is required even for deteriorated nozzle parts.

4.5.5 – Vane loading distributions

We now investigate the impact of increasing burn-back on the vane loading distributions. CFD-predicted vane surface isentropic Mach number distributions at 15%, 50%, and 85% span fraction for Geometry 1–4 is shown in Figure 4.14. The axial distance, x, is normalised with respect to the axial chord of Geometry 1, $C_{x,1}$. Note that the axial chord of the PS on all plots is shorter than the SS as the data on the overhang region is omitted. Also note that in each CFD case, the same inlet total pressure profiles were used for all simulations, but the exit static pressure boundary condition (see numerical methods for more detail) was varied to exactly match the mean experimental exit pressure based on identical monitor points. The measured (and matched-CFD) row pressure ratios for our data varied between 0.534 and 0.539, resulting in an exit Mach number range $0.983 < \mathrm{M_{exit}} < 0.991$. We will see that this is a small variation compared with that induced by the change in geometry.

Consider first the baseline geometry (Geometry 1). The surface isentropic Mach number distributions are typical of a moderately forward-loaded vane, with peak Mach number between 60% and 80% axial chord. Peak Mach numbers at 15%, 50% and 85% span were approximately 1.15, 1.12 and 1.08. The uncovered turning region (see Figure 4.5), $0.6 < x/C_{x,1} < 1.0$ has a complex interaction with the neighbouring passage flow, with transonic peaks beyond the controlling region around the point of minimum physical area. On the PS there is a well-behaved acceleration at all span locations.

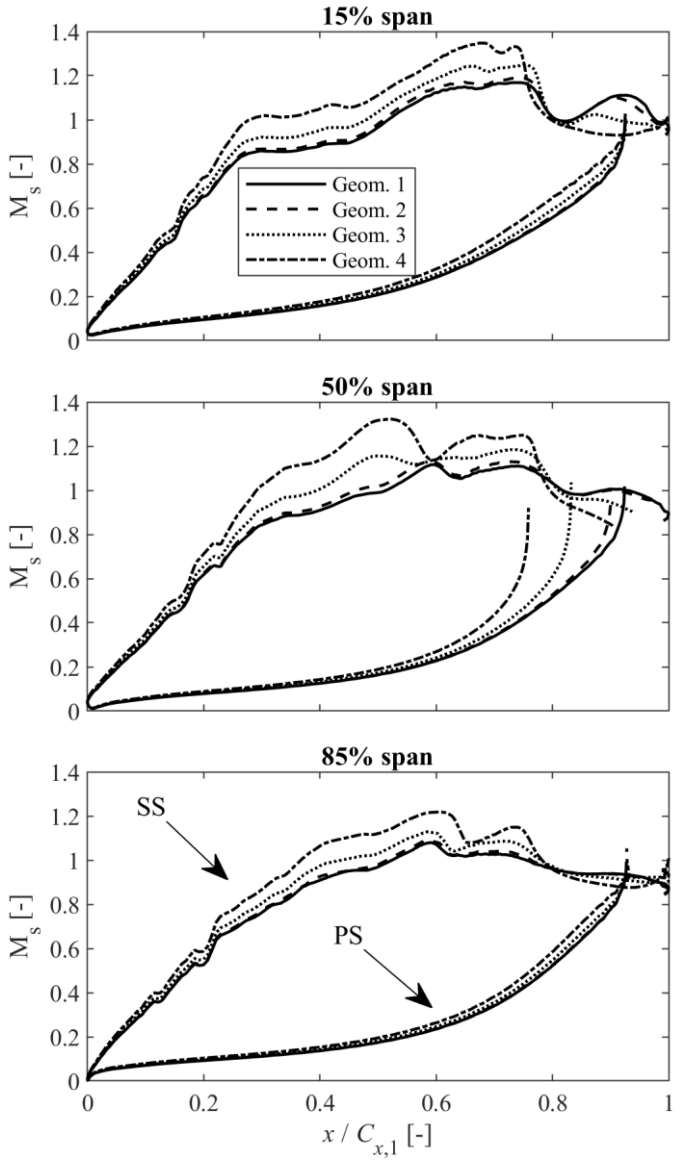


Figure 4.14: CFD-predicted NGV surface isentropic Mach number distributions at 15%, 50% and 85% span for Geometry 1–4.

Now consider the cases with TE burn-back. With increasing burn-back we see the following effects:

1. A significant increase in mid-chord ($0.3 < x/C_{x,1} < 0.7$) SS isentropic Mach number at all span locations, leading to both increased peak loading and increased forward loading. Peak SS M increased to 1.35, 1.32 and 1.20 at 15%, 50% and 85% span. At 50% span the location of peak M moves forward, from approximately $x/C_{x,1} = 0.6$ (Geometry 1) to approximately $x/C_{x,1} = 0.5$ (Geometry 4).

2. A decrease in late ($x/C_{x,1} > 0.8$) SS Mach number which—in combination with the previous effect—increases the adverse pressure gradient on the late SS leading to thickening of the SS BL (see next section). At the 15% and 50% span sections, with increasing cut-back the gradient in adverse pressure increases sharply (suggested presence of shock).

3. A mild increase in late ($x/C_{x,1} > 0.6$) PS Mach number. Note that in the cut-back region (50% span in Figure 4.14) there is also a more significant change in the position of the PS cutback location than the SS cutback location, because of the geometry of the cut-back (see Figure 4.2).

4.5.6 – Boundary layer profiles and loss

We now consider the effect of TE burn-back on the BL profiles. For our baseline design BL loss accounts for approximately 30% of total loss. The CFD-predicted normalized PS and SS BL profiles at 5%, 25%, 50%, 75%, and 95% span at the TE for Geometry 1–4 are shown in Figure 4.15. The surface-normal distance, y, has been normalized by a reference value equal to the minimum geometric throat-width of the Geometry 1 vane at 50% span, w_{ref}. The local velocity, $u(y)$, has been normalized by particular local freestream velocities, U_{PS} and U_{SS}, determined as follows: for the PS, the freestream velocity at $y/w_{\mathrm{ref}} = 0.05$; for the SS, the freestream velocity at $y/w_{\mathrm{ref}} = 0.20$. These values are just outside the thickest BLs on each surface (noting that in the case of the SS there is ambiguity because the scales of the BL velocity gradient and cross-passage velocity gradient are more similar). Normalised boundary layer displacement thickness, $\delta^*/w_{\mathrm{ref}}$, and momentum thicknesses, θ/w_{ref}, are also computed as a function of span for all builds.

Consider first the BL profiles for the baseline (Geometry 1) vane. This is shown by solid lines in Figure 4.15, where the red and black colours identify the PS and SS BL profiles, respectively. The SS BL is approximately 11 times thicker than the PS BL: the normalised displacement thicknesses ($\delta^*/w_{\mathrm{ref}}$) for the SS and PS BLs were 0.022 and 0.002, respectively.

The corresponding normalised momentum thicknesses (θ/w_{ref}) were 0.014 and 0.001 for the SS and PS BLs respectively. That is, the mean SS momentum thickness is 13 times larger than the PS momentum thickness and the loss is dominated by this surface. These results are in line with other studies, e.g. from Mee et al. [22], who measured a momentum thickness at the TE of a transonic turbine rotor that was 9 times larger on the SS than the PS. The BL is thicker on the SS as this fluid experiences an adverse pressure gradient near the TE, whereas the PS fluid experiences a favourable pressure gradient.

We now consider the impact of TE burn-back on the BL profiles. We see the following effects:

1. In the burn-back region, the PS BL displacement thickness reduced with increasing burn-back. At 50% span, there was a 55% reduction in $\delta^*/w_{\mathrm{ref}}$ when comparing Geometry 4 and Geometry 1. This was due to reduced wetted surface (material removed) and greater acceleration rate (shorter surface length; see Figure 4.14).

2. Outside the burn-back region, the PS BL displacement thickness increased slightly with increasing burn-back. At 5% and 95% span, $\delta^*/w_{\mathrm{ref}}$ was 23% and 70% greater—respectively—for Geometry 4 than for Geometry 1. This is a small effect, but hard to explain: there is very little change in either the PS loading (see Figure 4.14) or the surface streamline pattern in the near-endwall region (see Figure 4.11). The increase may arise because of a slight increase in TE Mach number very local to the TE.

3. On the SS in the near-endwall regions (5% and 95% span) the BL displacement thickness reduced with increasing burn-back. At 5% and 95% span, $\delta^*/w_{\mathrm{ref}}$ was 56% and 50% lower—respectively—for Geometry 4 than Geometry 1. The reduction in BL thickness appears to be due to local divergence of vane surface streamlines, caused by fluid migration towards midspan (see Figure 4.11).

4. On the SS away from the endwall (25%, 50% and 75% span) the effect was inverted and the BL thickened with increasing cut-back, due to the increasing strength of

adverse pressure gradient in the approach to the TE (possible weak shock, see Figure 4.14). At 50% span, $\delta^*/w_{\mathrm{ref}}$ was 118% greater for Geometry 4 than for Geometry 1.

The displacement thicknesses at all five span locations and for Geometry 1 to 4 are summarized in the bar-chart of Figure 4.16. Averaged across the five span locations, the PS boundary layer displacement thickness decreased by 9.8% in moving from Geometry 1 to Geometry 4. The corresponding change in the SS displacement thickness was an increase of 46.3%. The corresponding changes in momentum thickness (not shown in the figure) were a decrease on the PS by 18.5%, and an increase on the SS by 43.5%. As the overall loss is dominated by the SS loss (this surface accounts for 94% of the overall loss), the change in loss is dominated by the increase in SS momentum thickness.

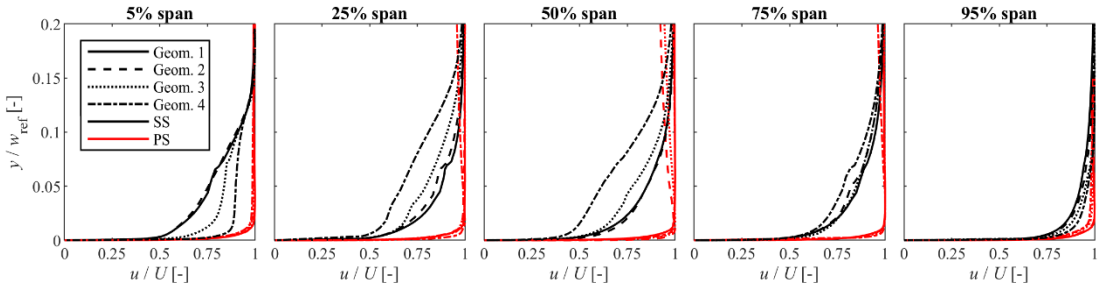


Figure 4.15: CFD-predicted normalized PS (red) and SS (black) BL profiles for Geometry 1–4 at five different span locations.

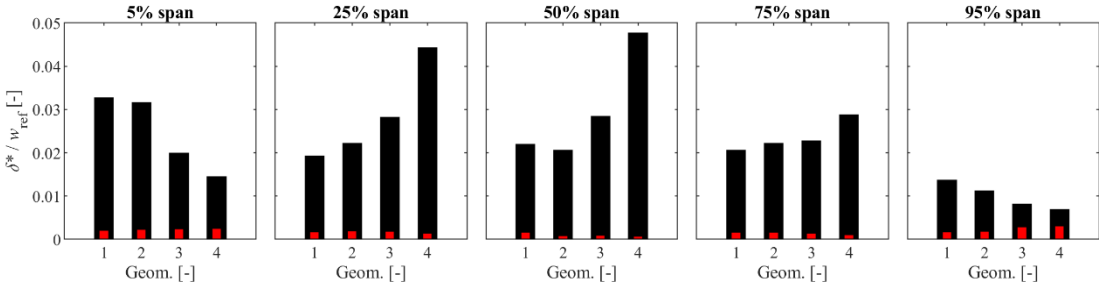


Figure 4.16: CFD-predicted normalized PS (red) and SS (black) displacement thicknesses for Geometry 1–4 at five different span locations.

We now estimate the contribution to overall loss of the PS and SS boundary layers. We define the local KE deficit in the BL (see discussion in Mee et al. [23]), $e_{\mathrm{KE}}(r)$, as the integral of the difference between the actual KE and the KE that the same gas would have had at freestream conditions

$$e_{\mathrm{KE}}(r) = 0.5 \int_0^{\delta_{99}} \rho(y,r) u(y,r) [U(r)^2 - u(y,r)^2] dy \tag{4.4}$$

where $\rho(y,r)$ and $u(y,r)$ are the local density and velocity as functions of surface-normal distance from the surface at a particular radial location, and $U(r)$ is the velocity at edge of BL at a particular radial location. The integration is performed at the damage front (location moves upstream as the vane is progressively cut back). Radial distributions $e_{\mathrm{KE}}(r)$ normalised by the maximum value across all simulations, $e_{\mathrm{KE,ref}}$ (i.e. $e_{\mathrm{KE}}(r)/e_{\mathrm{KE,ref}}$) are plotted in Figure 4.17 for Geometry 1–4.

Consider first the data for Geometry 1. We see that the SS dominates the boundary layer loss, with the mean value of $e_{\mathrm{KE}}(r)$ for the SS being 15 times that for the PS. In terms of spanwise distribution, both the SS and PS distributions are relatively constant with span, with some concentration of BL loss on the SS in the peaks at approximately 5% and 90% span corresponding to locations of the hub and case passage vortices (recall vorticity plots in Figure 4.7) which roll endwall fluid up into the BL.

With increasing burn-back we see the following effects:

1. On the PS there is a significant decrease (by up to 75% between Geometry 1 and Geometry 4) in loss within the burn-back region. This is due to reduced wetted surface, greater acceleration rate (see Figure 4.14).

2. On the SS, the BL loss increases over almost the entire span, with greater increase near hub than case. This is caused by the significant increase in BL thickness due to increasing adverse pressure gradient on the aft part of the vane (see Figure 4.14). The peaks in loss migrate towards midspan (from 4% to 9% span and from 87% to 81% span) leading to slight reductions in loss in the near wall regions. The migration is explained by the decreased static pressure downstream of TE within the burn-back region, creating local pressure gradients radially inwards.

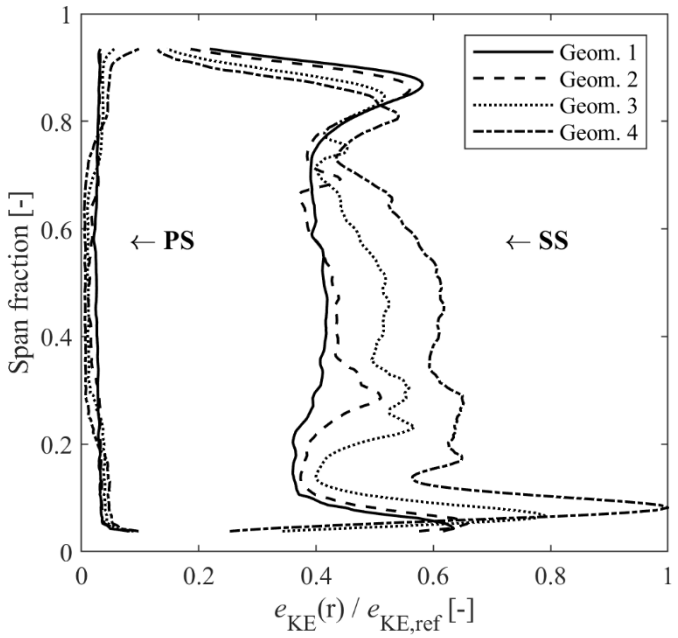


Figure 4.17: CFD-predicted spanwise distribution of normalised boundary layer KE dissipation coefficient, e_{KE}, for Geometry 1–4.

Now consider the BL loss coefficient (see, for example, Mee et al. [23]) which represents the ratio of KE deficit in the BL at the TE, to the ideal KE flux downstream of the vane if the flow expanded isentropically to the area average static pressure

$$\zeta_{BL} = \frac{\int e_{KE}(r)dr}{\dot{m}_m c_p T_{01}\left[1 - \left(\frac{\bar{p}_2}{p_{01}}\right)^X\right] + \dot{m}_c c_p T_{01}\left[1 - \left(\frac{\bar{p}_2}{p_{0c}}\right)^X\right]} \tag{4.5}$$

where $\dot{m}_m$ and $\dot{m}_c$ are the mainstream and coolant mass fluxes, respectively, $\bar{p}_2$ and $\bar{p}_{02}$ are the area-averaged static pressure and the mass-flux-averaged total pressure, respectively, and where p_{0c} is the coolant total pressure at coolant inlet (assumed uniform). T_{01} is the inlet total temperature (same for mainstream and coolant), c_p is the specific heat capacity, and $X = (\gamma - 1)/\gamma$, where γ is the isentropic exponent. The integral, and corresponding mass flow rates in the denominator, is evaluated between 5% and 95% span, which, note, means strict mass flow conservation between numerator and denominator across geometries is not maintained.

Evaluating the integral of KE flux dissipation over our set integral limits, we calculate the BL loss coefficients, ζ_{BL}. The PS loss coefficient, ζ_{BL}^{PS}, the SS loss coefficient, ζ_{BL}^{SS}, and total

BL loss coefficient, ζ_{BL}^{PS+SS}, are presented in Figure 4.18. With increasing burn-back, the PS BL loss decreases, and the SS BL loss increases. Between Geometry 1 and Geometry 4 the PS BL loss decreases by 34% and the SS BL loss increases by 12%. The total BL loss increases by 9%.

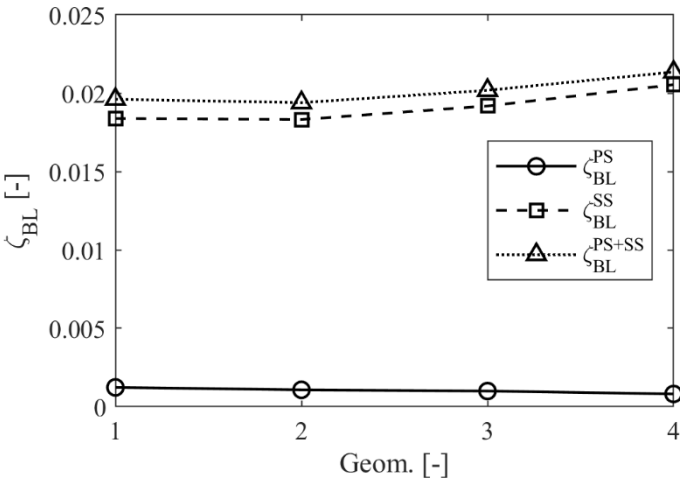


Figure 4.18: CFD-predicted BL loss coefficients for Geometry 1–4.

4.5.7 – Coolant mass flow rates and loss with introduction of coolant

We will now consider the impact of TE burn-back on the coolant mass flow rates and associated mixing losses. We find that in the progression from Geometry 1 to Geometry 4 the coolant flow increases for two reasons. Firstly, for fixed inlet total pressure and fixed coolant-to-mainstream total pressure ratio, as the vane Mach number increases, the surface static pressure reduces, driving more flow though the film cooling system. In addition, as the TE slot is cut back, the total pressure requirement to drive flow through the TE circuit reduces, and—separately—there is an increase in area of the slot. This leads to increased TE coolant flow. Increased cooling flow leads to greater mixing loss. In the particular case of cut-back, our base region increases in area, which—in the absence of other effects—we would expect to increase loss. The change in *overall* loss with increased cooling flow is a priori uncertain, however, because the total aerodynamic loss is significantly dependent on the TE flow dynamics, which depend on geometry, Mach number, and precise details of coolant ejection (mass flow, angle etc) as discussed by Melzer and Pullan [24], the competing effects are also hard to separate

(Burdet and Povey [25]), but we can quantify the overall change in loss when coolant is introduced by considering the difference in plane-averaged loss coefficient between cooled and uncooled simulations, i.e. $\Delta\zeta'''_{\mathrm{COOL}} = \zeta''' - \zeta'''_{\mathrm{UC}}$, where we define the mass-flux weighted plane-averaged loss coefficient in each case (method 3c in Burdett and Povey [15]) by

$$\zeta''' = 1 - \frac{(\dot{m}_{\mathrm{m}} + \dot{m}_{\mathrm{c}})\left[1 - \left(\frac{\bar{p}_2}{\bar{p}_{02}}\right)^X\right]}{\dot{m}_{\mathrm{m}}\left[1 - \left(\frac{\bar{p}_2}{p_{01}}\right)^X\right] + \dot{m}_{\mathrm{c}}\left[1 - \left(\frac{\bar{p}_2}{p_{0\mathrm{c}}}\right)^X\right]} \tag{4.6}$$

To reiterate, $\Delta\zeta'''_{\mathrm{COOL}}$ is not a mixing loss coefficient, but a change in total loss coefficient when cooling is introduced.

In Table 4.4 we present (for each build) the coolant mass flow normalised by the Geometry 1 total vane mass flow, $\dot{m}_{\mathrm{c}}/\dot{m}_{\mathrm{total,1}}$, and the change in overall loss coefficient with coolant introduction ($\Delta\zeta'''_{\mathrm{COOL}}$) as a fraction of the total mass-flux-averaged loss for the uncooled row, i.e. $\Delta\zeta'''_{\mathrm{COOL}}/\zeta'''_{\mathrm{UC}}$. We also present the percentage increase in these values from the Geometry 1 values.

Table 4.4: Summary of coolant fraction and overall loss change with coolant introduction for Geometry 1–4.

Geom.	$\frac{\dot{m}_{\mathrm{c}}}{\dot{m}_{\mathrm{total,1}}}$ [%]	$\frac{\Delta\zeta'''_{\mathrm{COOL}}}{\zeta'''_{\mathrm{UC}}}$ [%]	Δ w.r.t. Geom. 1 [%]	
			$\frac{\dot{m}_{\mathrm{c}}}{\dot{m}_{\mathrm{total,1}}}$	$\frac{\Delta\zeta'''_{\mathrm{COOL}}}{\zeta'''_{\mathrm{UC}}}$
1	6.6	12.0	–	–
2	6.7	17.1	+1.8	+42.4
3	7.0	16.0	+6.5	+33.1
4	7.5	20.0	+14.6	+67.0

We find that with increasing burn-back the total coolant mass flow rate increases from 6.6% to 7.5% of the Geometry 1 total vane flow. The additional loss associated with the introduction of coolant flow increases from 12.0% of the uncooled row loss to 20.0% of the uncooled row loss. The change in coolant flow fraction between Geometry 1 and Geometry 4 is 14.6%, but the change in loss increase (with introduction of coolant) is 67.0%. The

disproportionate increase in loss highlights the complexity of the TE flow dynamics, in that there is a different proportional response to cooling flow for different burn-back geometries.

4.5.8 – Overall aerodynamic performance

We will now consider the impact of TE burn-back on overall aerodynamic performance. We consider the plane-mass-flux-averaged loss, ζ''', and mixed-out loss, ζ''''. We also compute the residual secondary kinetic energy (SKE), ζ_{SKE}, at the downstream measurement plane, by difference from the plane-averaged loss and mixed-out loss (i.e. $\zeta_{\mathrm{SKE}} = \zeta'''' - \zeta'''$). Conceptually, the residual SKE is the additional loss that would be expected if the flow was allowed to reach its fully-mixed state. For the mixed-out loss coefficient (ζ'''') we used the Dzung method (see [26]; for discussion see Burdett and Povey [15]), in which the flow is mixed to an entirely uniform static pressure defined at a single, swirl-averaged radius

$$\zeta'''' = 1 - \frac{(\dot{m}_{\mathrm{m}} + \dot{m}_{\mathrm{c}})\left[1 - \left(\frac{\bar{p}_2{}'}{\bar{p}_{02}{}'}\right)^{\chi}\right]}{\dot{m}_{\mathrm{m}}\left[1 - \left(\frac{\bar{p}_2{}'}{p_{01}}\right)^{\chi}\right] + \dot{m}_{\mathrm{c}}\left[1 - \left(\frac{\bar{p}_2{}'}{p_{0\mathrm{c}}}\right)^{\chi}\right]} \tag{4.7}$$

where $\bar{p}_2{}'$ and $\bar{p}_{02}{}'$ are single values of static and total pressure at the measurement plane computed at nominal radius at which swirl velocity has its average value. We normalised all loss coefficients by a reference value, ζ''''_{ref}, equal to the value of the Geometry 1 mixed-out loss coefficient.

Normalised plane-averaged loss coefficients, ζ''', mixed-out loss coefficients, ζ'''', and residual SKE coefficients, ζ_{SKE}, for Geometry 1–4 are presented in Figure 4.19. Both experimental data and CFD predictions are compared. In the experimental data, the plane-averaged and mixed-out loss coefficients increase monotonically with increasing burn-back, with changes between Geometry 1 and Geometry 4 of 55% and 73% respectively. The SKE also increases monotonically, being 140% greater for Geometry 4 than for Geometry 1, and accounting for 29% of the change in mixed-out loss. The changes ($\Delta\zeta'''$, $\Delta\zeta_{\mathrm{SKE}}$, and $\Delta\zeta''''$) between each build are summarized in Table 4.5. Corresponding values for CFD predictions

are also presented, and characteristics are shown in Figure 4.19. The CFD is in excellent qualitative agreement with the experiment, and in reasonable quantitative agreement, particularly for the Geometry 1 to Geometry 4 change.

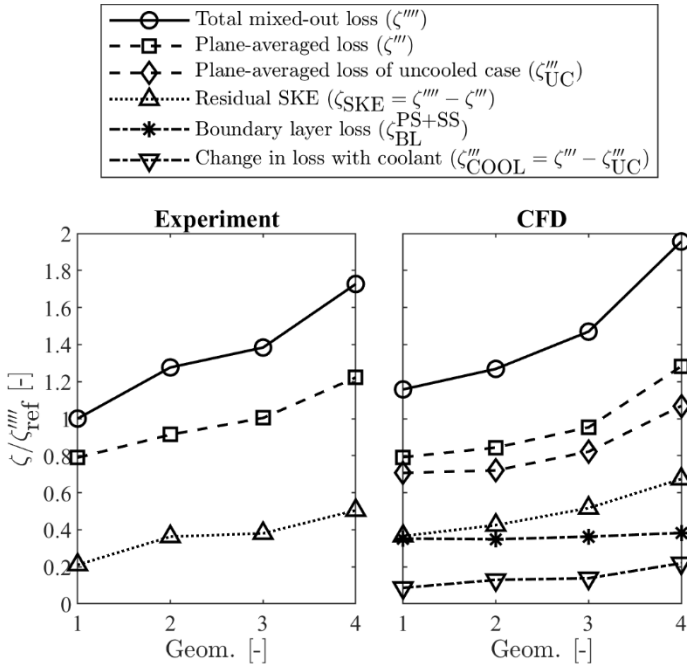


Figure 4.19: Coefficients for plane-averaged loss, mixed-out loss, SKE, loss with coolant (compared with uncooled case), and BL loss, for Geometry 1–4 for: (left) experimental measurements; and (right) CFD predictions.

For the CFD-predictions, we also present the change in the total BL (SS+PS) loss coefficient, $\Delta\zeta_{BL}^{PS+SS}$, and the loss coefficient associated with the overall change in loss with coolant introduction, $\Delta\zeta'''_{COOL}$. The total BL loss coefficient increases by 9% between Geometry 1 and Geometry 4, and—because the mixed out loss is increasing—reduces from making a contribution of 30% to mixed-out loss to 20%. The change in loss with the introduction of coolant increases by 153% between Geometry 1 and Geometry 4. Strictly we should not think of this term making a *contribution* to overall mixed-out loss, because it is more inseparably part of the defining the overall aerodynamics of the part. For completeness we note that this term is 8% of the mixed-out loss for Geometry 1 and 11% of the mixed-out loss for Geometry 4, however.

In summary, with increasing burn-back, there is little change in the BL loss (decreased wetted surface area near the midspan is offset by increased loading near the endwalls), but there is a significant increase in the plane averaged loss (increased projected area of base-pressure region; increased loading; already manifest secondary flow loss as a result of intensified vortices), and a significant increase in SKE (formation of strong pair of vortices at the burn-back edges; strengthening of some pre-existing secondary flows). This leads to a significant increase in overall mixed-out loss.

Table 4.5: Percentage changes (from Geometry 1) in coefficients for: plane-averaged loss, $\Delta\zeta'''$; SKE, $\Delta\zeta_{\mathrm{SKE}}$; mixed-out loss, $\Delta\zeta''''$; BL loss, $\Delta\zeta_{\mathrm{BL}}^{\mathrm{PS+SS}}$; and total loss change with introduction of coolant, $\Delta\zeta_{\mathrm{COOL}}'''$.

Geom.	$\Delta\zeta'''$ [%]	$\Delta\zeta_{\mathrm{SKE}}$ [%]	$\Delta\zeta''''$ [%]	$\Delta\zeta_{\mathrm{BL}}^{\mathrm{PS+SS}}$ [%]	$\Delta\zeta_{\mathrm{COOL}}'''$ [%]
Experiment					
$1 \rightarrow 2$	+16	+72	+28	–	–
$1 \rightarrow 3$	+27	+80	+38	–	–
$1 \rightarrow 4$	+55	+140	+73	–	–
CFD					
$1 \rightarrow 2$	+7	+16	+10	−1	+50
$1 \rightarrow 3$	+20	+41	+27	+3	+61
$1 \rightarrow 4$	+62	+84	+69	+9	+153

4.5.9 – Impact on capacity and stage performance

The impact of TE burn-back on NGV aerodynamic performance has been discussed. There is also an impact on vane and stage flow capacity, and on the stage aerodynamic performance. The changes from the Geometry 1 NGV capacity are +2.7%, +7.4% and +16.1% for Geometry 2 to 4 respectively. These changes are large, and, in conjunction with exit whirl angle changes, should be expected to have a significant impact on the inter-stage pressure, and therefore the stage performance. Detailed analysis of the stage behaviour using unsteady CFD simulations is clearly a necessary step to develop whole-life engine models.

4.6 – Conclusions

In this paper, we study the impact of TE burn-back on the aerodynamic performance of a high-pressure NGV. We present high-fidelity experimental measurements from an annular

cascade operating under engine-matched operating conditions. Fully-cooled real-engine parts have been used. The experimental data are complemented with cooled steady RANS of a part with a fully resolved internal and film cooling system. The parametric burn-back geometries used in the study were derived from statistical analysis of engine deterioration data.

We find the following:

1. *Damage shape.* Statistical analysis of engine deterioration data showed that the mean damage front centre was close to midspan, with a shape that was somewhat trapezoidal.

2. *General flow pattern.* With increasing burn-back; a strong pair of counter-rotating vortices were introduced at the burn-back edges, which caused increased loss and distortion of the wake; there was underturning in the burn-back region (change of metal angle) and overturning outside the burn-back-region (increased loading), which led to further distortion of the wake shape, and a significant increase in flow non-uniformity. We found that the CFD method did well at predicting the general flow situation, with some overprediction of peak loss due to underprediction of the mixing rate.

3. *Exit whirl angle distribution.* Increasing burn-back had a significant impact on the downstream vane exit flow angle distribution, partly as the direct result of TE material removal, but also due to the impact of new secondary flow vortices and vane re-loading in response to the material removal. Hub-to-tip whirl angle difference increased from 7.4 degrees to 16.4 degrees between Geometry 1 and Geometry 4. Local gradients were also significantly increased. This has implications for stage performance, and also rotor design, if acceptable stage performance is required even for deteriorated nozzle parts.

4. *Boundary layer profiles and loss.* The boundary layer loss accounted for approximately 30% of the overall mixed-out loss for the baseline part, of which

approximately 1/10th could be attributed to the PS and 9/10th to the SS. With increasing cut-back there was a complex redistribution of loss between the burn-back region and non-burn-back region. The total boundary layer loss increased by 9% for the most extreme burn-back geometry. This change was dominated by the change in the SS boundary layer. With increasing burn-back, the overall vane mixed-out loss increased at a greater rate than the boundary layer loss (formation of new secondary flows), so the BL loss accounted for a smaller proportion of the overall loss.

5. *Vane loading distribution, coolant flow and coolant mixing loss.* With increasing TE burn-back the SS Mach number increased (from-mild subsonic to mild-supersonic). This led to a reduction in surface static pressures, and there was an attendant increase in total coolant mass flow rate from 6.6% to 7.5% of the reference (Geometry 1) total passage flow. That is, the coolant mass flow increased by 14.6%. Using simulations with and without cooling it was shown that the *change in the increase in loss* with introduction of coolant was 67.0%. This change is significantly larger than the change in coolant mass flow rate, showing that the impact of coolant on overall loss depends on the entire TE flow dynamics, which depend on geometry, Mach number, and precise details of coolant ejection (mass flow, angle etc.). That is, the coolant mixing loss is perhaps subordinate to other effects.

6. *Overall aerodynamic performance.* With increasing burn-back, there is very little change in the BL loss (decreased wetted surface area near the midspan is offset by increased loading near the endwalls), but there is a significant increase in the plane averaged loss (increased projected area of base-pressure region; increased loading; already manifest secondary flow loss as a result of intensified vortices), and a significant increase in SKE (formation of strong pair of vortices at the burn-back edges; strengthening of some pre-existing secondary flows). This leads to a significant increase in overall mixed-out loss. Between Geometry 1 and Geometry 4 the mixed-out loss coefficient increased by 72.8%.

We hope this paper will prove a useful reference point for improved quantitative and qualitative understanding of the penalties associated with TE burn-back, and help improve whole-life performance assessment.

Nomenclature

Romans

A_{BB}	burn-back area [mm^2]
A_{ref}	reference area [mm^2]
C_{t}	tangential chord length [mm]
C_x	axial chord length [mm]
c_{p}	specific heat capacity [J kg^{-1} K^{-1}]
d	tangential depth of burn-back [mm]
e_{KE}	local KE deficit in boundary layer [–]
k	turbulent kinetic energy [m^2 s^{-2}]
M	Mach number [–]
$\dot{m}$	mass flow rate [kg s^{-1}]
$\dot{m}_{\mathrm{total,1}}$	Geometry 1 total vane mass flow rate [kg s^{-1}]
p	pressure (total or static) [Pa]
$\bar{p}$	circumferentially-averaged pressure [Pa]
$\bar{p}'$	mixed-out pressure [Pa]
R^2	coefficient of determination [–]
r	radial position [mm]
Re	Reynolds number [–]
S	span height [mm]
T	temperature [K]
Tu	turbulence intensity [%]
U	freestream velocity [m s^{-1}]
u	local velocity [ms^{-1}]
w_1	width of burn-back at TE [mm]
w_2	width of burn-back at damage front [mm]
w_{ref}	geometric throat width of Geometry 1 [mm]
x	axial position [mm]
y	surface-normal distance [mm]
y^+	non-dimensional wall distance [-]

Greeks

β	flow turning (or whirl) angle [deg]
β'	circumferentially-averaged whirl angle [deg]
δ^{99}	boundary layer thickness [mm]
δ^*	displacement thickness [mm]
θ	momentum thickness [mm]
γ	ratio of specific heat capacities [–]
ζ'	local KE loss coefficient [–]
ζ''	circumferentially-averaged KE loss coefficient [–]

ζ'''	plane-averaged KE loss coefficient [–]
ζ'''_{UC}	plane-averaged KE loss coefficient for uncooled simulation [–]
$\Delta\zeta'''_{\mathrm{COOL}}$	change in plane-averaged KE loss coefficient with the introduction of coolant [–]
ζ''''	mixed-out KE loss coefficient [–]
ζ_{BL}	boundary layer loss coefficient [–]
$\zeta_{\mathrm{BL}}^{\mathrm{PS}}$	PS boundary layer loss coefficient [–]
$\zeta_{\mathrm{BL}}^{\mathrm{SS}}$	SS boundary layer loss coefficient [–]
$\zeta_{\mathrm{BL}}^{\mathrm{PS+SS}}$	total boundary layer loss coefficient [–]
ζ_{SKE}	residual SKE loss coefficient [–]
ρ	local density [kg m^{-3}]
X	$(\gamma-1)/\gamma$
ω	specific turbulence dissipation rate [s^{-1}]
ω_{x}	component of vorticity in axial direction [s^{-1}]

Subscripts

0	stagnation condition
1	upstream of NGV; Geometry 1
2	downstream of NGV; Geometry 2
3	Geometry 3
4	Geometry 4
BB	burn-back region
non-BB	non burn-back region
c	coolant
s	isentropic condition
m	mainstream
MAX	maximum value
MEAN	mean value
PS	pressure side
ref	reference value
SS	suction side

References

[1] Sjolander, S. A., Isaacs, D., and Klein, W. A, 1993, "Aerodynamics of Turbine Blades with Trailing-Edge Damage: Measurements and Computations," Proceedings of the International Symposium on Air Breathing Engines 1993, Tokyo, Japan, 20–24 September 1993, Paper No. ISABE93-7130.

[2] Islam, A. M. T., 1999, "An Experimental and Computational Study of the Aerodynamics of Turbine Blades with Damage," Ph.D. thesis, Carleton University, Canada.

[3] Wang, S. S., Mao, J. R., Liu, G. W., and Feng, Z. P., 2010, "Performance deterioration of the governing stage nozzle caused by solid particle erosion in the steam turbine," Proceedings of the Institution of Mechanical Engineers, Part A: Journal of Power and Energy, 224(2), DOI: 10.1243/09576509JPE852.

[4] Bouchard, D., Asghar, A., LaViolette, M., Allan, W. D. E., and Woodason, R, 2014, "Experimental Evaluation of Service-Exposed Nozzle Guide Vane Damage in a Rolls Royce A-250 Gas Turbine," ASME J. Engineering for Gas Turbines and Power, 136(10), DOI: 10.1115/1.4027204.

[5] Meyer, M., Parchem, R., and Davison, P., 2011, "Prediction of Turbine Rotor Blade Forcing due to In-Service Stator Vane Trailing Edge Damage," Proceedings of the ASME Turbo Expo 2011, Vancouver, Canada, 6–10 June 2011, Paper No. GT2011-45204, DOI: 10.1115/GT2011-45204.

[6] Di Mare, L., Imregun, M., Smith, A. D., and Elliott, R., 2007, "A Numerical Study of High Pressure Turbine Forced Response in the Presence of Damaged Nozzle Guide Vanes," The Aeronautical Journal, 111(1125), DOI: 10.1017/S0001924000004929.

[7] Rajput, M. U., 2013, "Evaluation of Experimental Forced Response Data of a Turbine Stage with Respect to Different Stator Blade Damages," M.Sc. thesis, KTH Royal Institute of Technology, Sweden.

[8] Kost, F., and Giess, P. A., 2004, "Experimental Turbine Research at DLR Göttingen," J. Gas Turbine Society of Japan, 32(6).

[9] Michaud, M., Jackson, D., Goenaga, F., and Povey, T., 2023, "Experimental Study of Impact of In-Service Deterioration on Aerodynamic Performance of High-Pressure Nozzle Guide Vanes," ASME J. Turbomachinery, 145(6), DOI: 10.1115/1.4056774.

[10] Michaud, M., Chowdhury, N., and Povey, T., 2023, "Experimental Study of Impact of In-Service Deterioration on Thermal Performance of High-Pressure Nozzle Guide Vanes," ASME J. Turbomachinery, 145(2), DOI: 10.1115/1.4055864.

[11] Kirollos, B., Lubbock, R., Beard, P., Goenaga, F., Rawlinson, A., Janke, E., and Povey, T., 2017, "ECAT: An Engine Component Aerothermal Facility at the University of Oxford," Proceedings of ASME Turbo Expo 2017, North Carolina, USA, June 26–30 2017, Paper No. GT2017-64736, DOI: 10.1115/GT2017-64736.

[12] Messenger A, and Povey T., 2020, "Calibrated Low-Order Transient Thermal and Flow Models for Robust Test Facility Design," J. Global Power and Propulsion Society, 4(1), DOI: 10.33737/jgpps/122270.

[13] Michaud, M., Ornano, F., and Povey, T., 2022, "Annular Dump Diffuser and Deswirl System for Back-Pressure Control in Engine-Scale Transonic Annular Cascade," ASME J. Turbomachinery, 145(4), DOI: 10.1115/1.4055863.

[14] Burdett, D., Hambidge, C., and Povey, T., 2020, "Analysis of Ultra-Low Uncertainty Gas Turbine Flow Capacity Measurement Techniques," Proceedings of the Institution of Mechanical Engineers, Part A: J. Power Energy, 235(5), DOI: 10.1177/0957650920909718.

[15] Burdett, D., and Povey, T., 2022, "Analysis of Averaging Methods for Nonuniform Total Pressure Fields," ASME J. Turbomachinery, 144(5), DOI: 10.1115/1.4053020.

[16] Amend, J., and Povey, T., 2024, "Comparison of Eddy Viscosity Models for High Turbulence NGV Flows," ASME J. Turbomachinery, 146(8), DOI: 10.1115/1.4064484.

[17] Amend, J., Lubbock, R., Ornano, F., Chowdhury, N., and Povey, T., 2024, "Aerodynamic and Thermal Field Development of Cooled Transonic HP NGV," ASME J. Turbomachinery, 146(2), DOI: 10.1115/1.4063879.

[18] Smith Jr., L. H., 1966, "The Radial-Equilibrium Equation of Turbomachinery," ASME J. Engineering for Power, 88(1), DOI: 10.1115/1.3678471.

[19] Rowbury, D., 1998, "Discharge Coefficients of Nozzle Guide Vane Film Cooling Holes," Ph.D. thesis, University of Oxford, England.

[20] Burdett, D., and Povey, T., 2022, "Experimental and Numerical Analysis of Loss Characteristics of Cooled Transonic Nozzle Guide Vanes," ASME J. Turbomachinery, 144(5), DOI: 10.1115/1.4053019.

[21] Goldstein, R. J., and Spores, R. A., 1988, "Turbulent Transport on the Endwall in the Region Between Adjacent Turbine Blades," ASME J. Heat Transfer, 110(4a), DO: 10.1115/1.3250586.

[22] Mee, D. J., Baines, N. C., and Oldfield, M. L. G., 1992, "Detailed Boundary Layer Measurements on a Transonic Turbine Cascade," ASME J. Turbomachinery, 114(1), DOI: 10.1115/1.2927980.

[23] Mee, D. J., Baines, N. C., Oldfield, M. L. G., and Dickens, T. E., 1992, "An Examination of the Contributions to Loss on a Transonic Turbine Blade in Cascade," ASME J. Turbomachinery, 114(1), DOI: 10.1115/1.2927979.

[24] Melzer, A. P., and Pullan, G., 2019, "The Role of Vortex Shedding in the Trailing Edge Loss of Transonic Turbine Blades," ASME J. Turbomachinery, 141(4), DOI: 10.1115/1.4041307.

[25] Burdett, D., and Povey, T., 2022, "Impact of Trailing Edge Overhang Length on the Loss Characteristics of Fully Cooled Transonic Nozzle Guide Vanes," ASME J. Turbomachinery, 145(5), DOI: 10.1115/1.4056056.

[26] Dzung, L. S., 1971, "Konsistente Mittlewerte in der Theorie der Turbomaschinen für Kompressible Medien," BBC Mitteilungen, 58.

Chapter 5 – Vane flow capacity

This chapter builds on the aerodynamic study of Chapter 4 and extends it to consider how trailing-edge burn-back affects the flow capacity of high-pressure nozzle guide vanes. The work is presented in the form of a peer-reviewed journal article[2].

Abstract

In this paper we consider the impact of trailing edge burn-back (due to oxidation damage) on the flow capacity of cooled transonic high-pressure nozzle guide vanes. The purpose is to provide understanding that can lead to improved whole-life engine performance modelling. We present experimental results from an ultra-low uncertainty experiment in a full-annulus nozzle guide vane cascade, and compare these with results from high-fidelity computational fluid dynamics simulations. Experiments were performed in (the Engine Component Aero-Thermal (ECAT) facility at the University of Oxford), using a sequence of four geometries with increasing simulated burn-back. We find that for fixed vane pressure ratio, increased burn-back leads to: increased overall vane capacity, with changes from the nominal geometry of +2.7%, +7.4% and +16.1%; increased coolant capacity, with changes from the nominal geometry of +2.4%, +6.9% and +15.0%; and significant variation in whirl angle distribution within the burn-back region, with little effect on the outside region. There is very poor correlation between the change in geometric minimum area and the vane capacity change, highlighting the need to consider the aerodynamics in the entire controlling region of the vane. A related paper by Raduev et al. [1] considers the impact of burn-back on aerodynamic performance. Taken together these papers provide a basis for a HP stage model within a whole-life engine performance model.

[2] The text in this chapter is a verbatim reproduction of the published, multi-author, journal paper with some clarifications. It has also been stylistically adapted to match the typeface, margins, and pagination of this thesis.

Publication status and co-author contributions

This *journal* paper titled "*Impact of Trailing Edge Damage on Nozzle Guide Vane Flow Capacity*" has been accepted for publication in the ASME Journal of Turbomachinery [5]. The co-author contributions are as follows. Zelimhan Raduev (student): determined burn-back designs; collected all experimental data; performed all simulations; wrote processing scripts of experimental and numerical data; analysed all experimental and numerical data; generated all figures; and was responsible for the manuscript writing. Dougal Jackson (industry contact): provided engine parts for experiments; provided deterioration data so burn-back designs can be determined; contributed with analysis ideas. Nafiz Chowdhury (research associate): supported experimental campaign helping collect all experimental data. Thomas Povey (supervisor): supervised all aspects of the work. A statement of authorship is included at the end of the thesis.

5.1 – Introduction and literature review

High-pressure (HP) nozzle guide vanes (NGVs) are subject to trailing edge (TE) damage caused by erosion (impact of foreign objects such as sand) and oxidation. This latter effect is sometimes referred to as burn-back. Burn-back has implications for row and stage performance, and is of increasing interest to the community interested in whole-life performance modelling. While there are studies investigating the effects of in-service deterioration, including burn-back, on aerodynamic performance (such as those reviewed in Raduev et al. [1]), there are no studies addressing the specific impact of burn-back on NGV flow capacity, which is the subject of this paper. To provide wider context for this study, however, we now review the body literature on more general NGV flow capacity studies. So far as this literature is concerned, it can be broadly subdivided into five categories: impact of vane loading on capacity; impact of loss on capacity; impact of cooling flow on capacity; impact of manufacturing variation on capacity; impact of trailing edge on capacity; and low-uncertainty capacity measurement techniques. We now briefly review the literature under these headings.

Impact of vane loading on capacity. Afanasiev et al. [2, 3] numerically investigated two annular vane rows with identical geometric throats but different loading distributions. The first was forward-loaded (uncovered turning of 10 degrees), and the second aft-loaded (uncovered turning of 32 degrees). The authors demonstrated flow capacity differences of up to 12% for subsonic conditions between the two vane rows, and flow capacity differences of up to 5% for mildly supersonic conditions. This showed the importance of vane aerodynamics in setting capacity in addition to the geometric minimum area. The forward-loaded vane had a sonic region upstream of the geometric minimum area, and the aft-loaded vane downstream of the geometric minimum area. This showed that simple one-dimensional considerations (e.g. axisymmetric nozzle flow) are insufficient to explain NGV flows.

Impact of loss on capacity. Though the general impact of irreversibility on capacity was understood, Fielding [4] was the first to develop a boundary layer method for estimating the change in nozzle (and turbine) capacity with loss. Previous one-dimensional methods had considered the loss to be distributed evenly throughout the passage, leading to an underestimate of the flow capacity. By relating the boundary layer displacement thickness and energy thickness, Fielding developed a restriction factor (which represented the reduction in effective flow area due to BL blockage) which was expressed as function of the profile loss coefficient. Though this early work was two-dimensional in the sense that it was an adaption of boundary layer theory, the flow was considered to be one-dimensional from the point of view of aerodynamics: there was no concept of a two-dimensional (or three-dimensional) potential field. Though the principles of the Fielding loss theory are still sound, later work showed that aerodynamics and TE dynamics are generally more influential than loss in the problem of reconciling absolute capacity with geometric area.

Povey et al. [5] considered the impact of 1D (single mean pressure), 2D (radial pressure profile) and 3D (radial and circumferential pressure profile) modelling on capacity characteristics, comparing modelled results with high-accuracy experimental measurements. They showed that differences in fidelity of the modelling of the pressure field could give rise

to differences of up to 1.5% in the capacity value (for the same physical area), and that higher-fidelity modelling led to a closer match to the experimentally-measured characteristic shape, but that pressure-field modelling was only one of many aspects of the problem physics that was important for absolute capacity matching. The authors noted the primary importance of the vane aerodynamics (or pressure field) and vane loss, but also the secondary importance of: turbulence, affecting the state of the BL and thus loss; film cooling affecting the BL state, and passing through the throat as a partially-mixed film; strong 3D flow structures due to vane design (swept, leaned, or bowed designs) and endwall contouring; BL separation or separation induced by leakage flows; the geometry of the TE slot and the blowing through the TE slot influencing the flow dynamics of the base region.

Impact of cooling flow on capacity. Povey [6] analytically investigated the impact of film cooling on NGV flow capacity. The analytical model used a control volume mixing model. The impact of film cooling was expressed in terms of a mass flow rate correction parameter, which related the mass flow assuming partial mixing of mainstream and coolant streams to the mass flow assuming mainstream conditions for the entire passage flow (i.e. no coolant). At the cold-rig condition, the introduction of cooling flow decreased the total mass flow rate by 0.21%. The mass flow decreased because of total pressure loss in the mixing layer. At the engine conditions (of temperature ratio and gas properties), the introduction of cooling flow increased the total mass flow by 1.67%. In this case the effect of the increase in near-wall density (relatively cold coolant) outweighed the effect of near-wall mixing loss.

Hambidge and Povey [7] later performed a numerical investigation of the effect of coolant on HP NGV. A modern NGV design with ten film cooling rows was studied. The purpose was to study the influence of the NGV aerodynamic field, and to determine the accuracy with which the superposition principles could be used in both the CFD results and the analytical model [6]. The authors showed that with the introduction of coolant, CFD predicted a vane capacity reduction of 0.144% and the analytical model a vane capacity reduction of 0.125%. Results were for a coolant-to-mainstream mass flow rate fraction of approximately 4%, and at

a Mach number of unity. The results were taken to be in good agreement. The late PS and SS film rows had a significantly larger (mass-adjusted) effect than early rows, because they inject into a mainstream flow at a higher local Mach number. It was further shown that simple additive superposition approaches worked with a high degree of accuracy in both the CFD (simulations run with individual cooling holes blowing, to allow separated results) and analytical model.

Impact of manufacturing variation on capacity. The primary influence of vane loading distribution has been discussed. A secondary influence is the detailed vane shape within the manufacturing control limit: the manufacturing scatter. Hogner et al. [8] and later Voigt et al. [9] considered the impact of manufacturing variation on capacity in CFD studies based on a statistically-significant number of as-manufactured real-vane shapes reconstructed from high-accuracy 3D scans. Automated meshing routines were used. Hogner et al. [8] studied TE related parameters (SS and PS lip radius and length, PS lip profile angle, and TE slot width, height, and position), and other vane shape parameters (PS and SS profile offset, and hub and casing fillet radii). They found that TE slot position and PS profile offset had the greatest influence on flow capacity (statistically best correlation of these parameters with flow capacity). The authors also demonstrated linear superposition of these two parameters highlighting their relative independence. Voigt et al. [9] (same group; similar methods) extended the original study by introducing more parameters (twenty in total). They found that stagger angle was best correlated with flow capacity, and that parameters associated with the profiled endwall were the least correlated.

Impact of trailing edge on capacity. For a vane of cut-back PS TE design (overhanging SS) Burdett et al. [10] studied the effect of varying SS overhang length (fixed PS TE geometry). Four overhang lengths were tested in the range 13.4% to 0% of axial chord (approximately 6.3% to 0% tangential chord). Zero overhang is—by definition—a centred-ejection design. The authors used a highly accurate capacity measurement method (precision error 0.025%; bias error 0.495%; both figures quoted to 95% accuracy) and high-fidelity CFD.

They found that for their particular vane shape, the centred-ejection design had a capacity 2.52% greater than an equivalent design with SS overhang. There were small changes in film cooling and TE slot cooling (associated with the change in TE design) but these were not thought to be significant so far as the overall capacity change was concerned. Analysing the aerodynamic flow field in the controlling region (the wider transonic region around the point of minimum area), the authors found that the static pressure field was highly sensitive to the detailed TE design, and that changes in aerodynamics (or the potential field) were the primary reason for changes in overall capacity. This study emphasized that to understand capacity changes, it is necessary to consider aerodynamic changes in the controlling region more broadly: the capacity change is rarely explained purely by a change in minimum area. Indeed, it is possible to have a significant capacity change without a change in minimum area. This is in line with the result of Afanasiev et al. [2, 3] who showed large capacity differences between two vanes with identical geometric minimum area, but different loading.

Low uncertainty capacity measurement techniques. Vane capacity measurement has traditionally been the preserve of engine manufacturers because of the cost of the required experimental facilities, which necessarily need to be of high technology readiness level (TRL), i.e. closely replicating the engine flow field. A minimum requirement is for such a facility to be fully annular cascade, with real engine parts, at matched conditions of Reynolds number and Mach number, and—if relevant—matched cooling flow boundary conditions. Historically, steady-state facilities have been used for this type of measurement, operating with a megawatt compressor plant. More recently, Povey et al. [5] demonstrated a novel semi-transient experimental technique that was capable of measuring NGV capacity with higher accuracy and lower cost than the traditional techniques. The facility (the Oxford Capacity Facility) was a blowdown-type engine parts annular cascade run at matched Mach number, Reynolds number, and coolant-to-mainstream pressure ratios. Bias and precision uncertainties for capacity measurement of ±0.535% and ±0.028%, respectively, were achieved in this facility (all figures quoted to 95% confidence). The capability was later integrated into the Engine

Component Aerothermal Facility (ECAT) (see Kirollos et al. [11]), allowing simultaneous measurement of NGV capacity, thermal performance (metal effectiveness) and aerodynamic performance. In this facility further improvements led to bias and precision uncertainties for capacity measurement of ±0.301% and ±0.025%, respectively (see uncertainty analysis in Burdett et al. [12]). A large number of studies have been conducted in this facility, including a number which focus primarily on accurate capacity understanding [5, 10-12]. ECAT typically operates at a mainstream-to-coolant temperature ratio of 1.2. The recently-commissioned ECAT+ facility (see Messenger et al. [13]) has similar capacity measurement capability to ECAT (bias and precision uncertainties of ±0.535% and ±0.028% respectively), but has extended temperature capability, allowing mainstream-to-coolant temperature ratios up to 2.0 (covering the engine condition).

5.1.1 – Current study

In the current study we consider the impact of TE burn-back on NGV capacity. We use real engine parts, with four levels of simulated burn-back ranging from new to severely damaged (27.5% tangential chord removed). Experiments were performed in the Oxford ECAT facility [11], allowing ultra-low uncertainty capacity measurements. We compare the experimental data with high-fidelity computational fluid dynamics simulations. A related study by Raduev et al. [1] considers the impact of TE burn-back on aerodynamic performance. These are the first studies of the impact of TE burn-back on HP vane capacity and aerodynamic performance. The studies inform whole-life engine performance modelling because of the impact on intra-stage pressure, and the HP and following-stage pressure ratios, which impact engine efficiency as the turbine stages move away from the design condition.

5.2 – Trailing edge damage shapes

The baseline NGV geometry for this study is a cut-back PS (TE lip) design with an integrated TE cooling slot, from a modern aero-engine. This is shown in Figure 5.1. Four levels of simulated burn-back were tested, ranging from new parts to severely damaged. The particular burn-back shapes were based on a statistical analysis of hundreds of deteriorated

parts from real engines. The analysis (similar method and conclusions to Meyer et al. [14]) showed that the real TE burn-back regions were centred on midspan, and were of approximately trapezoidal form. Based on the statistical analysis we define four representative geometries, characterized by the following four non-dimensional parameters: burn-back depth normalised by the vane tangential chord, d/C_t; burn-back width at TE normalised by vane span, w_1/S; burn-back width at damage front normalised by span, w_2/S; and normalised burn-back area, A_{BB}/A_{ref}, where $A_{ref} = C_t \times S$. The burn-back geometries are shown in Figure 5.1. The values for each of the non-dimensional parameters are summarised in Table 5.1.

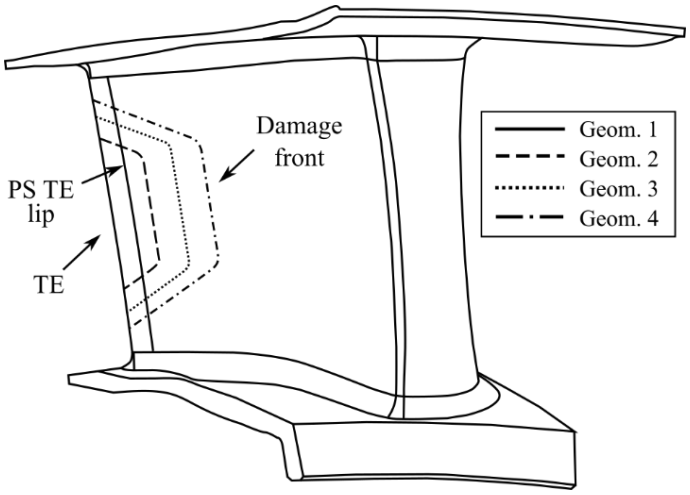


Figure 5.1: Simulated burn-back Geometry 1–4.

Table 5.1: Summary of damage shape parameters for Geometry 1–4.

Non-dimensional damage shape parameters	Geom.			
	1	2	3	4
Burn-back depth, d/C_t [%]	0	10.8	19.2	27.5
Burn-back width at TE, w_1/S [%]	0	42.5	54.6	66.8
Burn-back width at damage front, w_2/S [%]	0	29.8	33.3	36.8
Burn-back area, A_{BB}/A_{ref} [%]	0	3.9	8.4	14.2

5.3 – Experimental method

Capacity (mass-flow) measurements were performed using the Engine Component Aerothermal (ECAT) facility at the University of Oxford. The ECAT facility is a high technology-readiness-level (TRL) modular engine-scale blowdown facility. The test components were an annular cascade of NGVs from a modern civil engine. The facility was

operated at engine-representative conditions of Mach number, Reynolds number, and coolant-to-mainstream pressure ratio. Further details of the operation of the facility can be found in [11, 13, 15]. A cross-section schematic of the facility working section is presented in Figure 5.2, with the modular vane ring highlighted. Operating conditions used in this study are summarized in Table 5.2.

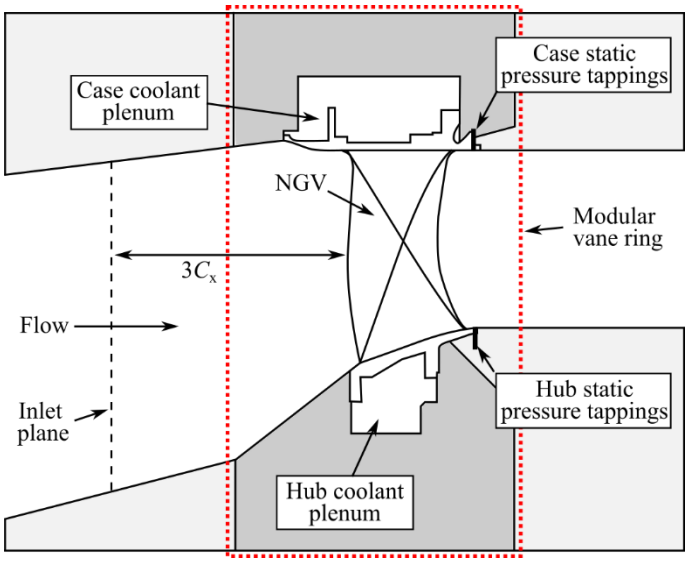


Figure 5.2: Schematic cross-section of the ECAT facility working section.

Table 5.2: ECAT facility operating conditions.

Variable	Value
Mainstream inlet total temperature, T_{01}	287 K
Coolant inlet total temperature, T_{02}	287 K
Vane pressure ratio range, p_{exit}/p_{01}	0.40–0.80
Design vane pressure ratio, p_{exit}/p_{01}	~0.54
Coolant-to-mainstream pressure ratio, p_{02}/p_{01}	1.026
Isentropic Mach number, M_s	0.58–1.22
Reynolds number based on tangential chord, Re	1.3–1.6×10^6
Inlet turbulence intensity, Tu	~13% [16]

The ECAT facility can be operated in either steady-state mode (typically used for traverse measurements) or blow-down mode (typically used for capacity characteristic measurements). In either mode, the run time is approximately 100 s and the flow can be instantaneously regarded as quasi-steady. Air is supplied from large pressurised tanks, through independently-metered mainstream, hub coolant, and case coolant lines. The facility was specifically

developed for ultra-high-accuracy capacity measurements, and detailed analysis of the development and method are presented in Povey et al. [5] and later in Burdett et al. [12]. We summarize some details briefly here.

The mainstream mass flow rate is metered using a choked Venturi nozzle calibrated at the Colorado Engineering Experiment Station, Inc. (CEESI) to a National Institute of Standards and Technology (NIST) traceable standard. The hub and case coolant lines are metered using sonic Venturi nozzles manufactured and installed according to ISO 9300:2022 [17]. Mass flow bias and precision uncertainties (in the mean of the data) were approximately ±0.312% and ±0.113% respectively for the mainstream, and are approximately ±0.873% and ±0.071% respectively for the coolant stream (quoted to 95% confidence).

Total pressure and total temperature of the mainstream flow was measured three axial chord lengths upstream of the vane leading edge (LE), using four pitot probes rakes and four thermocouple rakes. Each rake had eight measurement points. The vane exit boundary condition was measured using 84 static pressure tappings located a third axial chord downstream of the vane TE, distributed over six vane passages on the hub and case endwalls. We define the vane pressure ratio as the ratio between the mean exit static pressure and mean upstream total pressure (i.e. p_{exit}/p_{01}). The hub and case coolant stream total pressures (p_{02} and p_{03}) were measured using three pitot probes each, and the hub and case total temperatures (T_{02} and T_{03}) were measured using three thermocouples each. Measurement locations are indicated in Figure 5.2.

We define flow capacity (see discussion in Burdett et al. [12]) by

$$\Gamma_{\text{vane}}\left(\frac{p_{\text{exit}}}{p_{01}},\frac{p_{02}}{p_{01}},\frac{p_{03}}{p_{01}}\right)=\frac{\dot{m}_1\left(\frac{p_{\text{exit}}}{p_{01}},\frac{p_{02}}{p_{01}}\right)\sqrt{T_{01}}}{p_{01}} + \frac{\dot{m}_2\left(\frac{p_{\text{exit}}}{p_{01}},\frac{p_{02}}{p_{01}}\right)\sqrt{T_{02}}}{p_{02}}+\frac{\dot{m}_3\left(\frac{p_{\text{exit}}}{p_{01}},\frac{p_{03}}{p_{01}}\right)\sqrt{T_{03}}}{p_{03}} \tag{5.1}$$

where the subscripts 1, 2, and 3 are the mainstream inlet, hub coolant stream, and case coolant stream flows, respectively. In this definition capacity is not only a function of the vane static-to-total pressure ratio, p_{exit}/p_{01}, but also of the two coolant-to-mainstream total pressure ratios p_{02}/p_{01} and p_{03}/p_{01}. This definition is preferred (see Burdett et al. [12]) because it is robust to translation between different environments (rig and engine, for example) but also explicitly includes sensitivity to individual stream total pressures in the formulation. In the current study, however, all of our experiments and CFD were run with normalised *excess pressures* (i.e. $(p_{02} - p_{01})/p_{01}$ and $(p_{03} - p_{01})/p_{01}$) within 2.6% of the nominal value. We therefore simplify Equation 5.1 to

$$\Gamma_{\text{vane}}\left(\frac{p_{\text{exit}}}{p_{01}}\right) = \frac{\dot{m}_1\left(\frac{p_{\text{exit}}}{p_{01}}\right)\sqrt{T_{01}}}{p_{01}} + \frac{\dot{m}_2\left(\frac{p_{\text{exit}}}{p_{01}}\right)\sqrt{T_{02}}}{p_{02}} + \frac{\dot{m}_3\left(\frac{p_{\text{exit}}}{p_{01}}\right)\sqrt{T_{03}}}{p_{03}} \tag{5.2}$$

where, although we maintain the second and third terms on the right hand side as distinct, we note that in all of our experiments and simulations $T_{02} \approx T_{03}$ and $p_{02} \approx p_{03}$.

A detailed uncertainty analysis for capacity measurement in the ECAT facility is presented in Burdett et al. [12], and is also recorded in Appendix 2. The bias uncertainty in capacity was evaluated to be ±0.301% to 95% confidence. The single-run precision uncertainty was evaluated to be approximately 0.113% to 95% confidence. In our method we repeated each run at least 16 times to reduce the precision uncertainty in the mean to $0.113/\sqrt{16} = 0.028\%$ (95% confidence). This is the relevant uncertainty for comparative measurements with geometry changes.

To allow direct back-to-back comparison of the Geometry 1 to Geometry 4 measurements (with geometry changes in-between) we performed in-situ machining of individual vanes in an assembled NGV module. The NGV module is removable from the main working section, and was mounted to segmented ground-steel (rigid and flat) fixture plates. To ensure rigid support of the module during removal and machining, the design allowed the fixture plates to be mounted to the NGV module before the module was unbolted from the main working section. The NGV module with fixture plates is shown in Figure 5.3. Further details of this

method are given in Burdett et al. [10]. To modify the geometry between Geometry 1 and Geometry 4 the vanes were machined on a three-axis CNC with appropriate tooling for local alignment (against the local trailing edge and hub and casing walls). The machined cut is as shown in Figure 5.1.

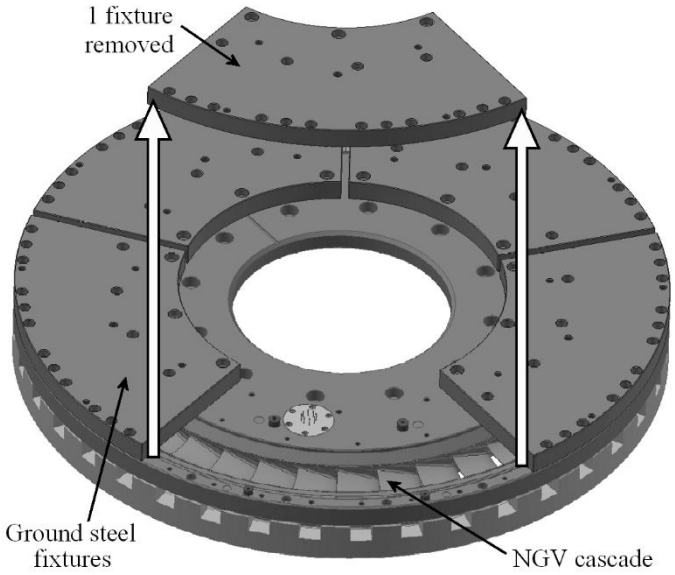


Figure 5.3: NGV module with fixture plates (from Burdett et al. [10]).

5.4 – Numerical method

Steady Reynolds-averaged Navier-Stokes (RANS) CFD simulations were performed for Geometry 1–4 using ANSYS CFX and BOXERMesh (unstructured octree-based mesh). The *k-ω* SST turbulence model was used, with second order discretization for the advection and turbulence terms. Note that in the previous chapter the BSL-EARSM turbulence model was used as it was shown to be more accurate for aerodynamic loss comparisons compared to the *k-ω* SST turbulence model, however, no significant improvement was shown for capacity predictions and hence, it was not used here. The computational domain was an 18-degree sector (two vanes, of forty) with the same annulus lines as the ECAT facility. The TE slot was explicitly modelled. Film cooling was modelled using area-patches, with individually-specified hole location, size, direction vector, and mass flow rate. An image of this domain is shown in Figure 5.4. A mesh detail is shown in Figure 5.5. A mesh sensitivity study was performed to ensure mesh-independence of capacity, and to ensure the viscous sub-layer was

adequately captured within the near-wall inflation layers. The mesh had approximately 60 million cells. The mesh was refined in the wake region, near the TE, around the NGV surface, the geometric throat, and along the burn-back edges. The average y^+ value on the wetted surfaces of the NGV was less than 2.0, with an average y^+ value less than 5.0 on other surfaces. 25 inflation layers were used. The method built on that of Burdett et al. [10] who also showed mesh independence of capacity solutions.

Boundary conditions of inlet total temperature and inlet turbulence intensity were matched to experimental values (Table 5.2). Inlet total pressure was set to a fixed value, and at exit, an area-averaged static pressure was set (no constraint on the local profile to satisfy radial equilibrium in the exit flow) to achieve design vane pressure ratio. The area-averaged exit static pressure was then varied to achieve different vane pressure ratios. When comparing experimental and CFD data, care was taken to evaluate the mean exit pressure in CFD using identical monitor points to the experiment (see analysis in Burdett et al. [12]). Walls were set to be adiabatic. A rotational periodic boundary was used in the circumferential direction.

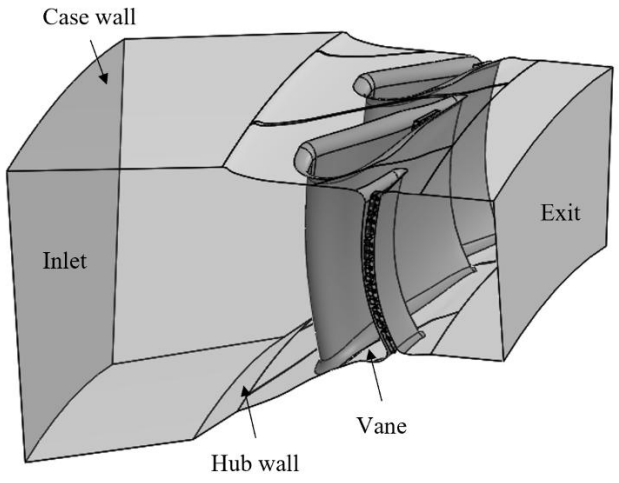


Figure 5.4: Computational domain for Geometry 1.

The film cooling system comprises of 11 film rows (6 on SS and 5 on PS), and a radially-partitioned TE slot. Mass flow rates for individual film cooling holes and TE slot channels were determined using an in-house low-order internal flow solver (loss-correlations-based).

Coolant inlet total pressure and total temperature are specified (matched to experimental values), with individual exit static pressures determined from an uncooled steady RANS CFD solution. The total mass flow rate calculated by this code was then scaled to match the experimentally measured mass flow rate (coolant-to-mainstream mass flow ratio is therefore also matched). This low order model was run for each geometry to set the relative distribution of mass flow rate between the different cases.

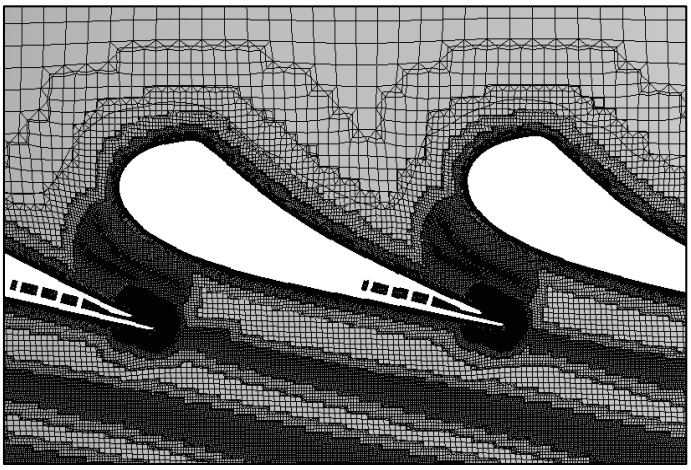


Figure 5.5: Midspan mesh detail (Geometry 1).

5.5 – Results and discussion

In this section we present the experimental and numerical results. We consider the following: the exit static pressure distributions; the flow capacity characteristics for each build; poor correlation of results with physical area change; the coolant capacity; the vane boundary layers characteristics; and the vane aerodynamic flow field.

5.5.1 – Vane exit circumferential static pressure distributions

Experimental and CFD-predicted normalised NGV exit static pressure distributions for each of the four builds are presented in Figure 5.6, the differences between hub and casing for each build from the CFD-predictions is also presented in Figure 5.7. Local static pressures are normalised by the mean inlet total pressure; the circumferential coordinate, θ, is normalised by the vane pitch angle, s. Solid lines show casing data and dotted lines hub data. Experimental trends are marked with circles at the experimental measurement points.

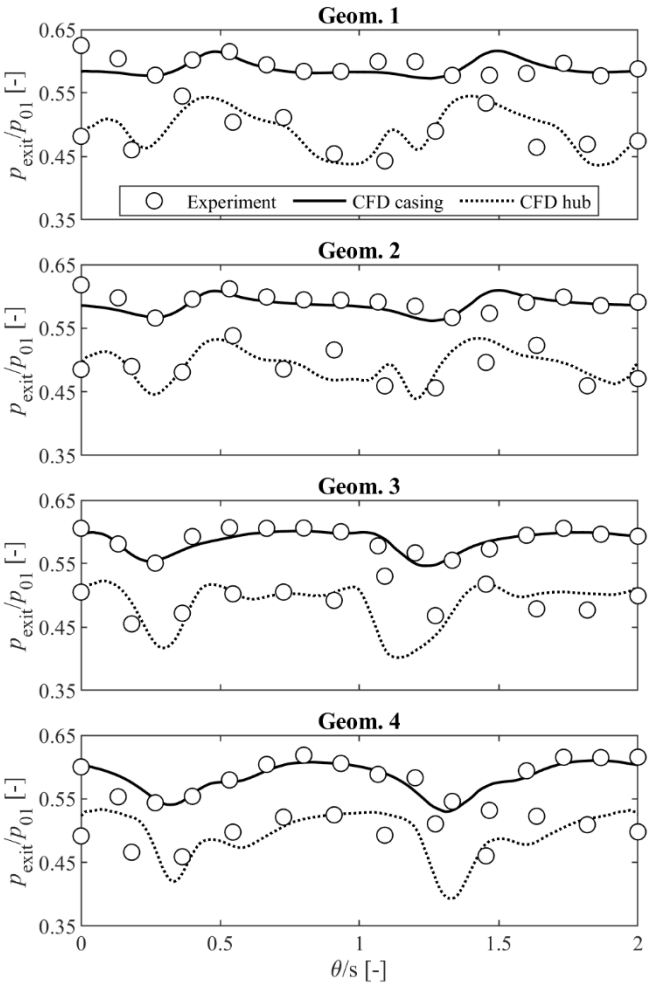


Figure 5.6: NGV exit circumferential static pressure distributions for Geometry 1–4. Solid lines show CFD casing data, dotted lines show CFD hub data, and circles show respective experimental data.

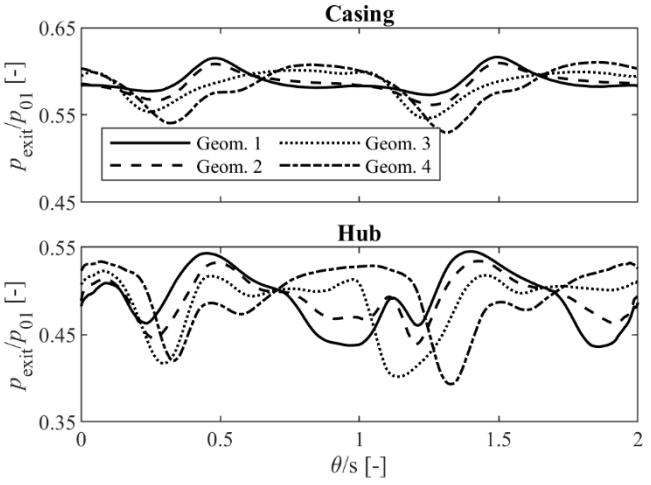


Figure 5.7: NGV exit circumferential static pressure distributions from CFD-predictions at hub and casing for Geometry 1–4.

Consider first the Geometry 1 data. The general trends are as expected: significant lower mean pressure ratio at hub than case (mean of 0.486 at hub; mean of 0.593 at case) in line with the radial pressure distribution; a gradual (approximately linear) decrease in pressure between PS and SS (direction of increasing θ), followed by a sudden rise across the wake. The minima ($\theta/s = 0.1, 1.1$ for hub; and $\theta/s = 0.3, 1.3$ for case) are axially downstream of the location of peak suction on the SS. We analyse this effect later when considering aerodynamic effects). Overall, CFD and experiment are in excellent agreement both in form and absolute values (difference between hub and case was 0.107 for experiment and 0.097 for CFD).

Consider now the progression between Geometry 1 and Geometry 4. We find with increasing burn-back that there is a significant decrease in case-to-hub pressure gradient: the difference in value of experimentally measured value of p_2/p_{01} between case and hub (i.e. $(p_{\text{exit}}/p_{01})_{\text{case}} - (p_{\text{exit}}/p_{01})_{\text{hub}}$) of 0.107 for Geometry 1 and 0.088 for Geometry 4. The trend is plotted in Figure 5.8, and is similar for experimental measurements and CFD predictions. This reduction in case-to-hub pressure gradient is consistent with a decrease in the mass-mean turning angle (β''): we see (Figure 5.8) that there are measured and predicted decreases in mass-mean whirl angle of 2.7 and 3.3 degrees respectively.

Consider now the change in circumferential pressure variation with increasing cut-back. At the casing there was a monotonic increase in variation seen in both experiment and CFD, likely explained by an increase in outlet Mach number. At the hub the experiment showed decreased circumferential variation and the CFD significantly increased variation. This apparent contradiction is possibly explained by increased peak SS Mach number with TE cutback, smoothed in the experiment by unsteady behaviour (unstable shock location caused by, for example, TE shedding and other feedback mechanisms) but artificially stable in the RANS solution. We consider the pressure field in greater detail in a later section.

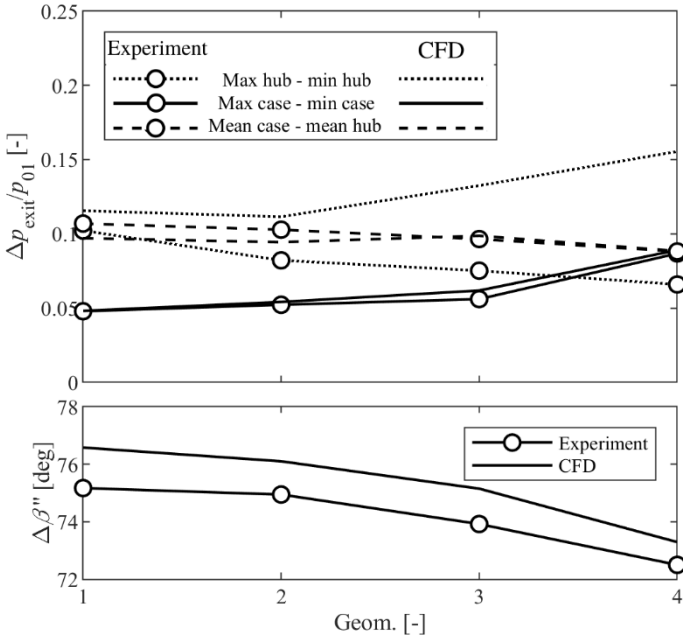


Figure 5.8: Changes in average pressures and mass-mean whirl angle in progression between Geometry 1 and Geometry 4.

5.5.2 – Overall vane flow capacity

The overall (mainstream and cooling) NGV flow capacity characteristics for Geometry 1–4 are shown in Figure 5.9 as a function of vane pressure ratio for Geometry 1–4. The experimental data is measured at all pressure ratios (full characteristics measured), and the CFD-predictions are performed at five nominal vane pressure ratios ($p_{\mathrm{exit}}/p_{01} = 0.48$, 0.54, 0.61, 0.66, and 0.72). All data are normalised with respect to a reference value, Γ_{ref}, equal to the experimental value for Geometry 1 at the design vane pressure ratio ($p_{\mathrm{exit}}/p_{01} \approx 0.54$; see Table 5.2). An isentropic capacity characteristic scaled to be equal to Γ_{ref} at the design pressure ratio is also presented.

Consider first the Geometry 1 results. The experimental trend is of very similar form to an isentropic capacity trend for subsonic flow ($p_{\mathrm{exit}}/p_{01} > 0.528$), but continues increasing beyond the nominally choked condition ($p_{\mathrm{exit}}/p_{01} = 0.528$). The CFD-predicted trend is of almost identical form to the experimental trend, but was lower by an average of 1.6% (mean across five points). We note that the CFD geometry was the design-intent and not a 3D-scanned actual part geometry; we take these values to match within expected manufacturing variation (a 0.1 mm offset in the controlling region is equal to approximately 1% of absolute capacity).

Difference of both the experimental data and CFD predictions from the isentropic trend should be expected for a variety of reasons: 2D (loading distribution) and 3D (hub-to-tip pressure variation) potential field effects mean that there should be no expectation that the sonic line (for transonic conditions) and more generally the pressure contours are aligned with the point of minimum geometric area (see, for example, Afanasiev et al. [2, 3], Hambidge and Povey [7], and Burdett et al. [10]); unsteady trailing edge vortex shedding effects; interaction of base region to cooling flow; etc.

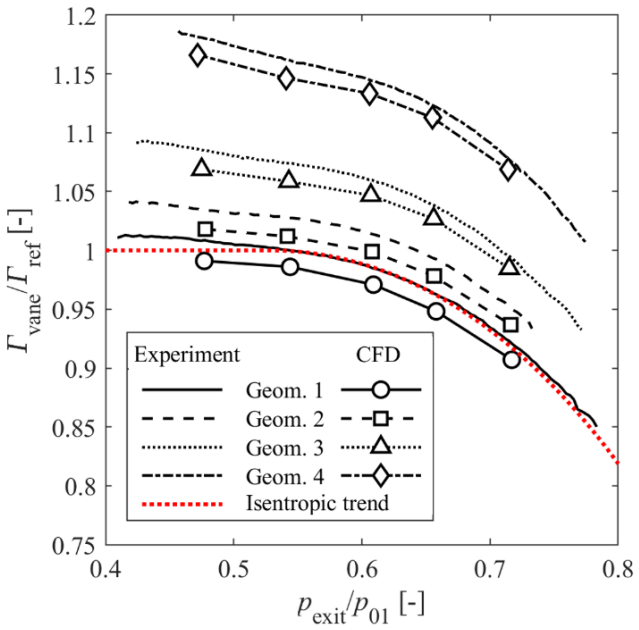


Figure 5.9: Vane capacity characteristics for Geometry 1–4 normalised by Γ_{ref} (reference vane capacity value at design vane pressure ratio).

Consider now the change between Geometry 1 and Geometry 4. With increasing TE burn-back, the capacity monotonically increases. The general form of the characteristics stay approximately the same but with slight steepening of the curve for higher Mach numbers. The discrepancy between CFD and experiment was approximately the same for all four builds: average differences (across five pressure ratios) for Geometry 1 to 4 were 1.6%, 1.5%, 1.3% and 1.0%. The change in capacity between Geometry 1 and all other builds is shown in Figure 5.10, for both experimental results and CFD predictions. Experimental data are compared to the Geometry 1 experimental data; CFD data are compared to the Geometry 1 CFD data. At

the design vane pressure ratio ($p_{\text{exit}}/p_{01} \approx 0.54$), the increases in flow capacity were 2.7% (Geometry 1–2), 7.4% (Geometry 1–3), and 16.1% (Geometry 1–4). The corresponding CFD-predicted increases in flow capacity were almost identical: 2.6%, 7.4%, and 16.3%, respectively. Thus, we consider the agreement between experiment and CFD data to be excellent. The values are summarised in Table 5.3. Away from the design pressure ratio there was a slightly greater difference between the CFD-predicted changes in capacity with burn-back and the experimental value, particularly for the most extreme burn-back case at very low Mach numbers.

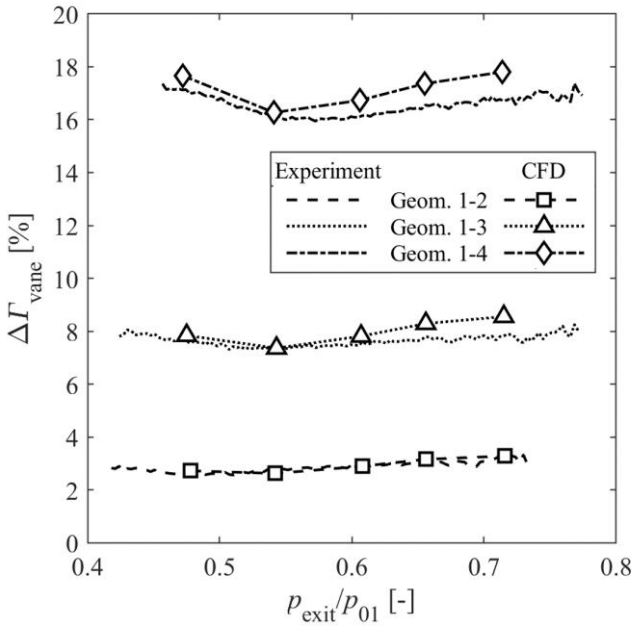


Figure 5.10: Difference in vane capacity characteristics for Geometry 1–2, Geometry 1–3, and Geometry 1–4 $\left(\boldsymbol{\Delta\Gamma_{\text{vane}} = \left(\frac{\Gamma_{\text{vane},i=2,3,4}}{\Gamma_{\text{vane},1}} - 1\right) \times 100}\right)$.

Table 5.3: Difference in flow capacity delta for Geometry 1–2, Geometry 1–3, and Geometry 1–4 at design vane pressure ratio ($p_{\text{exit}}/p_{01} \approx 0.542$).

Geom.	Experiment $\Delta\Gamma_{\text{vane}}$ [%]	CFD $\Delta\Gamma_{\text{vane}}$ [%]
1–2	+2.7	+2.6
1–3	+7.4	+7.4
1–4	+16.1	+16.3

5.5.3 – Correlation to geometrical parameters

We define the projected areas at the TE, A_{p}, as the spanwise integral of the projection in the direction of the mean metal angle of the local minimum width line adjoining PS TE to the SS of the adjacent vane. This is one possible definition of a *minimum effective geometric area*, and these are visualised in Figure 5.19 for each geometry. Calculating these values for all four builds, we see an increase in these projected areas of 0.9%, 3.7%, and 8.0% between 1–2, 1–3 and 1–4. We compare these values on a percentage basis to the capacity changes on a percentage basis. The correlation is poor with exchange rates between geometric area and capacity of 3.0, 2.0, and 2.0 for the three comparison points (summarised in Table 4). It is well established that an exchange rate of unity should not be expected (see Afanasiev et al. [2], Povey et al. [5], and Burdett et al. [10]).

Table 5.4: Comparison of change in minimum effective geometric area and change in capacity.

Geom.	Experiment $\Delta\Gamma_{\mathrm{vane}}$ [%]	Projected throat area ΔA_{p} [%]	Exchange rate $\Delta\Gamma_{\mathrm{vane}}(\%)/\Delta A_{\mathrm{p}}(\%)$
1–2	+2.7	+0.9	3.0
1–3	+7.4	+3.7	2.0
1–4	+16.1	+8.0	2.0

5.5.4 – Coolant capacity

Now we will consider the impact of TE burn-back on coolant mass flow rate and capacity. Experimentally measured normalised total coolant capacity characteristics, $\Gamma_{\mathrm{cool}}(p_{\mathrm{exit}}/p_{01})$, for Geometry 1–4 are shown in Figure 5.11. The data are normalised by the vane capacity of Geometry 1 at design vane pressure ratio, Γ_{ref} (i.e. $\Gamma_{\mathrm{cool}}(p_{\mathrm{exit}}/p_{01})/\,\Gamma_{\mathrm{ref}}$). We decompose the total coolant capacity into TE slot capacity (Γ_{TE}) and film capacity (Γ_{film}) using our internal flow solver: characteristics for these individual terms are also plotted in the figure.

Looking first at the Geometry 1 data, we see that the total cooling flow makes up approximately 6.4% of the overall vane flow (mainstream plus cooling) at the design vane pressure ratio. Of this, 5.2% is accounted for by film flow, and the remaining 1.2% by the TE

slot (model-based decomposition). The cooling capacity fraction ($\Gamma_{\text{cool}}(p_{\text{exit}}/p_{01})/\Gamma_{\text{vane}}(p_{\text{exit}}/p_{01})$) is weakly dependent on pressure ratio, varying by only 1.64% over the range $0.41 < p_{\text{exit}}/p_{01} < 0.78$. This is shown in Figure 5.12.

Consider now the variation in coolant capacity with burn-back. The percentage change in total coolant capacity with burn-back is shown in Figure 5.13, as a function of vane pressure ratio. At the design vane pressure ratio changes between Geometry 1–2, 1–3, and 1–4 were 2.4%, 6.9% and 15.0% respectively. The model-based decomposition shows that the corresponding changes in the film flow were 0.2%, 2.4% and 9.1%, and that the corresponding changes in TE slot flow were 13.6%, 25.9% and 40.3%. The increase in film flow is almost entirely due to an increase in flow through the last three SS film rows and the last PS film row, for which there is a reduction in external static pressure with increasing burn-back (we discuss this effect later). The increase in TE slot flow is due both to increased cross-sectional area with burn-back, and decreased channel pressure loss (shorter channel). That the percentage changes in total cooling flow between builds are very similar to the percentage changes in overall vane flow (see Table 5.3) we regard as co-incidental.

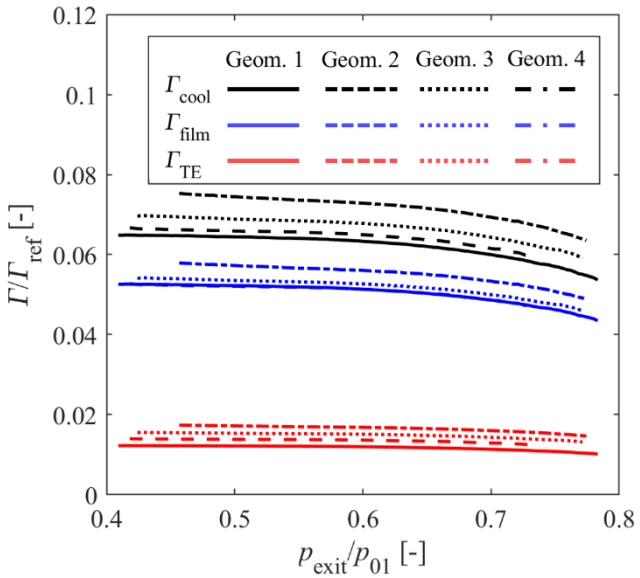


Figure 5.11: Experimentally-measured coolant capacity characteristics for Geometry 1–4 normalised by Γ_{ref} (reference vane capacity value at design vane pressure ratio).

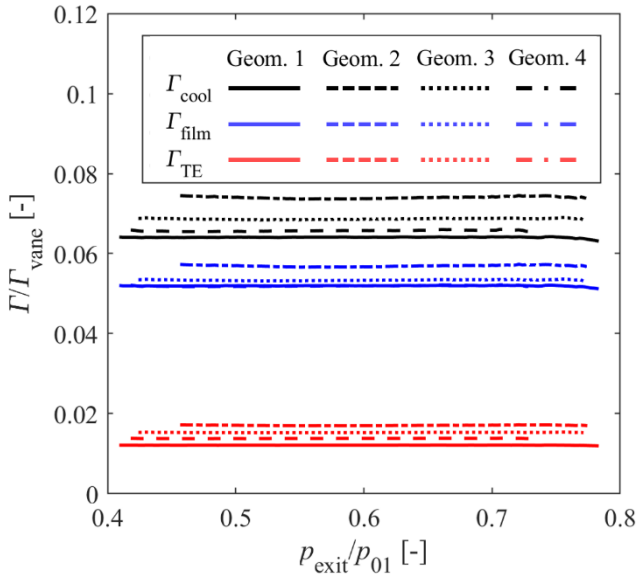


Figure 5.12: Experimentally-measured coolant capacity characteristics for Geometry 1–4 normalised by $\Gamma_{vane}(p_{exit}/p_{01})$, the vane capacity characteristic, of Geometry 1.

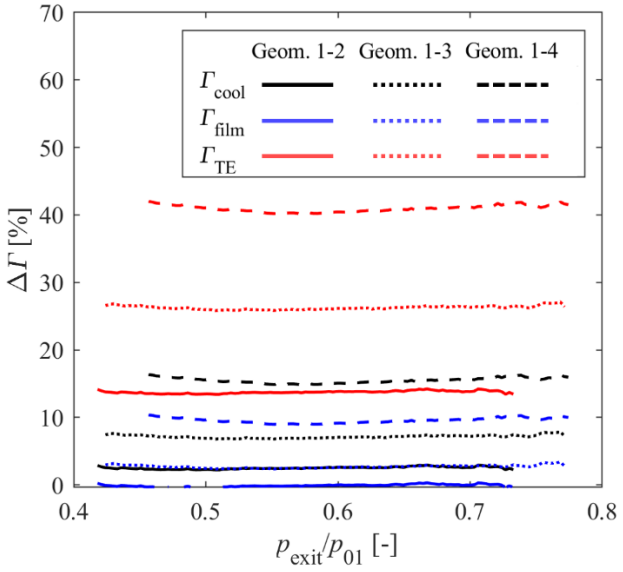


Figure 5.13: Difference in coolant capacity characteristics for Geometry 1–2, Geometry 1–3, and Geometry 1–4 $\left(\Delta\Gamma = \left(\frac{\Gamma_{i=2,3,4}}{\Gamma_1} - 1\right) \times 100\right)$.

5.5.5 – Impact of coolant capacity on vane capacity

There are two primary mechanisms by which a change in coolant capacity can affect the overall vane capacity. The first is that a change in the film cooling flow rate can change the near wall total pressure and temperature profiles. The second is that TE slot flow, introduced downstream of the *controlling region* (see [12, 10] for detailed discussion of this concept), can

directly increase the vane capacity by directly augmenting it, or—potentially—decrease the vane capacity by changing the structure of the TE flow (complex TE dynamics). We consider each of the effects in turn.

Consider first the impact of film cooling flow on vane capacity. In the cold-rig situation an increase in film cooing flow generally leads to a slight decrease in vane capacity due to increased total pressure loss in near-wall layer in an almost uniform total temperature field (no density effects). At engine temperature ratios (mainstream-to-coolant temperature ratio equal to approximately 2.0) the effect on vane capacity of increased film cooling flow is more complex because there are competing effects due to near-wall total pressure loss and near-wall density variation. Here the precise definition of capacity becomes important; specifically, the way total temperature and pressures are *averaged* in the capacity definition. There are, for example, three possible approaches for incorporating total temperature in the capacity definition: using the square root of the mainstream temperature; using the square root of the mass-flow-weighted temperature; and using the mass-flow-weighted sum of individual $\sqrt{T_0}$ terms. This is discussed in detail in Burdett et al. [12]. Equation 5.2 is the last of these three approaches: the advantages of this formulation have been discussed. Taking our particular experiment at the design point vane pressure ratio, the inferred (from model) *film-coolant-to-total* capacity ratios were approximately 5.20%, 5.19%, 5.32% and 5.67% for Geometry 1 to 4 respectively. That is, the largest change in film capacity ratio was 0.47% of Γ_{vane}. It has been shown in an analytical method developed by Povey [6], and later demonstrated in a CFD study of Hambidge and Povey [7], that for typical film cooling systems, a 1% increase in $\Gamma_{\mathrm{film}}/\Gamma_{\mathrm{vane}}$ leads to approximately a 0.027% reduction in Γ_{vane}. The decrease is on account of total pressure loss within the mixing layer. We therefore estimate that the variation in Γ_{vane} between builds arising from changes in film cooling mass flow rate alone should be of order 0.0127%, more than two orders of magnitude smaller than the observed changes in Γ_{vane} between builds. We conclude that the change in film cooling capacity is not a significant driver for overall capacity change in this study.

Now consider the (inferred) TE flow capacity. As a percentage of the vane capacity the TE cooling capacity (i.e. $\Gamma_{\mathrm{TE}}/\Gamma_{\mathrm{vane}}$) accounts for 1.21%, 1.38%, 1.53% and 1.70% for Geometry 1 to 4 respectively (see Figure 5.12). Burdett et al. [10] refer to models with *common* and *independent* controlling areas: these are shown schematically in Figure 5.14. Here w_{PS} is the minimum distance between the PS TE tip and the adjacent vane SS, w_{SS} is the minimum distance between the SS TE tip and the adjacent vane SS, and w_{TE} is the TE slot thickness. In the current experiments, in the burn-back region we move from the geometric configuration being better described by model (a) for Geometry 1, to being better described by model (b) for Geometry 2 to 4. Regardless of the model type, the maximum change in TE cooling capacity fraction of $\Gamma_{\mathrm{TE}}/\Gamma_{\mathrm{vane}}$ was 0.49% (between Geometry 1 and Geometry 4), over an order of magnitude smaller than the change in Γ_{vane} between Geometry 1 and Geometry 4. We conclude that the change in TE slot flow capacity is also not a significant driver for overall capacity change in this study.

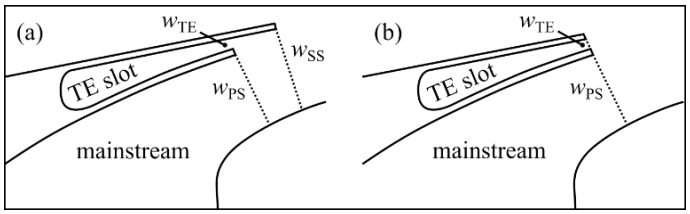


Figure 5.14: Schematic diagrams representing model (a), a model with common controlling area, and model (b), a model with independent controlling areas (adapted from Burdett et al. [10]).

5.5.6 – Vane boundary layer characteristics

Consider now the impact of TE burn-back on the vane boundary layer in the controlling region, and therefore the vane capacity. CFD-predicted BL profiles on the PS and SS of the vane at the point of minimum (spanwise) local passage width is used to calculate (by integration) the BL displacement thickness, δ^*. Outside the burn-back region the minimum width is the end of the PS overhang (see Figure 5.1), and inside the burn-back region the minimum width is the damage front (see Figure 5.1). For the integration, the method of Burdett et al. [10] was used, with an integration height $\delta^*/w_{\mathrm{PS}} = 0.05$, where w_{PS} is the local minimum distance between the PS TE tip and the adjacent vane SS for the Geometry 1 vane

(see Figure 5.14). Spanwise profiles of $\delta^*/w_{\mathrm{ref}}$ are shown in Figure 5.15 for Geometry 1 to 4, where w_{ref} is a reference value equal to the midspan w_{PS} value for the Geometry 1 vane. The spanwise average BL displacement thicknesses, normalised mass flow rate deficits, and change in normalised mass flow rate deficit between builds, are shown in Table 5.5. So far as Geometry 1 is concerned, the PS and SS boundary layers have span-averaged normalised thicknesses $\delta^*/w_{\mathrm{PS}} = 0.0024$ and 0.0033 respectively. We define a normalised mass flow deficit parameter by

$$\frac{\dot{m}_{\mathrm{deficit}}}{\dot{m}_{\mathrm{TOT}}} = \int_{r_1}^{r_2} \rho(r) U(r) \delta^*(r)\, dr \tag{5.3}$$

where $\rho(r)$ and $U(r)$ are the density and velocity values at the edge of the BL as functions of span height, $\delta^*(r)$ is the displacement thickness as a function of span height, and $\dot{m}_{\mathrm{TOT}}$ is the total mass flow rate. The normalised mass flow rate deficit for Geometry 1 was 0.46% (similar to the value of 0.40% determined by Burdett et al. [10]).

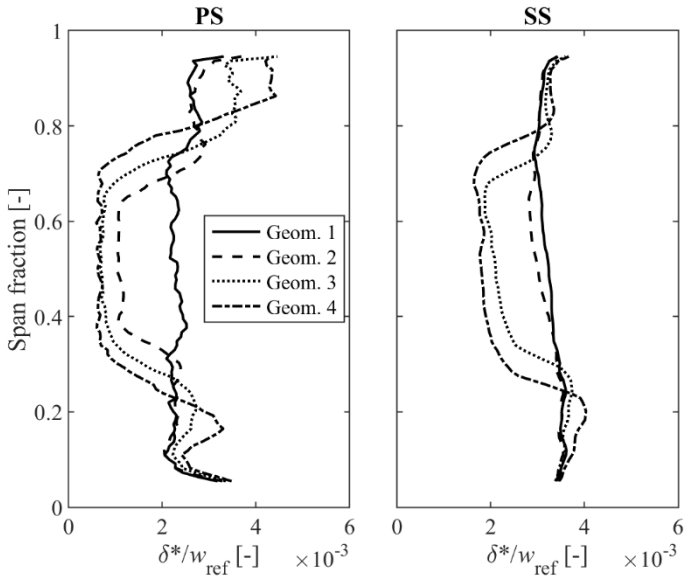


Figure 5.15: CFD-predicted spanwise variation in BL displacement thickness normalised by the midspan geometric minimum distance for baseline, $\delta^*/w_{\mathrm{ref}}$, for Geometry 1–4.

Table 5.5: Estimated spanwise average boundary layer displacement thickness, overall mass flowrate deficit, and change in mass flow deficit relative to Geometry 1.

Geom.	$\delta^*/w_{\text{ref}} \times 10^{-3}$ PS	SS	$\Delta\dot{m}/\dot{m}_{\text{TOT}}(\%)$ PS+SS	$\Delta\dot{m}/\dot{m}_{\text{TOT}}(\%)$ (w.r.t. Geom. 1)
1	2.37	3.26	0.463	—
2	1.99	3.17	0.418	−0.045
3	1.92	2.84	0.370	−0.093
4	1.82	2.62	0.322	−0.141

Consider now the change with burn-back. As we move from Geometry 1 to Geometry 4 there is a reduction in BL thickness on both SS and PS within the burn-back region, which we primarily attribute to change in wetted surface length (evaluation station moves upstream with the TE). The values of normalised mass flow rate deficit for Geometry 2 to 4 were 0.42%, 0.37%, and 0.32% respectively. The change in the mass flow rate deficit due to the surface BLs is at most −0.14% (difference between Geometry 1 and 4); more than two orders of magnitude smaller than the change in vane capacity. We conclude that BL effects have a negligible effect on capacity change.

5.5.7 – Aerodynamic flow field

Now we consider the effect of TE burn-back on the aerodynamic flow field at the design vane pressure ratio (p_{exit}/p_{01}~0.54). The CFD-predicted distributions of the local kinetic energy loss coefficient, $\zeta'(r,\theta)$, at a plane located a quarter axial chord length downstream of the vane TE are shown in Figure 5.16 for Geometry 1–4. The orientation is viewed from downstream. The $\zeta'(r,\theta)$ distribution is normalised by the plane-mass averaged loss coefficient for Geometry 1, ζ'''_{ref}. The local kinetic energy loss coefficient is defined by

$$\zeta'(r,\theta) = 1 - \frac{1 - \left(\frac{p_2(r,\theta)}{p_{02}(r,\theta)}\right)^{(\gamma-1)/\gamma}}{1 - \left(\frac{p_2(r,\theta)}{p_{01}}\right)^{(\gamma-1)/\gamma}} \tag{5.4}$$

where $p_2(r,\theta)$ and $p_{02}(r,\theta)$ are the local static and total pressures in the plane of interest, p_{01} is the inlet total pressure (assumed uniform), and γ is the ratio of specific heats (γ = 1.4 for air). See related precursor study by Raduev et al. [1] for a detailed analysis of the impact

of TE burn-back on NGV aerodynamic performance. We now briefly review the main observations.

For Geometry 1 there is a smooth curved wake due to vane compound lean. The loss along the line of the wake is greater at the endwall locations than at the midspan region. This is due to endwall BL fluid migration towards the vane-endwall SS corner. The mid-span region is slightly more mixed out because there is greater flow-wise distance between the TE and the traverse plane (consequence of the particular type of compound lean leading to the mid-span being axially upstream of the endwalls). At approximately 10% and 85% span there are regions of high loss associated with passage vortices (see also [1]). Slight peaks in loss along the line of the wake are associated with chordwise ribs within the TE slot.

Now we consider the impact of TE burn-back on the local loss coefficient distributions. With increasing TE burn-back, we see the following effects:

1. Formation and strengthening of two new loss cores associated with counterrotating vortices at the edges of the burn-back region (see also [1]). These from due to strong whirl and velocity gradients at the burn-back edges (lower whirl and velocity within the burn-back region, and higher whirl and velocity outside the burn-back region).

2. Significant counter-clockwise (CCW) lag of the wake in the burn-back region. This is associated with flow under-turning due to TE material removal.

3. Significant clockwise (CW) migration associated with *overturning* outside the burn-back region due to flow interaction with the counterrotating burn-back edge vortices.

4. Strengthening of the hub and case loss cores, and both circumferential (CCW) and radial migration (away from endwalls) of the loss cores.

5. Relative to Geometry 1, the plane-averaged loss coefficient increases were 6.5%, 20.3%, and 61.9% for Geometry 2–4.

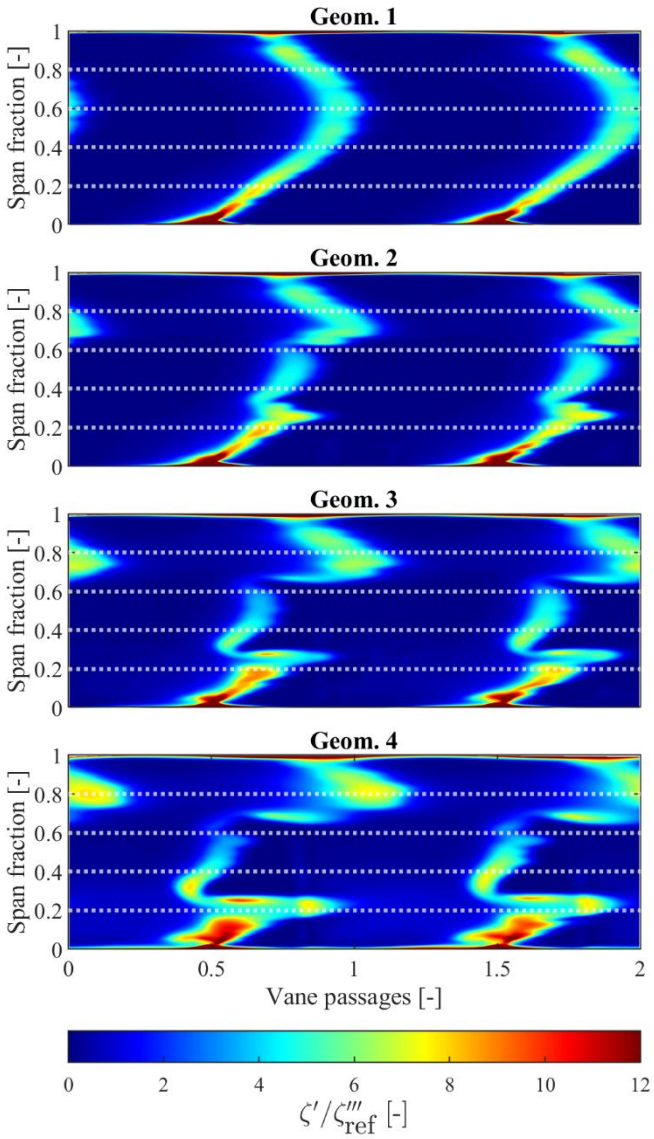


Figure 5.16: CFD-predicted distributions of normalised local KE loss coefficient, $\zeta'/\zeta'''_{\mathrm{ref}}$, for Geometry 1–4. Data is viewed from downstream; and the principal exit flow direction is clockwise.

Now consider the CFD-predicted NGV surface isentropic Mach number, M_S, distributions. These are shown in Figure 5.17 for Geometry 1–4 at 15%, 50%, and 85% span fraction. Axial distance (x) is normalised by the axial chord of Geometry 1 (C_{ref}). The LE is at $x/C_{\mathrm{ref}} = 0$. Note in the CFD method the inlet total pressure was fixed for all cases, but the exit static pressure was varied to achieve approximately the same row pressure ratio (p_{exit}/p_{01}~0.54) for each case.

Consider first Geometry 1. The loading distribution is typical of a moderately forward-loaded vane. On the SS, the flow reaches peak suction between 60–80% axial chord, with peak Mach numbers at 15%, 50%, and 85% span of approximately 1.15, 1.12, and 1.08, respectively. Beyond the locations of peak suction, the flow diffuses to meet the PS flow. On the PS, we see well-controlled acceleration at all span locations from the LE to the TE.

Now considering the impact of TE burn-back on the vane loading, we see the following with increasing burn-back:

1. Significant mid-chord region (30–70% axial chord) isentropic Mach number increase at all span locations. This is accompanied by increased forward loading. At 50% span, the peak Mach number increased from 1.12 (Geometry 1) to 1.13, 1.15, and 1.32 for Geometry 2–4 respectively. At 50% span the location of peak Mach number moves forward from approximately 60% axial chord for Geometry 1 to approximately 50% axial chord for Geometry 4.

2. Isentropic Mach number decrease on the late SS (greater than 80% axial chord) at all span locations. At 15% and 50% span, the decrease is more significant than at 85% span. This, in combination with the first effect, leads to greater adverse pressure gradient on the late SS, leading to thickening of the SS BL. This is discussed and quantified in [1] in the context of NGV aerodynamic performance.

3. Mild late PS (after ~60% axial chord) isentropic Mach number increase at all span locations, with acceleration remaining well-controlled across the surface.

4. The physical locations of the PS TE and SS TE move as the TE is physically burnt-back.

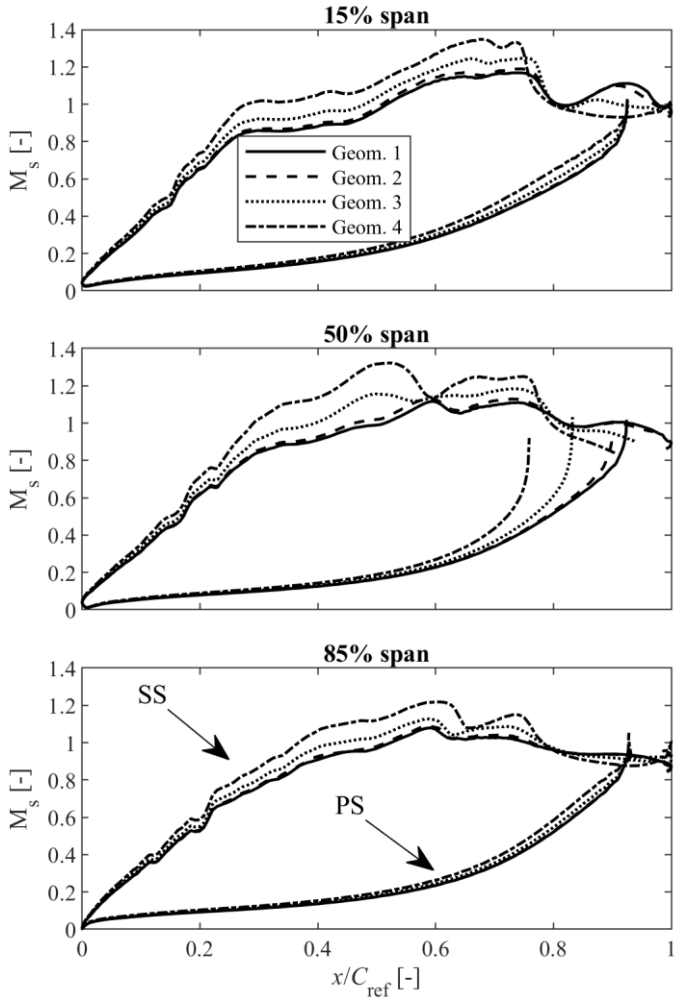


Figure 5.17: CFD-predicted NGV surface isentropic Mach number distributions for Geometry 1–4 at 15%, 50%, and 85% span.

To examine the flow field in more detail, we consider CFD-predicted contours of Mach number at 50% span for Geometry 1–4 at design vane pressure ratio. These are shown in Figure 5.18. The $\mathrm{M} = 1$ contour is shown as a bold line. To visualise the change in Mach distribution, for Geometry 2–4 we overlay the $\mathrm{M} = 1$ for Geometry 1 as a dotted line.

For Geometry 1 we see that peak lift is in the uncovered turning region downstream of the point of minimum area. This can also be seen in midspan surface isentropic Mach number distributions shown of Figure 5.17, where there is a broad peak (maximum value $\mathrm{M_s}$ = 1.12) in the range $0.60 < x/C_{\mathrm{ref}} < 0.80$. As the TE is cut back, we see (Figure 5.18) that the suction peak broadens, intensifies, and moves forward. Comparing the M = 1 contour for Geometry 1

(dashed line) with the equivalent contours for Geometry 2–4 (solid lines) these effects are clearly visible.

In the progression between Geometry 1 and Geometry 4, another striking feature of the change in the flow is the rotation of the wake downstream of the vane: the wake angles in the downstream flow are approximately 80.0, 77.5, 74.5 and 69.0 degrees for Geometry 1 to 4 respectively.

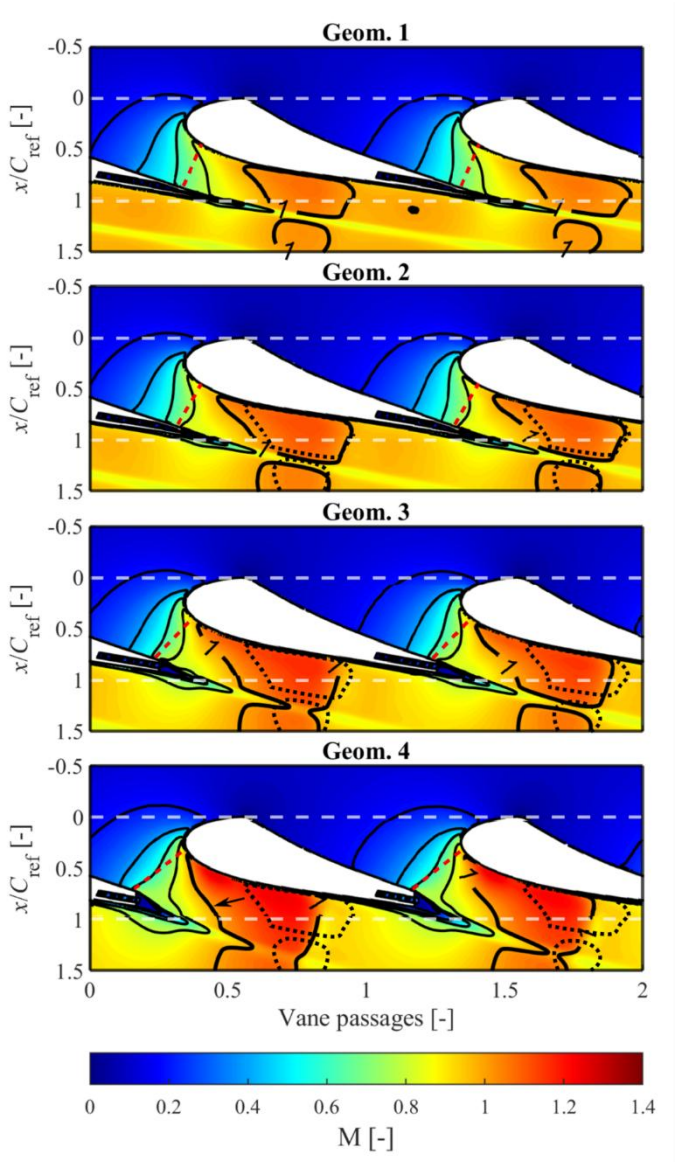


Figure 5.18: CFD-predicted midspan Mach number contours for Geometry 1–4. Minimum area shown by red dash line. M = 1 contour shown by bold black line.

We now consider the flow field on the surface passing through lines of minimum separation (i.e., the geometric throat) between SS and PS. This is an approximately planar surface for Geometry 1, but a stepped surface (following the TE cutback shape) for Geometry 2–4. We refer to these surfaces—loosely—as the *minimum area surfaces.* These surfaces are shown schematically in Figure 5.19. Flow angle parameters are now defined: whirl angle, β, is defined as the angle between the circumferential component of the local velocity vector, v, and the axial direction, $\hat{n}_x$; metal angle, φ_{PS} or φ_{SS}, is defined as the angle between the vane PS or SS tangents at the TE before the TE radius, and the axial direction; and lastly, flow deviation angle, δ, is defined as the difference between the whirl angle and the mean metal angle at the same radius (i.e. $\delta = \beta - \varphi_{\mathrm{MEAN}}$). The radial distribution of mean metal angle (average of φ_{PS} and φ_{SS}) is determined for each burn-back geometry. These are all shown in Figure 5.19.

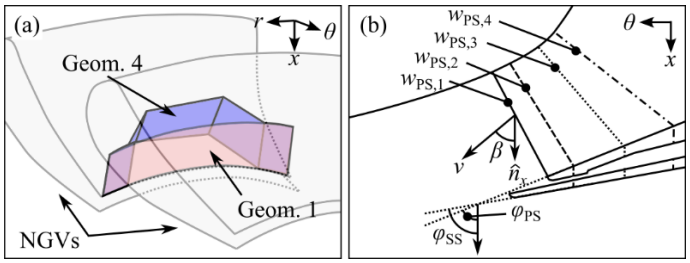


Figure 5.19: Schematic of (a) surfaces connecting lines of minimum distance between SS and PS; and (b) angle definitions.

CFD-predicted contours of local Mach number, normalised total pressure, whirl angle, and deviation angle on the surfaces of minimum area for Geometry 1–4 are shown in Figure 5.20. Considering first the Mach number distribution contours (top row) for Geometry 1–4, we find the following:

1. The Mach number distribution for Geometry 1 has stronger cross-passage variation than radial variation.

2. In the burn-back region (for Geometry 2–4) the Mach number is locally reduced. The effect intensifies as the degree of burn-back progresses. The minimum Mach number is 0.78, 0.77, 0.71, and 0.62 for Geometry 1–4, respectively.

3. Outside the burn-back region (for Geometry 2–4) the Mach number is locally increased. The effect is greatest near the SS, and the magnitude of the effect intensifies with increasing burn-back. The peak Mach numbers are 0.93, 1.01, 1.10, and 1.20 for Geometry 1–4, respectively.

Now consider the normalised total pressure distributions for Geometry 1–4, which are shown in the second row of Figure 5.20. We see the following:

1. For Geometry, the total pressure distribution is very uniform across most the passage, with gradients only in the near-wall boundary layer regions (also effect of film-cooling mixing). The SS boundary layer is more pronounced than the PS, as expected.

2. With increasing burn-back we observe relatively little change in the total pressure distributions. Small differences between the Geometry 2–4 distributions and that for Geometry 1 would not be significant in explaining changes in flow capacity.

3. The low total pressure loss in the passage means that the static pressure field (and not the total pressure field) is the main driver for the significant changes in the Mach number distribution.

Next consider the whirl angle distributions for Geometry 1–4, which are shown in the third row of Figure 5.20. We find the following:

1. For Geometry 1 the whirl angle distribution is relatively uniform, with a 3.1-degree decrease moving from the PS to the SS. We recall we are considering the flow on a minimum-area plane, not at the TE, so whilst the PS turning is complete, the SS turning is incomplete at this location.

2. With increasing burn-back, inside the burn-back region there is a rapid fall in whirl angle, particularly near the SS of the vane, leading to lower overall whirl angle, and greater cross passage variation. At 50% span the cross-passage-mean whirl angles are 64.8, 61.0, 53.7 and 45.6 for Geometry 1–4, respectively. The corresponding decreases

in the whirl angle from PS to SS were 3.8, 4.0, 10.1, and 20.4 degrees for Geometry 1–4, respectively. This effect is explained by the lines of minimum distance between PS and SS moving upstream (see w_{PS} lines for Geometry 1–4 in Figure 5.19(b) as the burn-back increases.

3. With increasing burn-back, outside the burn-back region, the cross-passage whirl angle variation remains relatively small. Moving from the PS to the SS, at 90% span the approximate decreases in whirl angle were 3.4, 3.5, 3.9, and 4.1 degrees for Geometry 1–4 respectively.

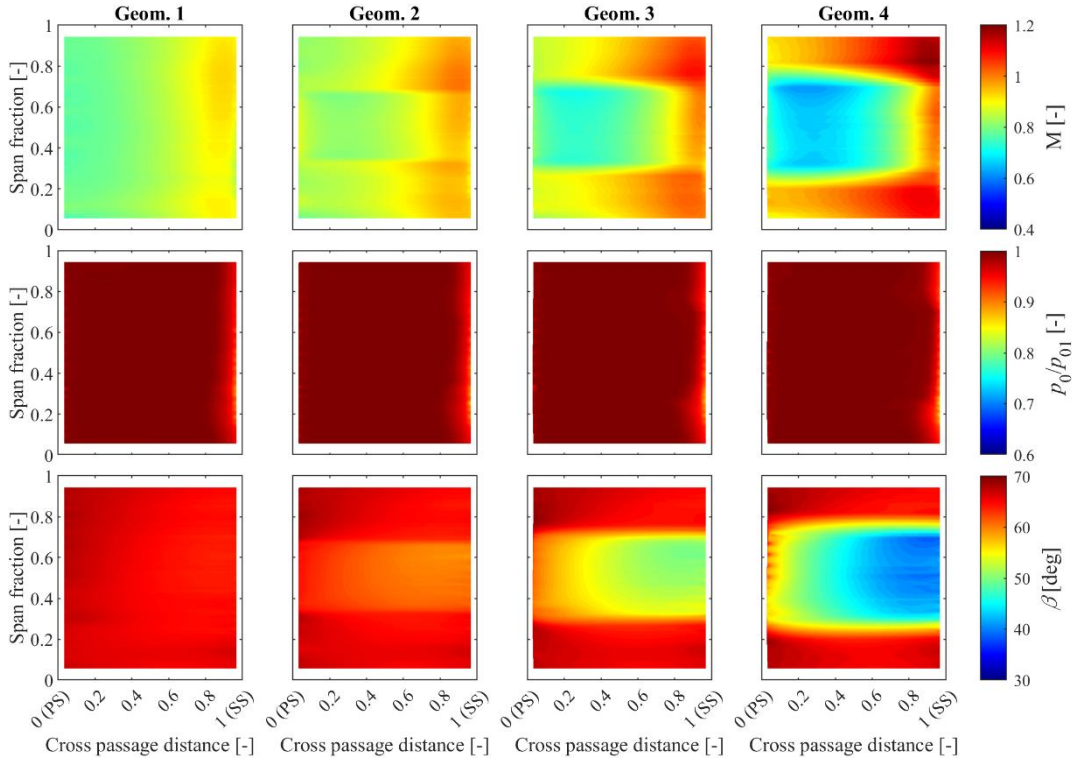


Figure 5.20: CFD-predicted flow-field on the surface of geometric minimum area for Geometry 1–4: (top row) Mach number; (second row) normalised total pressure; and (third row) flow angle.

Lastly, we consider the radial distributions of the circumferentially-averaged flow deviation angles, δ, for Geometry 1–4. Note again that the simpler mass-flux averaging was used to obtain the radial profiles, instead of the more physically grounded momentum-flux averaging. These are shown in Figure 5.21. Positive deviation angle represents overturning

with respect to the mean metal angle, and negative deviation angle underturning. We find the following:

1. For Geometry 1, the deviation angle is approximately constant (spanwise mean of −7.9 degrees).

2. With increasing burn-back, inside the burn-back region the negative deviation increases in magnitude. At 50% span, the deviation angles are −9.0, −11.9, −18.6, and −25.9 degrees for Geometry 1–4, respectively. The changes (from Geometry 1) in the mean metal angles with burn-back are −0.9, −1.4, and −2.0 degrees for Geometry 2–4, respectively. Higher deviation angle changes than metal angle changes likely arise because of the swallowing effect in the burn-back region, where there is an open window between parts leading to a potential field that is insufficiently complete to turn the flow uniformly.

3. With increasing burn-back, outside the burn-back region the flow deviation angles were unchanged.

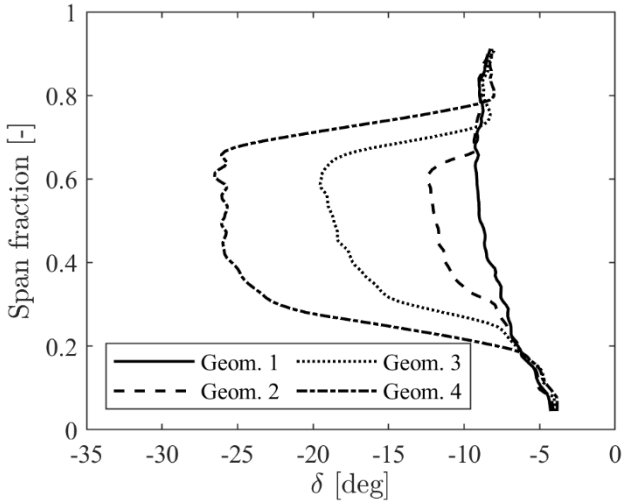


Figure 5.21: CFD-predicted spanwise variation in flow deviation angle, *δ*, for Geometry 1–4.

In general, it may be tempting to reconcile the flow capacity changes with integrals over some area of a local capacity function (method of Burdett et al. [10]). However, because there is no single rational area over which such an integral could be performed (changing geometry

between each burn-back case), one would need a model that departs too much from a 2D integral approach for it to provide much useful insight.

5.6 – Conclusions

In this paper, we perform a parametric study to investigate the impact of TE burn-back on the overall flow capacity of a high-pressure NGV. We present ultra-low uncertainty capacity measurements from an annular cascade operated at engine-matched conditions. The engine parts used were typical of modern civil jet engines, and the burn-back shapes were determined from statistical analysis of engine deterioration data. Experimental data are complemented with high-fidelity CFD simulations to provide insight into underlying physical mechanisms responsible for capacity changes.

We find the following:

1. *Damage shape*. Statistical analysis of engine deterioration data showed that mean burn-back region was trapezoidal in form, and centred on midspan. This characteristic shape was used for the current study. Four geometries were studied, with normalised (by tangential chord) burn-back depths of d/C_{t} = 0%, 10.8%, 19.2% and 27.5%. We refer to these as Geometry 1 to 4.

2. *Overall vane capacity characteristics*. With increasing TE burn-back, the overall vane capacity monotonically increased. The form of the characteristic (with vane pressure-ratio) remained approximately the same. At the design vane pressure ratio ($p_{\mathrm{exit}}/p_{01} \approx 0.542$), the measured changes in NGV flow capacity relative to Geometry 1 were +2.7%, +7.4%, and +16.1% for Geometry 2–4. Corresponding CFD-predicted changes were +2.6%, +7.4%, and +16.3%, respectively: very close agreement with the experimental data. Flow capacity changes would lead to intra-stage pressure changes, causing changes in stage reaction and efficiency.

3. *Impact on coolant capacity*. With increasing TE burn-back, the total coolant capacity monotonically increased. At the design vane pressure ratio, the measured changes in

total coolant capacity relative to Geometry 1 were +2.4%, +6.9%, and +15.0% for Geometry 2–4, respectively. These changes are similar in magnitude to the changes in overall vane capacity, but this fact appears co-incidental. Model-based decomposition of the total coolant capacity showed corresponding changes in film coolant capacity of +0.2%, +2.4%, and +19.1%, respectively, and corresponding changes in TE slot coolant capacity of +13.6%, +25.9%, and +40.3%, respectively. The increase in film coolant capacity is due to reduction in external static pressure with increasing burn-back. The increase in TE slot coolant capacity is due to both increased slot cross-sectional exit area and lower channel total pressure loss with increasing burn-back.

4. *Impact of cooling capacity changes on overall vane capacity.* The maximum changes in overall vane capacity associated with changes in film coolant capacity and TE slot coolant capacity were estimated to be approximately 0.013% and 0.490% respectively. These values are two orders of magnitude smaller than the measured changes in overall vane capacity, suggesting that neither film coolant capacity, nor TE slot coolant capacity are significant drivers for overall vane capacity changes.

5. *Impact of boundary layer on overall vane capacity.* With increasing TE burn-back, the CFD-predicted boundary layer mass flow rate deficits in the controlling region of the vane decreased. That is, there was a reduction in boundary layer thickness. This was primarily attributed to a reduction in wetted surface length. Changes in mass flow deficit relative to Geometry 1 were −0.045%, −0.093%, and −0.141% for Geometry 2–4. These values are two orders of magnitude smaller than the measured changes in overall vane capacity, suggesting that changes in boundary layer are not significant in explaining the overall vane capacity changes.

6. *Vortex formation and changes in loss distribution.* With burn-back, a pair of counterrotating vortices form at the edges of the burn-back region, leading to increased losses and significant loss redistribution and wake disturbance. These vortices strengthen with increasing burn-back.

7. *Changes in surface Mach number.* With increasing TE burn-back the peak Mach numbers increase, with the suction peak region broadening, intensifying, and moving forward on the vane. At 50% span the peak Mach number increases from 1.12 for Geometry 1, to 1.32 for Geometry 4. For fixed vane pressure ratio, this leads to greater adverse pressure gradient on the late SS, leading to thickening of the late SS BL.

8. *Changes in Mach number distribution on the minimum area surfaces.* With increasing burn-back, at the location of the minimum area surfaces, the Mach number decreased within the burn-back region, and increased outside it. On the minimum area surfaces *inside* the burn-back region, the minimum Mach number decreased from 0.78 to 0.62 when moving from Geometry 1 to Geometry 4. On the minimum area surfaces *outside* the burn-back region, the peak Mach number increased from 0.93 to 1.20 moving from Geometry 1 to Geometry 4. Total pressure changes were very small, demonstrating that it was the change in static pressure field which was responsible for changes in Mach number.

9. *Changes in passage whirl angle distribution.* With increasing burn-back, on the minimum area surfaces, the whirl angle rapidly decreased within the burn-back region, particularly near the SS, while regions outside the burn-back region saw relatively little change. At 50% span, the circumferentially-averaged whirl angle decreased from 64.8 for Geometry 1 to 45.6 for Geometry 4.

This is the first paper to study the impact of TE burn-back on NGV flow capacity. A related paper by Raduev et al. [1] considers the impact of TE burn-back on NGV aerodynamic performance. Taken together, we believe these studies open the way for improved whole-life engine performance modelling and assessment.

Nomenclature

Romans

A_{BB}	burn-back area [mm^2]
A_{ref}	reference area [mm^2]

A_p	projected throat area [mm^2]
C_t	tangential chord length [mm]
C_x	axial chord length [mm]
d	tangential depth of burn-back [mm]
k	turbulent kinetic energy [m^2 s^{-2}]
$\dot{m}$	mass flow rate [kg s^{-1}]
$\dot{m}_\mathrm{deficit}$	mass flow deficit due to BL [kg s^{-1}]
$\dot{m}_\mathrm{TOT}$	total mass flow rate [kg s^{-1}]
M	Mach number [-]
$\mathrm{M_S}$	isentropic Mach number [-]
$\hat{n}$	unit vector [-]
p	pressure (total or static) [Pa]
p_exit	mean vane exit static pressure [Pa]
Re	Reynolds number based on tangential chord [-]
r	radial position [mm]
S	span height [mm]
s	vane pitch angle [deg]
T	temperature [K]
Tu	turbulence intensity [%]
U	freestream velocity [m s^{-1}]
w_1	width of burn-back at TE [mm]
w_2	width of burn-back at damage front [mm]
w_PS	minimum distance between the PS TE tip and the adjacent vane SS [mm]
w_SS	minimum distance between the SS TE tip and the adjacent vane SS [mm]
w_TE	TE slot thickness [mm]
x	axial distance [mm]
y^+	non-dimensional wall distance [-]

Greeks

β	local flow whirl angle [deg]
β'	circumferentially-averaged whirl angle [deg]
β''	mass-mean whirl angle [deg]
Γ	flow capacity [kg s^{-1} K$^{1/2}$ Pa^{-1}]
Γ_vane	vane flow capacity [kg s^{-1} K$^{1/2}$ Pa^{-1}]
Γ_cool	total coolant capacity [kg s^{-1} K$^{1/2}$ Pa^{-1}]
Γ_film	film coolant capacity [kg s^{-1} K$^{1/2}$ Pa^{-1}]
Γ_TE	TE slot coolant capacity [kg s^{-1} K$^{1/2}$ Pa^{-1}]
δ	local flow deviation angle [deg]
δ^*	boundary layer displacement thickness [mm]
θ	circumferential coordinate [deg]
ζ'	local KE loss coefficient [–]
ζ'''	plane-averaged KE loss coefficient [–]
ρ	local density [kg m^{-3}]
φ_MEAN	vane mean metal angle [deg]
φ_PS	vane PS metal angle [deg]
φ_SS	vane SS metal angle [deg]
ω	specific turbulence dissipation rate [s^{-1}]

Subscripts

0	stagnation condition
1	mainstream vane inlet / Geometry 1
2	hub coolant stream inlet / Geometry 2
3	case coolant stream inlet / Geometry 3
4	Geometry 4
ref	reference value
s	isentropic condition

Superscripts

*	choked condition ($p_2/p_{01} = 0.5283$)

References

[1] Raduev, Z., Jackson, D., Chowdhury, N., and Povey, T., 2025, "Impact of Trailing Edge Damage on Nozzle Guide Vane Aerodynamic Performance," ASME J. Turbomachinery, 147(10), DOI: 10.1115/1.4067930.

[2] Afanasiev, I. V., Granovskiy, A. V., Kareline, A. M., and Kostege, M. K., 2004, "Effect of 3D Vane Shape on the Vane Capacity," Proceedings of ASME Turbo Expo 2004, Vienna, Austria, June 14–17 2004, Paper No. GT2004-53095, DOI: 10.1115/GT2004-53095.

[3] Afanasiev, I. V., Granovskiy, A. V., Kareline, A. M., and Kostege, M. K., 2004, "The Problems of Inaccuracy in Flow Capacity Definition by Using Different Numerical Techniques," J. Thermal Science, 13(1), DOI: 10.1007/s11630-004-0001-z.

[4] Fielding, L., 1981, "The Effect of Irreversibility on the Capacity of a Turbine Blade Row," Proceedings of the Institution of Mechanical Engineers, 195(1), DOI: 10.1243/PIME_PROC_1981_195_046_02.

[5] Povey, T., Sharpe, M., and Rawlinson, A., 2011, "Experimental Measurements of Gas Turbine Flow Capacity Using a Novel Transient Technique," ASME J. Turbomachinery, 133(1), DOI: 10.1115/1.4000481.

[6] Povey, T., 2010, "Effect of Film Cooling on Turbine Capacity," ASME J. Engineering for Gas Turbines Power, 132(1), DOI: 10.1115/1.3026564.

[7] Hambidge, C., and Povey, T., 2012, "Numerical and Analytical Study of the Effect of Film Cooling on HP NGV Capacity," Proceedings of ASME Turbo Expo 2012, Copenhagen, Denmark, June 11–15 2012, Paper No. GT2012-69066, DOI: 10.1115/GT2012-69066.

[8] Högner, L., Nasuf, A., Voigt, P., Voigt, M., Vogeler, K., Meyer, M., Berridge, C., and Goenaga, F., 2016, "Analysis of High Pressure Turbine Nozzle Guide Vanes Considering Geometric Variations," Proceedings of ASME Turbo Expo 2016, Seoul, South Korea, June 13–17 2016, Paper No. GT2016-57502, DOI: 10.1115/GT2016-57502.

[9] Voigt, P., Högner, L., Fiedler, B., Voigt, M., Mailach, R., Meyer, M., and Nasuf, A., 2019, "Comprehensive Geometric Description of Manufacturing Scatter of High-Pressure Turbine

Nozzle Guide Vanes for Probabilistic CFD Analysis," ASME J. Turbomachinery, 141(8), DOI: 10.1115/1.4042892.

[10] Burdett, D., Goenaga, F., and Povey, T., 2021, "Understanding Capacity Sensitivity of Cooled Transonic Nozzle Guide Vanes: A Parametric Experimental and Computational Study of the Impact of Trailing Edge Geometry," ASME J. Turbomachinery, 143(5), DOI: 10.1115/1.4050068.

[11] Kirollos, B., Lubbock, R., Beard, P., Goenaga, F., Rawlinson, A., Janke, E., and Povey, T., 2017, "ECAT: An Engine Component Aerothermal Facility at the University of Oxford," Proceedings of ASME Turbo Expo 2017, North Carolina, USA, June 26–30 2017, Paper No. GT2017-64736, DOI: 10.1115/GT2017-64736.

[12] Burdett, D., Hambidge, C., and Povey, T., 2020, "Analysis of Ultra-Low Uncertainty Gas Turbine Flow Capacity Measurement Techniques," Proceedings of the Institution of Mechanical Engineers, Part A: J. Power Energy, 235(5), DOI: 10.1177/0957650920909718.

[13] Messenger, A., Cartlidge, J., Chowdhury, N., Goenaga, F., and Povey, T., 2023, "ECAT+: A Second-Generation High-Temperature Engine Component Aerothermal Facility at the University of Oxford," Proceedings of ASME Turbo Expo 2023, Boston, USA, June 26–30 2023, Paper No. GT2023-102935, DOI: 10.1115/GT2023-102935.

[14] Meyer, M., Parchem, R., and Davison, P., 2011, "Prediction of Turbine Rotor Blade Forcing due to In-Service Stator Vane Trailing Edge Damage," Proceedings of the ASME Turbo Expo 2011, Vancouver, Canada, 6–10 June 2011, Paper No. GT2011-45204, DOI: 10.1115/GT2011-45204.

[15] Messenger, A., and Povey, T., 2020, "Calibrated Low-Order Transient Thermal and Flow Models for Robust Test Facility Design," J. Global Power and Propulsion Society, 4(1), DOI: 10.33737/jgpps/122270.

[16] Amend, J., Lubbock, F.; Ornano, F.; Chowdhury, N., and Povey, T., 2023, "Aerodynamic and Thermal Field Development of Cooled Transonic HP NGV," ASME J. Turbomachinery, 146(2), DOI: 10.1115/1.4063879.

[17] British Standards Institution, 2022, "BS EN ISO 9300:2022 Measurement of Gas Flow by Means of Critical Flow Venturi Nozzles," British Standards Institution, London.

This page is intentionally blank

Chapter 6 – Turbine stage performance

This chapter extends the investigation of trailing-edge burn-back from isolated vane rows to a full high-pressure turbine stage. Building on the analyses in Chapter 4 and Chapter 5, which showed significant effects on vane aerodynamics and flow capacity, it uses unsteady stage simulations to assess the overall performance impact. The work is presented in the form of a peer-reviewed journal article[3].

Abstract

In this paper we consider the impact of nozzle guide vane trailing edge burn-back (damage) on cooled high-pressure turbine stage performance. We analyse four levels of simulated burn-back ranging from new parts to severely damaged. The burn-back geometries are based on a statistical analysis of real deterioration data from operating engines. We use unsteady stage simulations to predict the impact of burn-back on capacity, reaction, specific work, and efficiency, among other performance metrics. Experimental data from a full-annulus nozzle guide vane cascade test (operated at engine-matched conditions) was used to validate the CFD predictions.

We find that for fixed stage pressure ratio, increasing burn-back leads to: a significant decrease in vane efficiency due to the formation of a pair of counter-rotating vortices at the burn-back edges; an increase in rotor efficiency due to weakened secondary flow in the rotor passage; a marginal overall decrease in stage efficiency; a decrease in stage specific work despite an increase in mass-mean absolute turning angle due to a greater magnitude of contrary change in rotor inlet and outlet velocities; a significant increase in vane capacity due to an increase in the effective area of the controlling region, and a milder decrease in vane capacity due to an increase in the intra-stage static pressure; and a significant increase in stage reaction.

[3] The text in this chapter is a verbatim reproduction of the published, multi-author, journal paper with some clarifications. It has also been stylistically adapted to match the typeface, margins, and pagination of this thesis.

Taken together with a related study on vane-only aerodynamic performance and flow capacity, these results improve understanding of the impact of burn-back on whole-life engine performance.

Publication status and co-author contributions

This *journal* paper titled "*Impact of Nozzle Guide Vane Trailing Edge Damage on High Pressure Turbine Stage Performance*" has been accepted for publication in the ASME Journal of Turbomachinery [6]. The co-author contributions are as follows. Zelimhan Raduev (student): determined burn-back designs; performed all simulations; wrote processing scripts of numerical data; analysed numerical data; generated all figures; and was responsible for the manuscript writing. Dougal Jackson (industry contact): provided deterioration data so burn-back designs can be determined; provided base simulation model that was the foundation of this work; provided significant support with industry software used; and contributed with analysis ideas. Thomas Povey (supervisor): supervised all aspects of the work. A statement of authorship is included at the end of the thesis.

6.1 – Introduction and literature review

High-pressure (HP) nozzle guide vanes (NGVs) operate under extreme conditions of pressure and temperature, often in flows with a peak temperature significantly exceeding the melting point of the component material. In-service deterioration arises from particle deposition, oxidation and impact. This manifests as surface roughness changes, collapsed film cooling holes, leading edge (LE) holing, and trailing edge (TE) erosion or oxidation. This last effect is sometimes referred to as burn-back. This can significantly affect row and stage performance, and engine operating point. Understanding the effects of burn-back is important for whole-life engine performance modelling.

We progress the literature review under two headings: impact of burn-back on engine life and fuel consumption; and impact of burn-back on vane and stage aerodynamic performance.

We include studies on deterioration effects in general, as many of these include—but do not isolate—burn-back effects.

6.1.1 – Impact of burn-back on engine life and fuel consumption

Naeem et al. [1] ran flight mission simulations to quantify the effect of engine deterioration on fuel consumption of a dual spool afterburning military turbofan. The TURBOMATCH code (see Palmer [2]) was used to estimate specific fuel consumption and thrust for each stage of a flight (climb, cruise, etc.). The effect of compressor and turbine components with varying levels of damage was considered in their study, both separately and in combination. In this work, turbine component deterioration was characterised by changes in capacity and stage efficiency together (directly based on Sallee [3]), both of which were inputs to their model. The authors reported that increasing deterioration of the high-pressure turbine (HPT) generally led to increased fuel consumption. For fixed engine thrust, they predicted that a 3% increase in capacity and a 6% decrease in isentropic efficiency of the HPT stage led to a 4.4% increase in specific fuel consumption over a complete flight mission when compared with non-deteriorated engine.

In a later, related, study using developments of the TURBOMATCH code, Naeem et al. [4] quantified the effect of engine deterioration on the thermal fatigue life of the HPT blades. They found that engine deterioration generally led to reduced thrust: they predicted that a 5% increase in capacity and a 10% decrease in stage efficiency would lead to a 14.5% decrease in thrust. To return the engine to the original thrust, a higher turbine entry temperature (TET) was required with associated increased fuel burn. They showed that an increase in TET of 170 K at cruise conditions would be required. The higher TET led to lower component life through more rapid thermal fatigue.

Tinga et al. [5] used an in-house lifing analysis tool to predict the life of components in a gas turbine. They studied the HPT of a dual-spool afterburning military turbofan, with deterioration characterised by an increase in capacity and a decrease in efficiency, both of

which were inputs to their model. They showed that HPT deterioration generally led to an increase in creep rate, and associated reduced component life. For a 1% increase in capacity and a 2% decrease in isentropic efficiency their model predicted an increase in the accumulated strain of the component by a factor of 1.9. They attributed this largely to the increase in TET (25–35 K) required to maintain thrust.

MacLeod et al. [6] experimentally investigated the effects of a number of in-service component changes on the performance of a single spool turboprop engine. The engine was modified such that the single shaft was coupled to a gearbox forward of the compressor stages, and then to a dynamometer which could measure the power output. In their setup, the shaft speed was regulated by a governor at a fixed speed. The effect of erosion, cracking, bowing, and corrosion of the first stage turbine NGVs was considered in part of the study. Erosion of the NGV assembly caused a 6.0% (±1.4%) increase in the effective flow area (capacity as measured in an air-flow rig) compared to a new assembly, and increased specific fuel consumption by 3.24%. There was also a change in turbine isentropic efficiency, but the magnitude was within the measurement uncertainty limits ($\pm 0.90\%$).

6.1.2 – Impact of burn-back on vane and stage aerodynamic performance

Sjolander et al. [7] investigated the aerodynamics of uncooled turbine blades with simulated TE burn-back in a low-speed linear cascade. They took area traverse measurements two-fifths axial of an axial chord length downstream of the TE. Simulated burn-back was represented with midspan semi-circle cut-outs. The authors measured increasing plane-averaged loss with increasing burn-back. An increase of +45% was measured with a cut-out depth equal to 25% of blade tangential chord. Inside the cut-out region flow under-turning was observed (less guided length). More surprisingly, outside the cut-out region, flow overturning was observed and this was associated with vortices shed from the cut-out edges.

Wang et al [8] performed numerical simulations of the aerodynamics of uncooled NGVs (from a steam turbine) with simulated TE damage. Simulated damage (with semi-circle cut-

outs) with depths up to 37% of the NGV tangential chord were studied. The location of the damage was varied so that it was either near the hub, at midspan, or near the casing. The authors reported that loss increased with cut-out size at all locations, and that the loss increase was smallest when the cut-out was placed at the midspan.

Bouchard et al. [9] performed an experimental investigation into the aerodynamics of uncooled NGVs with in-service TE distortion and cracking. Experiments were performed in a transonic annular cascade. Measurements included 360-degree traverse data taken half an axial chord downstream of the TE at four span locations (near case, midspan, and two radial heights near the hub). When compared with a reference as-manufactured NGV ring, there was a measured loss increase of 51%, with the largest increase at midspan.

In a precursor to the current study, Michaud et al. [10] investigated the aerodynamics of a heavily-cooled transonic NGV row with in-service deterioration. The service-exposed NGVs had increased surface roughness, thermal barrier coating spallation, damaged film cooling holes, and mild TE burn-back. As in the current study, experiments were performed in the Engine Component AeroThermal (ECAT) facility at the University of Oxford, an engine parts transonic annular cascade operated at engine matched conditions of Mach number, Reynolds number, and coolant-to-mainstream pressure ratio. The test ring consisted of a rainbow-set of new, mid-life, and end-of-life vanes. Full area traverse measurements were taken a quarter of an axial chord downstream of the vane TE. For deteriorated parts, the following changes were measured: an increase in mixed-out loss of up to 33%; flow under-turning of up to 6 degrees; film coolant capacity decrease of up to 6%; and vortex formation at the edges of the burn-back features. In a companion paper, Michaud et al. [11] investigated the thermal performance of the same parts. They performed in-situ infra-red temperature measurements of deteriorated parts and compared these to as-manufactured vanes. They found that changes in thermal performance was the greatest on the pressure surface (PS), with changes in area-averaged overall cooling effectiveness of −1.83% and −10.41% on the PS of the mid-life and end-of-life vanes, respectively.

Meyer et al. [12] and di Mare et al. [13] studied the forced response of the HP turbine to an upstream NGV with simulated burn-back (triangular cut-outs). Both studies used full-stage whole-annulus simulations with a single damaged NGV in an otherwise undamaged stator row. The studies showed that distortion of the flow field downstream of the damaged NGV (counter-rotating vortices, and changes in whirl angle distribution) led to changes in loading of the rotor blades in the vicinity of the NGV. The flow field of neighbouring NGVs was essentially unaffected by the damaged NGV.

6.1.3 – Current study

In this paper, we perform a detailed parametric study of the impact of TE burn-back on high-pressure stage aerodynamics and performance (the rotor geometry remains undamaged in all cases). We examine changes in efficiency, reaction, specific work, and stage capacity. We consider four levels of simulated burn-back ranging from new to severely damaged parts, and note that the surface roughness of the vanes or rotors were not adjusted as we were interested in isolating the impact of TE burn-back specifically. We use full-stage URANS simulations of a sector of the stage for the study, validated (to the extent possible) using experimental data taken in the ECAT facility (see Kirollos et al. [14]). Companion-papers consider the impact of TE burn-back on NGV aerodynamic performance [15], and NGV capacity [16]. Taken together, these studies improve understanding and benchmarking of whole-life engine performance models.

6.2 – Trailing edge damage shapes

The turbine stage (nozzle guide vane and rotor) used for this study is the high-pressure stage of a modern aero-engine. The NGV and rotor are both moderately forward-loaded transonic designs with thermal barrier coating and advanced internal and film cooling systems.

Four levels of simulated NGV burn-back were studied, ranging from undamaged to severely damaged. The damage shapes were based on a statistical analysis of hundreds of real engine parts which showed that the damage shapes were approximately trapezoidal in form,

centred on midspan, and could be characterized (similar method and conclusions to Meyer et al [12]) using four non-dimensional parameters: burn-back depth normalised by tangential chord, d/C_t; burn-back width at TE normalised by span height, w_1/S; burn-back width at damage front normalised by span height, w_2/S; and burn-back area normalised by the product of the vane tangential chord and span height, $A_{\mathrm{BB}}/A_{\mathrm{ref}}$. These are shown in Figure 6.1.

To generate a realistic design space for burn-back variation, four exploratory methods were applied to the dataset: an averaged-shape method based on mean profiles; a maximum-depth method using evenly spaced depths between baseline and maximum recorded damage; a quartile-based method using boxplot statistics; and a K-means clustering method using cluster means as representative shapes. These methods provided consistent bounds on the variation of the key non-dimensional parameters. The final parameter values were then chosen within these ranges to ensure realistic and progressively increasing burn-back damage. The resulting designs are referred to as Geometry 1 to Geometry 4 and a summary of the values for each of these parameters is given in Table 6.1 for each geometry. Geometry 1 corresponds to the undamaged baseline vane, while Geometry 2–4 represent increasing levels of in-service burn-back from mild through to severe. For the experimental campaign, parts were sequentially modified by machining them back, without unbuilding the vane module. The process is described in more detail in Raduev et al. [16].

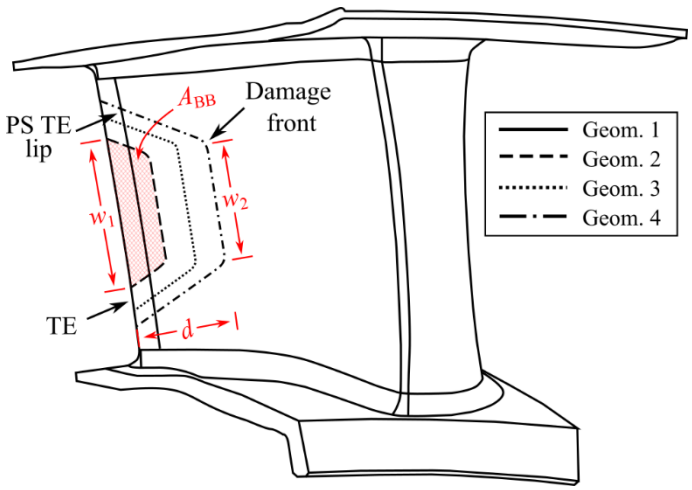


Figure 6.1: Schematic of NGV Geometry 1–4.

Table 6.1: Non-dimensional parameters representing NGV Geometry 1–4.

Non-dimensional parameter	Geom.			
	1	2	3	4
Burn-back depth, d/C_t [%]	0	10.8	19.2	27.5
Burn-back width at TE, w_1/S [%]	0	42.5	54.6	66.8
Burn-back width at damage front, w_2/S [%]	0	29.8	33.3	36.8
Burn-back area, A_{BB}/A_{ref} [%]	0	3.9	8.4	14.2

6.3 – Numerical method

Stage simulations were performed for Geometry 1–4 using the Rolls-Royce in-house CFD solver HYDRA (see Lapworth [17] for more detail). The k-ω SST turbulence model was used, with second order discretization for the advection and turbulence terms. The computational domain included four vanes (all identical in each geometry case), and seven blades for periodicity without geometry distortion, this also corresponded to two combustor pitches. Unsteady simulations were performed using a sliding plane interface. The computational domain extended 3 vane axial chords upstream of the NGV leading edge, and a rotor axial chord downstream of the rotor trailing edge. The inlet contraction represented the combustion liner contraction (also replicated in the experimental build). The computational domain is shown in Figure 6.2.



Figure 6.2: CFD domain for Geometry 1.

An unstructured octree-based mesh was generated by the author for the vane mesh block using BOXERMesh (version 3.8.3-3), and a block-structured mesh was generated by Rolls-

Royce for the rotor blade mesh block using the Rolls-Royce in-house meshing and parametric design tool PADRAM (see Milli and Shahpar [18]). In total, the mesh had approximately 150 million cells, with 125 million for the vane mesh block and 25 million for the rotor mesh block. A midspan cross section of the mesh is shown in Figure 6.3. A meridional schematic of the domain is shown in Figure 6.4.

The vane mesh was refined in five regions: the wake region; near the TE; around the NGV surface; in the geometric throat region; and along the burn-back edges. To capture the viscous sub layer, a y+ on the wetted surface with a value less than two was achieved. To achieve this y+, the NGV surface and the internal walls of the TE slot were refined with 30 and 15 inflation layers, respectively, with an initial step size of 3 μm. The turbine blade mesh block was refined around the turbine blade surface, and near the TE. To reduce the rotor mesh size, a y+ on the wetted surface with a value above thirty was used (in log-law region) allowing the use of wall functions. A mesh independence study was performed on the vane domain. With the chosen mesh setting, it was shown that capacity, mass averaged loss coefficient, and mass averaged whirl angle were mesh independent to within 0.02%, 0.50% and 0.06% respectively (difference between a mesh of 22 million cells and the chosen 31 million cells). The rotor mesh settings suitably resolve features in the flow direction especially at the transition between the SS (or PS) and the TE radius. Here, mesh changes can alter the flow detachment location and lead to capacity changes. Mesh settings were based on good-practice understanding at Rolls-Royce based on previous mesh sensitivity studies on similar geometries (see, for example, Milli and Shahpar [19]), using settings that achieve mesh independence of capacity, stage efficiency, and radial distributions of whirl.



Figure 6.3: Midspan cut showing octree NGV mesh (Geometry 1) and block structured turbine blade mesh (geometry distorted for commercial reasons).

We now discuss boundary conditions with reference to the meridional schematic shown in Figure 6.4. For the inlet flow (plane 1), uniform total pressure and a radial profile of total temperature was imposed. For the outlet flow (plane 4), a radial profile of static pressure was imposed. The outlet static pressure profile was determined using the through-flow code Q263 (Rolls-Royce in-house code) where flow angles are set to blade metal angles, and where losses are treated with correlations only. Three cavity purge flows were modelled with uniform inlet conditions of total pressure and temperature imposed at the duct inlets (see Figure 6.4). The rotor blade is of fully-shrouded design, and the domain was simulated at fixed rotational speed with walls set to be adiabatic. Rotational periodic boundaries were set in the circumferential direction. Boundary conditions imposed were representative of cruise engine condition.

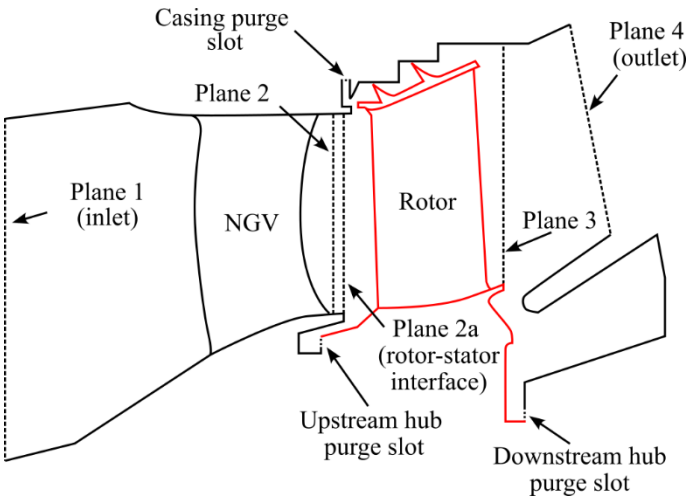


Figure 6.4: Meridional schematic of the CFD domain.

The modelled vane was fully cooled, with a film cooling system comprised of eleven film rows (six on SS and five on PS), and a radially-partitioned TE slot. The film cooling was modelled using a strip cooling method as described in Milli and Shahpar [19]. In this method, the original rows of film cooling holes are replaced with continuous strips with specified values of mass flow, total temperature, and direction is set. The TE slot was explicitly modelled and included features such as chordwise ribs that divide the plenum into seven ducts and pedestals. Coolant mass flows for each film cooling strip and TE slot were determined using an in-house low-order internal flow solver (loss-correlation based). In this solver, coolant inlet total pressure and temperature, and individual exit static pressures (determined from an uncooled simulation) were specified. The mass flow predicted by this code was scaled to match experimental data from cold-rig measurements taken using the Engine Component Aerothermal (ECAT) facility (described in Raduev et al. [16]), and further scaled to account for differences in the coolant-to-mainstream temperature ratio between cold-rig and engine (i.e., from $T_{0c,NGV}/T_{01} = 1$ to $T_{0c,NGV}/T_{01} \sim 0.5$). Coolant-to-mainstream pressure ratio, and overall vane pressure ratio were matched between rig and engine. For further discussion of this scaling problem see Cartlidge and Povey [21].

The blade film cooling system had nine film rows, also modelled using the strip model, with mass flows determined using the Q263 through-flow solver.

The convergence criteria for the unsteady simulations were that stage capacity, reaction, stage efficiency, and stage work were steady with additional iterations to within 0.5%, when averaged over a full rotor revolution, and that RMS residuals of mass flow and turbulence were below $10^{-9.5}$ and $10^{-12.5}$, respectively.

6.4 – Performance parameters

In this section, performance parameters used in this study are summarized.

6.4.1 – Loss coefficients

We use kinetic energy (KE) loss coefficients (ζ_{NGV} and ζ_{TB}) to express the inefficiency in the conversion of pressure energy to kinetic energy across the vane and blade row. Where the ratios of the actual exit KE to the ideal exit KE are η_{NGV} and η_{TB}, we write

$$\zeta_{\mathrm{NGV}} = 1 - \eta_{\mathrm{NGV}} = 1 - \frac{\mathrm{KE}_{\mathrm{NGV,actual}}}{\mathrm{KE}_{\mathrm{NGV,ideal}}} = 1 - \frac{h_{02} - h_2}{h_{01} - h_{2s}} \tag{6.1}$$

$$\zeta_{\mathrm{TB}} = 1 - \eta_{\mathrm{TB}} = 1 - \frac{\mathrm{KE}_{\mathrm{TB,actual}}}{\mathrm{KE}_{\mathrm{TB,ideal}}} = 1 - \frac{h_{03,\mathrm{rel}} - h_3}{h_{02,\mathrm{rel}} - h_{3\mathrm{s}}} \tag{6.2}$$

where h and h_0 are the static enthalpy and total enthalpy in the absolute frame, respectively, $h_{0,\mathrm{rel}}$ is the total enthalpy in the blade relative frame, and h_{s} is the static enthalpy based on an isentropic expansion. Subscripts 1–3 refer to the corresponding planes shown in Figure 6.4. For isenthalpic processes (in frames fixed relative to the stator and rotor, i.e. $h_{02} = h_{01} = h_0$ and $h_{03,\mathrm{rel}} = h_{02,\mathrm{rel}} = h_{0,\mathrm{rel}}$) and using the isentropic relation $T_2/T_1 = (p_2/p_1)^{\chi}$ where $\chi = (\gamma - 1)/\gamma$ and γ is the specific heat ratio ($\gamma = 1.4$ for air), the vane and rotor KE loss coefficients become

$$\zeta_{\mathrm{NGV}} = 1 - \frac{1 - h_2/h_0}{1 - h_{2s}/h_0} = 1 - \frac{1 - (p_2/p_{02})^{\chi}}{1 - (p_2/p_{01})^{\chi}} \tag{6.3}$$

$$\zeta_{\mathrm{TB}} = 1 - \frac{1 - h_3/h_{0,\mathrm{rel}}}{1 - h_{3s}/h_{0,\mathrm{rel}}} = 1 - \frac{1 - (p_3/p_{03,\mathrm{rel}})^{\chi}}{1 - (p_3/p_{02,\mathrm{rel}})^{\chi}} \tag{6.4}$$

where p and p_0 are the static and total pressure in the vane frame of reference, and $p_{0,\mathrm{rel}}$ is the total pressure in the blade relative frame.

Following Burdett and Povey [22], we use four loss metrics to represent our data. We consider first the loss coefficients for the NGV row.

Firstly, a local KE loss coefficient

$$\zeta'_{\mathrm{NGV}}(r,\theta) = 1 - \frac{1 - \left(\frac{p_2(r,\theta)}{p_{02}(r,\theta)}\right)^{\chi}}{1 - \left(\frac{p_2(r,\theta)}{\bar{p}_{01}}\right)^{\chi}} \tag{6.5}$$

where r, and θ represent the radial, and circumferential positions, respectively, and where $\bar{p}_{01}$ is the upstream mass-flux-averaged total pressure. Secondly, a circumferentially-averaged KE loss coefficient

$$\zeta''_{\mathrm{NGV}}(r) = 1 - \frac{1 - \left(\frac{\bar{p}_2(r)}{\bar{p}_{02}(r)}\right)^{\chi}}{1 - \left(\frac{\bar{p}_2(r)}{\bar{p}_{01}}\right)^{\chi}} \tag{6.6}$$

where $\bar{p}_2(r)$ is the circumferentially-path-averaged static pressure at a particular radial position, and $\bar{p}_{02}(r)$ is the circumferentially mass-flux-averaged total pressure. Thirdly, we define the plane-averaged KE loss coefficient as

$$\zeta'''_{\mathrm{NGV}} = 1 - \frac{\left(\dot{m}_1 T_{01} + \dot{m}_{\mathrm{c,NGV}} T_{0\mathrm{c,NGV}}\right)\left[1 - \left(\frac{\bar{p}_2}{\bar{p}_{02}}\right)^{\chi}\right]}{\dot{m}_1 T_{01}\left[1 - \left(\frac{\bar{p}_2}{\bar{p}_{01}}\right)^{\chi}\right] + \dot{m}_{\mathrm{c,NGV}} T_{0\mathrm{c,NGV}}\left[1 - \left(\frac{\bar{p}_2}{\bar{p}_{0\mathrm{c,NGV}}}\right)^{\chi}\right]} \tag{6.7}$$

where $\dot{m}_1$ and $\dot{m}_{\mathrm{c,NGV}}$ are the mainstream inlet and vane coolant mass fluxes, respectively, $\bar{p}_2$ is the area-averaged static pressure, $\bar{p}_{02}$ the mass-flux-averaged total pressure, $\bar{p}_{0\mathrm{c,NGV}}$ the vane coolant total pressure, and $T_{0\mathrm{c,NGV}}$ the vane coolant total temperature. Finally, we define the mixed-out KE loss coefficient as

$$\zeta''''_{\mathrm{NGV}} = 1 - \frac{\left(\dot{m}_1 T_{01} + \dot{m}_{\mathrm{c,NGV}} T_{0\mathrm{c,NGV}}\right)\left[1 - \left(\frac{\bar{p}'_2}{\bar{p}'_{02}}\right)^{\chi}\right]}{\dot{m}_1 T_{01}\left[1 - \left(\frac{\bar{p}'_2}{\bar{p}_{01}}\right)^{\chi}\right] + \dot{m}_{\mathrm{c,NGV}} T_{0\mathrm{c,NGV}}\left[1 - \left(\frac{\bar{p}'_2}{\bar{p}_{0\mathrm{c,NGV}}}\right)^{\chi}\right]} \tag{6.8}$$

where $\bar{p}'_2$ and $\bar{p}'_{02}$ are mixed-out average static and total pressure values. For the mixing process, the Main et al. method (see [23]; for discussion see Burdett and Povey [22]) was used,

in which the flow is mixed to a free-vortex condition. We also compute the residual secondary kinetic energy (SKE) as the difference from the plane-averaged loss coefficient and mixed-out loss coefficient (i.e. $\zeta_{\mathrm{NGV}}^{\mathrm{SKE}} = \zeta_{\mathrm{NGV}}'''' - \zeta_{\mathrm{NGV}}'''$).

Now consider the rotor-row loss coefficients. We define equivalent coefficients ($\zeta_{\mathrm{TB}}'(r,\theta)$, $\zeta_{\mathrm{TB}}''(r)$, ζ_{TB}''', ζ_{TB}'''' and $\zeta_{\mathrm{TB}}^{\mathrm{SKE}}$) using variables in the *rotor-relative frame.* Here, we reduce the radial variation in inlet total pressure (variation across in the plane caused by NGV loss) using mass-flux-averaging, to give a single value of rotor-relative inlet total pressure, $\bar{p}_{02,\mathrm{rel}}$. This must be considered when interpreting maps of *local* KE loss coefficient for the rotor, $\zeta_{\mathrm{TB}}'(r,\theta)$: specifically, the possibility of an artificially introduced *radial variation* in the local KE loss coefficient distribution caused by radial variation in the inlet distribution. Theoretically, a stream-tube-based approach could be used to avoid this problem, but is practically intractable (secondary flows, mixing, etc.).

6.4.2 – Whirl angle

Whirl angle is defined with respect to the axial direction

$$\beta = \tan^{-1}\left(\frac{V_\theta}{V_x}\right) \tag{6.9}$$

where V_x and V_θ are the axial and circumferential components of the absolute velocity. For blade relative whirl angle, the corresponding blade relative components are used.

6.4.3 – Capacity, reaction, specific work, and efficiency

The vane (flow) capacity is defined as

$$\Gamma_{\mathrm{NGV}} = \frac{\dot{m}_1\sqrt{T_{01}}}{p_{01}} + \frac{\dot{m}_{\mathrm{c,NGV}}\sqrt{T_{0\mathrm{c,NGV}}}}{p_{0\mathrm{c,NGV}}} \tag{6.10}$$

where all parameters have been previously defined. Similarly, the rotor capacity is defined as

$$\Gamma_{\mathrm{TB}} = \frac{(\dot{m}_1 + \dot{m}_{\mathrm{c,NGV}})\sqrt{T_{02,\mathrm{rel}}}}{p_{02,\mathrm{rel}}} + \frac{\dot{m}_{\mathrm{c,TB}}\sqrt{T_{0\mathrm{c,rel,TB}}}}{p_{0\mathrm{c,rel,TB}}} \tag{6.11}$$

where $\dot{m}_{\mathrm{c,TB}}$ is the rotor coolant mass flux which includes the three cavity purge flows, $p_{0\mathrm{c,rel,TB}}$ the rotor relative coolant total pressure, $T_{0\mathrm{c,rel,TB}}$ the rotor relative coolant total temperature, and where all other parameters have been previously defined.

In general, the vane capacity is a function of the vane static-to-total pressure ratio, and the vane coolant-to-mainstream total pressure ratio (see Burdett et al. [24] for discussion). In the current study, the coolant-to-mainstream total pressure ratio is constant, however. Similarly, in general, the rotor capacity is a function of the rotor static-to-total pressure ratio in the rotating frame, the rotor coolant-to-mainstream total pressure ratio in the rotating frame, and some secondary parameters which we will describe. In the current work the rotor coolant-to-mainstream total pressure ratio is constant. The secondary parameters are those which affect the radial distributions of rotor-relative total pressure, static pressure, total temperature, and whirl angle: we could take these to include the rotor geometry, the rotor operating point (i.e. the intra-stage stage pressure, which varies with geometry in this study), and the non-dimensional rotor speed (constant in this study). In our simulations, the vane and rotor static-to-total pressure ratios are established by setting the stage pressure ratio and non-dimensional rotor speed. We run our simulations at approximately fixed stage pressure ratio, and precisely fixed non-dimensional rotor speed.

Stage reaction is the ratio of static enthalpy drop across the rotor to the static enthalpy drop across the stage

$$\Lambda = \frac{h_2 - h_3}{h_1 - h_3} = \frac{\left(\frac{\bar{p}_2}{\bar{p}_3}\right)^{\chi} - 1}{\left(\frac{\bar{p}_1}{\bar{p}_3}\right)^{\chi} - 1} \tag{6.12}$$

where $\bar{p}_1$, $\bar{p}_2$, and $\bar{p}_3$ are the area-averaged static pressures at the vane inlet, vane exit (or rotor inlet), and rotor exit, respectively.

Specific work is the work extracted by the turbine per unit mass flow. Using the power-based approach, it is defined as

$$\dot{w} = \frac{P}{\dot{m}_{\text{stage}}} = \frac{\tau\Omega}{\dot{m}_{\text{stage}}} \tag{6.13}$$

where P is the rotor power (work done per second), τ is the torque exerted on the rotor, Ω is the rotor angular velocity, and $\dot{m}_{\text{stage}}$ is the mass flow through the stage.

Stage isentropic efficiency is defined as the ratio of the work extracted by the turbine, to the work associated with an ideal (isentropic) expansion between the same pressures as the real expansion, i.e. $\eta_{\text{stage}} = (h_{01} - h_{03})/(h_{01} - h_{03s})$. There is debate in the literature (see [25], [26] and [27]) about the most rational definition in the case of a cooled turbine. We adopt the formulation of Hartsel [27]) in which individual streams (coolant streams and mainstream) undergo separate expansions from inlet conditions to a mixed exit condition. This gives

$$\begin{aligned}\eta_{\text{stage}} &= \frac{(\dot{m}_1 h_{01} + \sum \dot{m}_{\text{ci}} h_{0\text{ci}}) - (\dot{m}_1 + \sum \dot{m}_{\text{ci}}) h_{03}}{\dot{m}_1 (h_{01} - h_{03\text{s}}) + \sum \dot{m}_{\text{ci}} (h_{0\text{ci}} - h_{03\text{s}})} \\ &= \frac{(\dot{m}_1 \bar{T}_{01} + \sum \dot{m}_{\text{ci}} \bar{T}_{0\text{ci}}) - (\dot{m}_1 + \sum \dot{m}_{\text{ci}}) \bar{T}_{03}}{\dot{m}_1 \bar{T}_{01} \left[1 - \left(\frac{\bar{p}_{03}}{\bar{p}_{01}}\right)^{\chi}\right] + \sum \dot{m}_{\text{ci}} \bar{T}_{0\text{ci}} \left[1 - \left(\frac{\bar{p}_{03}}{\bar{p}_{0\text{ci}}}\right)^{\chi}\right]}\end{aligned} \tag{6.14}$$

where the subscript c*i* represents the conditions for individual coolant streams.

6.5 – Numerical validation

In this section we consider numerical validation of the CFD method by comparison against experimental data taken using the ECAT facility. The experimental method for aerodynamic performance measurements is described in detail in Raduev et al. [15], and for flow capacity measurements in Raduev et al. [16]. In short, the ECAT facility is a transonic annular cascade that operates with engine components (fully cooled NGVs) and at engine-matched conditions of Reynolds number and Mach number. Pressurised air is supplied to the facility from large storage tanks which feed the mainstream and coolant feeds. For aerodynamic performance measurements, the facility was operated in a steady-state mode, in

which operating conditions are maintained constant for approximately 60 s. During this time, area traverse measurements were taken using a radial-circumferential traverse mechanism. A five-hole probe (calibrated over a wide range of incidence angles and Mach numbers) was used to measure flow angles, Mach number, and the total and static pressures between 5.8% and 93.2% span, In the near wall regions, a pitot probe was used to measure the total pressure. Overall, 96% of the vane span was covered by the combination of probes. For flow capacity measurements, the facility was operated in blowdown mode where flow conditions were allowed to naturally decay over a period of approximately 100 s. The mainstream mass flow was metered using a calibrated choked Venturi nozzle; coolant lines were metered Venturi nozzles designed to an ISO standard. The final bias and precision uncertainties in the capacity measurements were evaluated to ±0.301% and ±0.028%, respectively, to 95% confidence [24]. In both modes of facility operation, the total pressure and temperatures upstream of the NGV were measured using pitot probe rakes. Coolant stream flow conditions were measured using pitot probes and thermocouples. Exit static pressures were measured using static pressure tappings. The ECAT facility was an NGV cascade facility, so for validation the CFD was run as a single NGV row.

Experimentally-measured and CFD-predicted distributions of the local kinetic energy loss coefficient, $\zeta'_{\mathrm{NGV}}(r,\theta)$ at a plane one quarter axial chord length downstream of the NGV TE (plane 2 in Figure 6.4) for Geometry 1 are shown in Figure 6.5. The orientation is as viewed from downstream. The principal exit flow direction is clockwise (CW). Both distributions have been normalised by the experimentally measured plane-averaged loss coefficient, $\zeta'''_{\mathrm{ref,exp}}$.

Consider first the experimentally-measured loss coefficient distributions (Figure 6.5). We observe the following: wake curvature due to compound-lean in the aft region of the vane; local loss peaks along the line of the wake due to chordwise ribs within the TE slot; values of loss higher near the endwalls than the midspan due to endwall boundary layer (BL) fluid migration towards the vane-endwall SS corner; midspan flow more mixed out because the flow-wise distance between the TE and the traverse plane is greater, due to compound lean of

the vane; and regions of higher loss associated with passage vortices near the casing and hub (approximately at 5% and 85% span). This is analysed in detail in Raduev et al. [15].

Consider now the CFD-predicted loss coefficient distributions. Qualitatively we see that the shape of the wake and locations of secondary flow are well-predicted, but the wake is undermixed with respect to the experiment. Integrated loss in the CFD is 4.2% lower than the experiment: a relatively small difference. The peak value of loss in the CFD-prediction is 25.1% higher than that of the experiment. The higher peak value is offset by the thinner wake, explaining similar values of integral loss. The comparisons for all four geometries are discussed in more detail in Raduev et al. [15].

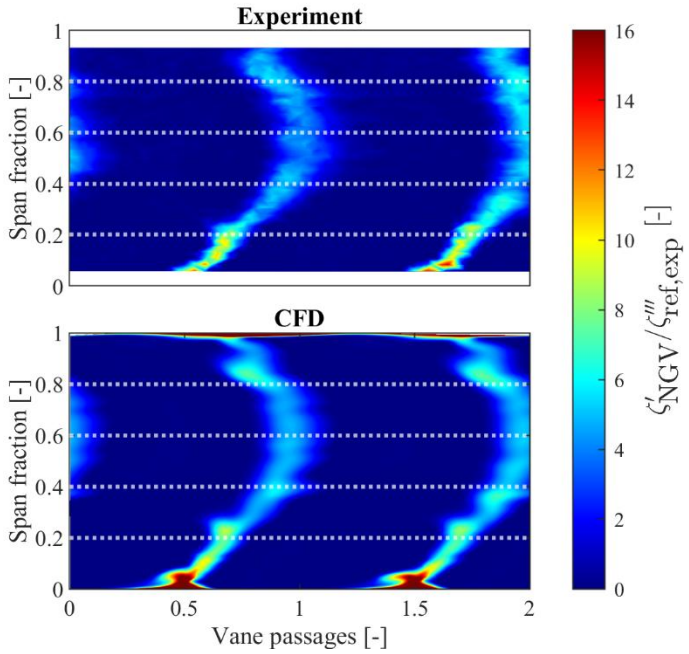


Figure 6.5: Experimentally-measured and CFD-predicted distributions of normalised local KE loss coefficient, $\zeta'_{NGV}/\zeta'''_{ref,exp}$, for Geometry 1.

We now compare experiment and CFD-predicted radial distributions of circumferentially mass-flux-averaged loss coefficient and whirl angle. These are shown in Figure 6.6. The experimental data range is between 6% and 93% span (five-hole probe size). Consider first the radial distributions of loss. In both experiment and CFD, the loss coefficient is relatively uniform between 20% and 75% span. This region is dominated by the vane surface BL and the dynamics of the TE flow. The impact of secondary flows in this region is confined to slight

redistribution of the vane surface BL fluid. The mean values of normalised loss coefficient in this region (normalised by experimentally measured plane-averaged loss coefficient, $\zeta'''_{\mathrm{ref,exp}}$) were 0.99 for the experiment and 0.93 for the CFD. In the near hub (0% to 20% span) and near casing (75% to 100% span) regions, the loss is higher due to endwall boundary layer fluid. At 5% and 85% span there are peaks of loss associated with passage vortices. The location of these local loss peaks was reasonably well predicted by CFD, but with an overestimation of loss.

Now consider the whirl angle distributions. Between 10% and 90% span, the experiment data and the CFD-prediction both have approximately linear distributions of whirl angle, with the CFD over-predicting by 1.4 degrees on average (mean of 76.7 degrees in the CFD, and mean of 75.3 degrees for the experiment). Some of this difference could be attributed to geometric differences between the experiment and CAD nominal design that would lead to a metal angle deviation effect, i.e., due to surface roughness, slight in-service wear, and manufacturing variability. Some differences could also arise if the flow is locally unsteady and because of probe bias error, which was determined to be ±0.8 degrees to 95% confidence (see [28] for uncertainty analysis).

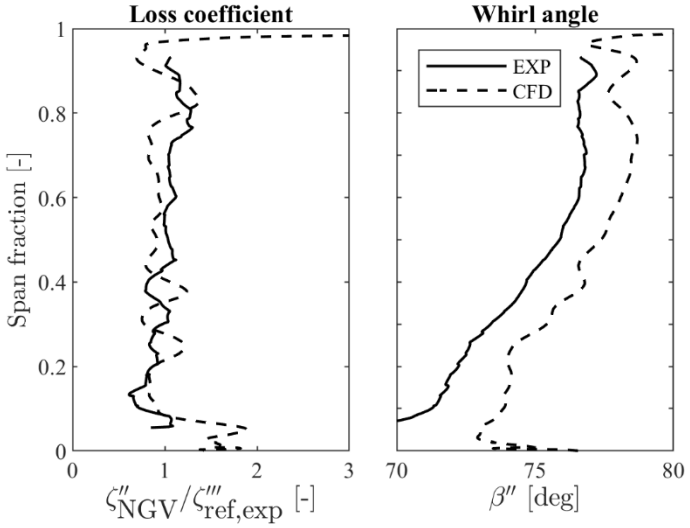


Figure 6.6: Radial distributions of circumferentially mass-flux-averaged KE loss coefficient and whirl angle for Geometry 1.

We now briefly discuss NGV flow capacity, Γ_{NGV} (see Equation 6.10). At the design vane pressure ratio ($p_2/p_{01} \approx 0.542$), the CFD-predicted flow capacity value was lower than the experimental value by 2.02%. This is within the typical range of accuracy for CFD based on design-intent CAD compared to a particular set of experimental parts. We note that a 0.1 mm surface offset in the controlling region of the vane is approximately equivalent to a 1% change in flow capacity. The test part in this study has a combined (PS + SS) thermal barrier coating thickness of approximately 0.25 mm in the controlling region: oxidation damage could also account for changes in flow capacity of order 1%. A detailed discussion of the impact of TE burn-back on NGV flow capacity is given in Raduev et al. [16].

Considering changes in plane-averaged loss coefficient (ζ'''_{NGV}) and flow capacity between Geometry 1 and all other builds, we see that: in terms of loss coefficient, trends are reasonably well-matched but with some difference in absolute values; in terms of flow capacity there is excellent agreement for all three differences. Values are summarised in Table 6.2.

Table 6.2: Percentage changes (from Geometry 1) in plane average loss coefficient and flow capacity.

Geom.	$\Delta\zeta'''_{\mathrm{NGV}}$ [%]		$\Delta\Gamma_{\mathrm{NGV}}$ [%]	
	EXP	CFD	EXP	CFD
1 → 2	+15.8	+10.7	+2.7	+2.6
1 → 3	+27.7	+21.9	+7.4	+7.8
1 → 4	+54.8	+56.7	+16.1	+16.2

6.6 – Results and discussion

In this section we consider the impact of increasing NGV TE burn-back on: local kinetic energy loss coefficient distributions; radial distributions of circumferentially-averaged loss coefficient, exit flow angle, total and static pressure, and Mach number; plane mass-flux-averaged loss coefficients; vane and blade loading charts; and overall turbine performance parameters such as stage capacity, reaction, specific work, and efficiency.

6.6.1 – Distributions of local KE loss coefficient

Distributions of local kinetic energy loss coefficient, $\zeta'(r,\theta)$, downstream of the NGV and TB are shown in Figure 6.7 for Geometry 1–4. All NGV row values are normalised by a reference value equal to the NGV mixed-out loss coefficient for Geometry 1. Likewise, rotor row values are normalised by the corresponding mixed-out loss coefficient for the rotor row for Geometry 1. The trends for Geometry 1 have been discussed in the context of Figure 6.5. In this section we focus on changes with increasing NGV TE burn-back. Considering first the trends of NGV loss coefficient with increasing burn-back (left column), we see the following:

1. Formation of two new loss cores at the edges of the burn-back (C), associated with two newly formed distinct counterrotating vortices.

2. Significant counter-clockwise (CCW) lag of the wake (B) in the burn-back region. This is due to flow underturning in this region because of the TE material removal.

3. Significant clockwise (CW) movement of the wake outside the burn-back region due to flow overturning. The flow overturning is associated with the newly formed counterrotating vortices, which act to increase the whirl angle in these regions.

4. Increased intensity of the hub and case loss cores (A), and radial migration of loss cores away from the endwalls.

These trends are discussed in more detail in Raduev et al. [15].

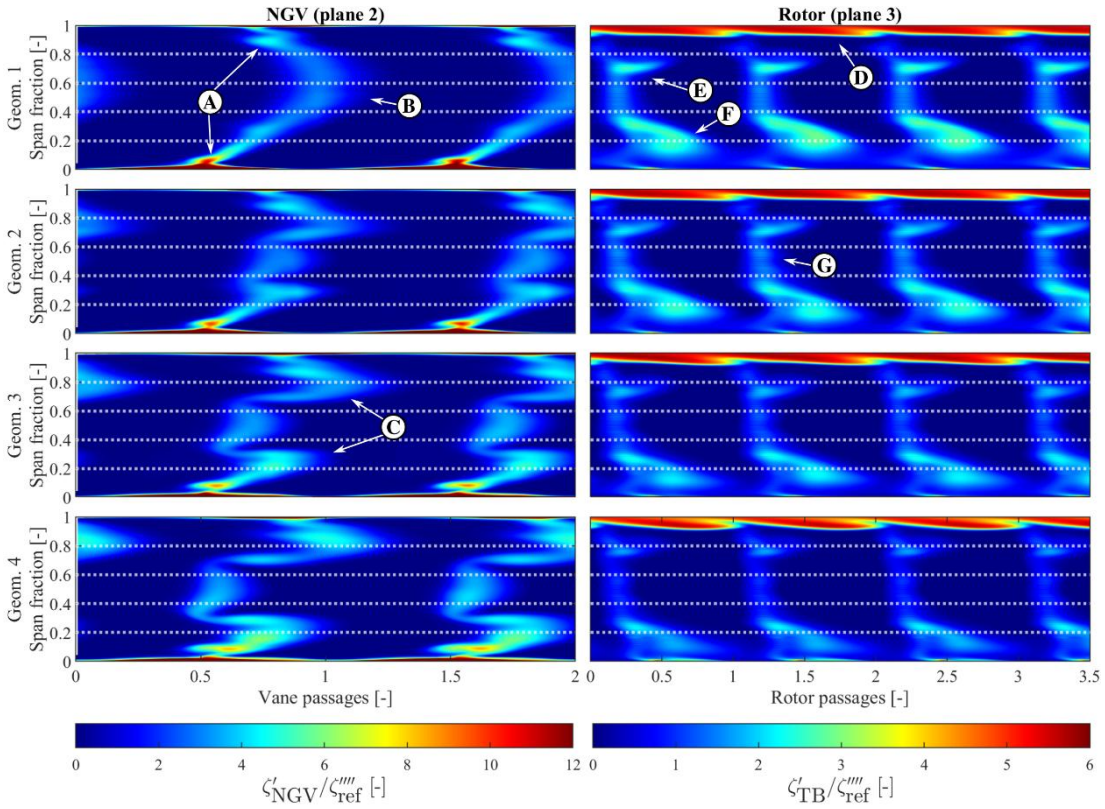


Figure 6.7: Distributions of normalised local KE loss coefficient, $\zeta'_{NGV}/\zeta''''_{ref}$ or $\zeta'_{TB}/\zeta''''_{ref}$, for Geometry 1–4. Data is viewed from downstream; and the exit flow direction is clockwise.

Now we consider the loss distributions downstream of the rotor (right column), which are presented in the rotor relative frame. Consider first the distribution for Geometry 1. We see the following features: the over-shroud leakage flow (D); the casing and hub passage vortices (E and F); and an approximately radial rotor wake (G); The casing and hub passage vortices are centred at approximately 70% and 25% span, and have similar normalised peak loss values of 2.73 (casing) and 3.12 (hub), but with the hub loss core being considerably more extensive. This is consistent with the literature (see, for example, Sharma et al. [29] and Moss et al. [30]), which shows migration of higher loss (lower momentum) fluid towards the hub endwall (overturned by radial pressure gradient). The most dominant feature of the flow is the over-shroud leakage loss in the near-casing region above 90% span. This is associated with the shroud clearance flow, a region of low mass flow and low rotor-relative total pressure, which forms a shear layer with the core flow as it mixes out. The normalised peak value in this region

was 5.69, which is almost twice as large as the peak values in the hub and casing passage vortices.

We now consider the impact of NGV TE burn-back on the rotor exit loss coefficient distributions, with increasing burn-back we see the following:

1. Increase in the loss in the over-shroud leakage flow region. The mass-mean loss value above 88% increases by 13%, 15%, and 34% for geometry changes 1–2, 1–3 and 1–4 respectively.

2. Migration of the over-shroud leakage loss region deeper into the passage by approximately 0.32% of span for each successive cut-back. The flow is highly unturned in the region above 88% span with mass mean values of absolute whirl angle of −11, −11, −14, and −17 degrees for Geometry 1–4, respectively, compared to mass mean values below 88% span of −27, −30, −34, and −38 degrees. There is also very low mass flux in this region on account of low total pressure (partially separated region which is filling in). Taken together these make the changes in this region hard to meaningfully interpret.

3. Outward (in the directions of the endwalls) radial migration of both casing (marked E in Figure 6.7) and hub passage vortex (marked F) loss cores. The casing passage vortex centre moves from approximately 70% for Geometry 1 to 76% span for Geometry 4; the corresponding hub loss core moves from 31% to 23% span. This can also be seen in the rotor SS streamline patterns, which are shown in Figure 6.8: the limits of the hub passage vortices are marked in the figure. The migration appears to be due to vane exit mass flow redistribution; we consider this in a later section.

4. Decreasing intensity of the casing and hub loss cores. The normalised (by the NGV plane-averaged loss coefficient for Geometry 1) peak loss value of the casing passage vortex core decreases from 2.73 for Geometry 1, to 1.80 for Geometry 4, similarly the

normalised peak loss value of the hub loss core decreases from 3.12 to 2.48. This is interesting and striking, but we do not find a simple explanation for it.

5. A decrease in loss over most of the passage. The mass-mean loss value in the region below 88% span decreased by 11%, 25%, and 41% for geometry changes 1–2, 1–3 and 1–4 respectively. This is primarily due to the weakening of the casing and hub loss cores (E and F in Figure 6.7), and reduced profile loss related to reduced relative flow turning in the burn-back region (discussed later).

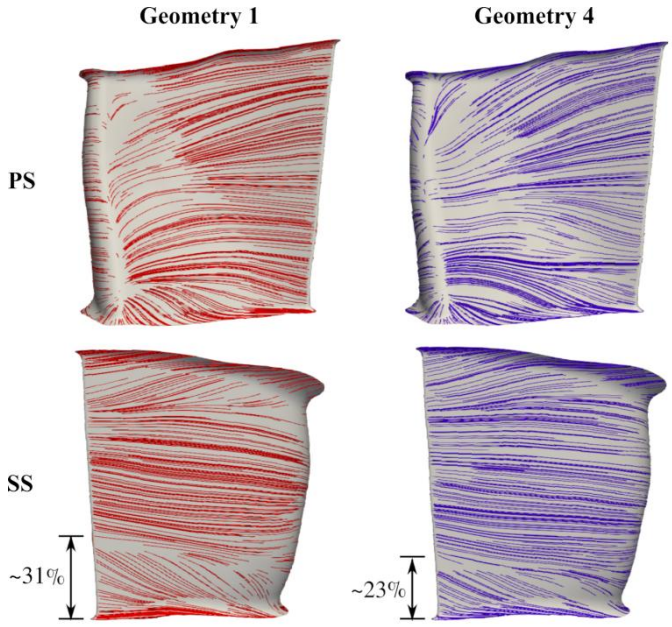


Figure 6.8: CFD-predicted rotor surface streamlines for Geometry 1 and Geometry 4 (geometry distorted for commercial reasons): (top) PS; and (bottom) SS.

6.6.2 – Distributions of axial vorticity

We now investigate the impact of NGV TE burn-back on the rotor secondary flow. We do this by investigating axial vorticity distributions at axial planes through the rotor passage, as shown in Figure 6.9 for Geometry 1 and Geometry 4. Axial vorticity in the rotor relative frame is defined by

$$\omega_x = \left(\frac{\partial W_z}{\partial y} - \frac{\partial W_y}{\partial z}\right) \tag{6.15}$$

where W_z and W_y are cartesian components of the relative velocity vector normal to the axial direction. The axial vorticity is normalised by the rotor angular speed. The axial location is normalised by the axial chord: $x/C_x = 0$ is the LE; $x/C_x = 1$ is the TE. Positive vorticity (red) indicates CCW rotation when viewed from downstream, and negative vorticity (blue) indicates CW rotation when viewed from downstream. We consider the time-averaged flow-field in the rotor relative frame.

First consider the vorticity distributions for Geometry 1 (left column of Figure 6.9). At a quarter axial chord upstream of the rotor LE ($x/C_x = -0.25$), the time-averaged vorticity field is relatively uniform over most of the passage. Thin bands of positive vorticity at the casing (marked A), and negative vorticity at the hub (marked B) appear due to shearing between endwall flow and main flow causing vorticity in the near wall flow. As the flow progresses through the rotor passage, this endwall fluid collects into two distinct vortices at the casing (marked A) and hub (marked B). These are the casing and hub passage vortices (originating from the PS leg of the horseshoe vortex; see, for example, Goldstein et al. [31]) and are of positive and negative sign respectively (sense of shear in the originating boundary layer fluid). Moving through the passage, these vortices strengthen, migrate towards the rotor SS then radially in the direction of the midspan. By $x/C_x = 0.50$, at the casing, the SS-leg of the horseshoe vortex (often called the counter vortex), marked C, can be see just below the casing passage vortex. Likewise, at the hub, by $x/C_x = 1.0$ the hub counter vortex (marked D) can be seen just above the passage vortex. Lastly, at the hub, by $x/C_x = 1.25$ the hub corner separation vortex (marked E) can be seen.

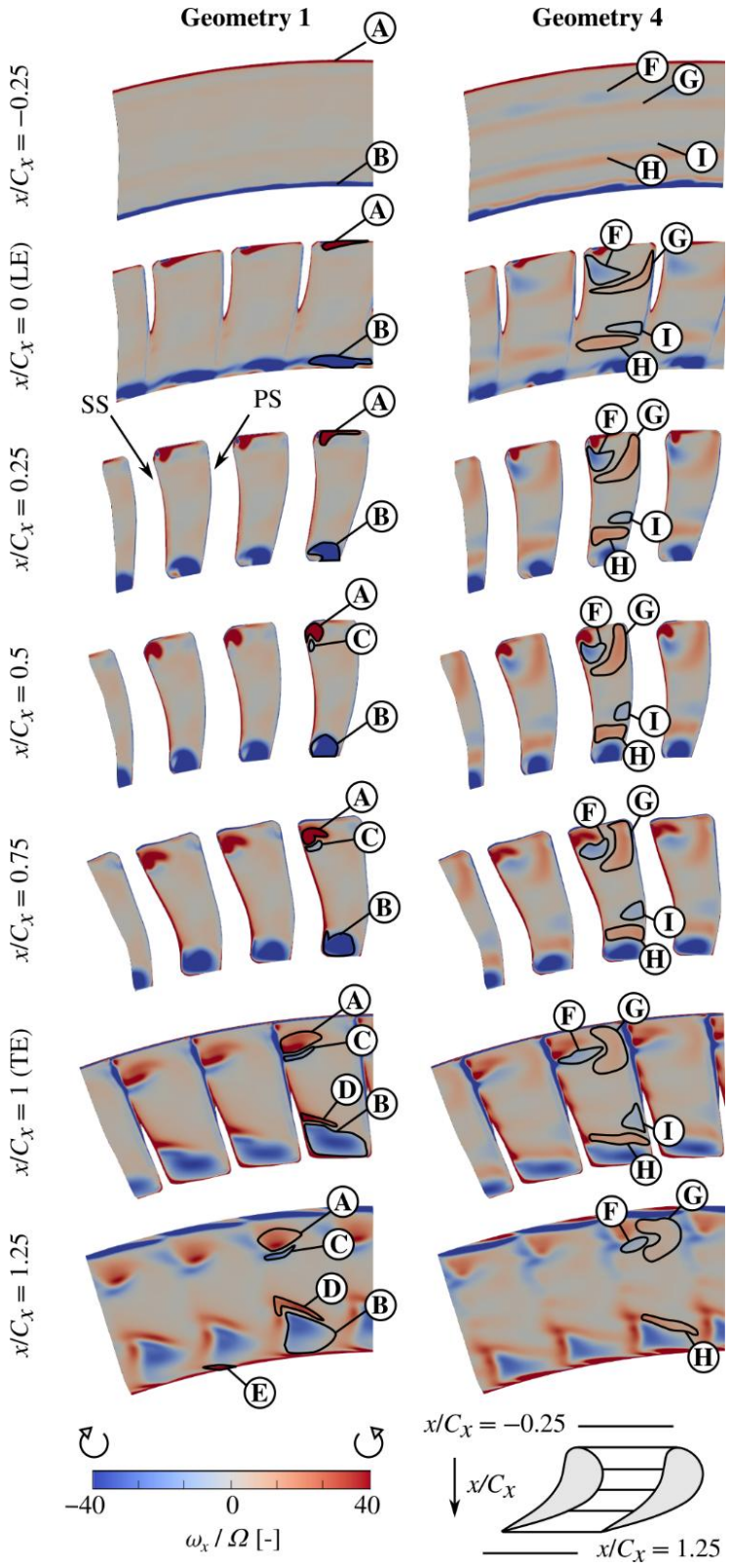


Figure 6.9: Time-averaged axial vorticity distributions at axial planes in the rotor passage (reminder that the rotor is undamaged in all cases) for Geometry 1 and Geometry 4 (upstream vane geometries). Data is viewed from downstream.

Now we compare the vorticity distributions for Geometry 4 (right column) to those for Geometry 1. Upstream of the LE ($x/C_x = -0.25$), the flow field is less uniform, with bands of negative (F) and positive (G) vorticity at 70% span associated with the vortex shed from the casing-most burn-back edge, and bands of positive (H) and negative (I) vorticity at the 30% span, associated with the vortex shed from hub-most burn-back edge. We also see these manifest as loss-cores in Figure 6.7. Tracking these features though the passage we see that:

1. G and I migrate towards the PS and cause greater streamline divergence on that surface (this is also clear in Figure 6.8) but are otherwise fairly non-interacting.

2. F and H appear to destructively interfere with the casing and hub passage vortices (A and B, respectively), leading to weakening of A and B in the outlet flow. This is strongly supported by the progression of images in Figure 6.7.

It is notable that the vortices shed from the burn-back edges (F and G, and H and I) always occur in counter-rotating pairs, just as the rotor native endwall vortices (A and B) do. This behaviour is expected because the vorticity field must remain divergence-free ($\nabla \cdot \omega = 0$), and circulation must be conserved. In other words, each generated vortex must be accompanied by an equal and opposite vortex to preserve vorticity continuity.

6.6.3 – Radial distributions of circumferentially averaged loss coefficient

We now consider radial distributions of circumferentially mass-flux-averaged total pressure loss coefficient.

Consider first radial distributions of circumferentially mass-flux-averaged loss coefficient $\zeta''(r, \theta)$ for Geometry 1–4 at NGV exit and rotor exit. These are shown in Figure 6.10. At the NGV exit (left column), with increasing burn-back we see:

1. Development and strengthening of two new loss cores at the edge of the burn-back region (marked B and C) associated with the formation of two counter-rotating vortices (see previous section). The peaks increase in value with increasing burn-back

and move radially outwards. Loss cores B and C increased in value by 58% and 65% between Geometry 2 and Geometry 4.

2. Strengthening of casing and hub loss cores (marked A and D) due to: newly formed vortices at the edges of the burn-back region; thickening of the SS BL with increasing burn-back (discussed and quantified in [15]) and entrainment into the two loss cores. The increase in peak value of loss between Geometry 1 and Geometry 4 was 64% and 146% for loss cores A and D, respectively. The increase in loss for the hub loss core (D) was larger than for the case loss core due to greater BL loss in this region. There is also mild inward radial migration of these loss cores: the hub loss core moved from 7% to 10% span; and casing loss core moved from 89% to 86% span. This is due to SS flow migration towards the low-pressure burn-back region.

3. A decrease in loss within the burn-back region (35–65% span). This is due to wake-region fluid being redistributed away from the midspan immediately downstream of the TE due to entrainment into the burn-back vortices. The effect is partially offset by an increase in BL loss (quantified in [15]) due to greater adverse pressure gradient late-SS (see NGV loading section later) that outweighs the reduced wetted surface in the burn-back region.

These trends are discussed in more detail in Raduev et al. [15]. Now consider the rotor exit distributions of $\zeta''(r,\theta)$ for Geometry 1–4. These are shown in the right column of Figure 6.10. Consider first the distribution for Geometry 1. For Geometry 1, the NGV exit loss radial distribution is relatively flat, and would not be expected to contribute significantly to radial non-uniformity at the rotor exit. In the near-casing region (above 90% span) there is a region of very high loss associated with the over-shroud leakage flow, where the mass flow and total pressure are low. The distinct peak at 71% span (marked E) is associated with the rotor blade passage vortex (see also Figure 6.7), and it sits in a broader region (between 65% and 85% span) of elevated background loss. Between 43% and 63% span (marked F) there is a relatively uniform region of loss. In this profile loss region, the loss is dominated by BL and TE loss.

There is a broad region of high loss between approximately 10% and 35% span, with two distinct peaks (marked G and H) at 17% and 30% span. These peaks in the radial profile appear to be associated with defined loss cores in the rotor relative frame (see Figure 6.7), with G being the counter vortex and H being the passage vortex. This is illustrated by considering the rotor-relative time-averaged axial vorticity distributions in Figure 6.9 (see contour for $x/C_x = 1.25$). Using the terminology of Goldstein et al. [31]), the CW (blue) vortex marked F is the passage vortex, and the CCW (red) vortex marked E is the counter vortex.

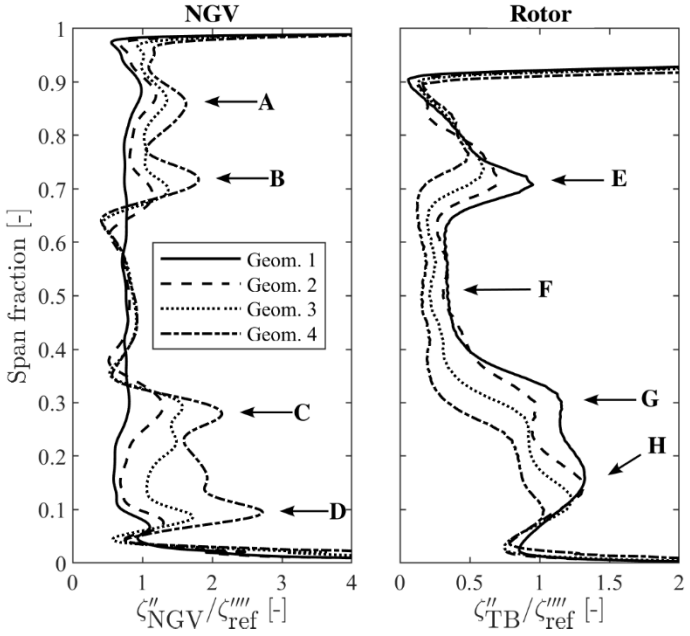


Figure 6.10: Radial distributions of circumferentially mass-flux-averaged normalised KE loss coefficient for Geometry 1–4.

With increasing burn-back we see the following changes in the rotor exit loss distributions:

1. Slight increase in the extent of the over-shroud leakage flow region. The location of the shearing layer between the over-shroud leakage flow and main flow moves from 90.4% to 89.4% between Geometry 1 and 4.

2. An increase in mass-mean loss in the over-shroud leakage flow region (above 88% span) by 34% between Geometry 1 and 4. We need to be cautious about the interpretation of this result because this is a low mass flow rate region.

3. Weakening of the case (marked E) and near hub loss cores (marked G and H). The magnitude of the peak loss value decreases between Geometry 1 and Geometry 4 by 48% at E, and by 22% at G.

4. Reduction of loss in the profile loss region (marked F; between 40 and 60% span) with a decrease in mass-mean loss value of 50% between Geometry 1 and Geometry 4. This is an apparently surprising result and does not seem to originate from the NGV loss distribution (see left hand side of Figure 6.10). A possible explanation may be the reduction in mid-span turning: we discuss this in a later section.

5. Migration of casing and hub loss cores in the direction of the endwalls. The location of the casing loss core peak (at E) moved from 71% to 77% span between Geometry 1 and 4, and the hub loss core peak (at H) moved from 17% to 10% span. This is attributed to higher rotor-relative total and static pressure at midspan, causing an outward spreading of streamlines as the flow progresses through the passage. This also has the effect of increasing the width of the profile loss region.

6.6.4 – Plane-averaged and mixed-out KE loss

We now consider the effect of NGV TE burn-back on the aerodynamic performance of the NGV and rotor. This is quantified using the plane mass-flux-averaged values of KE loss coefficients (ζ'''_{NGV} or ζ'''_{TB}), the mixed-out loss coefficients (ζ''''_{NGV} or ζ''''_{TB}), and the SKE coefficients ($\zeta^{\mathrm{SKE}}_{\mathrm{NGV}}$ or $\zeta^{\mathrm{SKE}}_{\mathrm{TB}}$). We recall that we defined ζ^{SKE} as the difference between the plane-averaged and mixed-out loss coefficients i.e. $\zeta^{\mathrm{SKE}} = \zeta'''' - \zeta'''$. The changes in these parameters between Geometry 1 and Geometry 1–4 are presented in Figure 6.11 for the NGV and rotor. All values for the NGV row are normalised by a reference value equal to the value of the NGV mixed-out loss coefficient for Geometry 1. Likewise, rotor row values are normalised by the corresponding mixed-out loss coefficient for rotor row for Geometry 1.

First consider the NGV. With increasing burn-back the NGV row mixed-out loss coefficient (ζ''''_{NGV}) increases from normalised value of unity (by definition) for Geometry 1 to

1.12, 1.30, and 1.57 for Geometry 2, 3, and 4 respectively: a steep and significant increase in NGV overall loss. This is caused by a significant increase in both loss and SKE at the evaluation plane. The plane mass-flux-averaged KE loss coefficient (ζ'''_{NGV}) increases from nominal value of 0.76 for Geometry 1 to 0.85, 0.95, and 1.06 for Geometry 2, 3, and 4: these increases are significant, but at a lower rate than the mixed-out loss. The mass-flux-averaged loss increases due to expanded base-pressure area with burn-back, strengthening of pre-existing secondary flow, and partial mixing (by the evaluation plane) of additional secondary vortices formed at the cut-back edges. Examining the SKE coefficient at the evaluation plane, we see it increasing from 0.24 for Geometry 1 to 0.27, 0.35, and 0.50 for Geometry 2, 3, and 4: that is, the SKE doubles between Geometry 1 and Geometry 4. This is consistent with the significant increase in secondary flow (see Figure 6.7 and analysis).

Now consider the rotor. With increasing burn-back the rotor mixed-out loss coefficient (ζ''''_{TB}) *decreases*, from a nominal normalised value of 1.00 for Geometry 1 to 0.92, 0.80, and 0.69 for Geometry 2, 3, and 4: a steep decrease with increasing burn-back. There is a corresponding decrease in the plane mass-flux-averaged KE loss coefficient (ζ'''_{TB}) from a nominal value of 0.68 for Geometry 1 to 0.64, 0.56, and 0.48 for Geometry 2, 3, and 4: i.e. decreasing at a proportionate rate to the mixed-out loss coefficient. The balancing term, the SKE coefficient ($\zeta_{\mathrm{TB}}^{\mathrm{SKE}}$) reducing from 0.32 for Geometry 1 to 0.28, 0.24, and 0.21 for Geometry 2, 3, and 4: also (of course) decreasing proportionally. In summary there is a significant reduction in both profile loss and secondary kinetic energy with increasing cutback. This is associated with changes in incidence and loading; effects we examine in detail in a later section.

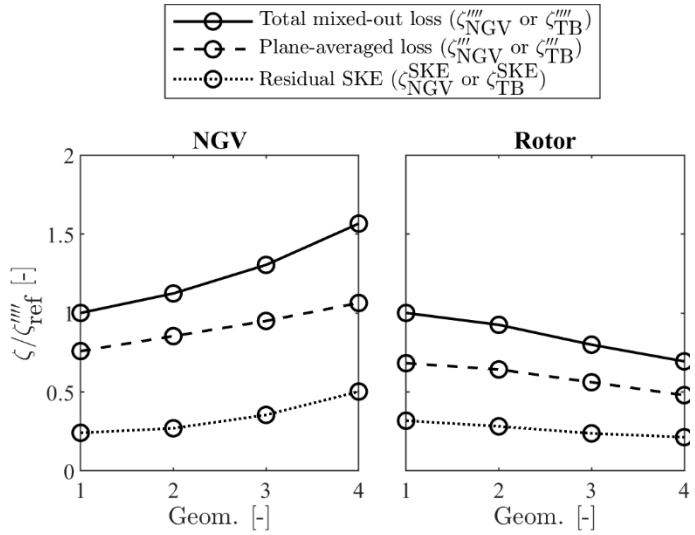


Figure 6.11: Coefficients for plane-averaged loss, mixed-out loss, and SKE for the NGV and rotor for Geometry 1–4.

6.6.5 – Radial distributions of circumferentially averaged pressures and angles

We now consider the radial distributions of circumferentially mass-flux-averaged static pressure, rotor-relative Mach number, rotor-relative total pressure, and absolute and relative whirl angle at the rotor inlet and exit. These are shown in Figure 6.12. Whirl angles are shown with respect to reference values, which we take as the mean values for Geometry 1. We use the symbol β^* for all reference values. Also note that the simpler mass-flux averaging was applied to the whirl angles, rather than the formally correct momentum-flux averaging. Nevertheless, as the same averaging method was applied consistently, the relative changes are still valid. Taking each variable in turn.

1. *Static pressure*. At the rotor inlet plane (plane 2 in Figure 6.4) the pressure profiles are almost linear, decreasing from casing to hub. For Geometry 1, the mean value of normalised static pressure is $p_2/p_{01} = 0.513$. With increasing burn-back, there is a monotonic increase in static pressure, to normalised values 0.532, 0.563, and 0.611 for Geometry 2, 3 and 4. The mean value of rotor exit static pressure is fixed in the simulation ($p_3/p_{01} = 0.340$) and there are only very small changes in the rotor exit static pressure profile with increasing burn-back. Increasing intra-stage static is primarily a response to the effective area of the vane opening up with burn-back,

which increases the vane flow capacity for a given vane pressure ratio. To maintain the same mass flow in the stator and rotor, the intra-stage static pressure increases, lowering the operating point on the capacity curve. While the vane capacity (at fixed pressure ratio) increases by 16.5% between Geometry 1 and 4, the stage capacity increases by only 12.9%. The difference is explained by the increase in intra-stage static pressure.

2. *Absolute total pressure*. For Geometry 1, the rotor inlet *absolute* total pressure is relatively uniform in the profile-loss region between 10% and 80% span. At 5% and 85% span, regions of low total pressure are associated with the hub and casing passage vortices. Lower total pressure in the very-near-hub (0–2% span) and very-near-casing (98–100% span) regions is due to accumulated endwall boundary layer fluid. With burn-back, three new regions of low total pressure develop at approximately 10%, 30% and 70% span. The regions at 30% and 70% span are associated with vortices shed at the edges of the burn-back region (see Figure 6.7 and associated discussion). The region at 10% span is associated with the vane near-hub passage vortex which—with increasing burn-back—both strengthens and migrates radially towards midspan (see analysis associated with Figure 6.10). With burn-back, the total pressure in the burn-back region increases. This appears to be due to low momentum wake fluid being rapidly redistributed (with axial distance downstream of the TE) away from the midspan, as it is entrained into the burn-back vortices. The rotor *exit* absolute total pressure for Geometry 1 is relatively uniform in the profile region between 40% and 70% span. Total pressure variations (mainly deficit) in the ranges 0–40% span and 70–90% span are associated with the migration of vane-loss through the rotor, and the formation of hub and casing passage vortices within the rotor passage. The very low total pressure region above 90% is associated with the over-shroud leakage flow; this is also an area of low mass flow rate. With increasing burn-back, there is an increase in total pressure over most of the span, with $p_{03,\mathrm{abs}}/p_{01}$ increasing by on average

4.7% (of its own value) between Geometry 1 and Geometry 4. This is due to lower work extraction (discussed later), leading to less total pressure to shaft power conversion in the absolute frame. At 30% span there is a pinch in the profiles that makes the effect apparently less pronounced: this appears to be a local effect associated with radial migration of the hub loss core (see Figure 6.7 and associated analysis).

3. *Rotor relative total pressure*. For Geometry 1, the rotor relative *inlet* total pressure has a linear trend of shallow gradient decreasing from casing to hub. There is a significant increase in rotor relative inlet total pressure with NGV burn-back, arising from an increase in intra-stage static pressure, partially offset by a decrease in rotor relative Mach number. This decrease is smaller in the cutback region due to a decrease in whirl angle (which increases the axial component of velocity). The rotor relative *exit* total pressure profiles follow the inlet profiles (relatively similar loss for all four geometries; see Figure 6.10 and associated analysis) but with two differences: in the region above 90% span there is a very significant total pressure deficit associated with the over-shroud leakage flow; in the ranges 65–85% span and 10–35% span there are noticeable minima associated with the casing and hub passage vortices respectively. This has been discussed in the context of Figure 6.10.

4. *Rotor relative Mach number*. The rotor relative Mach number trends at rotor inlet for Geometry 1 is approximately linear, increasing from casing to hub. The mean value is 0.45. With increasing NGV burn-back, there is a decrease in rotor relative Mach number. The decrease is less pronounced in the burn-back region, where the increase in rotor relative total pressure offsets the increasing static pressure. Mean values of inlet rotor relative Mach number were 0.42, 0.38 and 0.32 for Geometry 2, 3 and 4. The rotor relative Mach number at rotor exit is dominated by the rotor relative total pressure distribution at exit, which has been discussed. The rotor exit static pressure

distributions are similar for all geometries, so have little influence on the change with NGV burn-back.

5. *Absolute whirl angles*. Consider next the absolute whirl angle distributions. At rotor inlet the Geometry 1 distribution is approximately constant over most of the span, with a mean value of 76.3 degrees. With increasing burn-back there is negative incidence (reduced whirl angle) within the burn-back region, and—milder—positive incidence outside the burn-back region. The effect within the burn-back region is attributed to reduced metal angle and reduced lift of the cut-back airfoil profile. The increased turning outside the burn-back region is due to the reduced SS surface static pressure at all span locations (shown in the vane loading section later), creating a larger cross-passage pressure gradient and thus, enhancing turning. On average, the changes in inlet whirl angle with respect to Geometry 1 are −0.64, −1.92 and −4.0 degrees for Geometry 2–4 respectively: a mild reduction in mean inlet whirl angle with increasing burn-back. At the rotor exit, the Geometry 1 distribution is dominated by three effects: significant overturning above 90% in the region of over-shroud leakage flow; underturning below 20% span due to the hub corner separation vortex and endwall boundary layer flows; and local peaks in whirl angle at approximately 25% and 75% span associated with the rotor passage vortices. With increasing burn-back there is an increase in the magnitude of the exit whirl angle (note β^* is a negative value). The average changes (corresponding to increases in the magnitude) in the exit whirl angles with respect to Geometry 1 were −2.60, −6.39 and −10.18 degrees for Geometry 2–4 respectively. Radial distributions of absolute *turning angles* are plotted in Figure 6.13. Values are given with respect to a reference absolute turning angle, $\Delta\beta^*$, which is taken as the mass mean absolute turning angle for Geometry 1. Over most of the span, we see a mild increase in the magnitude (note $\Delta\beta^*$ is a negative value) of the absolute turning angle: the increases in the magnitude of the average

absolute turning angles with respect to Geometry 1 were 2.0, 4.5, and 6.2 degrees for Geometry 2–4, respectively.

6. *Rotor relative whirl angles*. For Geometry 1 the inlet rotor relative whirl angle is relatively uniform, with a mean value of 58.4 degrees. With increasing NGV burn-back, within the burn-back region, we see extreme negative incidence: in the 35–65% span region, the mean rotor relative whirl angle changes by −25 degrees between Geometry 1 and Geometry 4. At the rotor exit the rotor relative whirl angle follows the PS metal angle relatively closely, with some disturbances due to secondary flow. The only change with increasing NGV burn-back is a slight redistribution of whirl angle in the regions influenced by secondary flow. Radial distributions of *rotor relative turning angles* are plotted in Figure 6.13. Over most of the span, we see a significant decrease in the magnitude (note $\Delta\beta^*$ is a negative value) of the rotor relative turning angles: the decreases in the magnitude of the average rotor relative turning angles with respect to Geometry 1 were 2.3, 6.9, and 15.9 degrees for Geometry 2–4, respectively.

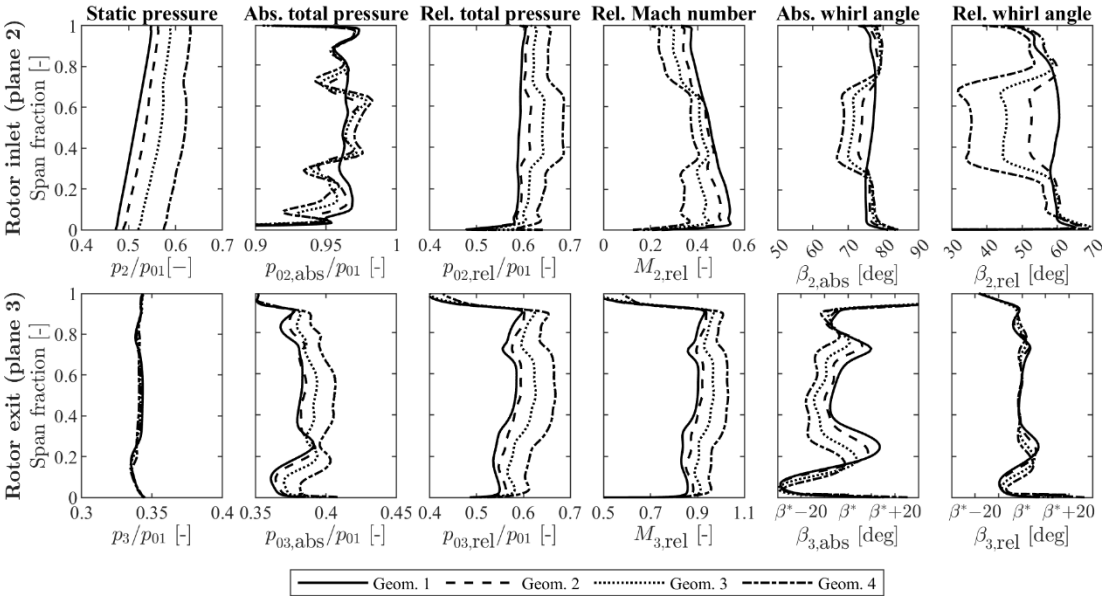


Figure 6.12: Radial distributions of circumferentially mass-flux-averaged static pressure, rotor-relative Mach number, rotor-relative total pressure, and absolute and rotor-relative whirl angles for Geometry 1–4 at the rotor inlet and exit.

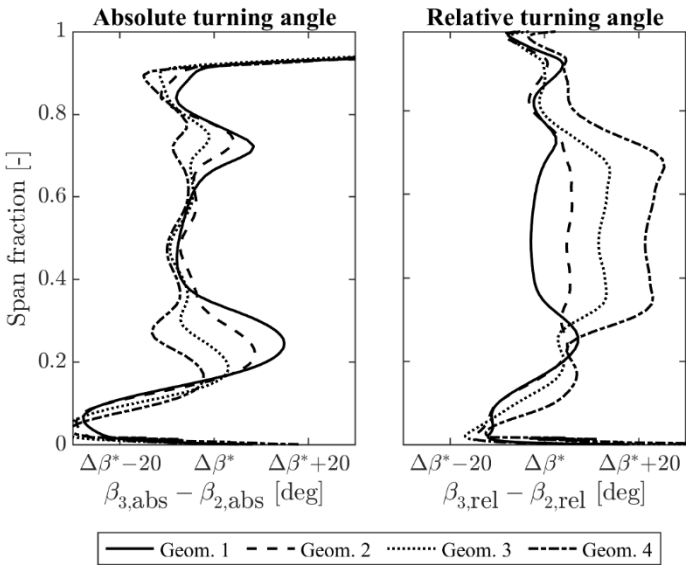


Figure 6.13: Radial distributions of circumferentially mass-flux-averaged absolute and rotor-relative rotor turning angles for Geometry 1–4.

6.6.6 – Radial mass flow distributions

We now consider radial distributions of circumferentially-summed mass flow per unit span at the NGV exit and stage exit for Geometry 1–4. These are shown in Figure 6.14. Mass flow (based on the local density, axial velocity, and cell area) per unit span is normalised by a reference value equal to the radial-mean mass flow per unit span for Geometry 1, evaluated at the NGV exit. At the NGV exit (left column), we see significantly increased mass flow within the burn-back region due to the effective area of the vane opening up with increasing burn-back. Between 35% and 65% span we see mean normalised mass flow rate increases of 23%, 41% and 60% for changes 1–2, 1–3, and 1–4, respectively. This is despite the mitigating effect of the increase in intra-stage static pressure (we analyse this effect in a moment). Outside the burn-back region, we see a decrease in mass flow rate caused by an increase in intra-stage static pressure (no change in geometric area). Taking the average across the sum of the 0–25% span and 75–100% span regions we see decreases in normalised mass flow rate of 10%, 17% and 21% for changes 1–2, 1–3, and 1–4, respectively. Across the entire passage the mean changes in mass flow rate were 3%, 8% and 15% for changes 1–2, 1–3, and 1–4, respectively. We analyse this in the context of the vane and rotor capacity characteristics in a moment.

Consider now the stage exit (right column) normalised mass flow rate distributions. There is a monotonic increase in normalised mass flow rate with increasing burn-back over almost the entire passage (consistent with the vane mass flow rates). We see later that this is associated with an increase in rotor relative total pressure and Mach number at outlet. We see a more pronounced version of the same effect below 15% span. In this region the previous effect is enhanced by a decrease in rotor relative (and absolute) whirl angles at rotor exit, caused by a decrease in secondary flow intensity in this region (flattening of the whirl profile with increasing burn-back).

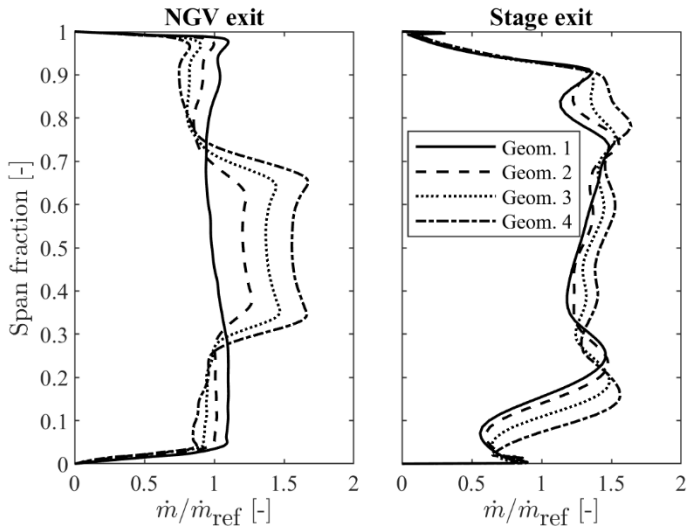


Figure 6.14: Radial distributions of circumferentially-summed mass flow per unit span for Geometry 1–4.

6.6.7 – Capacity and mass flow analysis

To understand the change with NGV burn-back in stage mass flow rate and capacity, it is instructive to consider the individual mass flow rate and capacity characteristics (with row pressure ratio) for the vane and rotor for each burn-back condition. This is because the change in stage capacity and mass flow is caused by both a change in underlying characteristic, and also an operating point change (caused by change in intra-stage pressure).

CFD-predicted mass flow and capacity characteristics for both vane and rotor are presented in Figure 6.15 for each of Geometry 1 to 4. Vane and rotor simulations were separate single-row simulations. This is necessary to allow the characteristics (variation with row

pressure ratio) to be determined. A necessary compromise—not significant for our present purpose, as we will see presently—is that the radial variation of static pressures at the vane outlet and rotor inlet cannot be exactly matched to the pressure distribution that develops at the intra-stage plane at the stage operating point. For the vane-row simulations, boundary conditions of constant inlet total pressure, and a downstream radial equilibrium condition for (five) static pressures (see [16] for details) were set. The radial equilibrium condition was set 1.25 axial chords downstream of the vane, but the mean vane exit static pressure (to define row pressure ratio) was evaluated at the intra-stage plane (plane 2). Simulations were run over a range of pressure ratios for Geometry 1 to 4. Rotor-row simulations were run by imposing constant total pressure at the intra-stage plane in the *non-rotating frame*, with a downstream radial equilibrium condition for (six) static pressures. Simulations were run for four inlet whirl angle distributions corresponding to Geometry 1 to 4. These boundary conditions have the consequence of significantly modifying the rotor-relative total pressure (as seen in Figure 6.12) in a manner that closely replicates the stage simulations. When computing mass flows, which are proportional to absolute pressure, both vane-row and rotor-row simulations run in this manner closely match the stage simulations: this is why the necessary compromise discussed previously was not significant in our study, and it is because there is relatively little change in intra-stage vane-relative total pressure at vane outlet between the Geometry 1 and 4 (including the small change in intra-stage pressure and therefore operating point of the rows).

Consider first the vane capacity and mass flow characteristics. In Figure 6.15 we present characteristics normalised by values for Geometry 1 at the nominal vane-row pressure ratio ($p_2/p_{01} = 0.513$). The capacity characteristics are well-behaved, of typical form for modern NGVs (see Kirollos et al. [14], Povey et al. [32], and Burdett et al. [33]), and with an approximately constant increase in capacity between each geometry across entire the pressure ratio range studied. At the nominal operating point, there are increases in capacity of 2.65%, 7.83% and 16.57% when moving from Geometry 1 to Geometry 2, 3 and 4, respectively. This is due primarily to an increase in the effective area of the controlling region of the vane (see

analysis in Raduev et al. [16]). In the stage simulations, there is also a change of operating point from $p_2/p_{01} = 0.513$ for Geometry 1, to $p_2/p_{01} = 0.523, 0.562, \text{and } 0.614$ for Geometry 2 to 4 respectively. This has the effect of reducing the capacity at the settled stage operating points for each design, reducing the increases in overall capacity to 2.50%, 7.02%, and 14.14% for changes 1–2, 1–3 and 1–4 respectively. For the vane, the characteristics of mass flow take identical form (the inlet total pressure is constant).

Now consider the rotor capacity and mass flow characteristics. In Figure 6.15 we present characteristics normalised by values for Geometry 1 (i.e. stage predictions with NGV exit whirl distribution inherited from the Geometry 1 vane) at the nominal *stage* pressure ratio, $p_2/p_{01} = 0.513$, for which there is a corresponding *reference rotor-row pressure ratio*, $p_3/p_{02,\text{rel}} = \text{PR}^*$. At the nominal operating point, there are increases in mass flow rate of 2.33%, 6.37%, and 12.74% for geometry changes 1–2, 1–3 and 1–4 respectively. In the stage simulations, there is also a change in the operating point (due to rotor relative inlet total pressure changes): the operating point changes between Geometry 1 and Geometry 2, 3 and 4, were −0.011, −0.032, and −0.065 respectively. This has the effect of—very slightly—increasing the mass flow rates through the rotor at the settled stage operating points for each design (to 2.34%, 6.44%, and 12.94%, for changes 1–2, 1–3 and 1–4 respectively). So far as the rotor capacity characteristics are concerned, at the settled stage operating points, the rotor capacity increases by 0.57%, 1.27%, and 1.95% for geometry changes 1–2, 1–3 and 1–4 respectively. This small change does not seem to be sensitive to the averaging method. We can compute capacity using two different methods: the integral of $\dot{m}\sqrt{T_{01}}/p_{01}$ for each cell in the flow field, i.e. non-linear weighting (see Burdett et al. [24] and Cumpsty and Horlock [34]); or computing $\dot{m}\sqrt{T_{01}}/p_{01}$ based on mass averaged values of T_{01} and p_{01} for the entire flow field, i.e. linear weighting. Doing so results in values that are different by only 0.03%. We conclude that the small capacity change is, therefore, more likely due to a change in effective blockage (changes in boundary layer behaviour, or secondary flow behaviour).

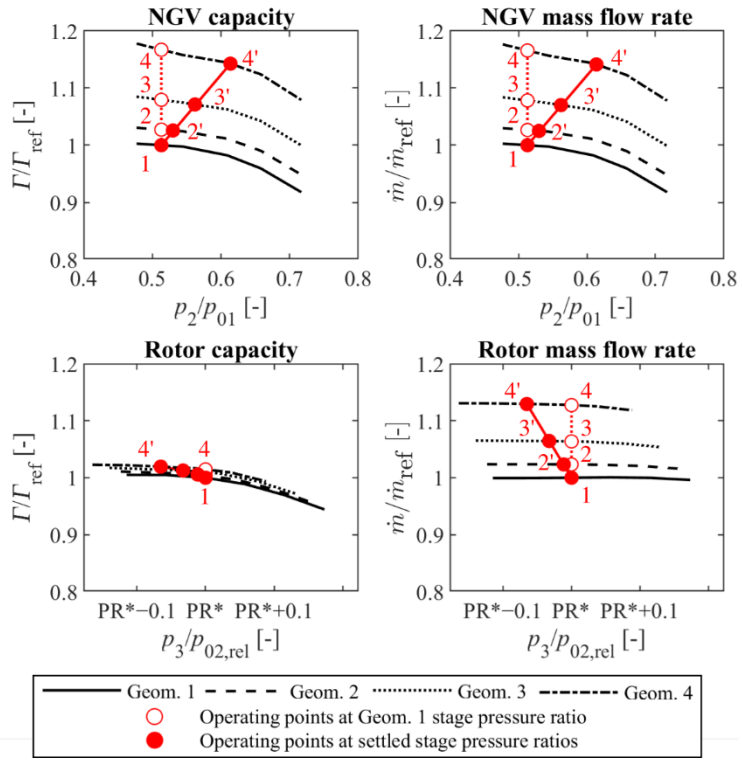


Figure 6.15: Analysis of the capacity and mass flow rate characteristics with row pressure ratio for NGV and rotor, for Geometry 1–4.

6.6.8 – Vane and blade loading isentropic Mach number distributions

We now consider the impact of NGV TE burn-back on the NGV and rotor isentropic Mach number distributions. These are shown in Figure 6.16 at 10%, 50%, and 90% span for all four geometries. Local isentropic Mach numbers are calculated based on the inlet total pressure (or relative total pressure) at the corresponding span location. All values for the NGV surface are normalised by the peak surface Mach number at 50% span for Geometry 1. Likewise, values for the rotor are normalised by the peak rotor surface Mach number at 50% span for Geometry 1. For the NGV we present Mach number as a function of axial distance normalised by the axial chord for Geometry 1. For the rotor we present Mach number as a function of streamwise surface distance from the LE, s, normalised by PS or SS total surface lengths for PS and SS, respectively (L_{PS} and L_{SS}).

Consider first the NGV distributions For Geometry 1. Peak suction is between 60% and 80% axial chord, followed by a mild shock on the late SS, where the flow is diffusing in the approach to the TE. The Mach number and shock intensity increase towards the hub, in line

with the radial pressure gradient. The vane has relatively neutral loading with well-controlled acceleration on the PS.

With increasing burn-back we see the following changes in the NGV Mach number distribution:

1. A significant increase in mid-chord SS Mach number at all span locations, with the location of peak suction moving forward on the vane.
2. A significant decrease in late SS Mach number at all span locations. In combination with an increase in the peak suction Mach number this leads to greater adverse pressure gradient on the aft vane section with associated BL thickening (see [15] for discussion).
3. Very little impact on early-to-mid PS loading, with a mild increase in late PS Mach number. In the cut-back region the strong acceleration on the aft PS moves forward (in absolute terms) due to the change in location of the TE.

Now consider the blade isentropic Mach number distributions. For Geometry 1, the loading distribution is typical of a modern forward-loaded blade (see Luymes et al. [35] for study on influence of forward loading on wake dynamics). At all span heights there is a very rapid acceleration on the LE of the rotor, with controlled acceleration beyond, and with peak suction occurring between 60% and 80% surface length. The PS Mach number is low across most of the surface, with a sudden acceleration at the TE. The Mach number distributions are relatively similar at all span locations. With increasing burn-back we see the following changes in the rotor Mach number distribution:

1. A decrease in forward loading (marked A Figure 6.16) and an increase in aft loading (marked B). This occurs at all span locations, and seems to be associated with a decrease (across most of the span) in the rotor relative inlet while angle (see Figure 6.12), whilst the rotor relative exit whirl angle is maintained. There is also a decrease

in rotor relative inlet Mach number and an increase in rotor relative exit Mach number (see Figure 6.12).

2. A forward movement in the stagnation point on the early PS (marked C Figure 6.16), associated with the change in midspan velocity triangles (shown schematically in Figure 6.17, and discussed later in this section) in the direction of negative incidence. This has the secondary effect of causing over-acceleration on the early PS, leading to a local peak in pressure (marked D) followed by mid-PS diffusion.

3. A decrease in PS Mach number outside the burn-back region (significant at 10% span; small at 90% span), and a small increase inside the burn-back region (50% span). Outside the burn-back region, this seems to be driven by an increase in rotor inlet static pressure that outweighs the increase in rotor inlet relative total pressure (leading to decreased Mach number). Inside the burn-back region, the situation is reversed, and the increase in rotor inlet relative total pressure outweighs the increase in rotor inlet static pressure (leading to increased Mach number).

Evaluating the lift (L) as the rotor torque over the mean radius of the rotor, and normalising by a reference value for Geometry 1, we get values of L/L_{ref} of 1.000, 1.020, 1.053 and 1.098 for Geometry 1 to 4, respectively. That is, an increase of 9.8% in the rotor lift between Geometry 1 and Geometry 4. The corresponding changes in mass flow rates (normalised by a reference value for Geometry 1) were 1.000, 1.023, 1.064, and 1.129. Taking the quotient $(L/L_{\mathrm{ref}})/(\dot{m}/\dot{m}_{\mathrm{ref}})$ we get values 1.000, 0.996, 0.989 and 0.972 for Geometry 1 to 4. Differences from unity are explained by changes in rotor relative inlet and outlet Mach number, and rotor relative inlet and outlet flow angle, both of which change significantly with burn-back.

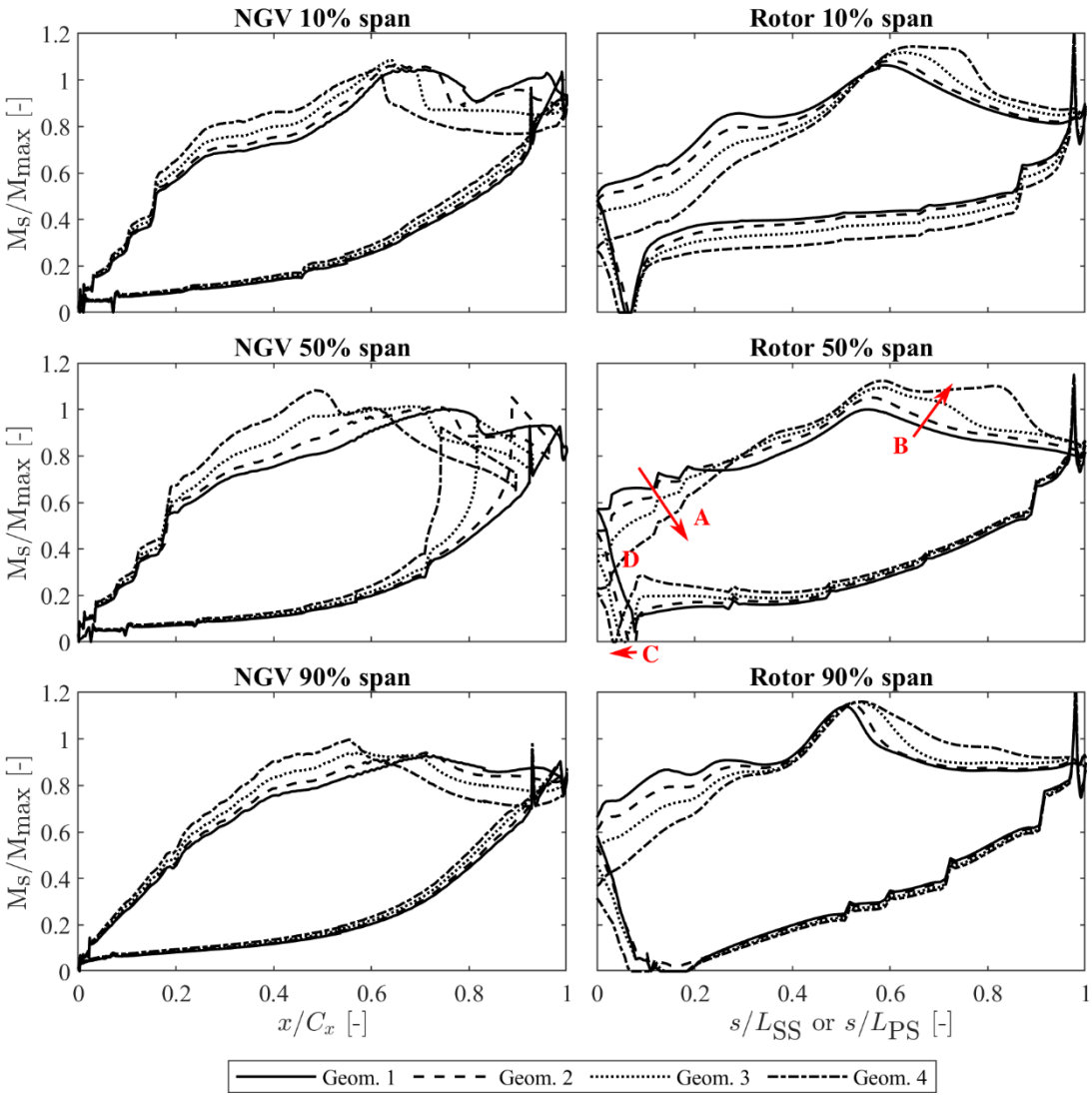


Figure 6.16: NGV and rotor loading distributions at 10%, 50% and 90% span for Geometry 1–4.

6.6.9 – Velocity triangle analysis

We now consider the midspan velocity triangles in more detail. A schematic of the velocity triangles upstream and downstream of the rotor at different span locations, for Geometry 1 (solid lines) and Geometry 4 (dotted lines) is shown in Figure 6.17. These velocity triangles are based on circumferentially mass-flux-averaged axial velocities and whirl angles at each span location. With burn-back we see the following at the midspan:

1. A decrease in rotor incidence angle (lower rotor-relative whirl angle), which is responsible for a decrease in forward loading, and a region of diffusion on the early PS (due to early acceleration).

2. Relatively little change in rotor-relative exit whirl angle (flow still fully turned by the rotor) but an increase in absolute whirl angle caused by an increase in rotor-relative outlet Mach number and rotor-relative velocity. This is caused by an increase in rotor-relative total pressure (exit static pressure is approximately constant).

3. A significant decrease in *rotor-relative* flow turning angle between Geometry 1 and Geometry 2–4 of 7.8, 14.4, and 24.3 degrees respectively. This is accompanied by a mild increase in *absolute* flow turning angle between Geometry 1 and Geometry 2–4 of 0.4, 1.5, and 2.1 degrees respectively. In combination, this tells us that whilst there are extreme incidence changes in rotor-relative frame, the change in stage specific work is minimally affected. This apparent contradiction is resolved by attendant changes in intra-stage pressure and Mach number.

Outside the burn-back region, at the rotor inlet, there is a mild increase in absolute whirl angle but no significant change in rotor incidence angle (rotor-relative inlet whirl angle) due to a reduction in Mach number (both absolute and rotor-relative). There is also little change in rotor-relative exit whirl angle, and relatively little change in rotor-relative flow turning. At 10% span, for example, the rotor-relative turning angle changes between Geometry 1 and Geometry 2, 3 and 4 were −0.1, −3.9, and −11.8 degrees respectively: i.e. decreasing rotor-relative turning. The corresponding changes in *absolute* turning angle from Geometry 1 were −0.2, −5.9, and −11.3 degrees for Geometry 2, 3 and 4 respectively, very similar to the changes in rotor-relative turning. This implies a drop in local specific work. Comparing changes with burn-back outside the burn-back region to within the burn-back region, we see that the change in rotor relative turning is smaller, but the change in absolute turning is larger.

Taking mass-averaged values across the passage, the mass-mean rotor-relative turning angle magnitude decreased between Geometry 1 and Geometry 2, 3 and 4 by 2.3, 6.9, and 15.9 degrees respectively: a significant reduction in rotor-relative turning with increasing burn-back. The corresponding changes in mass-mean *absolute* turning angle were increases between Geometry 1 and Geometry 2–4 of 2.0, 4.5, and 6.2 degrees respectively.

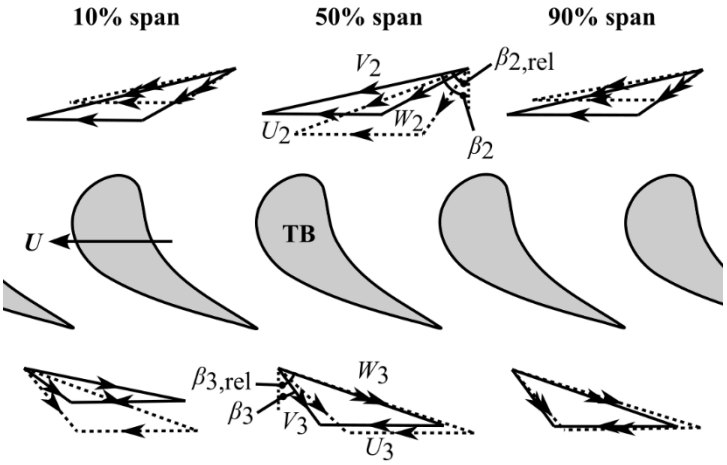


Figure 6.17: Velocity triangles at rotor inlet and exit for Geometry 1 (solid lines) and Geometry 4 (dotted lines).

6.6.10 – Overall stage performance

In this section, we discuss changes in overall stage performance parameters. The changes in stage mass flow rate, reaction, specific work, and efficiency (with increasing burn-back) are shown in Figure 6.18.

First consider the stage mass flow rate change with NGV burn-back, which is shown in the top left plot of Figure 6.18. With increasing burn-back the mass flow through the stage increases monotonically, by 2.3%, 6.4% and 12.9% for changes 1–2, 1–3, and 1–4, respectively. So far as the vane is concerned, (see analysis associated with Figure 6.15) we can attribute approximately +117% of these changes to an uplift in the underlying vane capacity characteristic (opening up of the controlling region), and approximately −17% to a decrease in vane pressure ratio (caused by an increase in intra-stage static pressure) which lowers the operating point on the capacity curve. This is illustrated in Figure 6.15. So far as the rotor is concerned, we can attribute approximately +98% of this change to a change in the underlying rotor characteristic (with changes in whirl distribution), and approximately +2% to an increase in rotor pressure ratio (an increase in rotor-relative inlet total pressure) which raises the operating point on the rotor capacity characteristic. It is interesting that the mechanisms in the stator and rotor are entirely different.

Next consider the impact of burn-back on stage reaction (Equation 6.12), which is shown in the top right plot of Figure 6.18. The Geometry 1 (design) reaction below 50% i.e. a stage with higher acceleration in stator than rotor, and high rotor turning. With increasing burn-back there is monotonic increase in stage reaction. The changes between Geometry 1 and Geometry 2, 3 and 4 were +3.3%, +8.5% and +16.2% respectively. The increase in intra-stage static pressure lowers the acceleration in the vane, and the increase in rotor-relative inlet total pressure increases the acceleration in the rotor. The effect is significant over the range of geometries tested.

Now consider the impact of burn-back on stage specific work (Equation 6.13), which is shown in the bottom left plot of Figure 6.18. With increasing burn-back there is a small monotonic decrease in stage specific work. The magnitudes were −0.4%, −1.6%, and −3.8% for changes 1–2, 1–3, and 1–4, respectively. In our simulations, rotor angular velocity is fixed so changes in specific work are proportional to changes in the tangential velocity components. This is driven by both the angle change and the rotor inlet and outlet absolute velocity (approximately proportional to Mach number). We have already noted that the mass-mean *absolute* turning angles increase with burn-back (changes between Geometry 1 and Geometry 2–4 of +2.0, +4.5, and +6.2 degrees respectively), but there is a contrary change of greater magnitude associated with the absolute flow velocities. Taken together this leads to the decrease in stage specific work.

Stage specific work changes can also be described in terms of changes in mass flow rate and torque, we see that there is a mass flow increase with burn-back (2.3%, 6.4% and 12.9% for changes 1–2, 1–3, and 1–4, respectively) that exceeds the change in rotor torque (2.0%, 5.3% and 9.8% for changes 1–2, 1–3, and 1–4, respectively). Together, these sum to the observed changes in stage specific work.

Finally, consider the impact on stage efficiency ($\Delta\eta_{\mathrm{stage}}$, Equation 6.14), which is shown in the bottom right plot of Figure 6.18. The change in stage efficiency with increasing burn-

back is—surprisingly—both small and positive: $\Delta\eta_{\text{stage}}$ took values of +0.16%, +0.42% and +0.33% for geometry changes 1–2, 1–3 and 1–4, respectively (summarized in Table 6.3, and plotted in Figure 6.18). These changes are too small to be considered significant, and the turning point in the trend is assumed to be a numerical artefact, rather than a physical result. The small changes are loosely explained by the corresponding *decreases* in NGV row efficiency, $\eta'''_{\text{NGV}} = 1 - \zeta'''_{\text{NGV}}$ (−0.61%, −1.22% and −1.94%, respectively), and the corresponding *increases* in rotor row efficiency, $\eta'''_{\text{TB}} = 1 - \zeta'''_{\text{TB}}$ (+0.52%, +1.59% and +2.67%, respectively). These changes are larger in magnitude but opposite in sign from each other. These values are also presented in Table 6.3. The NGV row efficiency decreases largely on account of enhanced secondary flow initiated at the cutback edges. The rotor row efficiency increases on account of weakened secondary flow in the passage and reduced profile loss due to reduced mid-span flow turning. We see that the change in product of NGV-row and rotor-row efficiencies ($\Delta(\eta'''_{\text{NGV}} \times \eta'''_{\text{TB}})$; last column of Table 6.3) is approximately in line with the change in stage efficiency ($\Delta\eta_{\text{stage}}$; second column of Table 6.3). Exact agreement is not expected because rotor-row efficiency is calculated in the rotor-relative frame and does not explicitly consider work (unlike the stage efficiency term).

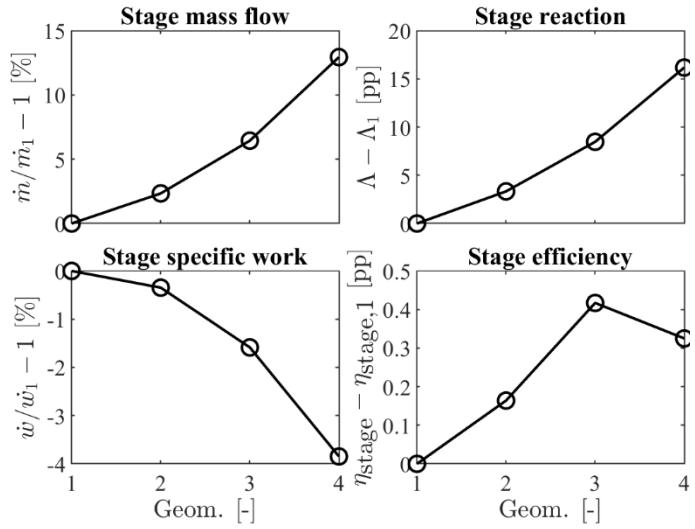


Figure 6.18: Changes in the values of stage performance parameters from their values for Geometry 1.

Table 6.3: Changes (from Geometry 1) in stage efficiency, NGV and rotor efficiencies, and the change in the product of NGV and rotor row efficiencies.

Geom.	$\Delta\eta_{\text{stage}}$ [pp]	$\Delta\eta'''_{\text{NGV}}$ [pp]	$\Delta\eta'''_{\text{TB}}$ [pp]	$\Delta(\eta'''_{\text{NGV}} \times \eta'''_{\text{TB}})$ [pp]
$1 \rightarrow 2$	+0.16	−0.61	+0.52	−0.06
$1 \rightarrow 3$	+0.42	−1.22	+1.59	+0.38
$1 \rightarrow 4$	+0.33	−1.94	+2.67	+0.72

6.7 – Conclusions

In this paper, we consider the impact of NGV TE burn-back on HP turbine stage performance, using full-stage URANS results for a modern cooled HP stage. The numerical method was partially validated using high-fidelity experimental data taken from an annular cascade of real-engine parts and operating at engine-matched operating conditions. The burn-back shapes studied were a parametric set based on statistical analysis of in-service-deteriorated vanes: trapezoidal forms, with the damage front centred at midspan. The normalised (by product of span height and tangential chord) damage areas of the four studied designs were 0%, 3.9%, 8.4%, and 14.2%. These are referred to as Geometry 1 to 4.

We find the following:

1. *Changes in NGV loss*. With burn-back, a pair of counter-rotating vortices are shed at the vane burn-back edges. At vane exit, this led to increased loss and significant distortion of the vane wake. Expanded area in the base-pressure region also contributed to increased loss. The result was changes in the values of mass-mean KE loss coefficient relative to Geometry 1 of +12.5%, +29.9%, and +52.3%, respectively, for Geometry 2–4.

2. *Changes in rotor loss*. At rotor exit, a trend of decreasing loss with increased burn-back was observed, opposite to the trend for the NGV alone. The changes in mass-mean KE loss coefficient relative to Geometry 1 were −8.3%, −20.5%, and −31.9%, respectively, for Geometry 2–4. This was attributed to weakening of the rotor near-

casing and near-hub passage vortices, and to the decrease in rotor profile loss across most of the passage.

3. *Changes in vane exit whirl angle distribution*. With burn-back, there was significantly reduced turning in the burn-back region, and surprisingly, significantly increased turning outside. The reduced turning in the burn-back region was due to both reduced metal angle, and reduced lift of the cut-back airfoil profile (incomplete turning, leading to greater deviation angle). Increased turning outside the burn-back region was due to reduced SS surface static pressures, leading to a larger cross-passage pressure gradient, and thus enhancing turning.

4. *Changes in rotor inlet and exit whirl angle distributions.* With burn-back, there was a significant decrease in the magnitude of mass-mean *rotor relative* turning angle (decreases in the turning angle between Geometry 1 and Geometry 2, 3 and 4 were 2.3, 6.9, and 15.9 degrees respectively). The mass-mean rotor relative turning angle magnitude decreases because there is significant negative incidence at rotor inlet with burn-back (rotor outlet flow largely follows the metal angle). A contrary trend was observed for the mass-mean *absolute* turning angles, with an *increase* in the magnitude of the turning angle (increases between Geometry 1 and Geometry 2, 3 and 4 were 2.0, 4.5, and 6.2 degrees respectively) with increasing burn-back. This is caused by a combination of a mild decrease in inlet absolute whirl angle and a slightly larger increase in the magnitude of the absolute exit whirl angle.

5. *Changes in vane capacity and mass flow rate.* With increasing burn-back the changes in vane capacity at the nominal operating point were +2.65%, +7.83%, and 16.57% for Geometry 2–4 relative to Geometry 1. In the stage simulations, there was also a change in vane operating point (increase in intra-stage static pressure). This had the effect of slightly reducing the vane capacity values at the settled operating points. Changes in vane capacity at the settled operating points relative to Geometry 1 were

+2.50%, +7.02%, and +14.14% for Geometry 2–4. As inlet total pressure was fixed, the changes in mass flow were the same as the changes in vane capacity.

6. *Changes in rotor capacity and mass flow rate.* With increasing burn-back, the mass flow changes relative to Geometry 1 reported in stage simulations at the settled stage operating point were +2.34%, +6.44%, and +12.94% for Geometry 2–4, respectively. The corresponding changes in capacity were +0.57%, +1.27% and +1.95% respectively. The conclusion was that the changes in mass flow rate arose almost entirely due to changes in mass-mean inlet total pressure, and not because of changes in rotor capacity: the opposite situation to that of the vane. The small change in rotor capacity with NGV burn-back was attributed to a change in effective blockage (changes in boundary layer behaviour, or secondary flow behaviour). Although there were significant changes in rotor operating point in the stage simulations (increasing rotor-relative total pressure), the rotor capacity characteristics with pressure ratio were relatively flat, and the change in operating point did not—on its own—contribute significantly to changes in rotor capacity or mass flow rate.

7. *Changes in NGV isentropic Mach number distributions*. Increasing burn-back led to significant increases in mid-chord SS Mach number at all span locations on the NGV, and a significant decrease in late SS Mach number. An increase in late SS adverse pressure gradient led to BL thickening and increased profile loss.

8. *Changes in rotor isentropic Mach number distributions*. Increasing NGV burn-back led to decreased rotor PS Mach number outside the burn-back region, and increased PS Mach number in the burn-back region. The decrease in PS Mach number outside the burn-back region was driven primarily by an increase in rotor inlet static pressure, rather than a decrease in rotor inlet relative total pressure. The increase in PS Mach number in the burn-back region was driven primarily by an increase in rotor inlet relative total pressure, rather than a decrease in rotor inlet static pressure. Overall,

NGV burn-back led to decreased forward loading and increased aft loading at all span locations.

9. *Changes in overall stage performance*. With increasing NGV burn-back the stage mass flow rate changes were +2.3%, +6.4%, and +12.9% for Geometry 2–4 relative to Geometry 1. Reasons for these changes have been discussed. The corresponding changes in stage reaction were +3.3%, +8.5%, and +16.2%, respectively. These are explained by: increases in intra-stage static pressure which reduced the acceleration in the vane; increases in rotor relative inlet total pressure which increased the acceleration in the rotor. The corresponding changes in stage specific work were −0.4%, −1.6%, and −3.8%, respectively. The stage specific work decreased *despite* an increase in mass mean absolute turning angle due to a greater magnitude of contrary change in the rotor inlet and outlet absolute flow velocities. Finally, the corresponding changes in stage efficiency were +0.16%, +0.42%, and +0.33%, respectively: surprisingly small changes. Significant decreases in NGV efficiency (by −0. 61%, −1.22% and −1.94%) were—surprisingly—offset by increases in rotor efficiency.

10. *Comparison between vane-row only and stage results*. The NGV downstream loss contours, whirl angles profiles, and static pressure profiles from the vane-row only and stage simulations were qualitatively similar, though the absolute magnitudes were different due to the influence of the rotor. The flow capacity plots also showed that the vane-row only result could be reconciled with the stage results when matched on pressure ratio (to within 0.4 percentage points). As explained above, the driving force in the change in vane operating point (that shifted the flow capacity down) was the change in intra-stage static pressure in the stage simulations.

This is the first paper to comprehensively study the impact of trailing edge burn-back on stage performance. Taken with two companion papers considering in detail the impact of TE burn-back on vane row performance [15] and vane flow capacity [16], we believe this is a significant step towards improved whole-life engine performance modelling.

Nomenclature

Romans

A_{BB}	burn-back area [mm^2]
A_{ref}	reference area [mm^2]
C_t	tangential chord length [mm]
C_{p}	specific heat capacity [J K^{-1} kg^{-1}]
C_x	axial chord length [mm]
d	tangential depth of burn-back [mm]
h	enthalpy (total or static) [J]
k	turbulent kinetic energy [m^2 s^{-2}]
L	lift [N]
L_{PS}	pressure side total surface length [mm]
L_{SS}	suction side total surface length [mm]
M	Mach number [–]
$\dot{m}$	mass flow rate [kg s^{-1}]
N	rotational speed [rpm]
P	power [W]
PR*	reference (nominal for Geometry 1) rotor-row pressure ratio [–]
p	pressure (total or static) [Pa]
pp	percentage point [-]
r	radial position [mm]
Re	Reynolds number [–]
S	span height [mm]
s	streamwise surface distance from LE [mm]
T	temperature (total or static) [K]
Tu	turbulence intensity [%]
U	blade speed [m s^{-1}]
V	absolute flow velocity [m s^{-1}]
V_x	axial component of abs. velocity [m s^{-1}]
V_θ	tangential component of abs. velocity [m s^{-1}]
W	relative flow velocity [m s^{-1}]
W_x	axial component of rel. velocity [m s^{-1}]
W_θ	tangential component of rel. velocity [m s^{-1}]
$\dot{w}$	stage specific work [J kg^{-1}]
w_1	width of burn-back at TE [mm]
w_2	width of burn-back at damage front [mm]
x	axial position [mm]
y	surface-normal distance [mm]
y^+	non-dimensional wall distance [–]

Greeks

β	flow turning (or whirl) angle [deg]
β''	circumferentially-averaged whirl angle [deg]
β^*	mass-mean rotor exit whirl angle (absolute or relative) for Geometry 1 (reference value)
Γ	flow capacity [kg s^{-1} K$^{1/2}$ Pa^{-1}]

Γ_{STAGE}	stage flow capacity [kg s^{-1} K$^{1/2}$ Pa^{-1}]
$\Delta\beta^*$	mass-mean rotor turning angle (absolute or relative) for Geometry 1 (reference value)
γ	ratio of specific heat capacities [–]
ζ	KE loss coefficient [–]
ζ'	local KE loss coefficient [–]
ζ''	circumferentially-averaged KE loss coefficient [–]
ζ'''	plane-averaged KE loss coefficient [–]
ζ''''	mixed-out KE loss coefficient [–]
ζ^{SKE}	residual SKE loss coefficient [–]
η	efficiency [–]
η_{tt}	total-to-total stage efficiency [–]
Λ	stage reaction [–]
τ	Torque [Nm]
ϕ	flow coefficient [–]
X	$(\gamma-1)/\gamma$
ψ	stage loading coefficient [–]
Ω	angular velocity [rad s^{-1}]
ω	specific turbulence dissipation rate [s^{-1}]
ω_x	component of vorticity in axial direction [s^{-1}]

Subscripts

0	stagnation condition
1	Plane 1; Geometry 1
2	Plane 2; Geometry 2
3	Plane 3; Geometry 3
4	Plane 4; Geometry 4
c	coolant
exit	exit condition
i	individual coolant stream
s	isentropic condition
m	mainstream
NGV	nozzle guide vane
PS	pressure side
ref	reference value
rel	rotor relative condition
SS	suction side
TB	turbine blade

References

[1] Naeem, M., Singh, R., and Probert, D., 1998, "Implications of Engine Deterioration for Fuel Usage," Applied Energy, 59(3), DOI: 10.1016/S0306-2619(98)00009-9.

[2] Palmer, J. R., 1990, "The TURBOMATCH Scheme for aero/industrial gas turbine engine design point/off design performance calculation," SME, Thermal Power Group, Cranfield Universtiy.

[3] Sallee, G. P., 1978, “Performance Deterioration Based on Existing (Historical) Data; JT9D Jet Engine Diagnostics Program,” NASA CR-135448.

[4] Naeem, M., Singh, R., and Probert, D., 2000, “Implications of Engine’s Deterioration Upon an Aero-Engine HP Turbine Blade’s Thermal Fatigue Life,” International Journal of Fatigue, 22(2), DOI: 10.1016/S0142-1123(99)00105-X.

[5] Tinga, T., Visser, W. P. J., de Wolf, W. B., and Broomhead, M. J., 2000, “Integrated Lifing Analysis Tool for Gas Turbine Components,” Proceedings of the ASME Turbo Expo 2000, Munich, Germany, 8–11 May 2000, Paper No. 2000-GT-0646, DOI: 10.1115/2000-GT-0646.

[6] Macleod, J. D., Taylor, V., and Laflamme, J. C. G., 1992, “Implanted Component Faults and Their Effects on Gas Turbine Engine Performance,” ASME J. Turbomachinery, 114(2), DOI: 10.1115/1.2906567.

[7] Sjolander, S. A., Isaacs, D., and Klein, W. A, 1993, “Aerodynamics of Turbine Blades with Trailing-Edge Damage: Measurements and Computations,” Proceedings of the International Symposium on Air Breathing Engines 1993, Tokyo, Japan, 20–24 September 1993, Paper No. ISABE93-7130.

[8] Wang, S. S., Mao, J. R., Liu, G. W., and Feng, Z. P., 2010, “Performance deterioration of the governing stage nozzle caused by solid particle erosion in the steam turbine,” Proceedings of the Institution of Mechanical Engineers, Part A: Journal of Power and Energy, 224(2), DOI: 10.1243/09576509JPE852.

[9] Bouchard, D., Asghar, A., LaViolette, M., Allan, W. D. E., and Woodason, R., 2014, “Experimental Evaluation of Service-Exposed Nozzle Guide Vane Damage in a Rolls Royce A-250 Gas Turbine,” ASME J. Engineering for Gas Turbines and Power, 136(10), DOI: 10.1115/1.4027204.

[10] Michaud, M., Jackson, D., Goenaga, F., and Povey, T., 2023, “Experimental Study of Impact of In-Service Deterioration on Aerodynamic Performance of High-Pressure Nozzle Guide Vanes,” ASME J. Turbomachinery, 145(6), DOI: 10.1115/1.4056774.

[11] Michaud, M., Chowdhury, N., and Povey, T., 2023, “Experimental Study of Impact of In-Service Deterioration on Thermal Performance of High-Pressure Nozzle Guide Vanes,” ASME J. Turbomachinery, 145(2), DOI: 10.1115/1.4055864.

[12] Meyer, M., Parchem, R., and Davison, P., 2011, “Prediction of Turbine Rotor Blade Forcing due to In-Service Stator Vane Trailing Edge Damage,” Proceedings of the ASME Turbo Expo 2011, Vancouver, Canada, 6–10 June 2011, Paper No. GT2011-45204, DOI: 10.1115/GT2011-45204.

[13] Di Mare, L., Imregun, M., Smith, A. D., and Elliott, R., 2007, “A Numerical Study of High Pressure Turbine Forced Response in the Presence of Damaged Nozzle Guide Vanes,” The Aeronautical Journal, 111(1125), DOI: 10.1017/S0001924000004929.

[14] Kirollos, B., Lubbock, R., Beard, P., Goenaga, F., Rawlinson, A., Janke, E., and Povey, T., 2017, “ECAT: An Engine Component Aerothermal Facility at the University of Oxford,” Proceedings of ASME Turbo Expo 2017, North Carolina, USA, June 26–30 2017, Paper No. GT2017-64736, DOI: 10.1115/GT2017-64736.

[15] Raduev, Z., Jackson, D., Chowdhury, N., and Povey, T., 2025, "Impact of Trailing Edge Damage on Nozzle Guide Vane Aerodynamic Performance," ASME J. Turbomachinery, 147(10), DOI: 10.1115/1.4067930.

[16] Raduev, Z., Jackson, D., Chowdhury, N., and Povey, T., 2025, "Impact of Trailing Edge Damage on Nozzle Guide Vane Flow Capacity," ASME J. Turbomachinery, 148(3), DOI: 10.1115/1.4069602.

[17] Lapworth, L., 2004, "HYDRA-CFD: A Framework for Collaborative CFD Development," Proceedings of the International Conference on Scientific and Engineering Computation 2004, Singapore, July 2004.

[18] Milli, A., and Shahpar, S., 2012, "PADRAM: Parametric Design and Rapid Meshing System for Complex Turbomachinery Configurations," Proceedings of the ASME Turbo Expo 2012, Copenhagen, Denmark, 11–15 June 2012, Paper No. GT2012-69030, DOI: 10.1115/GT2012-69030.

[19] Milli, A., and Shahpar, S., 2008, "Full-Parametric Design System to Improve the Stage Efficiency of a High-Fidelity HP Turbine Configuration," Proceedings of the ASME Turbo Expo 2008, Berlin, Germany, 9–13 June 2008, Paper No. GT2008-51348, DOI: 10.1115/GT2008-51348.

[20] Occhioni, G., Shahpar, S., and Li, H., 2017, "Multi-Fidelity Modelling of a Fully-Featured HP Turbine Stage," Proceedings of the ASME Turbo Expo 2017, North Carolina, USA, 26–30 June 2017, Paper No. GT2017-64478, DOI: 10.1115/GT2017-64478.

[21] Cartlidge, J., and Povey, T., 2024, "Fundamentals of Scaling of Overall Cooling Effectiveness with Temperature Ratio," ASME J. Turbomachinery, 146(1), DOI: 10.1115/1.4063730.

[22] Burdett, D., and Povey, T., 2022, "Analysis of Averaging Methods for Nonuniform Total Pressure Fields," ASME J. Turbomachinery, 144(5), DOI: 10.1115/1.4053020.

[23] Main, A. J., Oldfield, M. L. G., Lock, G. D., and Jones, T. V., 1997, "Free Vortex Theory for Efficiency Calculations from Annular Cascade Data," ASME J. Turbomachinery, 119(2), DOI: 10.1115/1.2841107.

[24] Burdett, D., Hambidge, C., and Povey, T., 2020, "Analysis of Ultra-Low Uncertainty Gas Turbine Flow Capacity Measurement Techniques," Proceedings of the Institution of Mechanical Engineers, Part A: J. Power Energy, 235(5), DOI: 10.1177/0957650920909718.

[25] Kurzke, J., 2002, "Performance Modelling Methodology: Efficiency Definitions for Cooled Single and Multistage Turbines," Proceedings of the ASME Turbo Expo 2002, Amsterdam, Netherlands, 3–6 June 2002, Paper No. GT2002-30497, DOI: 10.1115/GT2002-30497.

[26] Young, J. B., and Horlock, J. H., 2006, "Defining the Efficiency of a Cooled Turbine," ASME J. Turbomachinery, 128(4), DOI: 10.1115/1.2218890.

[27] Hartsel, J., 1972, "Prediction of Effects of Mass-Transfer Cooling on the Blade Row Efficiency of Turbine Airfoils," AIAA 10th Aerospace Sciences Meeting, California, USA, 17–19 Jan. 1972, Paper No. AIAA-72-11, DOI: 10.2514/6.1972-11.

[28] Amend, J., Lubbock, R., Ornano, F., Chowdhury, N., and Povey, T., 2024, "Aerodynamic and Thermal Field Development of Cooled Transonic HP NGV," ASME J. Turbomachinery, 146(2), DOI: 10.1115/1.4063879.

[29] Sharma, O. P., Pickett, G. F., and Ni, R. H., 1992, "Assessment of Unsteady Flows in Turbines," ASME J. Turbomachinery, 114(1), DOI: 10.1115/1.2928001.

[30] Moss, R. W., Ainsworth, R. W., Sheldrake, C. D., and Miller, R. J., 1997, "The Unsteady Pressure Field Over a Turbine Blade Surface: Visualisation and Interpretation of Experimental Data," Proceedings of the ASME Turbo Expo 1997, Florida, USA, 2–5 June 1997, Paper No. 97-GT-474, DOI: 10.1115/97-GT-474.

[31] Goldstein, R. J., and Spores, R. A., 1988, "Turbulent Transport on the Endwall in the Region Between Adjacent Turbine Blades," J. Heat Transfer, 110(4a), DOI: 10.1115/1.3250586.

[32] Povey, T., Sharpe, M., and Rawlinson, A., 2011, "Experimental Measurements of Gas Turbine Flow Capacity Using a Novel Transient Technique," ASME J. Turbomachinery, 133(1), DOI: 10.1115/1.4000481.

[33] Burdett, D., Goenaga, F., and Povey, T., 2021, "Understanding Capacity Sensitivity of Cooled Transonic Nozzle Guide Vanes: A Parametric Experimental and Computational Study of the Impact of Trailing Edge Geometry," ASME J. Turbomachinery, 143(5), DOI: 10.1115/1.4050068.

[34] Cumpsty, N. A., and Horlock, J. H., 2006, "Averaging Nonuniform Flow for a Purpose," ASME J. Turbomachinery, 128(1), DOI: 10.1115/1.2098807.

[35] Luymes, B. T., An, Q., Steinberg, A. M., Zhang, X., and Vandeputte, T., 2018, "Influence of Blade Loading Profile on Wake Dynamics in High-Pressure Turbine Cascades," ASME J. Turbomachinery, 140(10), DOI: 10.1115/1.4041141.

This page is intentionally blank

Chapter 7 – Conclusions

This thesis analyses the impact of high-pressure nozzle guide vane trailing edge damage on vane-row and stage performance. Despite the inevitability of this damage and the severe impact it can have on performance, the open literature on the subject remains scarce. This research contributes to filling that gap, highlighting the significance of burn-back on performance. It is hoped that these findings serve as a valuable reference for future research and contribute to improved whole-life engine performance modelling. The major conclusions are as follows:

- Statistical analysis of deterioration data showed that vane trailing edge burn-back often takes a trapezoidal form, with the mean damage front centre close to midspan.
- With burn-back, for the vane-row:
    - A strong pair of counterrotating vortices formed at the edges of the burn-back, increasing overall loss at vane exit and leading to significant wake distortion. These vortices also strengthened pre-existing secondary flow in the vane passage (e.g., the hub and case passage vortices), further increasing mixed-out loss and secondary kinetic energy.
    - Flow in the burn-back region was underturned due to material removal and vane reloading, while outside this region, flow overturned due to a strong cross-passage pressure gradient.
    - The suction surface Mach number increased significantly, whereas the pressure surface Mach numbers remained largely unchanged. For a fixed row pressure ratio, this led to increased coolant mass flow (and coolant capacity), and thus to higher coolant mixing loss.
    - Changes in boundary layer behaviour were notable, but the integral change in boundary layer loss remained small. The benefit of reduced wetted surface was offset by changes in loading, which produced a stronger adverse pressure

gradient near the suction side trailing edge. Accordingly, the impact of boundary layer changes on capacity (through effective flow area blockage) was also insignificant, accounting for at most 0.14% of the change in capacity.

- Vane capacity increased significantly, partly due to the throat area opening up, but also due to changes in the passage aerodynamics. Weak correlation between the geometric throat area changes and measured capacity changes reinforced the need to consider the aerodynamics in the entire controlling region of the vane.
- Excellent agreement was found between the vane-row simulations and the experimental results, validating the numerical method. This enabled the extension of the research to include the downstream rotor, and consequently, analysis on the impact of vane trailing edge burn-back on turbine stage performance.

- With burn-back, for the rotor-row and stage:
  - The loss in the rotor-relative frame decreased due to weakened rotor secondary flow and reduced profile loss across most of the span height (associated with reduced turning).
  - The mass-mean relative turning angle decreased significantly, while the mass-mean absolute turning angle saw a mild increase. The latter in isolation would lead to increased stage specific work, however, due to a contrary change of greater magnitude associated with the absolute flow velocities, the net effect was a decrease in stage specific work.
  - Stage reaction increased significantly due to intra-stage pressure variations, specifically, for fixed stage pressure ratio, increases in intra-stage static pressure led to reduced acceleration in the vane, whereas increased rotor-relative inlet total pressure led to increased acceleration in the rotor-row.

    - Only a mild change in stage efficiency was observed, likely due to contrary changes in the vane-row and rotor-row efficiencies.
- The validated numerical method was applied by Rolls-Royce to a different standard of vane. Comparable results were obtained, demonstrating that the conclusions from this research have application beyond the specific standard of the vane and engine studied.

This research, in collaboration with Rolls-Royce, has already shaped internal maintenance guidelines for burn-back, delivered empirical correlations for performance deterioration modelling, and provided a validated numerical process that has since been applied to study other engine geometries. For the wider field, it significantly advances understanding of burn-back effects and establishes a strong reference point for future work. More broadly, the findings have direct cost and environmental implications. By quantifying the impact of burn-back, an inevitable damage feature, maintenance schedules can be optimised to extend time on wing and to avoid unnecessary fuel penalties. Even modest improvements in these areas scale to significant benefits when accumulated across thousands of engines operating worldwide.

7.1 – Recommendations for future work

- The stage work of this thesis is based on cases with fixed rotor non-dimensional speed. In practice, the engine would rematch to accommodate changes in, for example, mass flow (or capacity). As air mass flow increases, the air-fuel mixture becomes leaner, reducing turbine temperatures and performance. To compensate, additional fuel would be injected to raise the gas temperature and restore thrust. Future studies should investigate this rematching behaviour to enable more accurate fuel consumption estimations.
- The capacity and stage efficiency exchange rates developed in this thesis could be incorporated in flight mission simulations to assess whole-engine performance impacts.

- Expanded simulations would be beneficial to examine the broader influence of trailing edge burn-back on performance. Potential areas include:
    - *Off-design performance.* Extending the stage simulations to consider a wider range of conditions, including different rotor non-dimensional speeds, stage pressure ratios, and Reynolds' numbers (e.g., to replicate take-off, cruise, and landing conditions).
    - *Burn-back design space*. Investigating different burn-back shapes (e.g., triangular or rectangular), different origin points for burn-back shapes (e.g., near-hub rather than at midspan), and a wider set of burn-back levels.
    - *Comparison across vane standards*. Simulating alternative standards of vanes to more formally assess whether the observed trends and correlations are comparable. Given the validated numerical method, the findings would be relatively reliable, especially for flow capacity predictions.
    - *Multi-stage analysis*. Extending the domain to include additional stages, which with industry collaboration would allow to leverage existing multi-stage turbine models, such as 2.5 stage turbine models.
- This research measured capacity changes experimentally, and subsequently, validated the simulations method. The findings suggest that capacity variations are primarily driven by aerodynamic flow field changes, particularly static pressure variations. Based on this, a low-order predictive model could be developed to estimate capacity changes using burn-back shape as an input.
    - One proposed approach would be to predict the vane exit static pressure distributions with burn-back in a simplified manner, and then use for example, isentropic flow relations (with appropriate discharge coefficient) to calculate the mass flow and evaluate capacity (assuming a stream-tube approach). While this may not be accurate, it would still offer valuable insights. Alternatively, existing lower-order methods could be used, in

increasing order of fidelity: mean-line design codes; throughflow codes; blade-to-blade solvers; and Euler solver solvers. Comparing these approaches would help determine the most efficient method for predicting capacity changes under varying conditions.

This page is intentionally blank

References

[1] Rolls-Royce, 2015, “The Jet Engine,” Fifth ed., John Wiley & Sons, Chichester, United Kingdom, ISBN: 1119065992.

[2] Dixon, S. L., and Hall, C. A., 2015, “Fluid Mechanics and Thermodynamics of Turbomachinery,” Seventh ed., Butterworth-Heinemann, Oxford, United Kingdom, ISBN: 9780124159549.

[3] Cumpsty, N. A., and Heyes, A., 2015, “Jet Propulsion: A Simple Guide to the Aerodynamic and Thermodynamic Design and Performance of Jet Engines,” Third ed., Cambridge University Press, Cambridge, United Kingdom, ISBN: 1107511224.

[4] Raduev, Z., Jackson, D., Chowdhury, N., and Povey, T., 2025, “Impact of Trailing Edge Damage on Nozzle Guide Vane Aerodynamic Performance,” ASME J. Turbomachinery, 147(10), DOI: 10.1115/1.4067930.

[5] Raduev, Z., Jackson, D., Chowdhury, N., and Povey, T., 2025, “Impact of Trailing Edge Damage on Nozzle Guide Vane Flow Capacity,” ASME J. Turbomachinery, 148(3), DOI: 10.1115/1.4069602.

[6] Raduev, Z., Jackson, D., and Povey, T., (in review), “Impact of Nozzle Guide Vane Trailing Edge Damage on High Pressure Turbine Stage Performance,” ASME J. Turbomachinery, DOI: (N/A).

[7] Denton, J. D., 1993, “Loss Mechanisms in Turbomachines,” Proceedings of the ASME 1993 International Gas Turbine and Aeroengine Congress and Exposition, Ohio, USA, May 24–27 1993, Paper No. 93-GT-435, DOI: 10.1115/93-GT-435.

[8] Day, C., 1997, “Aerodynamics of an Annular Film-Cooled Turbine Cascade,” Ph.D. thesis, University of Oxford, England.

[9] Mee, D. J., Baines, N. C., Oldfield, M. L. G., and Dickens, T. E., 1992, “An Examination of the Contributions to Loss on a Transonic Turbine Blade in Cascade,” ASME J. Turbomachinery, 114(1), DOI: 10.1115/1.2927979.

[10] Langston, L. S., 2001, “Secondary Flows in Axial Turbines—A Review,” Heat Transfer in Gas Turbine Systems, 934(1), DOI: 10.1111/j.1749-6632.2001.tb05839.x.

[11] Lampart, P., 2009, “Investigation of Endwall Flows and Losses in Axial Turbines. Part I. Formation of Endwall Flows and Losses,” Journal of Theoretical and Applied Mechanics, 47(2), DOI: (N/A).

[12] Sharma, O., and Butler, T., 1987, “Prediction of Endwall Losses and Secondary Flows in Axial Flow Turbine Cascades,” ASME J. Turbomachinery, 109(2), DOI: 10.1115/1.3262089.

[13] Wang, H. P., Olson, S. J., Goldstein, R. J., and Eckert, E. R., 1987, “Flow Visualization in a Linear Turbine Cascade of High Performance Turbine Blades,” ASME J. Turbomachinery, 119(2), DOI: 10.1115/1.2841006.

[14] Goldstein, R. J., and Spores, R. A., 1988, “Turbulent Transport on the Endwall in the Region Between Adjacent Turbine Blades,” ASME J. Heat Transfer, 110(4a), DO: 10.1115/1.3250586.

[15] Doerffer, P., and Amecke, J., 1994, “Secondary Flow Control and Streamwise Vortices Formation,” Proceedings of the ASME 1994 International Gas Turbine and Aeroengine Congress and Exposition, Hague, The Netherlands, June 13–16 1994, Paper No. 94-GT-376, DOI: 10.1115/94-GT-376.

[16] Sieverding, C. H., 1997, “Secondary and Tip-clearance flows in Axial Turbines,” Lecture Series, Von Karman Institute for Fluid Dynamics.

[17] Salvadori, S., Insinna, M., and Martelli, F., 2024, “Unsteady Flows and Component Interaction in Turbomachinery,” International J. Turbomachinery, Propulsion and Power, 9(2), DOI: 10.3390/ijtpp9020015.

[18] Wilfert, G., and Fottner, L., 1996, “The Aerodynamic Mixing Effect of Discrete Cooling Jets With Mainstream Flow on a Highly Loaded Turbine Blade,” ASME J. Turbomachinery, 118(3), DOI: 10.1115/1.2836692.

[19] Denton, J. D., and Xu, L., 1990, “The Trailing Edge Loss of Transonic Turbine Blades,” ASME J. Turbomachinery, 109(2), DOI: 10.1115/1.3262089.

[20] Nash, J. F., Quincey, V. G., and Callinan, J., 1963, “Experiments on Two-Dimensional Base Subsonic and Transonic Speeds,” Aeronautical Research Council Reports & Memoranda.

[21] Cicatelli, G., and Sieverding, C. H., 1997, “The Effect of Vortex Shedding on the Unsteady Pressure Distribution Around the Trailing Edge of a Turbine Blade,” ASME J. Turbomachinery, 119(4), DOI: 10.1115/1.2841192.

[22] Melzer, A. P., and Pullan, G., 2019, “The Role of Vortex Shedding in the Trailing Edge Loss of Transonic Turbine Blades,” ASME J. Turbomachinery, 141(4), DOI: 10.1115/1.4041307.

[23] Herman, W., Prust, H. W., and Helon, R. M., 1972, “Effect of Trailing-Edge Geometry and Thickness on the Performance of Certain Turbine Stator Blading,” NASA Technical Note, Report No. NASA TN D-6637.

[24] Granovskiy, A, Kostege, M, and Vassiliev, V., 2014, “Effect of Unguided Turning Angle and Trailing Edge Shape on Cooled Blade Loss,” Proceedings of ASME Turbo Expo 2014, Dusseldorf, Germany, June 16–20 2014, Paper No. GT2014-26215, DOI: 10.1115/GT2014-26215.

[25] Motallebi, F., and Norbury, J. F., 1981, “The Effect of Base Bleed on Vortex Shedding and Base Pressure in Compressible Flow,” Journal of Fluid Mechanics, 110, DOI: 10.1017/S0022112081000748.

[26] Melzer, A. P., 2017, “Aerodynamics of Transonic Turbine Trailing Edges,” Ph.D. thesis, University of Cambridge, England.

[27] Burdett, D., and Povey, T., 2022, “Impact of Trailing Edge Overhang Length on the Loss Characteristics of Fully Cooled Transonic Nozzle Guide Vanes,” ASME J. Turbomachinery, 145(5), DOI: 10.1115/1.4056056.

[28] Kirollos, B., Lubbock, R., Beard, P., Goenaga, F., Rawlinson, A., Janke, E., and Povey, T., 2017, "ECAT: An Engine Component Aerothermal Facility at the University of Oxford," Proceedings of ASME Turbo Expo 2017, North Carolina, USA, June 26–30 2017, Paper No. GT2017-64736, DOI: 10.1115/GT2017-64736.

[29] Gaetani, P., 2018, "Stator-Rotor Interaction in Axial Turbine: Flow Physics and Design Perspective.," IntechOpen, DOI: 10.5772/intechopen.76009.

[30] Lefcort, M. D., 1965, "An Investigation Into Unsteady Blade Forces in Turbomachines," ASME J. Eng. Power, 87(4), DOI: 10.1115/1.3678275.

[31] Payne, S. J., Ainsworth, R. W., Miller, R. J., Moss, R. W., and Harvey, N. W., 2005, "Unsteady Loss in High Pressure Turbine Stage: Interaction Effects," International J. Heat and Fluid Flow, 26(5), DOI: 10.1016/j.ijheatfluidflow.2005.04.005.

[32] Chaluvadi, V. P., Kalfas, A. I., Banieghbal, M. R., Hodson, H. P., and Denton, J. D., 2001, "Blade-Row Interaction in a High-Pressure Turbine," J. Propulsion and Power, 17(4), DOI: 10.2514/2.5821.

[33] Gaetani, P., Persico, G., Dossena, V., and Osnaghi, C., 2006, "Investigation of the Flow Field in a High-Pressure Turbine Stage for Two Stator-Rotor Axial Gaps—Part II: Unsteady Flow Field," ASME J. Turbomachinery, 129(3), DOI: 10.1115/1.2472393.

[34] Cerretelli, C., and Williamson, C. H. K., 2003, "The Physical Mechanism for Vortex Merging," Journal of Fluid Mechanics, 475, DOI: 10.1017/S0022112002002847.

[35] Bin, Y., Yang, X. I. A., Yang, Y., Ni, R., and Shi, Y., 2022, "Evolution of Two Counter-rotating Vortices in a Stratified Turbulent Environment," Journal of Fluid Mechanics, 951, DOI: 10.1017/jfm.2022.905.

[36] Binder, A., 1985, "Turbulence Production Due to Secondary Vortex Cutting in a Turbine Rotor," ASME J. Eng. Gas Turbines Power, 107(4), DOI: 10.1115/1.3239808.

[37] De´nos, R., Arts, T., Paniagua, G., Michelassi, V., and Martelli, F., 2000, "Investigation of the Unsteady Rotor Aerodynamics in a Transonic Turbine Stage," ASME J. Turbomachinery, 123(1), DOI: 10.1115/1.1314607.

[38] Miller, R. J., Moss, R. W., Ainsworth, R. W., and Harvey, N. W., 2003, "Wake, Shock, and Potential Field Interactions in a 1.5 Stage Turbine—Part I: Vane-Rotor and Rotor-Vane Interaction," ASME J. Turbomachinery, 125(1), DOI: 10.1115/1.1508386.

[39] Paniagua, G., Yasa, T., Loma, A., Castillon, L., and Coton, T., 2008, "Unsteady Strong Shock Interactions in a Transonic Turbine: Experimental and Numerical Analysis," J. Propulsion and Power, 24(4), DOI: 10.2514/1.34774.

[40] Rubechini, F., Marconcini, M., Giovannini, M., Bellucci, J., and Arnone, A., 2015, "Accounting for Unsteady Interaction in Transonic Stages," ASME J. Eng. Gas Turbines Power, 137(5), DOI: 10.1115/1.4028667.

[41] Burdett, D., Hambidge, C., and Povey, T., 2020, "Analysis of Ultra-Low Uncertainty Gas Turbine Flow Capacity Measurement Techniques," Proceedings of the Institution of Mechanical Engineers, Part A: J. Power Energy, 235(5), DOI: 10.1177/0957650920909718.

[42] Fielding, L., 1981, "The Effect of Irreversibility on the Capacity of a Turbine Blade Row," Proceedings of the Institution of Mechanical Engineers, 195(1), DOI: 10.1243/PIME_PROC_1981_195_046_02.

[43] Afanasiev, I. V., Granovskiy, A. V., Kareline, A. M., and Kostege, M. K., 2004, "Effect of 3D Vane Shape on the Vane Capacity," Proceedings of ASME Turbo Expo 2004, Vienna, Austria, June 14–17 2004, Paper No. GT2004-53095, DOI: 10.1115/GT2004-53095.

[44] Afanasiev, I. V., Granovskiy, A. V., Kareline, A. M., and Kostege, M. K., 2004, "The Problems of Inaccuracy in Flow Capacity Definition by Using Different Numerical Techniques," J. Thermal Science, 13(1), DOI: 10.1007/s11630-004-0001-z.

[45] Povey, T., Sharpe, M., and Rawlinson, A., 2011, "Experimental Measurements of Gas Turbine Flow Capacity Using a Novel Transient Technique," ASME J. Turbomachinery, 133(1), DOI: 10.1115/1.4000481.

[46] Povey, T., 2010, "Effect of Film Cooling on Turbine Capacity," ASME J. Engineering for Gas Turbines Power, 132(1), DOI: 10.1115/1.3026564.

[47] Hambidge, C., and Povey, T., 2012, "Numerical and Analytical Study of the Effect of Film Cooling on HP NGV Capacity," Proceedings of ASME Turbo Expo 2012, Copenhagen, Denmark, June 11–15 2012, Paper No. GT2012-69066, DOI: 10.1115/GT2012-69066.

[48] Högner, L., Nasuf, A., Voigt, P., Voigt, M., Vogeler, K., Meyer, M., Berridge, C., and Goenaga, F., 2016, "Analysis of High Pressure Turbine Nozzle Guide Vanes Considering Geometric Variations," Proceedings of ASME Turbo Expo 2016, Seoul, South Korea, June 13–17 2016, Paper No. GT2016-57502, DOI: 10.1115/GT2016-57502.

[49] Voigt, P., Högner, L., Fiedler, B., Voigt, M., Mailach, R., Meyer, M., and Nasuf, A., 2019, "Comprehensive Geometric Description of Manufacturing Scatter of High-Pressure Turbine Nozzle Guide Vanes for Probabilistic CFD Analysis," ASME J. Turbomachinery, 141(8), DOI: 10.1115/1.4042892.

[50] Burdett, D., Goenaga, F., and Povey, T., 2021, "Understanding Capacity Sensitivity of Cooled Transonic Nozzle Guide Vanes: A Parametric Experimental and Computational Study of the Impact of Trailing Edge Geometry," ASME J. Turbomachinery, 143(5), DOI: 10.1115/1.4050068.

[51] Balan, C., Tabakoff, W., 1984, "Axial Flow Compressor Performance Deterioration," AIAA 20th Joint Propulsion Conference, Ohio, USA, 11–13 June 1984, DOI: 10.2514/6.1984-1208.

[52] Swar, R., Hamed, A., Shin, D., Woggon, N., and Miller, R., 2012, "Deterioration of Thermal Barrier Coated Turbine Blades by Erosion," International J. Rotating Machinery, DOI: 10.1155/2012/601837.

[53] Tabakoff, W., Hamed, A., and Shanov, V., 1998, "Blade Deterioration in a Gas Turbine Engine," International J. Rotating Machinery, DOI: 10.1155/S1023621X98000190.

[54] Hamed, A., Tabakoff, W. C., and Wenglarz, R. V., 2012, "Erosion and Deposition in Turbomachinery," J. Propulsion and Power, 22(2), DOI: 10.2514/1.18462.

[55] Wakeman, T, and Tabakoff, W., 1982, "Measured Particle Rebound Characteristics Useful for Erosion Prediction," Proceedings of the ASME 1982 International Gas Turbine Conference and Exhibit, London, England, 18–22 April 1982, Paper No. 82-GT-170, DOI: 10.1115/82-GT-170.

[56] Pang, H. T., Li, F., Pahlavanyali, S., Edmonds, I. M., Brewster, G., and Rae, C. F., 2016, "Effects of Sea Salt on the Oxidation of CMSX-4 at 1100 °C," Proceedings of the 13th International Symposium of Superalloys, DOI: 10.1002/9781119075646.ch101.

[57] Eliaz, N., Shemesh, G., and Latanision, R. M., 2002, "Hot Corrosion of Gas Turbine Components," Engineering Failure Analysis, 9(1), DOI: 10.1016/S1350-6307(00)00035-2.

[58] Patarini, V., Bornstein, N. S., and DeCrescente, M. A., 1979, "Hot Corrosion of Gas Turbine Components," ASME J. Eng. Power, 101(1), DOI: 10.1115/1.3446441.

[59] Salehnasab, B., Poursaeidi, E., Mortazavi, S. A., and Farokhian, G. H., 2016, "Hot Corrosion Failure in the First Stage Nozzle of a Gas Turbine Engine," Engineering Failure Analysis, 60(1), DOI: 10.1016/j.engfailanal.2015.11.057.

[60] Sjolander, S. A., Isaacs, D., and Klein, W. A, 1993, "Aerodynamics of Turbine Blades with Trailing-Edge Damage: Measurements and Computations," Proceedings of the International Symposium on Air Breathing Engines 1993, Tokyo, Japan, 20–24 September 1993, Paper No. ISABE93-7130.

[61] Islam, A. M. T., 1999, "An Experimental and Computational Study of the Aerodynamics of Turbine Blades with Damage," Ph.D. thesis, Carleton University, Canada.

[62] Wang, S. S., Mao, J. R., Liu, G. W., and Feng, Z. P., 2010, "Performance deterioration of the governing stage nozzle caused by solid particle erosion in the steam turbine," Proceedings of the Institution of Mechanical Engineers, Part A: Journal of Power and Energy, 224(2), DOI: 10.1243/09576509JPE852.

[63] Bouchard, D., Asghar, A., LaViolette, M., Allan, W. D. E., and Woodason, R, 2014, "Experimental Evaluation of Service-Exposed Nozzle Guide Vane Damage in a Rolls Royce A-250 Gas Turbine," ASME J. Engineering for Gas Turbines and Power, 136(10), DOI: 10.1115/1.4027204.

[64] Meyer, M., Parchem, R., and Davison, P., 2011, "Prediction of Turbine Rotor Blade Forcing due to In-Service Stator Vane Trailing Edge Damage," Proceedings of the ASME Turbo Expo 2011, Vancouver, Canada, 6–10 June 2011, Paper No. GT2011-45204, DOI: 10.1115/GT2011-45204.

[65] Di Mare, L., Imregun, M., Smith, A. D., and Elliott, R., 2007, "A Numerical Study of High Pressure Turbine Forced Response in the Presence of Damaged Nozzle Guide Vanes," The Aeronautical Journal, 111(1125), DOI: 10.1017/S0001924000004929.

[66] Rajput, M. U., 2013, "Evaluation of Experimental Forced Response Data of a Turbine Stage with Respect to Different Stator Blade Damages," M.Sc. thesis, KTH Royal Institute of Technology, Sweden.

[67] Kost, F., and Giess, P. A., 2004, "Experimental Turbine Research at DLR Göttingen," J. Gas Turbine Society of Japan, 32(6).

[68] Michaud, M., Jackson, D., Goenaga, F., and Povey, T., 2023, “Experimental Study of Impact of In-Service Deterioration on Aerodynamic Performance of High-Pressure Nozzle Guide Vanes,” ASME J. Turbomachinery, 145(6), DOI: 10.1115/1.4056774.

[69] Michaud, M., Chowdhury, N., and Povey, T., 2023, “Experimental Study of Impact of In-Service Deterioration on Thermal Performance of High-Pressure Nozzle Guide Vanes,” ASME J. Turbomachinery, 145(2), DOI: 10.1115/1.4055864.

[70] Cartlidge, J., and Povey, T., 2024, “Fundamentals of Scaling of Overall Cooling Effectiveness with Temperature Ratio,” ASME J. Turbomachinery, 146(1), DOI: 10.1115/1.4063730.

[71] Kline, S. J., 1985, “The Purposes of Uncertainty Analysis,” ASME J. Fluids Eng., 107(2), DOI: 10.1115/1.3242449.

[72] Han, J.-C. and Wright, L.M., 2020, “Experimental Methods in Heat Transfer and Fluid Mechanics,” CRC Press, ISBN: 036789792X.

Appendix 1 – Numerical method detail

A1.1 – Introduction

This section will detail other aspects of the numerical method that were not discussed in the results chapters. They were omitted as they were not required in the journal papers that formed these chapters.

A1.2 – Mesh generation and mesh independence

A featured and coated computer aided design (CAD) of the Trent 900 high-pressure nozzle guide vane was delivered by Rolls-Royce. This CAD was modified to include the ECAT facility annulus lines so that the working section was adequately matched. The film cooling holes were removed, but the trailing edge slot was explicitly modelled up to the pin-fins. The film cooling holes were removed, rather, a film cooling source method was applied in the CFD as the burn-back feature studied did not affect the film cooling hole geometries. In contrast, the trailing edge slot was cut into and therefore was included. The final CFD domain was meshed with refinement focused on the following areas: around the vane surface, in the throat region, near the trailing edge, and in the wake region. These are highlighted in Figure A1.1.

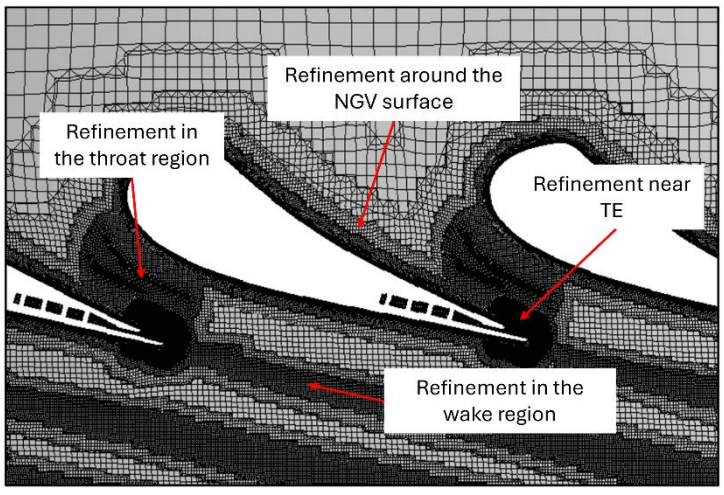


Figure A1.1: Meshing strategy (geometry distorted for commercial reasons).

A selective wake refinement (as opposed to inefficiently refining the entire downstream region) was achieved by exporting iso-volumes with a total pressure threshold from initial

CFD solutions. An example of an exported wake iso-volume from the baseline CFD case is shown in Figure A1.2. This would change with increasing burn-back, and so is re-exported for each case.

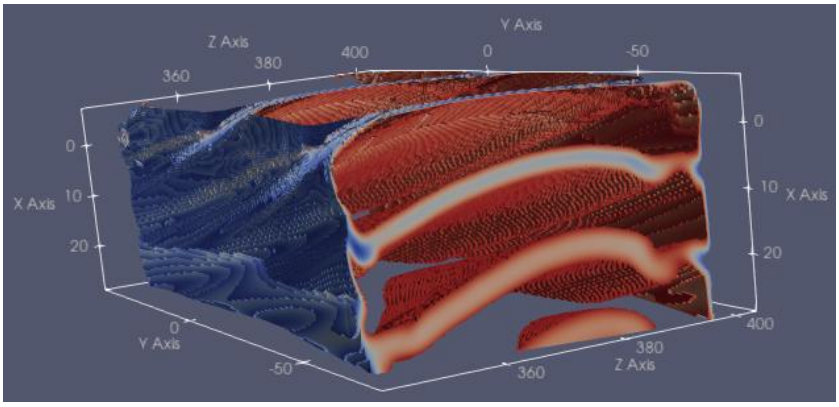


Figure A1.2: Vane wake iso-volume with a total pressure threshold.

The final meshes were approximately 60M cells in size, with average Y+ values of less than two on the wetted surfaces. The initial layer step size, and number of inflation layers were determined by doing a boundary layer profile analysis at various different (over a hundred) points on the vane surface. This was done to ensure that the viscous sub-layer was captured within the near-wall inflation layers. See Figure 4.15 in an earlier chapter for example of the boundary layer profiles captured.

In addition to the boundary layer profile analysis, to make sure the meshes were sufficiently resolution independent, the following four parameters were monitored with different mesh sizes: vane capacity value, local loss coefficient distributions, plane mass-flux-averaged loss coefficients, and whirl angle distributions. The latter three are compared in Figure A1.3 below, and the vane capacity value (not shown here) was within 0.01% between the last two mesh sizes.

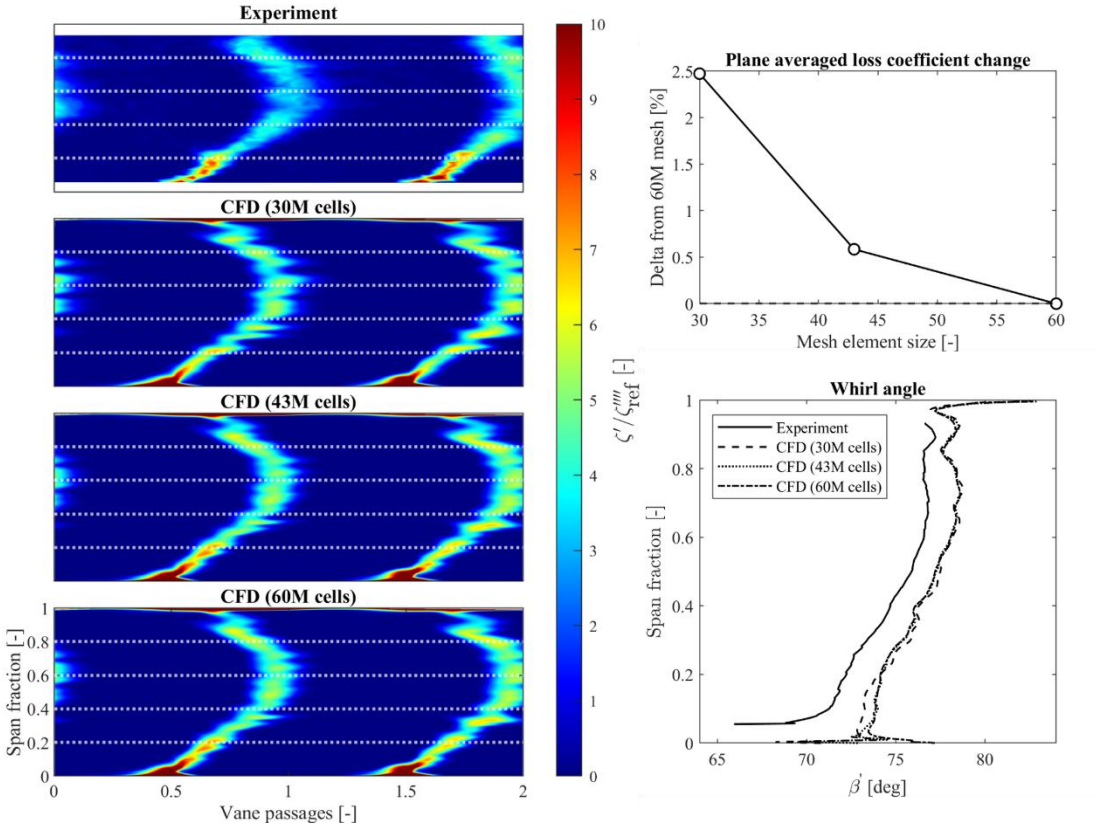


Figure A1.3: Monitored parameters for mesh independence study.

The vane exit platform static pressures in the CFD solutions were also compared at identical points to the experiment to ensure they were both running at the same operating point (defined in this work as the inlet-total to exit-static pressure ratio). The resultant hub and case profiles for each geometry were shown in an earlier chapter, specifically in Figure 5.6.

A1.3 – Film and trailing edge slot coolant flow boundary conditions

The first two results chapters relating to the vane-row simulations (at cold-rig ECAT conditions) briefly mention that the coolant mass flow rates for individual film holes and trailing edge slot are determined using an in-house low-order (one-dimensional) internal flow solver (loss-correlation based). The nodal representation of this internal flow solver is shown in Figure A1.4 (most of the cooling network is covered by a generic wall for intellectual property reasons). As shown, the internal geometry is recreated using ducts (e.g., front and rear ducts), loss features (e.g., pedestals and pins), and source exits (film holes and trailing slots) to name some. One of the benefits of this model is that the lengths, locations, and sizes

etc. of any individual feature can be changed with ease. In practice, this means that for cases with burn-back, the trailing edge slot duct length is locally modified to match the numerical and experimental geometry.

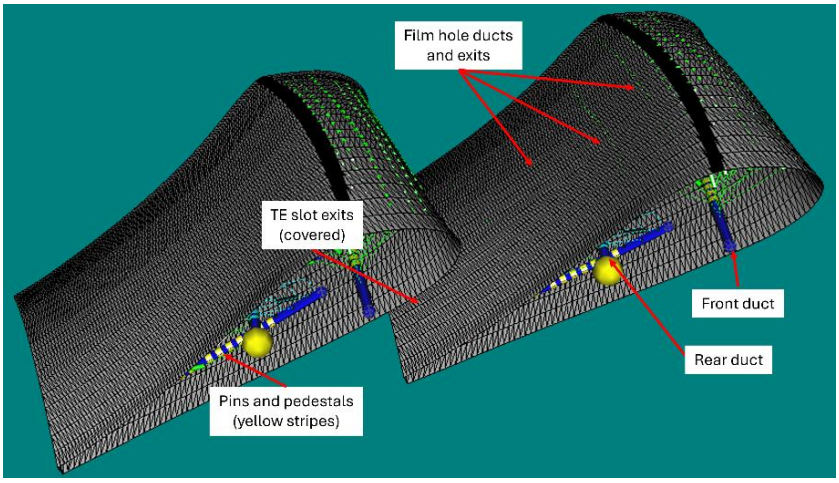


Figure A1.4: Nodal representation of the internal flow solver used in this work.

The inputs to this model are now detailed. The front duct and rear duct in Figure A1.4 represent the front and rear compartments of the real engine part. These compartments are connected to the rest of the internal flow geometry as seen in the figure. At the inlets of these two ducts, total pressure and total pressure boundary conditions are imposed, matched to experiment. At the exits of each trailing edge slot and film cooling holes, a static pressure boundary condition is imposed. This is achieved by exporting an external static pressure distribution form an initial uncooled CFD prediction and mapping this over the internal flow geometry. An example of this is shown in Figure A1.5.

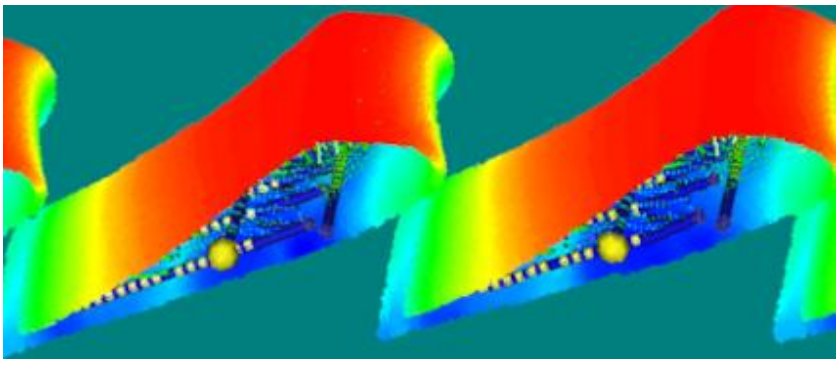


Figure A1.5: CFD-predicted external surface static pressure distribution mapped onto internal flow solver geometry (geometry distorted for commercial reasons).

This model outputs the mass flow rate, total temperature, and total pressure for each individual film cooling hole (of which there are over four hundred) and trailing edge slot. The mass flow rates are summed and then scaled to match the total measured mass flow in the experiments. These values are then used in the CFD cooled simulations.

A1.4 – Rig to engine coolant mass flow scaling

The last results chapter relating to stage simulations (at cruise conditions) briefly mentions that the mass flows determined from the above subsection is further scaled to account for differences in the coolant-to-mainstream temperature ratio between cold-rig and engine cruise conditions. The scaling approach is based on the work from [70] who show that blowing ratio and momentum flux ratio are simultaneously matched for approximately fixed coolant-to-mainstream pressure ratio and vane pressure ratio to the first order, the end result is that the coolant mass flows can be scaled by the square root of the rig-to-engine coolant-to-mainstream temperature ratio.

This page is intentionally blank

Appendix 2 – Measurement uncertainty

A2.1 – Introduction

This section will detail the process used to estimate the uncertainty of the vane capacity measurements performed in this work. The process detailed follows that of Burdett et al. [41] and Povey et al. [45]. The underlying error propagation technique is based on that of Kline [71], which Han and Wright [72] discuss more. This method states that if a result F is a function of several independent variables x, y, z such that $F(x, y, z)$ and $\sigma_x, \sigma_y, \sigma_z$ are the uncertainties in the independent variables, then the uncertainty in the result σ_F can be determined by

$$\sigma_F = \left[\left(\frac{dF}{dx}\right)^2 \sigma_x^2 + \left(\frac{dF}{dy}\right)^2 \sigma_y^2 + \cdots\right]^{1/2} \tag{A2.1}$$

and if the uncertainty is to be presented as a percent of the result, then it is determined by

$$\sigma_F^{\%} = \frac{\sigma_F}{F} = \left[\left(\frac{dF}{dx}\right)^2 \frac{x^2}{F^2} \sigma_x^{\%2} + \left(\frac{dF}{dy}\right)^2 \frac{y^2}{F^2} \sigma_y^{\%2} + \cdots\right]^{1/2} \tag{A2.2}$$

In our work, the vane capacity measurements are performed using the ECAT facility. An annotated pipework schematic of the CAP15 configuration of the facility is shown in Figure A2.1.

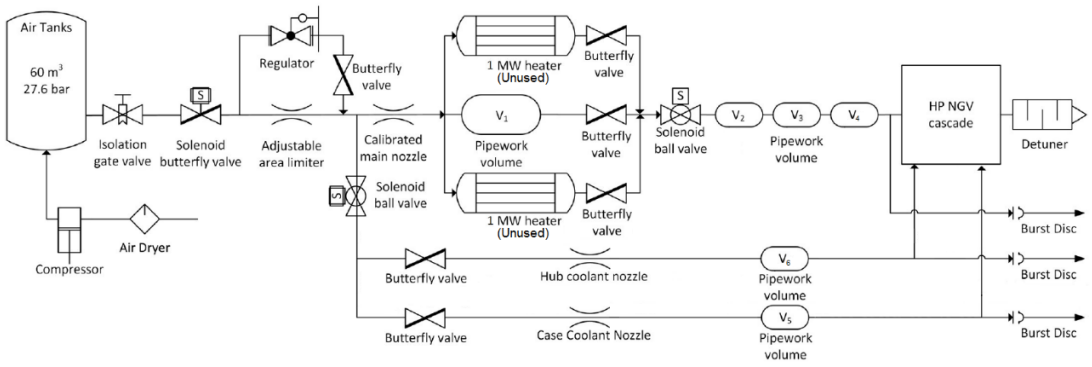


Figure A2.1: ECAT CAP15 configuration schematic (from Daniel Burdett, unpublished).

Vane capacity can be evaluated with different equations depending on the mainstream-coolant mixing treatment. In this work, the multi-stream assumption is used which means that the vane capacity is defined as

$$\Gamma_{\text{vane}} = \frac{\dot{m}_{\text{m}}\sqrt{T_{0\text{m}}}}{p_{0\text{m}}} + \frac{\dot{m}_{\text{hc}}\sqrt{T_{0\text{hc}}}}{p_{0\text{hc}}} + \frac{\dot{m}_{\text{cc}}\sqrt{T_{0\text{cc}}}}{p_{0\text{cc}}} \tag{A2.3}$$

where $\dot{m}$ is the mass flow rate, T_0 is the total temperature, and p_0 is the total pressure. The subscripts m, hc, and cc represent the mainstream, hub coolant, and case coolant properties. With respect to ECAT schematic nomenclature this is

$$\Gamma_{\text{vane}} = \frac{\dot{m}_{\text{CEESI}}\sqrt{T_{07}}}{p_{07}} + \frac{\dot{m}_{\text{HCN}}\sqrt{T_{08\text{h}}}}{p_{08\text{h}}} + \frac{\dot{m}_{\text{CCN}}\sqrt{T_{08\text{c}}}}{p_{08\text{c}}} \tag{A2.4}$$

where subscripts CEESI, HCN, and CCN represent the calibrated main nozzle, hub coolant, and case coolant nozzle properties. The subscripts 07, 08h, and 08c represent properties upstream of the NGV, and in the NGV hub and case coolant cavities, respectively. Capacity is a derived (as opposed to a measured) variable, so first, the bias uncertainties for each measured variable must be determined individually. Specifically, the uncertainties in the following variables are required:

1. Mass flow metering nozzle effective flow areas
2. Measured inlet feed mass flow rates
3. Unsteady mass flow correction terms
4. Vane inlet total pressures
5. Vane inlet total temperatures

A2.2 – Uncorrected mass flow terms

The mass flow rate through a choked Venturi is a function of the effective flow area, and the upstream total pressure and total temperature. First considering the calibrated mainstream nozzle, the uncorrected mass flow rate is given by

$$\dot{m}_{\mathrm{CEESI}} = (C_d C^* A_{\mathrm{CEESI}}) \frac{p_{01}}{\sqrt{RT_{01}}} \left(\frac{\gamma+1}{2}\right)^{\left(-\frac{\gamma+1}{2(\gamma-1)}\right)} = C A_{\mathrm{eff,CEESI}} \frac{p_{01}}{\sqrt{T_{01}}} \tag{A2.5}$$

where C_d is the discharge coefficient, C^* is the critical flow function, A is the effective flow area, R is the universal gas constant, and γ is the ratio of specific heat capacities. The subscript 01 represent properties upstream of the calibrated main nozzle. The CEESI nozzle effective area was calibrated with a bias uncertainty of $\pm 0.500\%$, and is now $\pm 0.250\%$ after a recent recalibration in 2021. This means that $\sigma^{\%}_{\mathrm{A_{eff,CEESI}}} = \pm 0.250\%$ (with 95% confidence). The upstream total pressure was measured with a single 20 bar transducer (DRUCK UNIK 5000 PMP5019-TA-A3-CA-H0-PB) with quoted bias uncertainty of $\pm 0.04\%$ of the transducer range. The nominal upstream total pressure value was 12.0 bar. This means that $\sigma^{\%}_{p_{01}} = \frac{20 \times 0.04}{12} \times \frac{1}{\sqrt{1}} = \pm 0.067\%$. The upstream total temperature was measured using eight K-type thermocouples with quoted bias uncertainty of ± 1.5 K. The nominal upstream total temperature was 280 K. This means that $\sigma^{\%}_{T_{01}} = \frac{1.5}{280} \times \frac{1}{\sqrt{8}} \times 100 = \pm 0.189\%$. Using the Kline and McClintocks method, this gives

$$\sigma^{\%}_{\dot{m}_{\mathrm{CEESI}}} = \left[{\sigma^{\%}_{A_{\mathrm{eff,CEESI}}}}^2 + {\sigma^{\%}_{p_{01}}}^2 + \frac{1}{4} {\sigma^{\%}_{T_{01}}}^2 \right]^{1/2} = \left[0.250^2 + 0.067^2 + \frac{1}{4}(0.189)^2 \right] = 0.275\% \tag{A2.6}$$

Now considering the hub and case coolant nozzles, the uncorrected mass flow rates are given by (equation is only shown for hub nozzle, but is identical for case nozzle)

$$\dot{m}_{\mathrm{HCN}} = (C_d A_{\mathrm{HCN}}) \sqrt{\gamma R T_{\mathrm{throat}}} \frac{p_{\mathrm{throat}}}{\sqrt{RT_{\mathrm{throat}}}} = C A_{\mathrm{eff,HCN}} \frac{p_{4\mathrm{h}}}{\sqrt{T_{04\mathrm{h}}}} \tag{A2.7}$$

The subscript 4h and 04h represent properties upstream of the hub coolant nozzle, similarly, 4c and 04c would represent the case coolant nozzle. The coolant nozzles were measured with an assumed accuracy of ± 0.050 mm. The HCN had a nominal diameter of 18.2 mm, and the CCN had a nominal diameter of 9.4 mm. This means that $\sigma^{\%}_{D_{\mathrm{h}}} = \frac{0.05}{18.2} \times 100 = \pm 0.275\%$ and $\sigma^{\%}_{D_{\mathrm{c}}} = \pm 0.532\%$. This, for a circular shape where $A = \pi r^2$, gives $\sigma^{\%}_{A_{\mathrm{eff,HCN}}} =$

$2 \times 0.275 = \pm 0.550\%$ and $\sigma^{\%}_{A_{\text{eff,CCN}}} = \pm 1.064\%$. The upstream hub and case nozzle total pressure was measured with a single 35 bar transducer with quoted bias uncertainty of $\pm 0.100\%$. The nominal upstream total pressure value was 12.0 bar. This means that $\sigma^{\%}_{p_{4\text{h}}} = \sigma^{\%}_{p_{4\text{c}}} = \frac{35 \times 0.100}{12} \times \frac{1}{\sqrt{1}} = \pm 0.292\%$. The upstream hub and case nozzle total temperature was measured using four K-type thermocouples with quoted bias uncertainty of ± 1.5 K. The nominal upstream total temperature was 280 K. This means that $\sigma^{\%}_{T_{04\text{h}}} = \sigma^{\%}_{T_{04\text{c}}} = \frac{1.5}{280} \times \frac{1}{\sqrt{4}} \times 100 = \pm 0.268\%$. Using Kline and McClintocks method, this gives $\sigma^{\%}_{\dot{m}_{\text{HCN}}} = \pm 0.637\%$ and $\sigma^{\%}_{\dot{m}_{\text{CCN}}} = \pm 1.111\%$.

A2.3 – Mainstream inlet instrumentation

The uncertainty in the mainstream inlet conditions, p_{07} and T_{07}, measurements are now estimated. The upstream mainstream total pressure was measured using thirty-two 5 bar transducers with quoted bias uncertainty of $\pm 0.1\%$ of the transducer range. The nominal upstream mainstream total pressure was 2.0 bar. This means $\sigma^{\%}_{p_{07}} = \frac{5 \times 0.10}{2} \times \frac{1}{\sqrt{32}} = \pm 0.044\%$. The upstream mainstream total temperature was measured using thirty-two K-type thermocouples with quoted bias uncertainty of ± 1.5 K. The nominal upstream mainstream total temperature was 280 K. This means that $\sigma^{\%}_{T_{07}} = \frac{1.5}{280} \times \frac{1}{\sqrt{32}} \times 100 = \pm 0.095\%$.

A2.4 – Coolant cavity instrumentation

The uncertainty in hub and case coolant cavity total pressures and total temperatures is now estimated. The hub and case total pressures, p_{08h} and p_{08c}, are measured in the coolant cavity relative to the mainstream inlet total pressure (differential measurements). Thus

$$p_{08h} = p_{07} + \Delta p_{08\text{h}} \tag{A2.8}$$

The hub and case coolant total pressures were each measured using three 0.35 bar differential transducers (relative to mainstream inlet total pressure) with quoted bias uncertainty of $\pm 0.2\%$ of the transducer range. The nominal coolant-to-mainstream differential

pressure, $\Delta p_{08\mathrm{h}}$ and $\Delta p_{08\mathrm{c}}$, was 0.050 bar. This means that $\sigma^{\%}_{\Delta p_{08\mathrm{h}}} = \sigma^{\%}_{\Delta p_{08\mathrm{c}}} = \frac{0.35\times0.20}{0.05} \times \frac{1}{\sqrt{3}} = \pm 0.808\%$. Where Δp refers to the pressure differential. The uncertainty in the absolute values of coolant inlet total pressure is given by

$$\sigma^{\%}_{p08\mathrm{h}} = \sigma^{\%}_{p08\mathrm{c}} = \sqrt{\left(\frac{p_{07}}{p_{08\mathrm{h}}}\right)^2 {\sigma^{\%}_{p_{07}}}^2 + \left(\frac{\Delta p_{08\mathrm{h}}}{p_{08\mathrm{h}}}\right)^2 {\sigma^{\%}_{\Delta p_{08\mathrm{h}}}}^2} = \sqrt{\left(\frac{2}{2.05}\right)^2 (0.044)^2 + \left(\frac{0.05}{2.05}\right)^2 (0.808)^2} = \pm 0.047\% \quad \text{(A2.9)}$$

The above equation also shows that the uncertainty in the absolute coolant total pressure is dominated by the uncertainty in the mainstream total pressure. This due to the small relative value of the differential pressure with respect to the absolute total pressure. The hub and case coolant total temperatures, $T_{08\mathrm{h}}$ and $T_{08\mathrm{c}}$, were each measured using three K-type thermocouples with quoted bias uncertainty of ± 1.5 K. The nominal coolant capacity total temperature was 280 K. This means that $\sigma^{\%}_{T_{08\mathrm{h}}} = \sigma^{\%}_{T_{08\mathrm{c}}} = \frac{1.5}{280} \times \frac{1}{\sqrt{3}} \times 100 = \pm 0.309\%$.

A2.5 – Unsteady mass flow correction terms

The facility uses 6 intermediate plena to condition the flow. These are labelled V1–V6 in Figure A2.1. V1–V4 contribute to the mainstream flow, V5 to the case coolant stream, and V6 to the hub coolant stream. As the external tank is emptied, the pressure and temperature decays. This is passed down the pipework system and eventually the working section. As this happens, the mass stored in the volumes decreases with time. However, in this process, some mass is stored in the volumes. This must be accounted for. Assuming ideal gas behaviour, the rate of change of mass in a volume is given by

$$\frac{\mathrm{d}m}{\mathrm{d}t} = \dot{m} = \frac{V}{RT}\left(\frac{\mathrm{d}p}{\mathrm{d}t} - \frac{p}{T}\frac{\mathrm{d}T}{\mathrm{d}t}\right) \quad \text{(A2.10)}$$

This is a $pV = mRT$ calculation and uses the quotient rule. The volumes were measured with an estimated uncertainty of $\pm 5\%$, and the uncertainty in the rates of change of pressure and temperature, $\frac{\mathrm{d}p}{\mathrm{d}t}$ and $\frac{\mathrm{d}T}{\mathrm{d}t}$, were estimated to be $\pm 15\%$. The temperature and pressure

measurement uncertainty same as before (± 1.5 K, and $\pm 0.10\%$ respectively). Nominal values and estimated bias uncertainty for each main variable is listed in the table below. Note pressures in V1-V2 (feed pipe 1 and feed pipe 2) are each measured with a single 35 bar transducer, and in V3 (which is the axial stiffener location) is measured using six 5 bar pressure transducers. Temperatures in V1-V2 each measured with seven K-type thermocouples, and in V3 measured with six K-type thermocouples. V4-V6 we have previously calculated (these volumes represent the working section, hub coolant stream, and case coolant stream respectively).

Table A2.1: Nominal values and bias uncertainties in intermediate plena.

	V1	V2	V3	V4	V5	V6
Nominal value						
V_i (m^3)	1.558	0.384	0.355	0.091	0.101	0.076
T_i (K)	280	280	280	280	280	280
p_i (bar)	6.5	6.0	2.0	2.0	2.05	2.05
$\mathrm{d}p_i/\,\mathrm{d}t$ (bar/s)	-0.06	-0.06	-0.02	-0.02	-0.02	-0.02
$\mathrm{d}T_i/\,\mathrm{d}t$ (K/s)	-0.20	-0.18	-0.14	-0.14	-0.03	-0.04
$\dot{m}''$ (kg/s)	-0.1073	-0.0268	-0.0084	-0.0022	-0.0025	-0.0019
Bias uncertainty ($\sigma^{\%}$)						
V_i (%)	5.0					
T_i (%)	0.202	0.202	0.219	0.095	0.309	0.309
p_i (%)	0.538	0.583	0.102	0.044	0.047	0.047
$\mathrm{d}p_i/\,\mathrm{d}t$ (%)	15.0					
$\mathrm{d}T_i/\,\mathrm{d}t$ (%)	15.0					
$\dot{m}''$ (%)	17.06	16.82	16.58	16.58	15.97	16.03

The uncertainty in the mass flow correction terms (last row in above table) for a single plenum was estimated by

$$\sigma^{\%}_{\dot{m}_i''} = \left[\left(\frac{V_i}{\dot{m}_i'' R T_i}\right)^2 \left(\frac{\mathrm{d}p_i}{\mathrm{d}t} - \frac{p_i}{T_i}\frac{\mathrm{d}T_i}{\mathrm{d}t}\right)^2 \sigma^{\%\,2}_{V_i} + \left(\frac{p_i V_i}{\dot{m}_i'' R T_i^2}\frac{\mathrm{d}T_i}{\mathrm{d}t}\right)^2 \sigma^{\%\,2}_{p_i} + \left(\frac{V_i}{\dot{m}_i'' R T_i}\right)^2 \left(\frac{2p_i}{T_i}\frac{\mathrm{d}T_i}{\mathrm{d}t} - \frac{\mathrm{d}p_i}{\mathrm{d}t}\right)^2 \sigma^{\%\,2}_{T_i} + \left(\frac{V_i}{\dot{m}_i'' R T_i}\frac{\mathrm{d}p_i}{\mathrm{d}t}\right)^2 \sigma^{\%\ 2}_{\frac{\mathrm{d}p_i}{\mathrm{d}t}} + \left(\frac{p_i V_i}{\dot{m}_i'' R T_i^2}\frac{\mathrm{d}T_i}{\mathrm{d}t}\right)^2 \sigma^{\%\ 2}_{\frac{\mathrm{d}T_i}{\mathrm{d}t}}\right]^{1/2} \tag{A2.11}$$

The correction terms for the hub and case coolant streams require V5 and V6 plena respectively only, so no further work on this required. However, the mainstream is determined

by considering plena V1-V4. The mainstream unsteady mass flow correction term, $\sigma^{\%}_{\dot{m}''}$, is the sum of all unsteady mass flow correction terms for V1-V4, i.e., this equals -0.1447 kg/s. To find the bias uncertainty in the mainstream mass flow correction term, the following is required

$$\sigma^{\%}_{\dot{m}''} = \left[\sum_{i=1}^{4}\left(\frac{\dot{m}''_i}{\dot{m}''}\right)^2 {\sigma^{\%}_{\dot{m}''_i}}^2\right]^{1/2}$$

$$= \left[\left(\frac{0.1073}{0.1447}\right)^2 (17.06)^2 + \left(\frac{0.0268}{0.1447}\right)^2 (16.82)^2 \right. \quad \text{(A2.12)}$$

$$\left. + \left(\frac{0.0084}{0.1447}\right)^2 (16.58)^2 + \left(\frac{0.0022}{0.1447}\right)^2 (16.58)^2\right]^{1/2} = \pm 13.0682\%$$

A2.6 – Corrected mass flow terms

The uncorrected mass flow term ($\dot{m}$), the mass flow correction term ($\dot{m}''$), and the actual mass flow delivered to the vane ($\dot{m}'$) is shown in the table below

Table A2.2: Nominal values and bias uncertainties for all mass flow rates.

	Mainstream V1-V4	Case coolant V5	Hub Coolant V6
Nominal values			
$\dot{m}$ (kg/s)	12.563	0.1876	0.7041
$\dot{m}''$ (kg/s)	0.1447	0.0025	0.0019
$\dot{m}'$ (kg/s)	12.708	0.1901	0.7060
Bias uncertainty ($\sigma^{\%}$)			
$\dot{m}$ (%)	0.275	1.111	0.637
$\dot{m}''$ (%)	13.068	15.97	16.03
$\dot{m}'$ (%)	0.310	1.116	0.637

As an example, the bias uncertainty in the corrected mass flow rate was determined by the following expression

$$\sigma^{\%}_{\dot{m}'} = \sqrt{\left(\frac{\dot{m}}{\dot{m}'}\right)^2 {\sigma^{\%}_{\dot{m}}}^2 + \left(\frac{\dot{m}''}{\dot{m}'}\right)^2 {\sigma^{\%}_{\dot{m}''}}^2} = \sqrt{(0.9886)^2(0.275)^2 + (0.0114)^2(13.068)^2} \quad \text{(A2.13)}$$

$$= \pm 0.310\%$$

A2.7 – Final capacity value uncertainty

To estimate the measurement uncertainty in the final capacity value, we must first determine the measurement uncertainty in the individual capacity terms. This is determined, for example, for the mainstream term as below

$$\sigma^{\%}_{\Gamma_{\mathrm{ms}}} = \sqrt{{\sigma^{\%}_{\dot{m}'}}^2 + {\sigma^{\%}_{p_{07}}}^2 + {\sigma^{\%}_{T_{07}}}^2} = \sqrt{0.310^2 + 0.044^2 + 0.25 \times 0.095^2} = \pm 0.317\% \qquad \text{(A2.14)}$$

Similarly, $\sigma^{\%}_{\Gamma_{\mathrm{hc}}} = \pm 0.657\%$ and $\sigma^{\%}_{\Gamma_{\mathrm{cc}}} = \pm 1.128\%$. Now finally, going back to the original form of the exit capacity equation, the measurement uncertainty in the vane exit capacity is

$$\sigma^{\%}_{\Gamma_{\mathrm{vane}}} = \sqrt{\left(\frac{\Gamma_{\mathrm{ms}}}{\Gamma_{\mathrm{vane}}}\right)^2 {\sigma^{\%}_{\Gamma_{\mathrm{ms}}}}^2 + \left(\frac{\Gamma_{\mathrm{hc}}}{\Gamma_{\mathrm{vane}}}\right)^2 {\sigma^{\%}_{\Gamma_{\mathrm{hc}}}}^2 + \left(\frac{\Gamma_{\mathrm{cc}}}{\Gamma_{\mathrm{vane}}}\right)^2 {\sigma^{\%}_{\Gamma_{\mathrm{cc}}}}^2} = \pm 0.299\% \qquad \text{(A2.15)}$$

For completeness, the single run precision error in our experiments of exit capacity was evaluated to be $\pm 0.113\%$. In our method, we repeated a run at least sixteen times reducing this error to $0.113/\sqrt{16} = \pm 0.028\%$. This means our combined uncertainty (both bias and precision error) is $\sqrt{0.299^2 + 0.028^2} = \pm 0.300\%$.

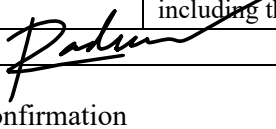
Statements of authorship

Chapter 4 – Statement of authorship

The statement shall describe the candidate's and co-authors' independent research contributions in the thesis publications.

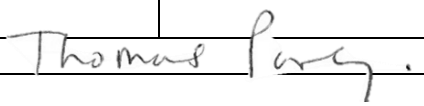
Title of paper	Impact of Trailing Edge Damage on Nozzle Guide Vane Aerodynamic Performance	
Publication status	■ Published	□ Accepted for Publication
	□ Submitted for Publication	□ Unpublished and unsubmitted work written in a manuscript style
Publication details	Raduev, Z., Jackson, D., Chowdhury, N., and Povey, T., 2025, "Impact of Trailing Edge Damage on Nozzle Guide Vane Aerodynamic Performance," ASME J. Turbomachinery, 147(10), DOI: 10.1115/1.4067930.	

Student confirmation

Student name	Zelimhan Raduev		
Contribution to the paper	Zelimhan Raduev (student): determined burn-back designs; collected all experimental data; performed all simulations; wrote processing scripts of experimental and numerical data; analysed all experimental and numerical data; generated all figures; and was responsible for the manuscript writing. Dougal Jackson (industry contact): provided engine parts for experiments; provided deterioration data so burn-back designs can be determined; and contributed with analysis ideas. Nafiz Chowdhury (research associate): supported experimental campaign helping collect all experimental data. Thomas Povey (supervisor): supervised all aspects of the work, including the writing of the published papers.		
Signature		Date	14/02/2025

Supervisor confirmation

By signing the Statement of Authorship, you are certifying that the candidate made a substantial contribution to the publication, and that the description described above is accurate.

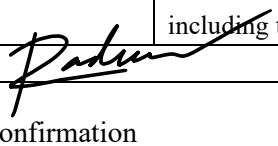
Supervisor name and title	Prof. Thomas Povey		
Supervisor comments	These authorship statements are accurate.		
Signature		Date	28/03/2025

Chapter 5 – Statement of authorship

The statement shall describe the candidate's and co-authors' independent research contributions in the thesis publications.

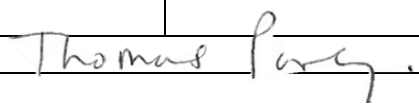
Title of paper	Impact of Trailing Edge Damage on Nozzle Guide Vane Flow Capacity	
Publication status	■ Published	□ Accepted for Publication
	□ Submitted for Publication	□ Unpublished and unsubmitted work written in a manuscript style
Publication details	Raduev, Z., Jackson, D., Chowdhury, N., and Povey, T., 2025, "Impact of Trailing Edge Damage on Nozzle Guide Vane Flow Capacity," ASME J. Turbomachinery, 148(3), DOI: 10.1115/1.4069602.	

Student confirmation

Student name	Zelimhan Raduev		
Contribution to the paper	Zelimhan Raduev (student): determined burn-back designs; collected all experimental data; performed all simulations; wrote processing scripts of experimental and numerical data; analysed all experimental and numerical data; generated all figures; and was responsible for the manuscript writing. Dougal Jackson (industry contact): provided engine parts for experiments; provided deterioration data so burn-back designs can be determined; and contributed with analysis ideas. Nafiz Chowdhury (research associate): supported experimental campaign helping collect all experimental data. Thomas Povey (supervisor): supervised all aspects of the work, including the writing of the published papers.		
Signature		Date	17/01/2025

Supervisor confirmation

By signing the Statement of Authorship, you are certifying that the candidate made a substantial contribution to the publication, and that the description described above is accurate.

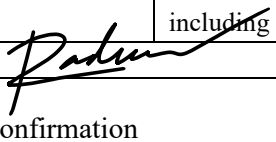
Supervisor name and title	Prof. Thomas Povey		
Supervisor comments	These authorship statements are accurate.		
Signature		Date	28/03/2025

Chapter 6 – Statement of authorship

The statement shall describe the candidate's and co-authors' independent research contributions in the thesis publications.

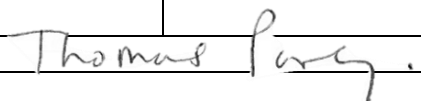
Title of paper	Impact of Nozzle Guide Vane Trailing Edge Damage on High Pressure Turbine Stage Performance	
Publication status	■ Published	□ Accepted for Publication
	□ Submitted for Publication	□ Unpublished and unsubmitted work written in a manuscript style
Publication details	Raduev, Z., Jackson, D., and Povey, T., 2026, "Impact of Nozzle Guide Vane Trailing Edge Damage on High Pressure Turbine Stage Performance," ASME J. Turbomachinery, 148(8), DOI: 10.1115/1.4071186.	

Student confirmation

Student name	Zelimhan Raduev		
Contribution to the paper	Zelimhan Raduev (student): determined burn-back designs; performed all simulations; wrote processing scripts of numerical data; analysed numerical data; generated all figures; and was responsible for the manuscript writing. Dougal Jackson (industry contact): provided deterioration data so burn-back designs can be determined; provided base simulation model that was the foundation of this work; provided significant support with industry software used; and contributed with analysis ideas. Thomas Povey (supervisor): supervised all aspects of the work, including the writing of the published papers.		
Signature		Date	28/03/2025

Supervisor confirmation

By signing the Statement of Authorship, you are certifying that the candidate made a substantial contribution to the publication, and that the description described above is accurate.

Supervisor name and title	Prof. Thomas Povey		
Supervisor comments	These authorship statements are accurate.		
Signature		Date	28/03/2025